Combustion Stabilization, Structure, and Spreading in a Laboratory Dual-Mode Scramjet Combustor

by

Daniel James Micka

A dissertation submitted in partial fulfillment
of the requirements for the degree of
Doctor of Philosophy
(Aerospace Engineering)
in The University of Michigan
2010

Doctoral Committee:

Professor James F. Driscoll, Chair
Professor Arvind Atreya
Assistant Professor Matthias Ihme
Campbell D. Carter, Air Force Research Laboratory
Mark R. Gruber, Air force Research Laboratory

Dedicated to my brother Abram

ACKNOWLEDGEMENTS

My time at Michigan has been both enriching and enjoyable, mostly due to the friends and co-workers I have gotten to know here. I could not have asked for a better advisor than Prof. Driscoll. He has been patient and accommodating almost to a fault. He allowed me great freedom to explore, while always providing sound guidance and technical expertise. I will truly miss our planned one hour meetings which frequently extended into three hour discussions about everything from scramjets to good food and wine.

I would also like to thank my other committee members who have all made this work possible. Cam Carter has gone out of his way to provide help at all stages of my thesis, from loaning equipment to always being available to discuss my latest diagnostics problem. Mark Gruber has been an invaluable resource in helping me to understand the broad field of scramjet propulsion and how I can find a niche for my work. Prof. Ihme has provided a modeling perspective that I am often lacking and I am thankful for that. Thanks to Prof. Atreya for agreeing to serve and for your input. I also owe a special thanks to John Tam at Taitech for providing the CFD simulations of my experiment.

My friends and co-workers have also been a big part of my work. I came to Michigan at the same time as Adam "MMT" Steinberg and Alex "Physco" Schumaker and we worked in the same office (cage) together for five years. We had many fruitful conversations about research, and many more pointless but enjoyable conversations about turguckenens, the plausibility of knife hunting deer, and how nothing good has ever come out of Ohio. So thanks Adam and Alex. While I might have graduated sooner had I been in a quieter office, I wouldn't have had it any other way.

Others in the department have also been a big help and I will remember them fondly. Chad Rasmussen was a great mentor when I first started at Michigan. Andy Lapsa was like an honorary member of the Driscoll group and sings a solid YMCA. Sulabh Dhanuka taught me the importance of a sales pitch during presentations and we amazingly had almost no conflicts sharing air tanks for our research. Jacob, Nansi, Sean, Matt, and Derek are more recent additions to the lab who I'm sure will keep the group strong. Good luck to Matt Fotia in taking over my lab and thanks for the processing work. Eric Kirk, Tom Griffin, Dave McClean, and Terry Larrow provided excellent technical support and went out of their way to make my work a success. Denise Phelps has been a big help in many ways and I will miss her stopping by my office for cokes every day.

Many other friends have made my time here memorable. While I was friend with Shawn O before coming to Michigan, we had a lot of great times here. Shawn and I learned important things together like fireworks are outside toys and a gallon of pudding is not a single serving size. I probably should have mentioned Hyce in the work section because her cookies and cakes were instrumental in keeping me fueled for research. Watch out for Hyce on the broomball ice, she's an animal. Also watch out for Erin around a turkey carcass, you might lose a finger. Tailgates at Prashant's house were a staple of my time at Michigan and I enjoyed hanging out with Adam, Alex, Hyce, Andy, Shawn, Matt, Evan, Erin, Kristina, Elena and many others at these events.

Finally, I'd like to thank my family. I would not be here without their support and encouragement. I am incredibly grateful for the example my parents have set and the path they have led me down.

TABLE OF CONTENTS

DEDICATION . . . . **ii**

ACKNOWLEDGEMENTS . . . . **iii**

LIST OF FIGURES . . . . **viii**

LIST OF TABLES . . . . **xiv**

NOMENCLATURE . . . . **xv**

CHAPTER

I. Introduction **1**

1.1 Dual-Mode Scramjet Background 1
  1.1.1 High Speed Air-breathing Propulsion 1
  1.1.2 Dual-Mode Combustion 2
  1.1.3 Dual-Mode Scramjet Combustion Issues 5
1.2 Previous Work 8
  1.2.1 Proposed Combustor Geometries 9
  1.2.2 Experimental Scramjet Combustor Studies 10
  1.2.3 CFD and Combustion Modeling in Scramjet Combustors 14
1.3 Objectives of the Current Study 15
  1.3.1 Combustion Stabilization 16
  1.3.2 Reaction Zone Imaging 17
  1.3.3 Heat Release Distribution 17
  1.3.4 CFD++ Simulation 18

II. Experimental Facilities and Diagnostics **19**

2.1 University of Michigan Supersonic Combustion Laboratory 19
  2.1.1 Vitiated Air Heater and Piping 20
  2.1.2 Dual-mode Scramjet Combustor 25
  2.1.3 Flow Control 30
  2.1.4 Test Procedure 31
  2.1.5 Vitiator Exit Measurements 32
2.2 Test Conditions 35
2.3 Wall Pressure Measurements 38
2.4 Combustion Luminosity Imaging 39
  2.4.1 High Speed Combustion Luminosity Imaging 39
  2.4.2 CH* and OH* Imaging 40
2.5 Planar Laser Induced Fluorescence Imaging 42
  2.5.1 CH PLIF 42
  2.5.2 Simultaneous OH and Formaldehyde PLIF 49

2.6 Computational Fluid Dynamics Approach . . . 61
    2.6.1 Method . . . 61
    2.6.2 Conditions . . . 62

III. Combustion Stabilization and Dynamics . . . 65

3.1 Upstream Fuel Injection . . . 65
    3.1.1 Combustion Stabilization Modes . . . 66
    3.1.2 Ramjet-mode Dynamics . . . 76
    3.1.3 Discussion of Mechanisms . . . 84
    3.1.4 Comparison with CFD solution . . . 97
3.2 Downstream Fuel Injection . . . 99
3.3 Ram-to-Scram Mode Transition . . . 105

IV. Reaction Zone Structure . . . 109

4.1 Run Conditions . . . 109
4.2 CH-PLIF Results . . . 111
    4.2.1 CH-PLIF of Cavity Stabilized Combustion . . . 112
    4.2.2 CH-PLIF of Jet-Wake Stabilized Combustion . . . 115
4.3 Simultaneous OH/Formaldehyde-PLIF Results . . . 122
    4.3.1 OH/Formaldehyde-PLIF of Cavity Stabilized Combustion . . . 127
    4.3.2 OH/Formaldehyde-PLIF of Jet-Wake Stabilized Combustion . . . 132
4.4 Combustion Mechanisms . . . 139
    4.4.1 Pure Flame . . . 139
    4.4.2 Pure Auto-ignition . . . 146
    4.4.3 Auto-ignition Assisted Flame . . . 148

V. Heat Release Distribution . . . 150

5.1 Run Conditions . . . 150
5.2 Wall Pressure and Quasi-One-Dimensional Data Analysis Model . . . 150
5.3 OH* and CH* Distributions . . . 159
    5.3.1 Comparison of OH* and CH* Results . . . 162
    5.3.2 Cavity Stabilized Combustion . . . 162
    5.3.3 Jet-Wake Stabilized Combustion . . . 167
5.4 Factors Controlling the Heat Release . . . 173
    5.4.1 Jet-Wake Stabilized Combustion . . . 173
    5.4.2 Cavity Stabilized Combustion . . . 178
5.5 Comparison with CFD solution . . . 181

VI. Conclusions and Future Work . . . 186

6.1 Conclusions . . . 186
6.2 Future Work . . . 190

APPENDIX . . . 192

BIBLIOGRAPHY . . . 201

LIST OF FIGURES

Figure

1.1 Specific impulse vs Mach number for different engine types [34]. 2

1.2 Example profiles of pressure and Mach number in a dual-mode scramjet combustor undergoing ram-to-scram transition due to decreasing heat addition (or increasing $T_{0,air}$). The heat addition decreases from profile A to profile D (or $T_{0,air}$ increases from profile A to profile D). Ram-to-scram transition occurs between profiles B and C. Profile C has a weak pre-combustion shock train with a supersonic isolator exit Mach number. 4

2.1 University of Michigan Supersonic Combustion Laboratory air flow schematic. . . . 20

2.2 Variation of air stagnation temperature ($T_{0,air}$) with flight Mach number (M_{flight}) at 75,000 ft altitude. 21

2.3 Vitiator and piping cut-away view. 22

2.4 Average vitiator exit composition. Data from individual runs shown as circular symbols. 2nd order polynomial fits shown as lines and equations. 24

2.5 Test section with dimensions. 26

2.6 Test section photos. 27

2.7 Cavity and fuel injection detail. 28

2.8 Flow and spark timing for a typical run. 32

2.9 Typical time history of the stagnation temperature and pressure measurements in the settling chamber during a run (case 2B conditions). 34

2.10 Illustration of the OH* and CH* luminosity integration. 41

2.11 CH-PLIF system optics arrangement. 44

2.12 CH-PLIF system example flame luminosity images with and without a 390.50 nm laser sheet for case 2B conditions, FOV 1. ICCD 1 and ICCD 2 images acquired 50 ns apart. Air flow is from left to right. 46

2.13 CH-PLIF system example high noise image with 390.50 nm laser sheet showing the effects of luminosity subtraction. The PLIF scale is the same as for the results displayed in Sec. 4.2. Case 2B conditions, FOV 1. Air flow is from left to right. . . 48

2.14 Example instantaneous CH-PLIF image (390.30 nm laser sheet) showing the effects of luminosity subtraction. Case 2B conditions, FOV 1. Air flow is from left to right. 48

2.15 Example simultaneous OH/formaldehyde-PLIF images in a Bunsen burner with an inner rich premixed flame and an outer diffusion flame. 51

2.16 Camera and laser sheet arrangement for simultaneous OH/formaldehyde PLIF. . . 53

2.17 Simultaneous OH/formaldehyde-PLIF system optics arrangement for test section centerline imaging. 55

2.18 Example instantaneous formaldehyde and OH PLIF images with iso-contour from CH_2O image overlaid. Shows flame luminosity interference with CH_2O-PLIF signal. 58

2.19 Diagram of the cross-section formaldehyde PLIF camera and the placement of the metal tabs used to block direct reflections of the laser sheet off window imperfections. 60

2.20 Example processed cross-section PLIF and noise images from formaldehyde camera. Images cover the 25.4 mm by 38.1 mm cross-section of the combustor at $x/H = 0.0$. 61

3.1 Combustion luminosity images averaged over 75 ms for upstream injection of hydrogen fuel. $T_{0,air} = 1250$ K, $\phi = 0.23$, no cavity fueling. Yellow line is an iso-luminosity contour. 67

3.2 Combustion luminosity images averaged over 40 ms for upstream injection of blended fuel (50% ethylene 50% hydrogen). $T_{0,air} = 1370$ K, $\phi = 0.42$, $\dot{m}_{cavfuel}/\dot{m}_{totalfuel} = 0.05$. Yellow line is an iso-luminosity contour. 67

3.3 Histogram of the reaction zone leading edge location based on 22,500 images. Upstream injection of hydrogen with $T_{0,air} = 1130-1400$ K, $\phi = 0.21$, $\dot{m}_{cavfuel}/\dot{m}_{totalfuel} = 0.02$. Luminosity images show example instantaneous cavity and jet-wake reaction zones. Dashed lines illustrate how the reaction zone leading edge is calculated. . . 69

3.4 Reaction zone leading edge signal for a case of oscillation between modes. Upstream injection of hydrogen with $T_{0,air} = 1220$ K, $\phi = 0.27$, $\dot{m}_{cavfuel}/\dot{m}_{totalfuel} = 0.05$. Dashed line represents the division between jet-wake and cavity stabilized combustion. 69

3.5 Combustion stabilization mode vs. $T_{0,air}$ for hydrogen fuel. Upstream main fuel injection, cavity rear wall fueling. 71

3.6 Combustion stabilization mode vs. $T_{0,air}$ for hydrogen fuel and blended fuel with upstream main fuel injection. 71

3.7 Image from Mathur et al [69] showing a cavity stabilized reaction zone structure in a dual-mode combustor. 73

3.8 Average cavity stabilized combustion luminosity for data set A, $T_{0,air} = 1130$ K. Yellow and blue solid lines are iso-luminosity contours of 30 and 50 counts respectively. Dashed lines show the spreading angles determined from each iso-luminosity contour. 74

3.9 Measured reaction zone spreading angles for cavity stabilized combustion mode vs. $T_{0,air}$ for the two values of the critical iso-luminosity contour shown in Fig. 3.8. Solid lines are linear regression fits to the data. 75

3.10 Top view, jet-wake stabilized, average combustion luminosity. H_2 fuel, $T_{0,air} = 1370$ K, $\phi = 0.27$, $\dot{m}_{cavfuel}/\dot{m}_{totalfuel} = 0.07$. 76

3.11 Lift-off distances (l_{ign}) for jet-wake stabilized combustion vs. $T_{0,air}$. Conditions for each set given in Table 3.2. Solid lines are linear regression fits to the hydrogen and blended fuel data. 77

3.12 Wall pressure standard deviation (solid symbols) and average (open symbols) for upstream injection of hydrogen fuel with different stabilization modes. 79

3.13 Figure from Lin et al [64] showing acoustic-convective feedback loops in a scramjet combustor. 80

3.14 Synchronized reaction zone leading edge location and wall pressure data. Upstream hydrogen fuel injection with $\phi = 0.27$, $\dot{m}_{cavfuel}/\dot{m}_{totalfuel} = 0.05$, $T_{0,air} = 1220$ K. 82

3.15 Power spectra of the flamefront location and pressure signal shown in Fig. 3.14. There is no spike due to a resonant mode. 83

3.16 Diagram showing relationship between the turbulent flame speed (S_T), the flow velocity (U), and the flame spreading angle θ. 84

3.17 Temperature dependence of CHEMKIN calculated flame spreading angles and the measured spreading angles. 86

3.18 Image from Ben-Yakar [4] showing an example reaction zone for pure auto-ignition with a negligible ignition delay time. OH-PLIF signal for hydrogen injection into a Mach 3.4 air crossflow with $T_{0,air} = 3750$ K. 88

3.19 Schematic from Yu, Wilson, and Schadow [117] showing a reaction zone similar to jet-wake stabilized combustion. Vitiated fuel ($T_{0,fuel} = 2600$) K consisted of 28% C_2H_4, 36% CO_2, and 36% H_2O. 89

3.20 Calculated ignition distances assuming the combustion is controlled by auto-ignition compared with the measured lift-off distances of jet-wake stabilized combustion. Calculated distance is obtained with CHEMKIN assuming that the local equivalence ratio, static temperature, and Mach number remain constant from injection to ignition. 92

3.21 Flame base stabilization locations. 93

3.22 Typical flash-forward event from cavity stabilized location to jet-wake stabilized location. Hydrogen fuel injection with $\phi = 0.27$, $\dot{m}_{cavfuel}/\dot{m}_{totalfuel} = 0.05$, $T_{0,air} = 1220$ K. High speed movie of combustion luminosity acquired at 4000 frames/sec. 96

3.23 Comparison of the upstream reaction zone computed by CFD++ at case 1C with the experimentally observed reaction zone at case 1H. 98

3.24 Comparison of the upstream reaction zone computed by CFD++ at case 2C with the experimentally observed reaction zone at case 2H. 98

3.25 Reaction zone locations for upstream and downstream injection. 100

3.26 Wall pressure standard deviation (solid symbols) and average (open symbols) for downstream injection of hydrogen fuel for no cavity fueling and $\dot{m}_{cavfuel}/\dot{m}_{totalfuel} = 0.10$. 101

3.27 Flame luminosity images averaged over 1000 ms for downstream main fuel injection of hydrogen. $T_{0,air} = 1250$ K, $\phi = 0.27$, $\dot{m}_{cavfuel}/\dot{m}_{totalfuel} = 0.10$ for cases with cavity fueling. Yellow line is an iso-luminosity contour. Image (b) is blacked out in the rear corner of the cavity due to buildup on the window which was glowing brightly. 102

3.28 Flame luminosity images averaged over 1000 ms for downstream main fuel injection of hydrogen. $T_{0,air} = 1250$ K, $\phi = 0.18$, $\dot{m}_{cavfuel}/\dot{m}_{totalfuel} = 0.10$ for cases with cavity fueling. Yellow line is an iso-luminosity contour. 103

3.29 Figure from Sun et al [91] showing the mechanism of flame spreading for hybrid cavity/jet-wake stabilized combustion with downstream main fuel injection. 105

3.30 Average wall pressure for ramjet mode combustion, scramjet mode combustion, and the no fueling case. Upstream injection of blended fuel at $T_{0,air} = 1270$ K, $\phi = 0.40$, $\dot{m}_{cavfuel}/\dot{m}_{totalfuel} = 0.05$. 107

3.31 Flame luminosity images of scramjet and ramjet mode operation averaged over 50 ms. Upstream injection of blended fuel, $T_{0,air} = 1270$ K, $\phi = 0.40$, $\dot{m}_{cavfuel}/\dot{m}_{totalfuel} = 0.05$. Yellow line is an iso-luminosity contour. The vertical line of increased intensity near the cavity trailing edge is due to camera over-exposure from glowing metal at the rear wall, and is not due to increased combustion in this region. 108

4.1 Mean CH* luminosity for case 1B (cavity stabilized) and case 2B (jet-wake stabilized) conditions shown in false color. 110

4.2 Mean wall pressure for case 1B (cavity stabilized), case 2B (jet-wake stabilized), and the no fueling case. The cavity leading edge is at $x/H = 0$ and the fuel injection is at $x/H = -1.75$. 111

4.3 Mean and instantaneous CH-PLIF images for cavity stabilized case 1B at field of view (FOV) 1. $x/H = -0.15$ to 2.3. 116

4.4 Mean and instantaneous CH-PLIF images for cavity stabilized case 1B at field of view (FOV) 2. $x/H = 2.05$ to 2.5. 117

4.5 Mean and instantaneous CH-PLIF images for cavity stabilized case 1B at field of view (FOV) 3. $x/H = 4.25$ to 6.7 118

4.6 Mean and instantaneous CH-PLIF images for cavity stabilized case 1B at field of view (FOV) 4. $x/H = 6.55$ to 9.0. 119

4.7 Profiles of CH mole fraction (X_{CH}) and gas temperature in a laminar premixed flame at case 1B (cavity stabilized) conditions computed using CHEMKIN. 120

4.8 Mean and instantaneous CH-PLIF images for jet-wake stabilized case 2B at field of view (FOV) 1. $x/H = -0.45$ to 2.0. 123

4.9 Mean and instantaneous CH-PLIF images for jet-wake stabilized case 2B at field of view (FOV) 2. $x/H = 1.8$ to 4.25. 124

4.10 Mean and instantaneous CH-PLIF images for jet-wake stabilized case 2B at field of view (FOV) 3. $x/H = 4.3$ to 6.75. 125

4.11 Mean and instantaneous CH-PLIF images for jet-wake stabilized case 2B at field of view (FOV) 4. $x/H = 6.55$ to 9.0. 126

4.12 Centerline instantaneous OH/CH_2O-PLIF images for case 1B. The OH-PLIF signal is displayed using a color scale while the outer contour of the simultaneous CH_2O-PLIF signal is shown as the white line. Formaldehyde is generally present in the entire region between the white line and the OH. Images (a)-(g) show examples of cavity stabilized combustion. Image (h) shows an example of jet-wake stabilized combustion at case 1B conditions. 130

4.13 Cross-section OH/CH_2O-PLIF images at $x/H = 1.0$ for case 1B, cavity stabilized combustion. The outer contour of the CH_2O-PLIF is shown as a white line in the instantaneous PLIF images. 133

4.14 Cross-section OH/CH_2O-PLIF images at $x/H = 1.8$ for case 1B, cavity stabilized combustion. The outer contour of the CH_2O-PLIF is shown as a white line in the instantaneous PLIF images. 134

4.15 Cross-section OH/CH_2O-PLIF images at $x/H = 3.2$ for case 1B, cavity stabilized combustion. The outer contour of the CH_2O-PLIF is shown as a white line in the instantaneous PLIF images. 135

4.16 Instantaneous PLIF images showing 3D reaction zone structure for case 1B, cavity stabilized combustion. Outer contour of CH_2O-PLIF signal is shown as white line. Images in different planes were acquired at different times. 136

4.17 Centerline instantaneous OH/CH_2O-PLIF images for case 2B (jet-wake stabilized combustion). The OH-PLIF signal is displayed using a color scale while the outer contour of the simultaneous CH_2O-PLIF signal is shown as the white line. Formaldehyde is generally present in the entire region between the white line and the OH. . 137

4.18 Cross-section OH/CH_2O-PLIF images at $x/H = 0.0$ for case 2B, jet-wake stabilized combustion. The outer contour of the CH_2O-PLIF is shown as a white line in the instantaneous PLIF images. 140

4.19 Cross-section OH/CH_2O-PLIF images at $x/H = 1.0$ for case 2B, jet-wake stabilized combustion. The outer contour of the CH_2O-PLIF is shown as a white line in the instantaneous PLIF images. 141

4.20 Cross-section OH/CH_2O-PLIF images at $x/H = 1.8$ for case 2B, jet-wake stabilized combustion. The outer contour of the CH_2O-PLIF is shown as a white line in the instantaneous PLIF images. 142

4.21 Cross-section OH/CH_2O-PLIF images at $x/H = 3.2$ for case 2B, jet-wake stabilized combustion. No formaldehyde is present at this location. Signal seen in formaldehyde images is due to reflections of pump beam off imperfections in the window (see Sec. 2.4.2). 143

4.22 Structure of the jet-wake stabilized reaction zone based on the formaldehyde and OH PLIF images. The location of the PLIF imaging planes are labeled. 144

4.23 Instantaneous PLIF images showing 3D reaction zone structure for case 2B, jet-wake stabilized combustion. Outer contour of CH_2O-PLIF signal is shown as white line. Images in different planes were acquired at different times. 144

4.24 Expected reaction zone structure for cavity and jet-wake stabilized combustion occurring as a pure flame (no chemical reactions upstream of the flame preheat zone).146

4.25 Expected reaction zone structure for combustion occurring as pure auto-ignition (no diffusion of heat from the reaction zone). 148

4.26 Reaction zone structure for cavity and jet-wake stabilized combustion occurring as an auto-ignition assisted flame. Finite rate kinetics occur well upstream of the reaction zone. Diffusion of heat and radicals is important in the flame preheat layer.149

5.1 Mean wall pressure distribution for cases 1B (cavity stabilized) and 2B (jet-wake stabilized) with spline fit used in the data analysis model. 152

5.2 Mean wall pressure distribution for cases 1H (cavity stabilized) and 2H (jet-wake stabilized) with spline fit used in the data analysis model. 153

5.3 Case 1B distribution of combustion efficiency and its axial derivative calculated by the 1-D data analysis model (from the measured wall pressure) with different assumed (constant) wall temperatures. 155

5.4 Case 2B distribution of combustion efficiency and its axial derivative calculated by the 1-D data analysis model (from the measured wall pressure) with different assumed (constant) wall temperatures. 156

5.5 Case 1H distribution of combustion efficiency and its axial derivative calculated by the 1-D data analysis model (from the measured wall pressure) with different assumed (constant) wall temperatures. 157

5.6 Case 2H distribution of combustion efficiency and its axial derivative calculated by the 1-D data analysis model (from the measured wall pressure) with different assumed (constant) wall temperatures. 158

5.7 Distribution of flow variables calculated by the 1-D data analysis model (from the measured wall pressure) for cases 1B and 2B. 160

5.8 Distribution of flow variables calculated by the 1-D data analysis model (from the measured wall pressure) for cases 1H and 2H. 161

5.9 Mean CH* luminosity for case 1B and 2B conditions shown in false color. 163

5.10 Mean OH* luminosity for case 1B and 2B conditions shown in false color. 163

5.11 1-D CH* and OH* signals for cases 1B and 2B. Signals are normalized by the area under the curve ($\int I_{OH^*} dx$ and $\int I_{CH^*} dx$). 164

5.12 Mean OH* luminosity for case 1H and 2H conditions shown in false color. 165

5.13 1-D OH* signals for cases 1B, 2B, 1H, and 2H. Signals are normalized by the area under the curve ($\int I_{OH^*} dx$). 166

5.14 Mean OH* luminosity for data set E shown in false color. Conditions are listed in Table 5.1. 169

5.15 1-D OH* signals for data set E with and without the signal from the wall cavity included. $T_{0,air}$ is varied. Signals are normalized by the area under the curve ($\int I_{OH^*} dx$). 170

5.16 Mean OH* luminosity for data set F shown in false color. Conditions are listed in Table 5.1. 171

5.17 1-D OH* signals for data set F with and without the signal from the wall cavity included. Equivalence ratio is varied. 172

5.18 1-D OH* signal for data set F (solid lines) and extrapolated linear best fit lines (dashed lines). Data was acquired up to the end of the window at approximately $x/H = 9.5$. Linear regression lines fit to the data from $x/H = 5.5$ to 9.5 are shown as dashed lines for $x/H > 9.5$. 174

5.19 Total area under the extrapolated $I_{OH^*}(x)$ curves in Fig. 5.18 vs. the overall equivalence ratio. A linear regression fit which passes through origin is shown as a solid line. 174

5.20 Measured flame length vs. ϕ for data set F conditions. The flame length $l_{90\%}$ is the distance between the fuel injection location and the location where the area under the $I_{OH^*}(x)$ curve shown in Fig. 5.18 is 90% of the total area. This is approximately equal to the length it takes for 90% of the heat release to occur. A linear regression fit is shown as a solid line. 175

5.21 Illustration of the factors limiting the heat release rate in different regions for cavity (case 1B) and jet-wake stabilized combustion (case 2B). 176

5.22 1-D OH* signals with and without the co-flow mixing correction applied. Cavity reaction excluded. 179

5.23 Fuel distribution in the jet-wake cross section (y-z plane) at x/H=1.0 as computed by non-reacting CFD++ at case 1H conditions. The fuel mass flow rate per unit height through this plane ($\dot{m}_f(y)$) is also shown. 181

5.24 Axial distribution of the heat release rate per unit length ($\dot{Q}(x)$) calculated by CFD++ and measured experimentally. The experimental heat release distribution was obtained from the OH* chemiluminescence. 183

5.25 Mean wall pressure calculated by CFD++ and measured experimentally. 185

LIST OF TABLES

Table

2.1 Test conditions for upstream main fuel injection ($x/H = -1.75$) tests. High speed chemiluminescence imaging and wall pressure measurements performed. 37

2.2 Test conditions for data sets A-D. Upstream main fuel injection ($x/H = -1.75$). High speed chemiluminescence imaging and wall pressure measurements performed. 37

2.3 Test conditions for downstream main fuel injection ($x/H = -0.55$). High speed chemiluminescence imaging and wall pressure measurements performed. 37

2.4 Baseline cavity and jet-wake stabilized cases for hydrogen and blended fuel. Detailed wall pressure distribution and OH* luminosity obtained for all cases. PLIF images and CH* luminosity obtained for blended fuel cases 1B and 2B. 38

2.5 Test conditions for data sets E and F. OH* luminosity images and wall pressure measurements obtained. 38

2.6 Run conditions for CFD++ simulations. 63

2.7 Major species mole fractions of vitiated air used in CFD simulations. 63

2.8 Minor species mole fractions of vitiated air used in CFD simulations. 64

3.1 Test conditions for upstream main fuel injection ($x/H = -1.75$) tests. High speed chemiluminescence imaging and wall pressure measurements performed. 66

3.2 Test conditions for determining fraction of time spent in each stabilization mode for upstream main fuel injection ($x/H = -1.75$). 70

3.3 Test conditions for downstream main fuel injection ($x/H = -0.55$). 100

4.1 Test conditions for PLIF imaging of the reaction zone structure. 110

5.1 Test conditions for OH* and CH* chemiluminescence measurements. 150

NOMENCLATURE

Symbols

A	Area
A^*	Throat area
C	Multiple scaling and proportionality constants
c_p	constant pressure specific heat
$c_{p,i}$	constant pressure specific heat of species i
$\overline{c_p}$	Mixture average constant pressure specific heat
d_{inj}	Main fuel injection orifice diameter
e_{OH^*}, e_{CH^*}	Emission intensity of OH* or CH* chemiluminescence per unit volume
f	Fraction of time the combustion is located in the jet-wake stabilized combustion mode
H	Test section height in the constant area isolator (y-direction)
i_{OH^*}, i_{CH^*}	Intensity of OH* or CH* chemiluminescence recorded by camera per unit area
I_{OH^*}, I_{CH^*}	Intensity of OH* or CH* chemiluminescence recorded by camera per unit length
J_0	Drag imposed by the transverse fuel jet
l_{ign}	Lift-off distance between the fuel injection and the start of the reaction zone
$l_{90\%}$	Flame length based on distance required for 90% of the heat release to occur
$\dot{m}$	Mass flow rate
$\dot{m}_f(y)$	Mass flux rate of fuel through the $y - z$ plane integrated in the z direction
$\dot{m}_i$	Mass flow rate of species i
$\dot{m}_{tot}$	Total mass flow rate
M	Mach number
M_{flight}	Flight Mach number
$M_{i,entrance}$	Isolator entrance Mach number
$M_{i,exit}$	Isolator exit Mach number
MW	Molecular weight
MW_i	Molecular weight of species i
$\overline{MW}$	Mixture average molecular weight

P	Static pressure
P_w	Wall static pressure
$\overline{P_w}$	Time average of wall static pressure
P^*	Static pressure at the nozzle throat
P_0	Stagnation pressure
$P_{0,i}$	Air stagnation pressure in the settling chamber
$\dot{q}$	Heat release rate per unit volume
$\dot{Q}$	Heat release rate per unit length
$\Re$	Universal gas constant
S_L	Laminar flame speed
S_T	Turbulent flame speed
T	Static temperature
$\overline{T}$	Mixture average static temperature
T_w	Wall temperature
T^*	Static temperature at the nozzle throat
T_0	Stagnation temperature
$\overline{T_0}$	Mixture average stagnation temperature
$T_{0,air}$	Stagnation temperature of air or vitiated air
u	Axial flow velocity
u_c	Jet or wake centerline flow velocity
u_∞	Freestream axial flow velocity
W	Test section width (z-direction)
x	Axial location in the test section measured from the cavity leading edge
X_i	Mole fraction of species i
y	Vertical location in test section measured from the top of the cavity
Y_i	Mass fraction of species i
z	Spanwise location in test section measured from the side wall

Greek

γ	Ratio of specific heats
γ_i	Ratio of specific heats of species i
$\overline{\gamma}$	Mixture average ratio of specific heats
γ^*	Ratio of specific heats at the nozzle throat
$\eta_c(x)$	Combustion efficiency up to location x ($\dot{m}_{fuel,burned}(x)/\dot{m}_{fuel,injected}$)

σ	Standard deviation
ϕ	Fuel-air equivalence ratio

Acronyms

CFD	Computational fluid dynamics
FOV	Field of view
ICCD	Intensified charge-coupled device camera
LES	Large eddy simulations
LIF	Laser-induced fluorescence
PAH	Polycyclic aromatic hydrocarbons
PLIF	Planar laser-induced fluorescence
RANS	Reynolds averaged Navier-Stokes

CHAPTER I

Introduction

1.1 Dual-Mode Scramjet Background

1.1.1 High Speed Air-breathing Propulsion

Scramjets have the potential to provide efficient air-breathing propulsion at high flight Mach numbers (M_{flight}). Figure 1.1 shows how the specific impulse varies with Mach number for different engine types. Turbofans and turbojets are the preferred choice for propulsion from mid subsonic speeds up to approximately Mach 3. At higher speeds the temperature limitations of the turbine blades and shock losses in the turbomachinery pose severe problems. At these speeds it is best to remove the compressor and turbine and use the ram effect of the air for compression. This type of engine is a ramjet. In traditional ramjets the flow is slowed to low subsonic speeds before the combustion [34]. Ramjets consist of a duct with a converging diverging nozzle inlet, a constant area section where the combustion occurs at relatively low subsonic speeds, and a converging diverging nozzle where the exhaust is re-accelerated to supersonic speeds.

As the flight Mach number increases ramjets suffer rising losses caused by shock waves and air dissociation due slowing the flow to subsonic speeds. For $M_{flight} \gtrsim 6$ it is most efficient to have the flow remain supersonic throughout the engine [34]. Ramjets in which the combustion occurs at supersonic conditions are called scramjets.

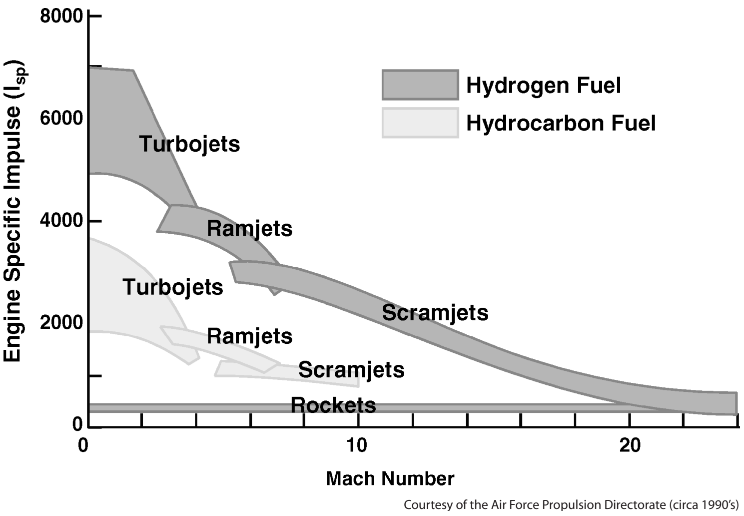

Figure 1.1: Specific impulse vs Mach number for different engine types [34].

Scramjets can not have the converging diverging nozzle in the inlet and nozzle that subsonic combustion ramjets have. Scramjets consist of a duct with a decreasing area inlet, a constant area or slightly diverging section where fuel is added, and a diverging nozzle where the supersonic exhaust is accelerated.

1.1.2 Dual-Mode Combustion

Ramjets and scramjets do not produce thrust at zero flight speed since there is no ram effect to provide compression. These engines must be accelerated to an initial speed by some other propulsion system, usually a rocket or turbojet. This initial flight speed is typically Mach 2-3 for ramjets and Mach 5-6 for scramjets. It is desirable to have an engine that can operate as both a ramjet and a scramjet with a fixed geometry. Such an engine is called a dual-mode ramjet/scramjet, or simply a dual-mode scramjet. Dual-mode scramjets retain the high speed capability of scramjets while allowing the lower initial boost speed of ramjets.

Dual-mode scramjets have the same basic geometry as the scramjet mentioned in Sec. 1.1.1. A dual-mode scramjet, however, must have an isolator to contain a pre-combustion shock train and a diverging section in the combustor. The engine operates in the ramjet mode at low flight Mach numbers due to the presence of a thermal throat. The start of the reaction zone is subsonic, but the heat addition from the combustion drives the flow to Mach 1. The thermal throat sets a boundary condition which causes a pre-combustion shock train to be formed. The pre-combustion shock train in the isolator slows the flow to subsonic conditions before the start of the reaction zone. The quasi-1-dimensional differential equation that relates heat addition (represented by dT_0), area change, and Mach number is given by Eq. 1.1.

$$\frac{1}{M}\frac{dM}{dx} = \left(\frac{1+\frac{\gamma-1}{2}M^2}{1-M^2}\right)\left(\frac{1}{A}\frac{dA}{dx} + \frac{1+\gamma M^2}{2}\left(\frac{1}{T_0}\frac{dT_0}{T_0}\right)\right) \tag{1.1}$$

Curran, Heiser, and Pratt [21, 53] explain why the thermal throat must be located in a diverging section of the combustor. A 1-D stability analysis indicates that for a fixed area thermal throat, there is a single value of heat release that can occur such that the flow is choked and the mass flow through the thermal throat is equal to the incoming mass flow. If this second condition is not met, the shock train will move outside of the isolator and decrease the mass flow through the engine. This phenomena is referred to as isolator unstart.

As a dual-mode combustor accelerates, the isolator entrance Mach number ($M_{i,entrance}$) and stagnation temperature increase. For a fixed amount of heat release this causes the pre-combustion shock train to become weaker (resulting in a lower pressure rise and higher exit Mach number). The thermal throat moves to a smaller area. Eventually the isolator entrance Mach number and incoming air stagnation temperature ($T_{0,air}$) become large enough that the heat release is no longer sufficient to choke the flow. At this point the strong pre-combustion shock train is swallowed and the flow remains supersonic throughout the engine. This is called scramjet mode operation.

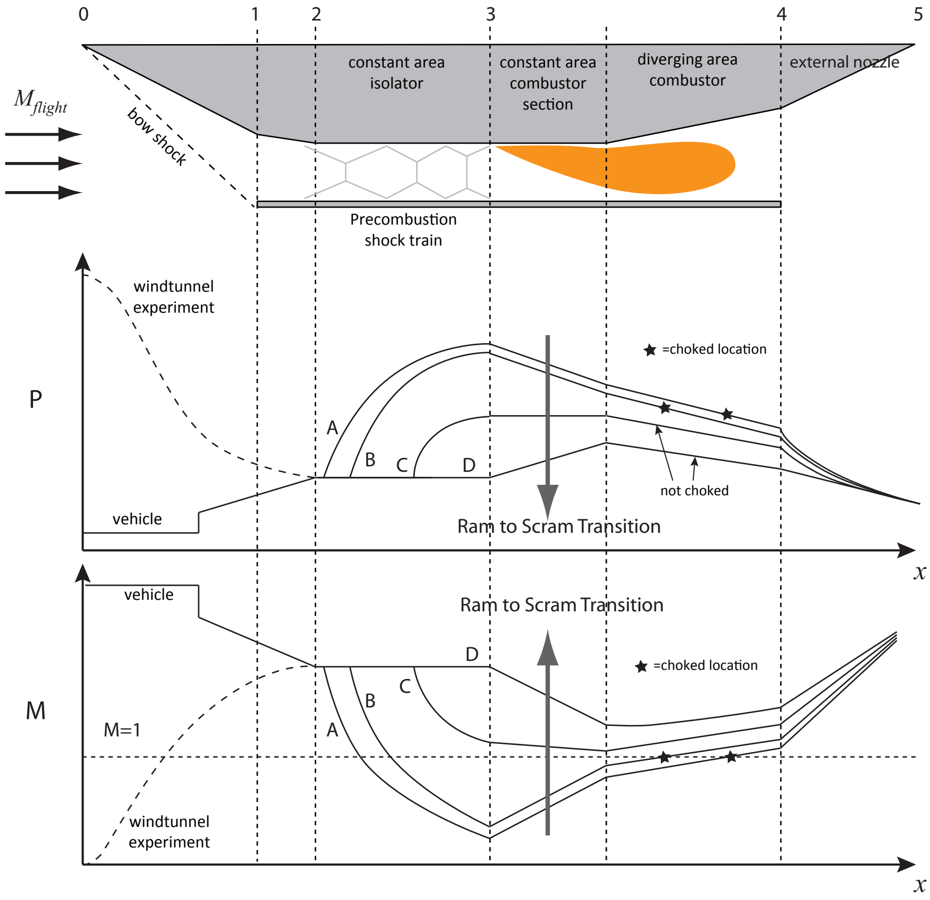

Figure 1.2: Example profiles of pressure and Mach number in a dual-mode scramjet combustor undergoing ram-to-scram transition due to decreasing heat addition (or increasing $T_{0,air}$). The heat addition decreases from profile A to profile D (or $T_{0,air}$ increases from profile A to profile D). Ram-to-scram transition occurs between profiles B and C. Profile C has a weak pre-combustion shock train with a supersonic isolator exit Mach number.

There is a step change in the isolator exit Mach number at the ram-to-scram transition. Figure 1.2 illustrates how the pressure and Mach number varies through a dual-mode combustor during a mode transition. For simplicity, the profiles in Fig. 1.2 are drawn for a fixed incoming Mach number. The ram-to-scram transition is caused by decreasing $\Delta T_0/T_{0,air}$ (either by decreasing the amount of heat release or increasing $T_{0,air}$).

1.1.3 Dual-Mode Scramjet Combustion Issues

1.1.3.1 Combustion Stabilization and Mechanism

Combustion stabilization is a significant challenge in dual-mode scramjet combustors due to the high velocities involved. There are two distinct mechanisms for combustion stabilization; premixed flame propagation and auto-ignition. Both are expected to be important for the range of conditions over which dual-mode scramjet combustors operate.

A premixed flame is characterized by a thin reaction layer with high temperature and species concentration gradients [101]. It propagates into a reactant mixture at the flame speed S_L (laminar) or S_T (turbulent). Diffusion of heat from the reaction layer raises the temperature of the incoming reactants to above the ignition temperature in the preheat layer. Combustion then occurs in the reaction layer. The laminar flame speed S_L is set by the finite rate kinetics and the thermal diffusivity of the reactants.

For auto-ignition controlled reactions the heat release from the combustion does not play a role in initiating or sustaining the reactions. The reactants are initially heated to a temperature that is above the ignition temperature by some external means. Combustion occurs once the auto-ignition delay time has been reached. This auto-ignition delay time is controlled by the finite rate kinetics that are associated with the reactant mixture initial conditions. The combustion is not a propagating wave so the local flow speed does not determine the stabilization location. The convection distance during the auto-ignition delay time is set by the integrated flow speed however.

At low flight Mach numbers the incoming air stagnation temperature $T_{0,air}$ is insufficient for auto-ignition, or the ignition delay time is very long. Under these conditions, the base of the reaction zone must be stabilized as flame. A premixed flame base is located in a region of proper equivalence ratio, temperature, and pressure where the local flame speed is equal to the local flow speed (on average). At very high flight Mach numbers $T_{0,air}$ is very large and the auto-ignition delay time is negligible. Therefore the fuel burns as soon as it mixes with the air. The combustion problem then reduces to a mixing problem. For an intermediate range of flight Mach numbers, $T_{0,air}$ is above the auto-ignition temperature, but the ignition delay time is not negligible. For these conditions both auto-ignition and flame properties may be important.

It is of practical importance to understand the combustion mechanism from a design and modeling perspective. In the flame regime flame stabilization and stability are two primary considerations in designing the combustor. For a flame the base of the reaction is the critical location since it must propagate normally against the flow. Thus the combustor must have a region of low speed and proper equivalence ratio in which the base of the flame is stable. If a fluctuation pushes the base outside this region, the flame speed will be lower than the flow speed, and the flame will blow-off completely. A pilot flame may be necessary to reignite the main flame in the case of blow-off.

In the auto-ignition regime efficient mixing with a minimum pressure drop replaces flame stabilization as the designer's priority. Stabilizing the reaction base in a low speed region is not necessary for auto-ignition. The only requirement is that the fuel and air must remain mixed for a time that exceeds the ignition delay time. Combustion stability also is expected to be less of an issue when auto-ignition occurs. If a fluctuation pushes the reaction significantly downstream, it will generally not blow out completely. Moving the reaction downstream only increases the amount of time the fuel and air have been mixed at a high temperature, thus increasing the probability of ignition. In the case of complete blow-out due to a large fluctuation, re-ignition is not a concern because it will happen automatically with no need for a pilot.

The modeling requirements are different for combustion that is controlled by auto-ignition and flames. Auto-ignition controlled reactions require a high fidelity chemistry model to properly predict the ignition delay time governing the heat release distribution. A steady RANS fluids model is likely to be sufficient since flame blow-off is not a concern. For a flame it is generally not possible to directly resolve the high gradients at the turbulent reaction layer, so a flame model must be used. An unsteady fluids model is believed to be necessary to address flame stability concerns.

1.1.3.2 Ignition

Achieving ignition in dual-mode scramjets is a somewhat different problem than flame stabilization. Such combustors would generally be ignited at low flight Mach numbers where they will operate in the ramjet mode. For ramjet mode operation the pre-combustion shock train lowers the velocity and raises the static temperature and pressure. Before ignition this pre-combustion shock train does not exist and so the conditions are far less favorable for combustion. This problem may be solved by using an external ignition aid such as an aerothrottle [76], a plasma torch [57], or silane injection [37]. These aids are turned on to slow the flow speed or raise the reaction rate. They are then removed once the pre-combustion shock train is established.

1.1.3.3 Heat Release Distribution

The axial distribution of heat release is quite important in dual-mode scramjet combustors since it determines the conditions under which isolator unstart and ram-to-scram transition occurs. For ramjet mode operation this distribution affects the location of the thermal throat, and thus the entire distribution of Mach number, pressure, and other flow quantities in the combustor [52, 53]. Due to its effect on overall engine performance and operability limits, it is important to be able to predict the heat release distribution over the range of operating conditions.

The University of Michigan has developed a quasi-1-dimensional code called MASIV (Michigan-Air Force Scramjet In Vehicle) for scramjet stability applications [100]. The goal is to model the interaction of the vehicle exterior aerodynamics, airframe flexibility, and engine performance. Proper treatment of the heat release is key to modeling the dual-mode combustor. Experimental heat release distributions acquired in the current study were used to provide a physical basis for the combustion model in this code.

1.2 Previous Work

While research into scramjets has been ongoing since the 1950's, an operationally useful scramjet engine has not yet been produced [20]. Flight tests of experimental scramjets have been rare. The NASA X-43A program successfully demonstrated scramjet propulsion with gaseous hydrogen fuel at flight Mach numbers of 7 and 10 in 2004 [68]. The use of gaseous hydrogen fuel limited the X-43A to 10 seconds of thrust, making it a research only vehicle. The AFRL/DARPA X-51A program plans to flight test a liquid hydrocarbon fueled scramjet and demonstrate acceleration from Mach 4.5 to 6.5 in 2009 [47]. There has been a large amount of ground based research related to supersonic combustion and dual-mode scramjet combustors. This section highlights the studies that are most relevant to the current work.

1.2.1 Proposed Combustor Geometries

Various fuel injection and flame holding configurations have been proposed for dual-mode scramjet combustors [6, 8, 25, 42, 41, 98]. The combustion stabilization and heat release distribution is expected to be strongly dependent on the fuel injection and flame-holding geometry. Fuel injection methods can be divided into the categories of pylon (or strut) based injection and flush wall based injection. For pylon based injection the fuel is introduced from pylons that extend into the flow. This allows the fuel to be well distributed across the entire combustor cross section. Additionally, such pylons can serve as bluff body flame-holders [10]. Pylons cause a performance penalty though due to the stagnation pressure loss they cause. They also present a very difficult cooling problem. Both these issues become much more problematic as the flight Mach number increases.

Injecting the fuel from flush wall ports eliminates the cooling requirements and pressure drop imposed by pylons. Wall fuel injection is generally paired with a wall cavity downstream which serves as a flame-holder [6, 42, 69]. The cavity recirculation zone provides a long residence time for the fuel and air to mix and burn. The cavity combustion provides a source of heat and radicals to ignite and stabilize combustion in the main flow. The distance required to completely mix the fuel and air may be greater for wall injection than for pylon injection. Wall fuel injection can be normal to the main flow to achieve maximum penetration, or angled to recover some of the jet momentum as thrust. Achieving fuel jet penetration across the height of the combustor becomes more of a challenge as the engine size is increased. The current study focuses on combustors with normal wall fuel injection upstream of a cavity flameholder.

1.2.2 Experimental Scramjet Combustor Studies

Many scramjet combustor studies have used wall pressure measurements because they are non-intrusive and easy to obtain. Tomioka et al measured the wall pressure for ramjet mode combustion of hydrogen in dual-mode combustor with fuel injection from the wall [96, 97] and from a strut [96, 97, 98]. The isolator entrance Mach number ($M_{i,entrance}$) was 2.5 and the air stagnation temperature ($T_{0,air}$) was 1500K. These conditions simulate a flight Mach number (M_{flight}) of approximately 5.5. A range of equivalence ratios, fuel injectors configurations, and combustor divergence angles were examined. Ignition and combustion stabilization was less reliable for wall fuel injection than for strut based fuel injection [97]. The pre-combustion shock train length and pressure rise increased with the equivalence ratio for a fixed fueling location. The overall equivalence ratio could be raised without increasing the pre-combustion shock train length by injecting a portion of the fuel downstream of the thermal throat [96]. Ryan et al [86] reached a similar conclusion about the effect of staging the fuel injection on the pre-combustion shock train.

Wall pressure measurements have also been used to obtain an estimate of the axial distribution of flow properties in dual-mode scramjet combustors. The wall pressure distribution can be used in conjunction with a model that solves the quasi-1-dimensional mass, momentum, and energy conservation equations (with area change). Tomioka et al [96, 97, 98] and Donbar et al [27] have both used this approach. The overall combustion efficiency can also be obtained using such a model. Additional measurements such as exhaust gas sampling, wall temperature, or thrust are often needed to obtain an accurate combustion efficiency measurement [27, 98]. In the study by Tomioka et al [96], the combustion efficiency varied between 90% and 50%.

The combustion efficiency was lower for higher overall equivalence ratios, larger combustor divergence angles, and fuel injection further downstream.

Yu et al [114] used wall pressure measurements and a 1-D model to study ramjet and scramjet mode combustion of hydrogen for $M_{i,entrance} = 2.5$ and $T_{0,air} = 1200 - 2000$ K. The combustor was tested with and without wall cavities present for fuel injection through wall ports. The range of conditions where stable combustion existed expanded significantly with a wall cavity present.

Yu et al [113] and Fan et al [33] used wall pressure measurements to study wall fuel injection of kerosene upstream of a cavity flame holder for $M_{i,entrance} = 2.5$ and $T_{0,air} = 1700 - 1900$ K. They investigated various atomization and barbotage techniques for the kerosene injection. Ramjet mode combustion was achieved with combustion efficiencies ranging from 57% to 91%. The maximum combustion efficiency was achieved for hydrogen barbotage and heated fuel.

Wall pressure measurements have proven useful for obtaining information about the overall performance and operability limits of scramjet combustors. They are of little use for determining the combustion stabilization locations and mechanisms however. Reaction zone imaging and flow visualization are useful for studying these issues.

Gruber et al [42] studied angled fuel injection upstream of a wall cavity flameholder in reacting and non-reacting flow with and without an upstream shock train. Planar laser-induced florescence (PLIF) of NO revealed that the pre-combustion shock train caused deflection of the wall fuel jet which reduced the fuel entrainment into the cavity. This suggests that direct cavity fueling is preferable to passive entrainment to maintain stable combustion in the cavity through the ignition transient. Gruber et al [42] and Rasmussen [82] measured the stability limits of directly fueled wall cavities with a supersonic freestream and found that fueling through the rear wall allowed stable combustion over the widest range of conditions.

Mathur et al [69] acquired images of ramjet mode combustion luminosity for angled ethylene injected upstream of a wall cavity flame holder. The isolator entrance Mach number was 1.8 to 2.2 and $T_{0,air}$ was varied from 945 K to 1222 K. The reaction zone was anchored at the cavity leading edge for all cases. It spread into the flow at an approximately constant angle of 24 to 30 degrees.

Planar laser-induced florescence (PLIF) of OH has been used in several studies to image the reaction zone in dual-mode scramjet combustors [29, 77, 86, 92, 91, 5, 58, 115]. OH is a combustion intermediate that exists in regions of combustion and hot products. PLIF allows imaging of the instantaneous distribution of OH in a plane.

Donbar et al [29] performed OH-PLIF in the same combustor examined by Mathur [69]. Both ethylene and liquid JP-7 were used as fuel. The images showed that the reaction zone spreading angle for JP-7 was less than for ethylene, but the magnitude of the spreading angles was not reported. Large scale turbulent structures appeared to play a major role in the structure of the reaction zone in instantaneous images. The OH was often clustered near the sidewall regions suggesting that the spanwise dimension is important.

Ryan et al [86] used OH-PLIF and wall pressure measurements to study a dual-mode combustor fueled by ethylene and methane for $M_{i,entrance} = 2.8$ and $T_{0,air} =$ 1388 K. The combustor had a wall cavity and a flameholding step. Fuel was injected through angled or normal wall ports upstream of the wall cavity. Fuel could also be injected through normal wall ports downstream of the cavity. The combustion efficiency was found to be higher for normal fuel injection than for angled injection. The average downstream distribution of OH was similar between ethylene and methane fuel and between angled and normal injection. The instantaneous images indicated that the ethylene combustion was more stable than the methane combustion. The wall pressure measurements showed that the pre-combustion shock train length and pressure rise was smaller for methane fuel than for ethylene fuel at the same conditions. This indicates that the heat release distribution was shifted downstream for the methane fuel case, but no measurements of the heat release distribution were reported. The overall combustion efficiency was approximately 80% for both cases.

Sun et al [91] acquired OH-PLIF at several imaging planes for scramjet mode combustion of hydrogen upstream of a wall cavity flameholder. Different cavity geometries were investigated at fixed flow conditions of $M_{i,entrance} = 1.7$ and $T_{0,air} = 1221$ K. The reaction zone leading edge was found to be stabilized in the cavity shear layer in all cases. The instantaneous PLIF images suggest that the reaction spreads to the top of the fuel jet through transport of hot products by the counter rotating vortex pair in the fuel jet-wake. The conditions studied corresponded to a very low overall equivalence ratio of 0.08 with minimal fuel jet penetration. The combustion spreading mechanism in this case of scramjet mode combustion may not be the same as for ramjet mode combustion with greater fuel jet penetration.

Shock tubes have been used to study combustion in very high stagnation temperature flows which simulate large values of M_{flight}. Ben-Yakar and Hanson [5] used OH-PLIF and schlieren imaging to investigate the combustion of hydrogen that was injected normally into crossflows of air at Mach 3.5 and 4.7 with $T_{0,air} = 3750$ K and 7200 K. These conditions simulate flight Mach numbers of 10 and 13 respectively. The reaction zone was attached to the fuel injection jet for both cases. The combustion mechanism is almost certainly mixing limited auto-ignition at these high temperatures. Jeong et al [58] used OH-PLIF to image the combustion of angled injection of hydrogen upstream of a wall cavity. The crossflow Mach number was 3.7 to 4.0 and the air stagnation temperature was 4422 K to 3087 K. For high fuel flow rates the reaction zone was attached to the fuel injector. For lower fuel flow rates the reaction zone leading edge moved downstream. This lift-off of the reaction zone was attributed to heat transfer to the cold wall during the very short duration shock tube tests.

1.2.3 CFD and Combustion Modeling in Scramjet Combustors

Simulating the combustion in dual-mode scramjets is a challenge due to the high Reynolds number, the compressible flow with a thermal throat, and the complexity of the combustion mechanism. Review papers by Baurle [2] and Ladeinde [61] describe the common approaches to modeling such flows. The RANS approach to turbulence modeling is used for most engineering and research studies. Large eddy simulations (LES) of simple scramjet combustors have been reported by Berglund and Fureby [7] and Sun et al [91]. The chemistry is generally computed by simplified mechanisms with Arrhenius finite rate reactions. Turbulence-chemistry interactions are computed using assumed PDF methods or are not considered. Flamelet models for the combustion have also been used [7].

A few CFD simulations in the literature that are relevant to the current study are reviewed in this section. Baurle and Eklund [3] used VULCAN to simulate the combustion of ethylene in the AFRL dual-combustor studied experimentally by Mathur [69], Donbar [29], and Gruber [42]. VULCAN is a RANS based code designed specifically for compressible, reacting flows in ducts. Finite rate chemistry was computed with an assumed PDF for turbulence chemistry interactions. Ramjet mode combustion was considered for $M_{flight} = 4.0$ conditions and scramjet mode combustion was considered for $M_{flight} = 6.5$ conditions. The computed reaction zone stabilization location and flame spreading differed significantly from that imaged by Mathur et al [69]. The CFD solution showed the reaction zone stabilized in, and spreading from, the separated flow sidewall region for ramjet mode combustion. Images of the combustion luminosity acquired by Mathur [69] showed the reaction zone stabilized and spreading from the cavity leading edge. The computed solution was extremely sensitive to variations in the turbulent Schmidt and Prandtl numbers. This places limits on its ability to provide predictive results.

Mitani and Kouchi [73] performed simulations of a strut based scramjet combustor with hydrogen fuel at $M_{flight} = 6$ conditions. An unsteady RANS code with finite rate chemistry was used. The computed performance was especially sensitive to the combustion in the first 150 mm downstream of the fuel injection. Past this region a mixing limited diffusion flame was predicted. The authors suggest that it may be most efficient to use different grids and chemistry models in these two regions.

Recently, Sun et al [91] used a hybrid RANS/LES approach to simulate the combustion of normal hydrogen injection upstream of a wall cavity with $M_{i,entrance} = 1.7$ and $T_{0,air} = 1221$ K. This same condition also was studied experimentally as mentioned in Sec. 1.2.2. The combustion was treated as finite rate Arrhenius chemistry with no turbulence-chemistry interactions. The computed flame stabilization location for this low fueling, scramjet mode case agreed reasonably well with the experimental OH-PLIF results.

1.3 Objectives of the Current Study

The goal of the current study is to yield physical insight into the mechanisms controlling the combustion stabilization, structure, and spreading in a dual-mode scramjet combustor. A laboratory dual-mode combustor with normal wall fuel injection through a single port upstream of a wall cavity flame-holder is studied experimentally. This simple configuration has the basic flow elements proposed for practical combustor designs. It is therefore expected to exhibit combustion stabilization and spreading properties that are applicable to this type of combustor in general. Ramjet mode combustion is studied for conditions which correspond to flight Mach numbers of 4.3 to 5.5. This is near the low end of the flight Mach number regime where combustion stabilization is expected to be more of a challenge (see Sec. 1.1.3.1).

1.3.1 Combustion Stabilization

In previous experimental studies combustion properties in dual-mode scramjet combustors were investigated over a wide range of simulated flight Mach numbers. The changes in performance due to changes in fuel injection and flame-holder geometry have been measured. Achieving stable combustion and high combustion efficiency is problematic for some geometries and conditions. The location and physical mechanism of the combustion stabilization is poorly understood. This information is needed by engineers to provide guidance for fuel injector and flame holder design. No previous studies have focused on the combustion stabilization mechanisms in a dual-mode combustor operating in the ramjet mode.

The above studies show that engineering CFD codes generally do a poor job of predicting the combustion stabilization location. This location is particularly complex since it may be based on details of the auto-ignition delay time or the local flame speed (which depends on the local composition, strain rate, turbulence levels, turbulent diffusion, and finite rate chemistry). It is important to understand the combustion stabilization mechanism so that the right approximations and combustion models are used in CFD codes.

In the current study, the combustion stabilization location is imaged for a range of air stagnation temperatures and fueling rates for two fuel injection locations and fuel types. The dynamics of the combustor are measured from the wall pressure and high speed movies of the combustion luminosity. The physical mechanism of the combustion stabilization and the role of the cavity are discussed. The practical implications of changes in the combustion stabilization in an accelerating flight vehicle also are examined.

1.3.2 Reaction Zone Imaging

Reaction zone imaging can be used to gain insight into the combustion mechanism. Previous reaction zone imaging in scramjets combustors has consisted of only OH-PLIF and flame luminosity measurements. Neither of these methods can distinguish the reaction zone from the hot products. In the current study CH-PLIF and simultaneous OH/formaldehyde-PLIF are performed in a scramjet combustor for the first time. This provides new information about the structure of the reaction zone and fuel breakdown region. CH is a very short lived intermediate hydrocarbon combustion species that exists only in the local heat release layer [80]. Formaldehyde (CH_2O) is formed in the preheat layer of hydrocarbon flames as part of the initial fuel decomposition. It is consumed in the reaction layer. Formaldehyde also has been shown to be an important precursor which builds up prior to auto-ignition [38, 40]. Hydroxyl (OH) is produced in the reaction layer, and consumed by slow recombination reactions. It is a marker of the hot products in high speed reacting flows [29].

1.3.3 Heat Release Distribution

It is known from 1-D models and experiments that the heat release distribution affects combustor performance and operability limits. No previous studies have focused on measuring the heat release distribution in a dual mode combustor. In the current study the heat release distribution is measured for a range of conditions using the chemiluminescence from OH* and CH*. A quasi-1-dimensional model is also created and used to solve for the average distribution of flow variables and heat release rate from the wall pressure. The mechanism controlling the rate of heat release in different regions of the combustor is determined from the results.

1.3.4 CFD++ Simulation

The experimental combustion stabilization and heat release distribution results are compared to a solution obtained from the commercial CFD code CFD++. The CFD++ simulations were performed by Dr. C.-J. John Tam from Taitech/AFRL. The modeling approach used is based on the standard practice employed for scramjet combustor design and analysis at the Air Force Research Laboratory. It is not intended to represent the most advanced research methods for combustion modeling. Rather the goal is to examine the strengths and weakness of the current “industry standard” method and to suggest areas for improvement.

CHAPTER II

Experimental Facilities and Diagnostics

Experiments were conducted in the University of Michigan Supersonic Combustion Laboratory. The design and operation of this facility are described in this chapter. The diagnostics used in this study are also covered.

2.1 University of Michigan Supersonic Combustion Laboratory

The University of Michigan Supersonic Combustion Laboratory was designed to study dual-mode scramjet combustion at simulated flight Mach numbers up to 5.5. A schematic of the facility is show in Fig. 2.1. Compressed air is supplied through a blow-down system. An Ingersoll Rand compressor pressurizes external tanks up to 138 bar and a dome valve regulates the pressure in the lab. The air is heated by a 250 kW Hynes electric heater and a hydrogen-oxygen vitiator. Previous studies performed in this lab by Yoon [112], Huh [55], Bryant [9], Nakagawa [75], and Rasmussen [82] used only the electric heater to achieve air stagnation temperatures up to 800 K. The hydrogen-oxygen vitiator was added for the current study to extend the range of achievable $T_{0,air}$ to 1520 K. A dedicated exhaust removes the air and combustion products from the building.

Run times were limited by the uncooled heat sink combustor. Each run consisted of five seconds of vitiator only operation followed by three seconds of combustor op-

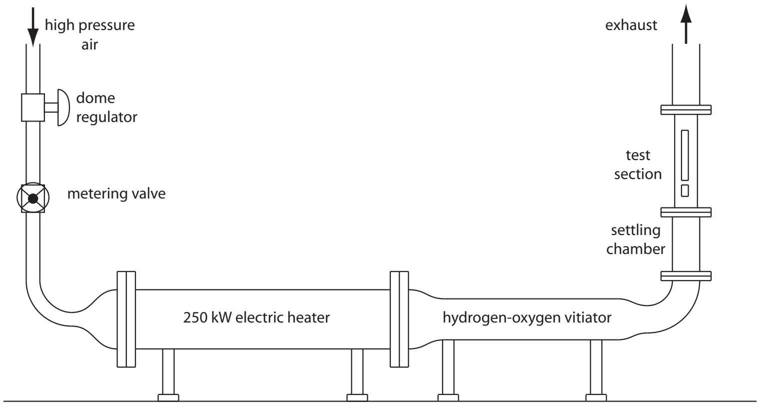

Figure 2.1: University of Michigan Supersonic Combustion Laboratory air flow schematic.

eration. All flow control and data acquisition was automated and controlled through a Labview program. Cooling between tests was provided by the continuous flow of air through the combustor.

2.1.1 Vitiated Air Heater and Piping

The air entering scramjet combustors has a high stagnation temperature that increases with flight Mach number. Figure 2.2 shows the variation of $T_{0,air}$ with M_{flight} at an altitude of 75,000 ft. Achieving such air temperatures in ground test facilities is a challenge. Shock tunnels can be used to achieve very high temperatures, but have run times of only milliseconds. Arc heaters and storage heaters can provide relatively clean air at high temperatures, but at a very high cost. Vitiators are a cost effective way to provide high temperature air by direct mixing with combustion products. They are not appropriate for certain studies because the heated air they produce contains combustion products and radicals.

For the current study a hydrogen fueled vitiator was constructed to supplement the electric heater and provide $T_{0,air}$ up to 1520 K. A cut-away view of the vitiator is shown if Fig. 2.3. The vitiator was contained in 6 inch diameter, schedule 40 stainless steel pipe between the electric heater and the combustor. The hydrogen

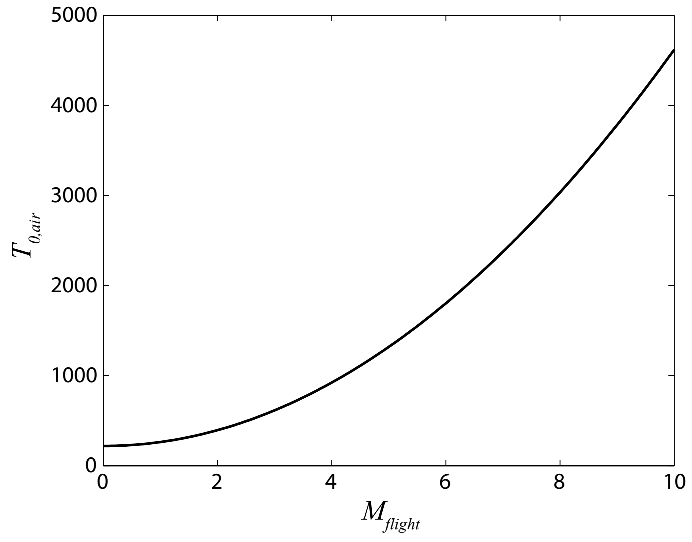

Figure 2.2: Variation of air stagnation temperature ($T_{0,air}$) with flight Mach number (M_{flight}) at 75,000 ft altitude.

was burned in diffusion flames allowing stable operation and reliable ignition over a wide range of operating conditions. The hydrogen was injected parallel to the air through twelve, 2.1 mm diameter holes in a circular manifold with diameter of 76 mm. Make-up oxygen was added so that the vitiator products contained 21% O_2 by mole. The oxygen was injected normally to the air flow 400 mm upstream of the hydrogen manifold through ten, 3.2 mm diameter ports.

A spark ignited hydrogen torch located 100 mm downstream of the hydrogen manifold was used to for vitiator ignition. The torch consisted of a central electrode inside of a ceramic tube and a stainless steel sheath. The ceramic tube provided insulation between the electrode and the sheath except at the tip where electric arcing occurred. Hydrogen fed through the 12.7 mm diameter sheath provided a stable pilot flame.

After a 1.2 m mixing section, the vitiator products were turned 90 degrees into the settling chamber. The 102 mm diameter settling chamber was 305 mm long. A perforated plate containing twenty, 12.7 mm diameter holes was positioned at

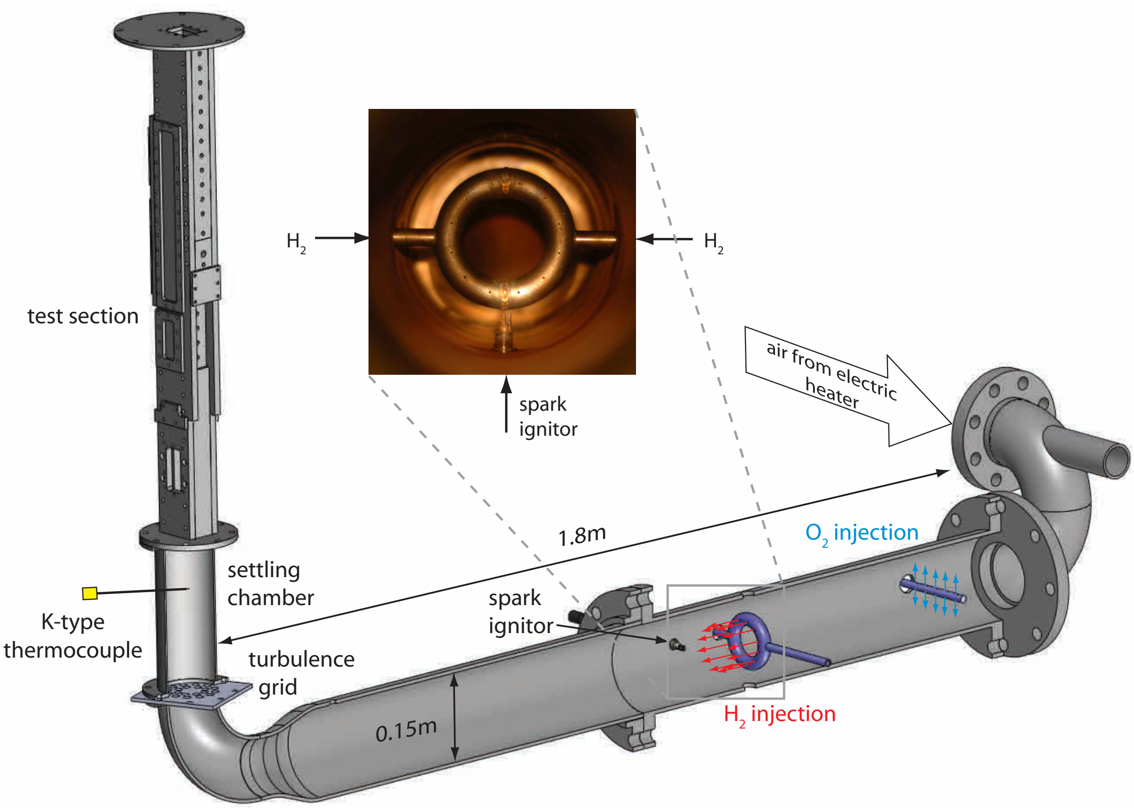

Figure 2.3: Vitiator and piping cut-away view.

the start of the settling chamber to straighten the flow and break up large scale structures. An original 0.25 inch thick plate made of steel began to deform due to the high air stagnation temperature and was replaced by a plate made of Inconel. The central 40 mm of the 102 mm diameter plate was free of holes to lessen the effect of the thermal boundary layer in the mixing section.

The electric heater was used to heat the air to a constant stagnation temperature of 450 K. The vitiator then supplied the rest of the desired temperature increase by burning the necessary amount of hydrogen. Therefore the vitiated air composition changed depending on the value of $T_{0,air}$. Figure 2.4 shows how the vitiated air mole fraction of H_2O, average molecular weight, and average ratio of specific heats varied with $T_{0,air}$. The circles represent individual runs of the vitiator at test conditions and the lines represents the regression fits for second order polynomials. The vitiator exit composition was calculated using the measured air stagnation temperature and pressure, the measured mass flow rate of hydrogen and oxygen added to the vitiator, and the known test section throat area. All the hydrogen was assumed to react with oxygen to form water vapor. The final composition and mass flow through the throat was then calculated using Eqs. 2.1 to 2.6. The * symbol represents properties at the nozzle throat. The temperature dependence of the ratio of specific heats for each species at the throat $(\gamma_i(T^*))$ was calculated from the GRI-Mech therm.dat file [90].

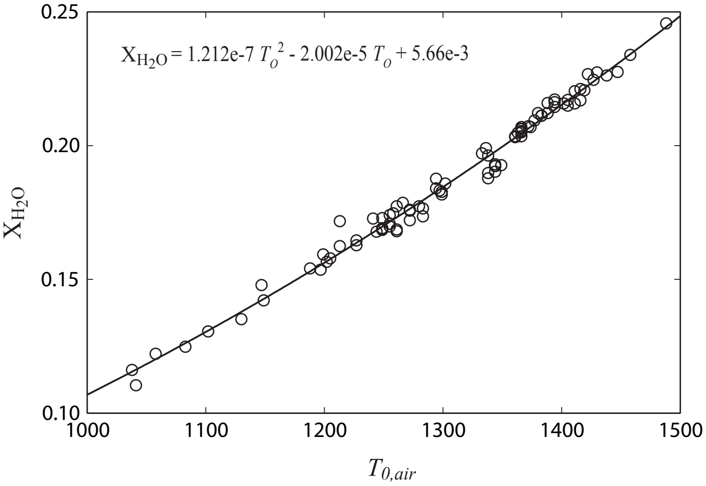

(a) Mole fraction of water vapor (X_{H_2O}).

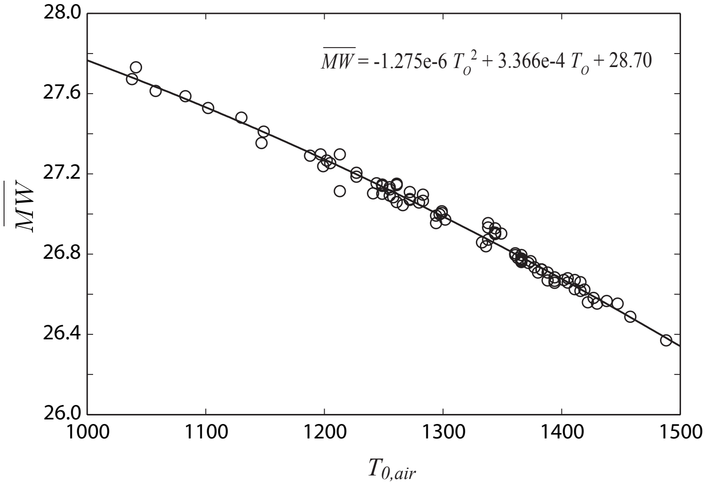

(b) Mixture average molecular weight ($\overline{MW}$).

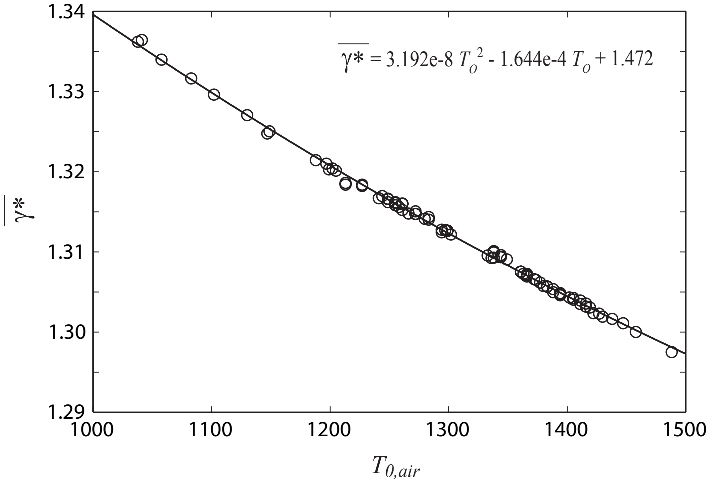

(c) Mixture average ratio of specific heats at the throat temperature ($\overline{\gamma^*}$).

Figure 2.4: Average vitiator exit composition. Data from individual runs shown as circular symbols. 2nd order polynomial fits shown as lines and equations.

$$\dot{m}_{tot} = A^* P^* \sqrt{\frac{\overline{\gamma^*}\,\overline{MW}}{T^* \Re}} = \sum_i \dot{m}_i \tag{2.1}$$

$$P^* = P_{0,i} \left(1 + \frac{\overline{\gamma^*} - 1}{2}\right)^{\overline{\gamma^*}/(1-\overline{\gamma^*})} \tag{2.2}$$

$$T^* = T_{0,air} \left(1 + \frac{\overline{\gamma^*} - 1}{2}\right)^{-1} \tag{2.3}$$

$$\overline{MW} = \sum_i X_i MW_i \tag{2.4}$$

$$\overline{\gamma^*} = \sum_i X_i \gamma_i(T^*) \tag{2.5}$$

$$Y_i = X_i \frac{MW_i}{\overline{MW}} = \frac{\dot{m}_i}{\dot{m}_{tot}} \tag{2.6}$$

2.1.2 Dual-mode Scramjet Combustor

The direct connect test section constructed for the current study is shown in Figs. 2.5 and 2.6. The test section was made of stainless steel and consisted of a converging-diverging nozzle, a constant area isolator, and a combustor. It was designed to provide a simple flow path that employs normal wall fuel injection and a wall cavity flame-holder.

A two dimensional nozzle with a design Mach number of 2.2 exited into a constant area isolator. This isolator entrance Mach number ($M_{i,entrance}$) simulates the flow after the inlet compression on a flight vehicle and corresponds to a flight Mach number of approximately 4.5. The nozzle was designed using NOZCS2, a computer program developed by Carroll et al [11] that creates nozzle contours using the method of characteristics. The constant area isolator had a height (H) of 25.4 mm and width (W) of 38.1 mm. It extended 358 mm from the nozzle exit to the first fuel injection location at the start of the combustor region.

Main fuel could be injected normally to the crossflow through one of two ports on

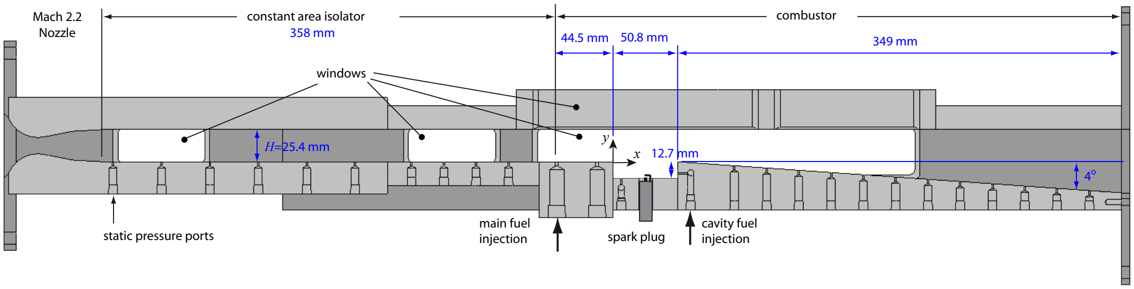

(a) Side view and dimensions.

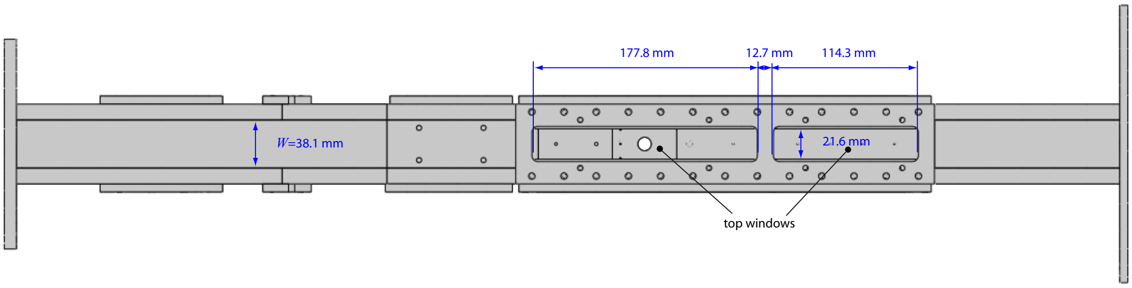

(b) Top window dimensions.

Figure 2.5: Test section with dimensions.

the test section centerline located 44.5 or 14 mm upstream of the cavity leading edge. Sonic injection is the most common method for injecting gaseous fuels and was used in the current study. As discussed by Curran and Murthy [22], sonic injection holes are much easier to manufacture than supersonic nozzles and achieve nearly the same penetration. A replaceable injector block allowed 2.49 mm or 2.18 mm diameter ports to be used at either fueling location depending on the desired flow rate. These ports served as a choked orifice for flow metering.

The wall cavity flame-holder had a length of 50.8 mm, a depth of 12.7 mm, and spanned the width of the test section. Behind the cavity trailing edge there was a 349 mm long, 4 degree diverging section. This section emptied into a 152 mm diameter exhaust at atmospheric pressure. Pilot fuel could be injected directly into the cavity through 3, 1.19 mm diameter spanwise ports in the cavity floor or rear wall. The floor ports were located 6.4 mm downstream of the cavity leading while the rear wall

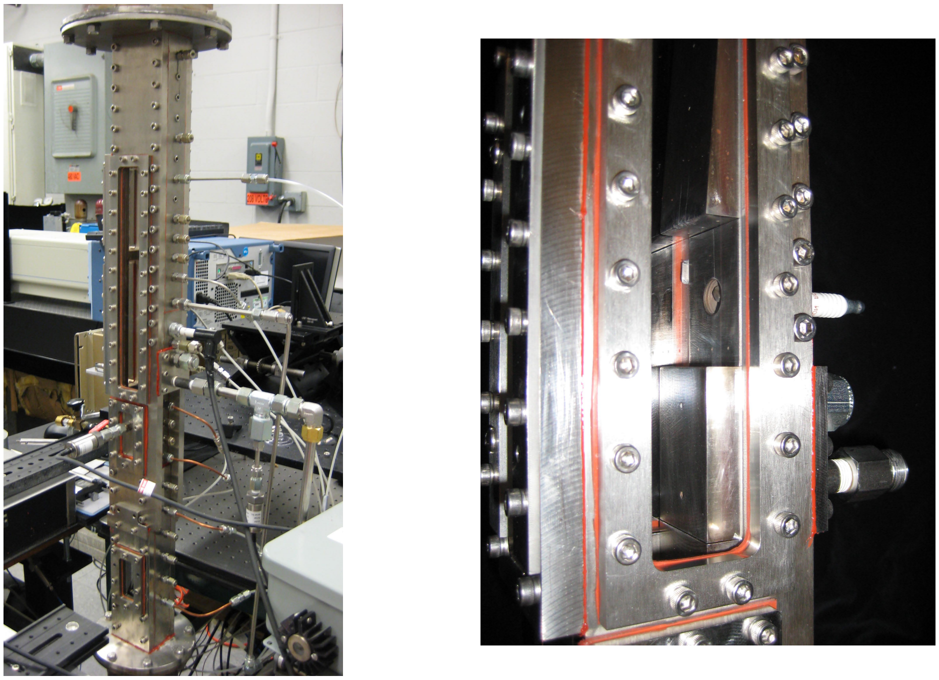

(a) test section installed

(c) fuel injection and cavity

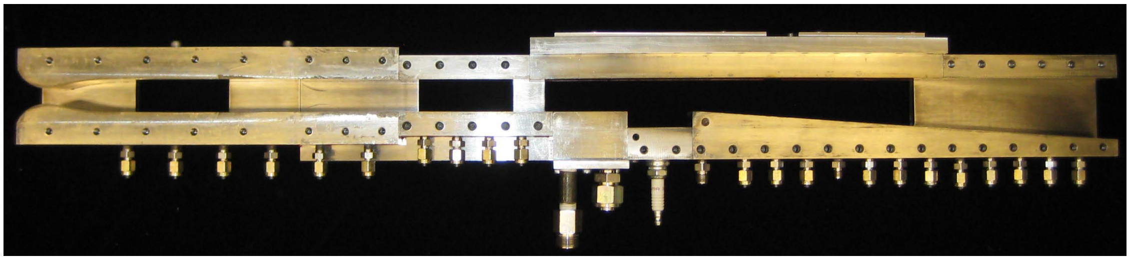

(c) test section without sidewall

Figure 2.6: Test section photos.

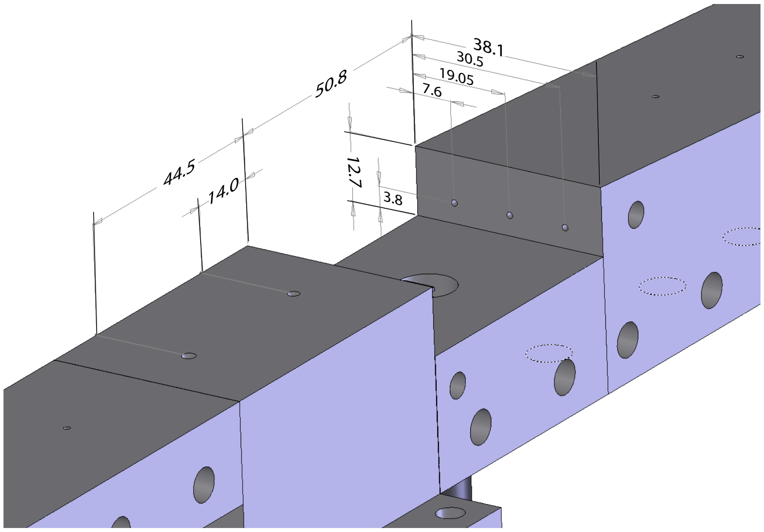

Figure 2.7: Cavity and fuel injection detail.

ports were located 3.8 mm above the cavity floor. This cavity geometry is similar to that previously studied by Rasmussen [82]. Figure 2.7 shows a detail of the cavity and fuel injection locations. Previous studies performed at the Air Force Research Laboratory and the University of Michigan reported different flame structures and stability properties when the cavity was fueled from different locations [42], [83], [31].

Custom fused silica windows shown in Fig. 2.5 provided optical access to the combustor. All windows were mounted flush to the interior walls to minimize the flow disturbance. Two pairs of 70.3 mm long windows were located in the isolator side walls. A pair of 304.8 mm long windows in the combustor side walls allowed imaging of the fuel injection and combustion region. These windows spanned the height of the test section, but the window frames blocked the bottom 2.5 mm of the cavity and a small portion of the downstream diverging section. Windows were also located in the top wall of the combustor over the same 304.8 mm region as the large side windows as shown in Fig. 2.5(b). These top windows were used primarily to transmit a laser sheet for PLIF imaging, but were also used for combustion luminosity measurements. The necessity of a frame to hold these windows meant that only the central 21.6 mm of the 38.1 mm combustor width could be viewed. A 177.8 mm window and a 114.3 mm window were separated by a 12.7 mm frame section. The top window assembly could be rotated making the entire length of the large sidewall windows accessible by the top windows.

Problems with the large combustor side windows cracking at the cavity trailing edge were encountered during combustion tests. This cracking was due to a pressure point at the top of the cavity trailing edge created by thermal expansion. The problem was mitigated by filing this corner down approximately 0.3 mm on each side. Additionally, a very thin layer of silicon sealant was placed between the metal and the these windows to provide a flexible interface.

There were 42 static pressure ports located in the combustor walls and stainless steel blanks that could be inserted in any window location. These ports spanned the entire length of the combustor and isolator with an axial spacing of 25.4 to 38.1 mm.

A spark plug located in the cavity floor was used to ensure ignition of the pilot flame. This was generally sufficient to cause ignition of the main flow for the conditions studied. An aerothrottle [63] was used only for the blended fuel cases (1B and 2B in Table 2.4) to increase the reliability of main flow ignition from approximately 90% to 100%. The aerothrottle consisted of a 3.8 mm diameter port in a window blank 140 mm upstream of the cavity leading edge. Approximately 1% of the main airflow was injected through this port. This caused a flow disturbance sufficient to allow main flow ignition and the formation of the pre-combustion shock train. After the pre-combustion shock train formed, the aerothrottle injection was no longer necessary and it was turned off with a solenoid prior to data collection.

2.1.2.1 Combustor Coordinate System

The coordinate system used for identifying locations in the combustor and isolator is shown in Figs. 2.5 and 2.10. The cavity leading edge is used as the origin instead of the fuel injection location because its location does not change during any test. Most locations and lengths reported in the current study are non-dimensionalized by the isolator height H (25.4 mm). This notation is useful for visualizing locations in the region of the reaction zone leading edge and is maintained throughout the dissertation for consistency.

2.1.3 Flow Control

Due to the limited run times, all flow control except the main air was automated and managed through a Labview program. A National Instruments 6229 data acquisition card was used to send commands to the solenoids, mass flow controller, and electronic pressure regulator that controlled the flow streams. The vitiator and combustor ignition sparks were also controlled by Labview using relay switches. The vitiator hydrogen and oxygen and the combustor fuel were supplied by separate banks of high pressure gas cylinders.

The vitiator hydrogen and the combustor pilot fuel were metered by choked orifices and were turned on and off by Asco solenoids valves. A 500 psi (3.45 MPa) Cooper PTG 403 transducer was used to measure the vitiator fuel pressure and a 200 psi (1.38 MPa) Cooper PTG 403 transducer was used to measure the combustor pilot fuel pressure. Both transducers had an accuracy of ±0.25% full scale. The flow rate for each stream was set by needle valves before the combustion tests. The vitiator oxygen was metered and controlled by a Brooks 5835S thermal mass flow controller. For the main combustor fuel, the injection port served as the choked orifice for flow metering. The injection orifices were calibrated using the thermal mass flow meter in the Brooks 5835S. An Asco solenoid valve turned the combustor fuel flow on and off while a Parker Pneumatic EPDN electronic pressure regulator was used to set the injection pressure. This regulator provided a maximum injection pressure of 1.10 MPa. A 200 psi (1.38 MPa) Cooper PTG 404 transducer with a accuracy of ±0.10% full scale was used to measure the fuel pressure just upstream of the injection. The mass flow or pressure of all flow streams was read by the NI-6229 DAQ card and recorded at 40 Hz during each test.

2.1.4 Test Procedure

For each test run, the main air was turned on and the settling chamber pressure ($P_{0,i}$) was set manually with the dome valve. The electric heater was turned on and used to raise the air stagnation temperature to 450 K. At this point the Labview program controlling the vitiator and combustor flow streams and data acquisition was initiated. The flow and spark timing for a typical run is shown in Fig. 2.8. The vitiator oxygen flow was started first since the mass flow controller took $1 - 4$ to reach a steady flow rate. The vitiator ignition torch was turned on one second after the oxygen flow and was followed one second later by the vitiator hydrogen flow. The vitiator ignition torch was turned off 1 second later because it caused sufficient electrical noise to trigger the intensified cameras used for PLIF imaging. The cavity spark was turned on 3.5 seconds after vitiator ignition and was followed 0.5 seconds later by the cavity fuel flow. The cavity spark caused no noticeable electrical interference and so was left on during the combustion tests. The main fuel was turned on one second after the cavity fuel and was typically maintained for 3 seconds. Runs of 2 to 4 seconds of main fuel were also investigated during the high speed combustion luminosity imaging discussed in Chapter III. No difference

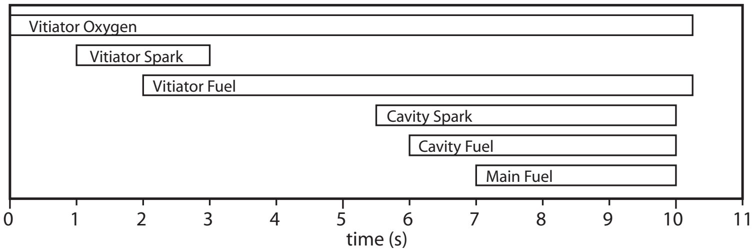

Figure 2.8: Flow and spark timing for a typical run.

in the combustion behavior was observed for the longer run times after the ignition transient of approximately 200 ms (which was also approximately the rise time of the combustor main fuel pressure).

After the end of the main fuel injection, all flow streams except the main air were terminated and the electric heater was turned off. The main air continued to flow through the combustor for approximately 3 minutes between runs to provide cooling before the next test. Approximately 8 combustion tests could be performed in a day before the pressurized air tanks were drained. The first run of each day was performed with vitiator only operation. This first vitiator run partially preheated the walls of the combustor and provided information to help achieve the desired $T_{0,air}$ and $P_{0,i}$ values for the first main flow combustion test.

The total main flow combustion time was limited by the heat transfer to the combustor, primarily at the top corner of the cavity trailing edge. This location showed significant discoloration and some cracking after the few thousand combustion runs performed. The overall shape, however, remained intact throughout the study.

2.1.5 Vitiator Exit Measurements

The air stagnation temperature ($T_{0,air}$) and initial stagnation pressure ($P_{0,i}$) were measured in the settling chamber. The notation $P_{0,i}$ is used to denote the settling chamber pressure because the air stagnation pressure changes throughout the combustor due to shocks. $P_{0,i}$ was measured by a 100 psi (690 kPa) $\pm 0.1\%$ Cooper PTG 404 transducer and was recorded at 40 Hz during each run. $T_{0,air}$ was measured by a K-type, 1/16 inch diameter, grounded thermocouple with the tip located in the center of the settling chamber. This temperature was recorded at 4 Hz during each run using a NI-9211 DAQ card. A 1/8 inch diameter stainless steel tube surrounded most of the length of the thermocouple for stability.

As discussed in Sec. 2.1.4, each three second run of the combustor followed five seconds of vitiator operation. The initial five seconds of vitiator only operation partially preheated the combustor walls allowed the settling chamber conditions to approach equilibrium. After vitiator ignition, the pressure in the settling chamber rose quickly by 60-120 kPa as the dome regulator valve adjusted to the reduced mass flow rate. Approximately 1 second after ignition, $P_{0,i}$ leveled off and remained constant. The magnitude of the settling chamber pressure increase was dependent on the mass flow rate of hydrogen and the air pressure upstream of the dome valve. It was not entirely predictable which made achieving very specific run conditions challenging. All data was acquired for $P_{0,i} = 590 \pm 10$ kPa. The variation comes from the inability to precisely predict the pressure rise from the vitiator.

The stagnation temperature of the air exiting the vitiator increased very quickly at ignition, and continued to increase more slowly through the three seconds of main combustor fueling. This variation in $T_{0,air}$ was caused by decreasing heat transfer to the vitiator piping as it heated up during a run. $T_{0,air}$ typically increased approximately 30 K during the three seconds of combustor operation. The mean temperature during this time is reported as $T_{0,air}$ for the run. Figure 2.9 shows a typical time history of $P_{0,i}$ and $T_{0,air}$ during a run.

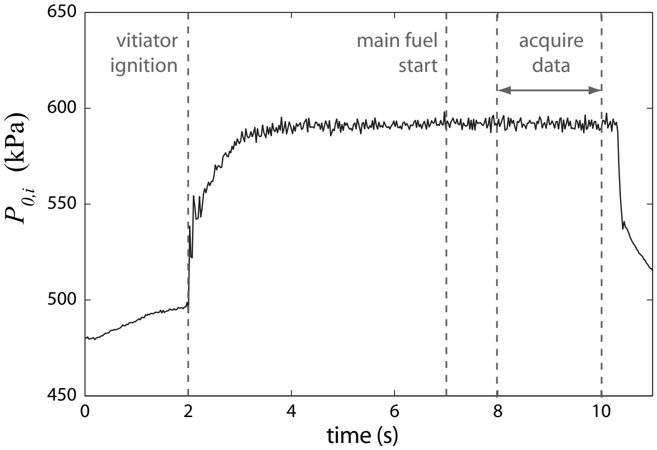

(a) Settling chamber pressure.

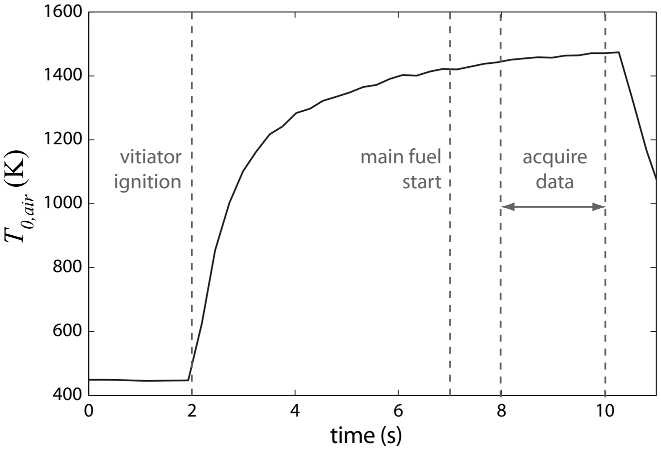

(b) Settling chamber temperature.

Figure 2.9: Typical time history of the stagnation temperature and pressure measurements in the settling chamber during a run (case 2B conditions).

2.2 Test Conditions

The focus of the study was on ramjet mode combustion (thermally choked with a subsonic isolator exit Mach number). The highest air stagnation temperature achievable by the experimental facility was $T_{0,air} = 1520K$, which corresponds to a flight Mach number of approximately 5.5. For flight Mach numbers below this value, dual-mode engines operate in the ramjet mode. Combustion stabilization is expected to be more of a challenge at these low stagnation temperature conditions where the auto-ignition delay time is not negligible.

All fuel was injected at Mach 1 in gaseous form. The fuel stagnation temperature was fixed at approximately 290 K (room temperature). Hydrogen fuel was used for most of the tests due to its fast kinetics. This allowed flame stabilization mechanisms to be explored that correspond to higher temperatures for hydrocarbon fuels. There was also a wider range of equivalence ratios for hydrogen fuel than for hydrocarbon fuels for which a) ignition was achieved, and b) the pre-combustion shock train was fully contained in the isolator.

A blend of 50% ethylene, 50% hydrogen by volume was also studied to explore the effects of fuel composition. Carbon content in the fuel was necessary for PLIF of CH and formaldehyde (CH_2O) to be performed. This fuel blend was used as a hydrocarbon surrogate because it allowed the major flame stabilization modes observed for the hydrogen fuel to be repeated with the surrogate fuel in the range of air stagnation temperatures achievable by the facility. This is explained further in Sec. 3.1.1.1.

The combustor was first studied with wall pressure measurements and high speed movies of the flame luminosity to determine the range of operating conditions that led to ignition and ramjet mode combustion without isolator unstart. Ramjet mode combustion with fuel injection through the upstream port (at $x/H = -1.75$) was achieved for the range of conditions shown in Table 2.1. Hydrogen fuel equivalence ratios (ϕ) were $0.20 - 0.27$. Higher values of ϕ led to the shock train moving into the nozzle for some conditions and lower values led to ram-to-scram oscillations at low values of $T_{0,air}$. Except for Sec. 3.3, only results for ramjet mode combustion with a pre-combustion shock train fully contained in the isolator are covered in the current study. Isolator exit Mach numbers ($M_{i,exit}$) varied between 0.68 and 0.82 for the hydrogen fueling cases at the conditions covered in Table 2.1. The isolator exit Mach number ($M_{i,exit}$) was calculated from the measured wall pressure at the isolator exit using the method given by Curran, Heiser, and Pratt [21]. This is a quasi-1-method which assumes that T_0 and momentum in the isolator are constant, but allows for area change due to separated boundary layers. Isolator exit Mach numbers ($M_{i,exit}$) varied between 0.68 and 0.82 for the hydrogen fueling cases. Larger values of ϕ and $T_{0,air}$ led to lower $M_{i,exit}$.

The blended ethylene-hydrogen fuel was studied for $\phi = 0.42$. This larger value of equivalence ratio was necessary to thermally choke the flow and cause ramjet mode operation due to the different heat release distribution for the blended fuel (discussed in Chap. V). Only one equivalence ratio was studied because there was not much operating margin in the current combustor for this fuel. Ram-to-scram oscillations occurred for low values of ϕ, and isolator unstart occurred for high values of ϕ. Only results for ramjet mode combustion with a fully contained shock train are presented in this section. The isolator exit Mach number varied between 0.62 and 0.80 for the blended fuel. The higher $T_{0,air}$ values led to the lower isolator exit Mach number due to the changing heat release distribution with $T_{0,air}$.

Parameter	H_2 Fuel Conditions	50% H_2, 50% C_2H_4 Fuel (by mole) Conditions
$P_{0,i}$	590±10 kPa	590±10kPa
$T_{0,air}$	1050 - 1500K	1250 - 1500K
ϕ	0.20-0.27	0.42
$\dot{m}_{cavfuel}/\dot{m}_{totalfuel}$	0 - 0.12	0.05
main fuel injector diameter	2.18, 2.49mm	2.49mm
cavity fuel injection location	rear wall, floor, both	rear wall

Table 2.1: Test conditions for upstream main fuel injection ($x/H = -1.75$) tests. High speed chemiluminescence imaging and wall pressure measurements performed.

	fuel type	ϕ	$\frac{\dot{m}_{cavfuel}}{\dot{m}_{totalfuel}}$	d_{inj} (mm)	$T_{0,air}$ (K)
data set A	H_2	0.21	0.02	2.18	1130-1400
data set B	H_2	0.21	0.12	2.18	1040-1410
data set C	H_2	0.26	0.0	2.49	1050-1370
data set D	50-50 H_2,C_2H_4	0.42	0.05	2.49	1250-1500

Table 2.2: Test conditions for data sets A-D. Upstream main fuel injection ($x/H = -1.75$). High speed chemiluminescence imaging and wall pressure measurements performed.

Analysis of the high speed flame luminosity and wall pressure measurements in Sec. 3.1 focuses on four data sets which are given in Table 2.2. There are three data sets with hydrogen fuel and one with the blended fuel. Each data set has a fixed ϕ and cavity fueling configuration while $T_{0,air}$ is varied.

The results from the upstream fuel injection tests in Table 2.2 were used to determine the run conditions for the downstream fuel injection tests. High speed flame luminosity imaging and wall pressure measurements were obtained for downstream main fuel injection ($x/H = -0.55$) at the conditions listed in Table 2.3.

As will be discussed in Sec. 3.1, two distinct reaction zone structures were found for upstream main fuel injection. These structures are called cavity stabilized com-

Parameter	Value
fuel type	H_2
$T_{0,air}$	1250 K
ϕ	0.18, 0.27
$\dot{m}_{cavfuel}/\dot{m}_{totalfuel}$	0.0, 0.10
cavity fueling location	rear wall, floor

Table 2.3: Test conditions for downstream main fuel injection ($x/H = -0.55$). High speed chemiluminescence imaging and wall pressure measurements performed.

	fuel type	ϕ	$\frac{\dot{m}_{cavfuel}}{\dot{m}_{totalfuel}}$	d_{inj} (mm)	$T_{0,air}$ (K)	$M_{i,exit}$
case 1H	H_2	0.27	0.05	2.49	1130±20	0.72
case 2H	H_2	0.27	0.05	2.49	1370±20	0.68
case 1B	50-50 H_2,C_2H_4	0.42	0.05	2.49	1270±20	0.73
case 2B	50-50 H_2,C_2H_4	0.42	0.05	2.49	1470±20	0.62

Table 2.4: Baseline cavity and jet-wake stabilized cases for hydrogen and blended fuel. Detailed wall pressure distribution and OH* luminosity obtained for all cases. PLIF images and CH* luminosity obtained for blended fuel cases 1B and 2B.

	fuel type	ϕ	$\frac{\dot{m}_{cavfuel}}{\dot{m}_{totalfuel}}$	d_{inj} (mm)	$T_{0,air}$ (K)
data set E	H_2	0.26	0.05	2.49	1220-1520
data set F	H_2	0.23-0.36	0.05	2.49	1500±20

Table 2.5: Test conditions for data sets E and F. OH* luminosity images and wall pressure measurements obtained.

bustion and jet-wake stabilized combustion. Conditions for baseline cases of cavity and jet-wake stabilized combustion using hydrogen and the blended fuel were defined to be studied in more detail. These baseline cases are given in Table 2.4. For the blended fuel cases (1B and 2B) the average CH* chemiluminescence and PLIF images were obtained. For all cases the detailed wall pressure distribution and average OH* chemiluminescence was obtained. The average OH* chemiluminescence was also measured for cases in data sets E and F given Table 2.5.

2.3 Wall Pressure Measurements

Wall static pressure measurements were acquired at 40 Hz at 8 locations during every test. Cooper PTG 403 transducers with a -14.7 to 50 psig range (0 to 446 kPa absolute) and ±0.25% full scale accuracy were connected to the test section pressure ports with flexible tubing. This allowed the locations monitored by the transducers to be easily changed between runs to obtain detailed average pressure distributions. The NI-6229 DAQ card read the pressure transducer output and the Labview control program recorded the results.

High frequency pressure data was also acquired for a few runs. A Cooper PTG

404 transducer (with a 690 kPa range and ±0.10% full scale accuracy) was mounted directly to a 3.8 mm diameter hole in a side window blank at $x/H = -5.5$. The pressure transducer signal was recorded at 4000 Hz by a digital oscilloscope (Lecroy Waverunner 6100A).

2.4 Combustion Luminosity Imaging

Imaging of combustion luminosity, or chemiluminescence, is a simple way to gain information on the location of the reaction zone. Chemiluminescence comes from electrically excited species created in the reaction zone [36]. Images of chemiluminescence are inherently line of sight integrated measurements.

2.4.1 High Speed Combustion Luminosity Imaging

High speed movies of the combustion luminosity were acquired to determine the location and dynamics of the reaction zone. A Vision Research Phantom 9.0 camera imaged the combustion luminosity at 4000 frames per second through the combustor side windows for the conditions in Table 2.1. Images of 768 by 240 pixels were acquired for 2 seconds after the main fuel flow was initiated. The field of view was approximately 150 mm in length and spanned the height of the test section and cavity.

For a few cases a high frequency pressure signal (discussed in Sec. 2.3) was measured in the isolator and synchronized with the high speed combustion luminosity images. A DG535 pulse generator was used to create 4000 Hz timing signals that triggered both the Phantom camera and the oscilloscope reading the pressure transducer data. The timing signal was turned on and off using a digital relay to ensure synchronization between the images and the pressure reading.

2.4.2 CH* and OH* Imaging

It is difficult to directly measure the heat release rate in any combustion environment. The heat release rate can be inferred from the measurement of other flow quantities which are correlated to it. Chemiluminescence is often used as a marker of the heat release rate in flames [81, 74, 48, 71]. The chemiluminescence in hydrocarbon flames comes primarily from OH*, CH*, C_2*, and CO_2* [44]. CH* and C_2* are confined to much thinner layers than OH* and CO_2* [110], and thus may be better markers of the location of heat release for scramjet combustor conditions. Evidence that the heat release rate is proportional to the chemiluminescence first came from Price [81] who showed that the sound pressure generated by turbulent flames was directly proportional to the rms of the chemiluminescence signal. Heat release has also been shown to be proportional to the luminosity from OH*, CH*, and CO_2* individually for many cases [48]. However the luminosity from OH* and CH* can be dependent on the local equivalence ratio and strain rate as well [74, 48]. Therefore care must be taken when interpreting images of OH* and CH* for cases where local conditions at the flame surface can vary significantly across the image (as in the case of thermally choked ramjet mode combustion).

The luminosity from OH* and CH* was imaged using ±10 nm bandwidth interference filters centered at 310 nm and 430 nm respectively. Images of the unfiltered luminosity are not reported due to significant radiation from the hot cavity rear wall which saturated the camera. Two Andor Istar intensified cameras were used to collect the OH* and CH* luminosity images simultaneously from opposite sides of the test section during each run. The OH* camera was fitted with a f4.5/105 mm UV Nikkor lens while the CH* camera used a f4.0/50 mm Nikkor lens. Both cameras imaged an area of approximately 310x42 mm on a 1024x140 pixel array. This array

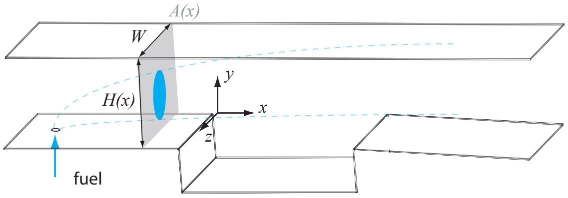

Figure 2.10: Illustration of the OH* and CH* luminosity integration.

was binned 2 × 2 to allow 8 Hz operation of the cameras due to the limited run times. Each run condition was repeated until 50-75 luminosity images were obtained.

It was useful to convert the CH* and OH* images into a one-dimensional signal for further analysis. It can be shown that these 1-D measured intensities of CH* and OH* ($I_{CH*}(x)$ and $I_{OH*}(x)$) are proportional to the local heat release rate per unit length ($\dot{Q}(x)$) if the local heat release rate per unit volume is proportional to the intensity of CH* (or OH*) emissions per unit volume. Let $\dot{q}(x, y, z)$ the be the local heat release per unit volume and $e_{OH*}(x, y, z)$ be the intensity of OH* chemiluminescence per unit volume. The axial distribution of the OH* luminosity per unit length $E_{OH*}(x)$ is then found by integrating e over the $y - z$ plane for each x as shown in Fig. 2.10.

The intensity of the OH* signal measured by the camera ($i_{OH*}(x, y)$) is proportional to e_{OH*} integrated in the z direction as shown in Eq. 2.7. The constant of proportionality is related to the geometry and efficiency of the collection optics and camera.

$$i_{OH*}(x, y) \propto \int_0^W e_{OH*}(x, y, z)dz \tag{2.7}$$

Then the measured 1-D OH* (or similarly CH*) signal is given by 2.8.

$$I_{OH*}(x) = \int_0^{H(x)} i_{OH*}(x, y)dy \tag{2.8}$$

Similarly, if the local volumetric heat release rate $q(x, y, z)$ is proportional to the local intensity of the chemiluminescence emissions e_{OH*} and e_{CH*}, then the heat release rate per unit length $\dot{Q}(x)$ is proportional to the 1-D signal of OH* (or CH*) given by Eq. 2.8.

$$\dot{Q}(x) \propto I_{OH*}(x) \propto I_{CH*}(x) \tag{2.9}$$

2.5 Planar Laser Induced Fluorescence Imaging

Planar laser-induced fluorescence is a popular technique for qualitative and quantitative imaging of species concentrations in reacting and non-reacting flows. In the current study PLIF of CH and simultaneous PLIF of OH and formaldehyde was imaged to yield insight into the reaction zone structure.

2.5.1 CH PLIF

Visualization of CH in flames is useful because CH exists only in the local heat release layer as originally shown by Porter et al. [80]. CH has been used to mark the reaction layer in many premixed and non-premixed flame studies [12, 46, 28, 87, 107, 108]. Rasmussen [82] used PLIF to image OH and CH in a wall cavity flame with a supersonic freestream. He found that the CH was confined to relatively thin layers while the OH was spread through a large volume of the cavity. No imaging of CH has been previously reported for scramjet combustors with main flow combustion.

The CH PLIF system used in the current study is based on the method outlined by Garland and Crosley [35] and demonstrated by Carter et al [12]. The $Q_1(7.5)$ transition of the $B^2\Sigma - X^2\Pi$(0,0) band of the CH molecule was excited by pumping at 390.30 nm. The wavelength was measured using a HighFinesse WS-6 wavelength meter. The resulting fluorescence from the A-X(1,1), A-X(0,0), and B-X(0,1) bands was detected in the 420 nm to 440 nm range. This method gives a relatively high fluorescence yield and large separation between the excitation and fluorescence wavelengths which allows for sufficient filtering of the excitation beam. A diagram of the PLIF system arrangement is shown in Fig. 2.11. The second harmonic of an Nd:YAG laser (Spectra-Physics LAB-150) was used to pump a dye laser (Sirah CSTR-D-24). A mixture of Rhodamine 610 and Rhodamine 640 dyes were used to obtain a beam near 616 nm. This beam was mixed with the 1064 nm beam from the Nd:YAG laser using a KD*P mixing crystal. The resulting 390.30 nm beam was separated from the 616 nm and 1064 nm beams using a Pelin-Broca prism. The 390.30 nm beam was expanded using a 3:1 Galilean telescope and a concave cylindrical lens with a focal length of -100 mm. The central $\sim$40% of the beam was then focused into a sheet using a convex spherical lens with a focal length of 1000 mm. The resulting sheet had a height of 60 mm and a thickness of 300 μm ($1/e^2$ width) in the region of interest. The sheet thickness was measured by recording the power in the beam as a knife edge was traversed with a micrometer across the location of interest with the cylindrical lens removed.

The energy in the sheet was 8 mJ/pulse. The 9 ns duration of each pulse and 1 cm^{-1} linewidth of the beam gave a spectral intensity of approximately 5×10^6 (W/cm^2)/cm^{-1}. This is five time greater than the spectral intensity needed for saturation [93]. Saturation is therefore expected in the center of the sheet width and the center of the pulse, but not in the edges of time or space. Due to this partial saturation, the PLIF signal is assumed to have a nonlinear response to variations in intensity across the height the laser sheet. The edges of the 60 mm high laser sheet had approximately half the power as the middle of the sheet. This was determined by diverting the sheet into a dye cell. Because the focus of this investigation is the structure and location of the reaction zone, quantitative interpretation of the signal was not necessary and no sheet correction was made.

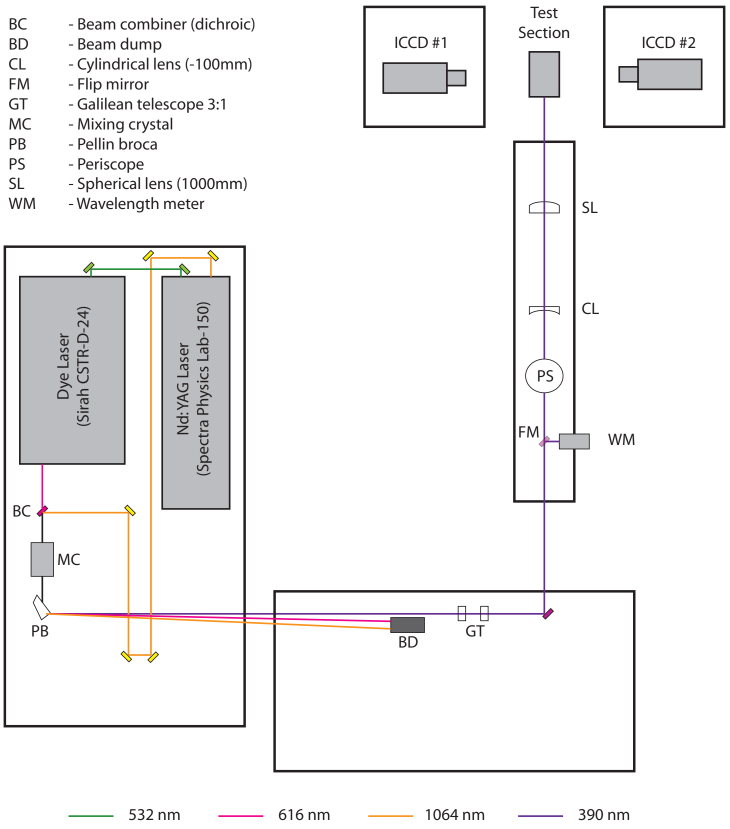

Figure 2.11: CH-PLIF system optics arrangement.

A 16-bit Andor Istar intensified CCD camera was used to collect the fluorescence. A bandpass interference filter with a 430 nm center wavelength and 10 nm full-width at half-maximum was used to block scattering from the pump beam and flame luminosity. A KV418 filter was also used to further block scattering from the pump beam. A f/2.0, 50 mm Nikkor lens with a 12 mm extension tube was used to obtain the desired field of view size. The CCD was binned 3 × 3 and cropped to obtain an array of super pixels 341 × 137 or 341 × 214 with each superpixel covering approximately 220 μm. The smaller array could be acquired at 5 Hz and the larger array at 3.33 Hz. Images were acquired on the test section centerline at four fields of view (FOVs) spanning the axial range of $-0.45 \leq x/H \leq 9.0$.

The timing of the camera and laser was controlled with a DG535 pulse generator and was optimized in a Bunsen flame before being applied in the scramjet combustor. The minimum camera gate width that did not suppress the PLIF signal in the bunsen flame was found to be 15 ns. The resulting PLIF signal was 1000-3000 counts above the mean background. The background noise was randomly distributed with a standard deviation of approximately 200 counts, giving an acceptable signal to noise ratio. When this system was applied to the scramjet combustor, however, the primary component of the noise became the flame luminosity which caused a signal of 3000+ counts above the mean background. The PLIF signal ranged up to 10000 counts above the background, but in many areas it was significantly lower and could not be distinguished from the flame luminosity signal. Figure 2.12(a) shows an example flame luminosity image acquired with no laser sheet for case 2B conditions. Figure 2.12(b) was acquired 50 ns later with a 390.50 nm laser sheet to show the effect of broadband fluorescence from polycyclic aromatic hydrocarbons (PAH) is relatively minor. The high flame luminosity signal was a somewhat surprising result

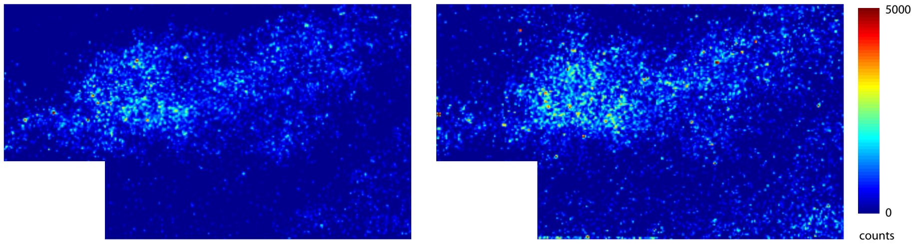

(a) ICCD 2, no laser sheet.

(b) ICCD 1, 390.50 nm laser sheet.

Figure 2.12: CH-PLIF system example flame luminosity images with and without a 390.50 nm laser sheet for case 2B conditions, FOV 1. ICCD 1 and ICCD 2 images acquired 50 ns apart. Air flow is from left to right.

given the minimal PAH in the flame and the use of a 15 ns camera gate with a bandpass interference filter. Increasing the camera gate time to 50 ns resulted in a proportional increase in the flame luminosity signal. This verified that the signal observed was indeed acquired during the short gate open time, and was not due to leakage through the closed gate during the hundreds of milliseconds between frames.

To help separate the PLIF signal from the flame luminosity signal, a second identical intensified camera, lens, and filter stack was set up to view the test section from the opposite side as the first camera (ICCD 1). This camera arrangement was similar to that shown in Fig. 2.16 for simultaneous OH/formaldehyde-PLIF. The second camera, ICCD 2, was also gated to 15 ns and was triggered 50 ns before the arrival of the laser sheet and thus recorded only flame luminosity. Ideally, the flame luminosity signal from ICCD 2 could be subtracted from the images containing the flame luminosity and PLIF signal from ICCD 1, leaving only the PLIF signal. In reality though, the two cameras can only be mapped to one another on the focal plane. The flame luminosity signal is a line of sight integrated property which suffers from perspective error over the width of the test section when mapped to the focal plane. Thus this correction reduces, but does not eliminate, the flame luminosity signal.

The final image processing consisted of the following steps. First, the mean background was subtracted and a whitefield correction was applied to both cameras in the method detailed by Clemens [18]. The mean background was obtained for each run by continuing to take data with each camera for 4 seconds after the main fuel was turned off. The two cameras were then mapped to the same coordinates on the focal plane using DaVis software and images of a clear target. Next, the images from each camera were filtered with a 2 × 2 superpixel moving average filter. This relatively minimal filter helped improve the luminosity correction by smoothing out the perspective error between the two cameras. Finally the processed ICCD 2 images were subtracted from the processed ICCD 1 images leaving the luminosity corrected PLIF images.

The noise level of the luminosity corrected PLIF images was determined by tuning the laser sheet to 390.50 nm and acquiring images of the combustor reaction zone with both cameras. The final processed images in this case represent the upper bound of the noise level. Using a 390.50 nm laser sheet in the ICCD 1 images allowed the effect of any PAH or other particles emitting broadband fluorescence to be accounted for in the noise images. Very little signal was found above 1500 counts in these filtered, luminosity corrected images. The few pixels above this value tended to be randomly distributed with no structure. Therefore 1500 counts was set to be the lower threshold for the CH-PLIF images shown in Sec. 4.2. Figure 2.13 shows an example of the noise reduction obtained by the image processing for one of the highest signal images obtained with the 390.50 nm laser sheet. Figure 2.14 shows this image processing applied to an example CH-PLIF image (390.30 nm laser sheet). Both Figs. 2.13 and 2.14 are shown on the same scale as the processed PLIF images in Sec. 4.2.

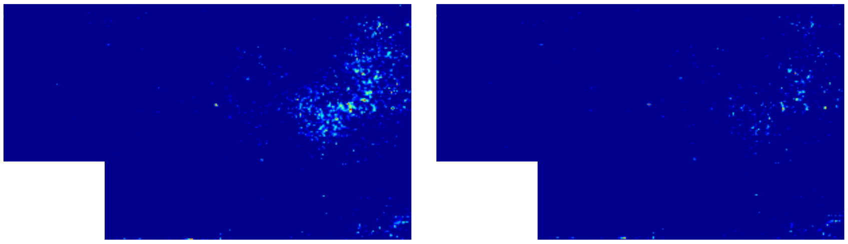

(a) No filtering or luminosity subtraction. (b) No filtering, with luminosity subtraction.

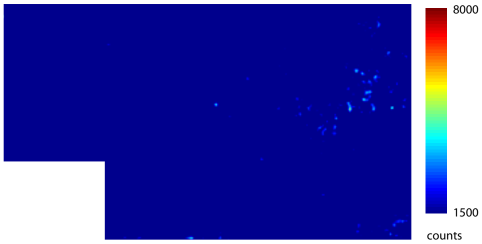

(c) With filtering and luminosity subtraction.

Figure 2.13: CH-PLIF system example high noise image with 390.50 nm laser sheet showing the effects of luminosity subtraction. The PLIF scale is the same as for the results displayed in Sec. 4.2. Case 2B conditions, FOV 1. Air flow is from left to right.

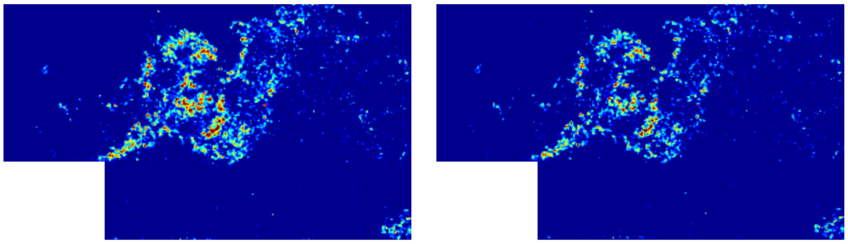

(a) No filtering or luminosity subtraction. (b) No filtering, with luminosity subtraction.

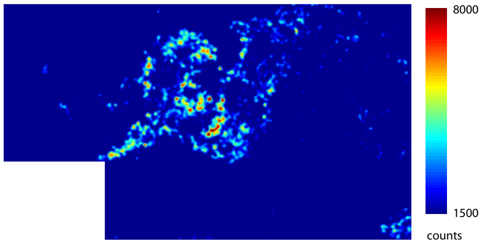

(c) With filtering and luminosity subtraction.

Figure 2.14: Example instantaneous CH-PLIF image (390.30 nm laser sheet) showing the effects of luminosity subtraction. Case 2B conditions, FOV 1. Air flow is from left to right.

2.5.2 Simultaneous OH and Formaldehyde PLIF

Simultaneous OH/formaldehyde PLIF was performed at one location on the combustor centerline ($x - y$ plane) and at four combustor cross sections ($y - z$ planes). The centerline PLIF image location was chosen to capture the most upstream instance of formaldehyde and OH. The cross-section PLIF images were acquired at three axial locations for case 1B conditions ($x/H = 1.0$, 1.8, and 3.2), and four axial locations for case 2B conditions ($x/H = 0.0$, 1.0, 1.8, and 3.2).

Planar laser induced fluorescence of OH is a popular diagnostic for reaction zone imaging due to the high signal achievable. OH is formed in the primary reaction layer of flames leading to a sharp gradient in OH concentration at this location [28]. It is consumed by slow recombination reactions [1] and therefore can exist downstream of the primary reaction zone. OH-PLIF previously performed in scramjet combustors shows that OH is spread over broad regions and is not confined to thin layers. In such high speed flows OH is mostly a marker of the regions of hot products instead of the reaction zone [29].

Formaldehyde (CH_2O) is an important intermediate species in hydrocarbon flames [104]. It is formed as part of the initial fuel decomposition reactions [85] and is consumed in the primary reaction layer. Formaldehyde is therefore found in the preheat layer of premixed flames. Formaldehyde has also been shown to be an important precursor which builds up prior to auto-ignition [40, 38].

Figure 2.15 shows example simultaneous OH and formaldehyde PLIF images acquired in a Bunsen flame. These images were acquired as part of the calibration of the PLIF systems for this study. The Bunsen flame consists of a rich premixed flame cone and an outer diffusion flame. A small amount of OH is produced at the rich premixed flame surface and exists in the entire region between the premixed flame and the diffusion flame. Around the diffusion flame a large amount of OH is produced. The formaldehyde is confined to a relatively thin (approximately 2 mm wide) layer that marks the premixed flame preheat layer. There are a few thicker clumps of formaldehyde that are most likely due to out of plane effects or flame merging. All the formaldehyde is destroyed in the reaction layer of the rich premixed flame. There is no formaldehyde associated with the outer diffusion flame.

Figure 2.15(c) shows the product of the OH and formaldehyde PLIF signals. Paul and Najm [78] showed that the product of OH and CH_2O concentrations is approximately proportional to the local heat release rate. This overlap occurs in the same layer as CH [26]. Thus Fig. 2.15 shows an example of the location where all the species imaged in the current study exist in a reaction zone. The OH and CH_2O overlap layer in Fig. 2.15(c) is $0.5 - 1.0$ mm thick.

Laser induced fluorescence of OH was obtained by exciting the $Q_1(6)$ transition of the $A^2\Sigma - X^2\Pi$ band at 283.01 nm. The resulting fluorescence from the A-X(1,1) and (0,0) bands was collected near 310 nm. The excitation beam was created by frequency doubling the 566 nm light from an Nd:YAG pumped dye laser with Rhodamine 590 dye. The resulting 283 nm beam had a pulse duration and energy of 10 ns and 9 mJ.

Previous combustion studies have obtained PLIF of formaldehyde using several different excitation wavelengths from 338 nm to 370 nm [78, 49, 102, 60]. Excitation using the third harmonic of an Nd:YAG laser at 355 nm is popular due to the ease of obtaining high pulse energies. Rasmussen [83, 82] successfully used 355 nm excitation to obtain formaldehyde PLIF in a supersonic combustor. Dhanuka [26] successfully demonstrated this method in a very bright flame in a laboratory gas turbine combustor. A shortcoming of using this excitation wavelength is that it overlaps weak rotational transitions in the 4_0^1 band. Thus it requires very high pulse

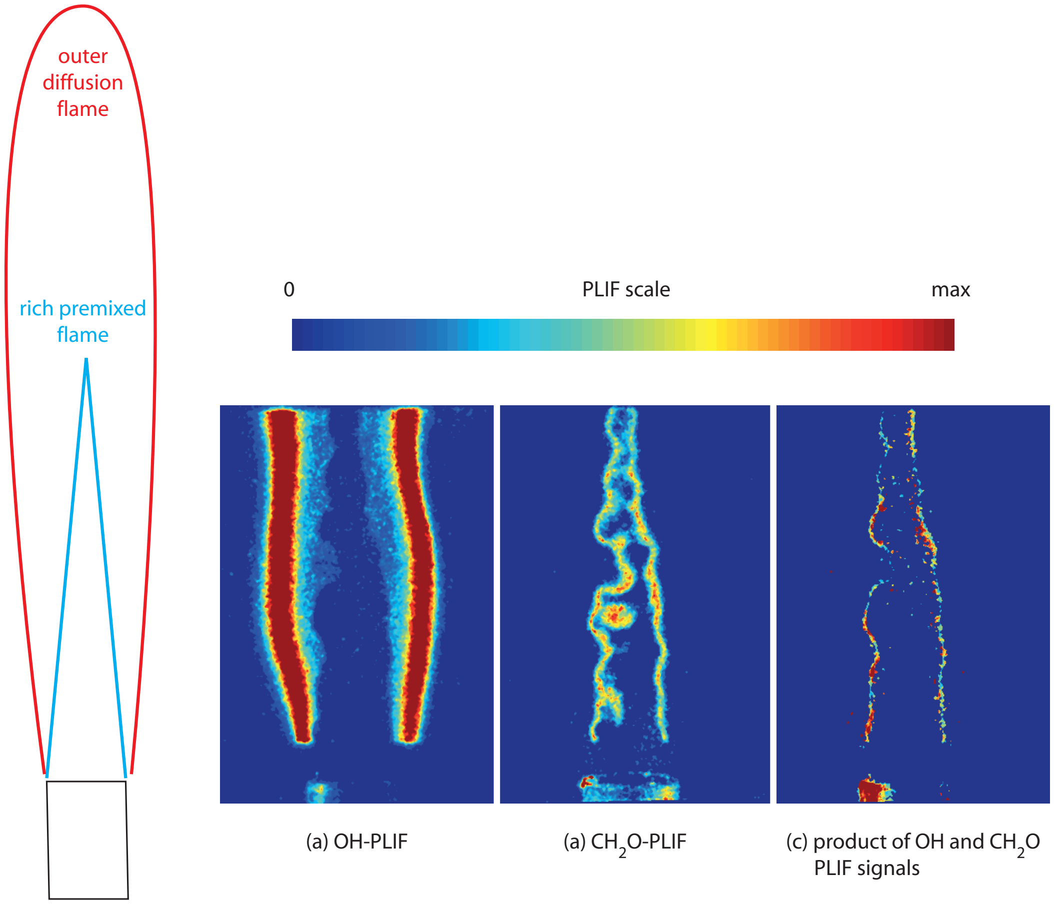

(a) OH-PLIF

(a) CH$_2$O-PLIF

(c) product of OH and CH$_2$O PLIF signals

Figure 2.15: Example simultaneous OH/formaldehyde-PLIF images in a Bunsen burner with an inner rich premixed flame and an outer diffusion flame.

energies to obtain a good signal.

For the centerline PLIF imaging, the laser sheet impinges on the floor of the test section and cavity as shown in Fig. 2.16(a). When 355 nm excitation was tested in this arrangement, very high noise was encountered from reflections of the high power laser sheet off the rear wall. The noise could not be reduced to acceptable levels by optical filters because: a) formaldehyde LIF occurs over a wide range of 385-470 nm and b) many substances emit broadband fluorescence when excited by UV light. Rasmussen [83, 82] was able to overcome this problem in a similar configuration by taking advantage of the long fluorescence lifetime of formaldehyde at sub-atmospheric pressures [95, 111]. This allowed the camera gate to be delayed 200 ns with respect to the laser pulse, virtually eliminating noise from laser sheet reflections. The fluorescence lifetime of formaldehyde is very short at the high temperature and pressure combustion conditions of the current study however [72]. Thus the camera imaging time must overlap the laser pulse time. This necessitated the use of an excitation wavelength with a higher LIF signal per input laser power for the centerline imaging.

LIF of formaldehyde on the test section centerline was obtained by exciting the ${}^{R}R_3$ rotational band of the 4^1_0 vibrational band in the $A^1A_2 - X^1A_1$ electronic band near 352.48 nm. Harrington and Smyth [49] found a peak in fluorescence intensity using this excitation wavelength. Fluorescence from several transitions was collected over the range of 385 to 470 nm. An Nd:YAG pumped dye laser with LDS 698 dye produced a 705 nm beam which was frequency doubled to obtain the formaldehyde excitation beam. Each 10 ns pulse contained 12 mJ near 352 nm. Noise from sheet reflections was acceptable at this pulse energy level. No discernable signal from PAH fluorescence was found by tuning the laser off resonance to 352.465 nm as suggested

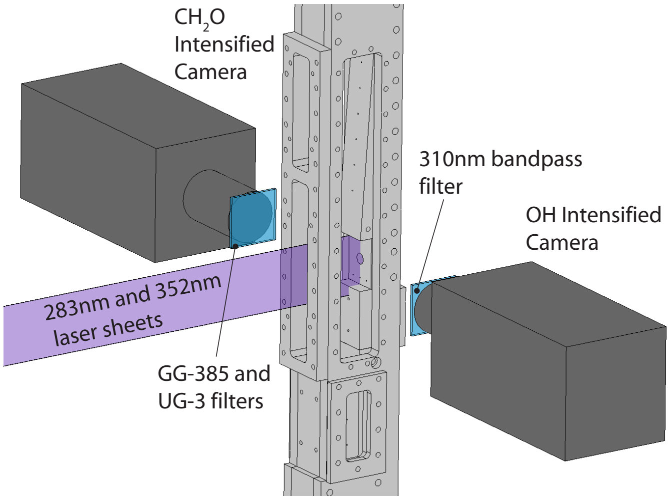

(a) Test section centerline imaging ($x - y$ plane).

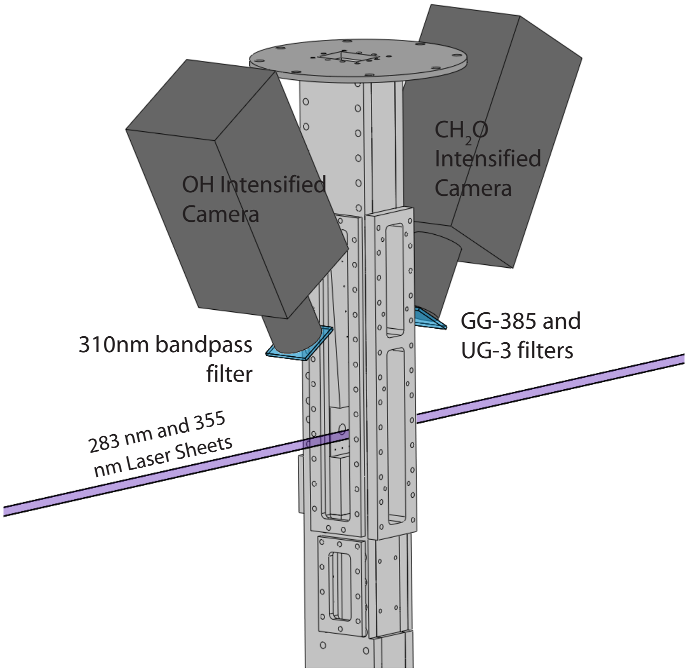

(b) Test section cross section imaging ($y - z$ planes).

Figure 2.16: Camera and laser sheet arrangement for simultaneous OH/formaldehyde PLIF.

by Harrington and Smyth [49].

The optics arrangement for the centerline OH/formaldehyde PLIF measurements is shown in Fig. 2.17. The OH and formaldehyde excitation beams were combined using a dichroic mirror before passing through the same sheet forming optics. A -100 mm focal length cylindrical lens and 1000 mm focal length spherical lens were used to form a 67 mm high sheet that was aligned with the test section centerline. The sheet thickness was approximately 250 μm for the 283 nm beam and 350 μm for the 352 nm beam in the region of interest. The sheet thickness was measured using the same technique described in Sec. 2.5.1. Beam alignment was performed each day by passing both beams through an iris just past the dichroic. The beams were then traversed along an optical path of approximately 7 meters where they were aligned again visually. Measurement of the sheet thickness at the focal point verified that this method aligned the beams to within 50 μm in the imaging region.

The fluorescence images were captured by a pair of Andor Istar intensified CCD cameras. The two cameras viewed the imaging plane through opposite sides of the test section as shown in Fig. 2.16(a). The OH-LIF camera used a 50 ns gate time and was fitted with an f/4.5 105 mm Nikkor UV lens. A bandpass interference filter with a 310 nm center wavelength and 10 nm half-width at half maximum was used to block scattering from the pump beam and flame luminosity. The CH_2O-LIF camera was fitted with an f/2.8 50 mm Nikkor lens. It used a shorter 30 ns gate time to minimize the flame luminosity contribution to the signal. Schott glass GG-385 and BG-3 filters were used to respectively block the laser beam and the flame luminosity above about 490 nm. The cameras were cropped and 2 × 2 binned to image a 227 by 512 array of superpixels with a resolution of 155 μm / superpixel. Images from the two cameras were mapped to the same coordinates in the imaging plane

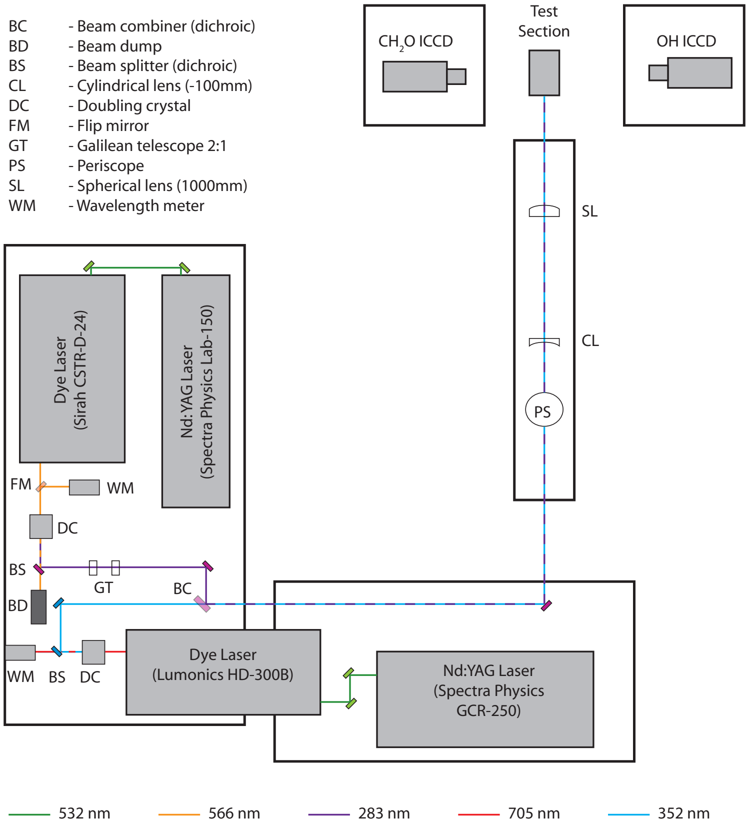

Figure 2.17: Simultaneous OH/formaldehyde-PLIF system optics arrangement for test section centerline imaging.

using DaVis software and images of a clear target. The images were corrected for the camera whitefield and the mean background. Background images were obtained for each run by continuing to acquire images for 5 seconds after the main fuel was turned off. The laser and camera timing was controlled by two DG535 digital pulse generators. The 352 nm pulse was delayed by 150 ns with respect to the 283 nm pulse in order to minimize interference between the LIF signals. With a calculated mean flow velocity of approximately 500 m/s in the region of the cavity (see Sec. 5.2), this delay corresponds to a fluid movement between laser pulses of approximately one half of a superpixel.

The OH PLIF images were processed with a 3 × 3 median filter and had a good signal to noise ratio of around 20 to 1. The formaldehyde PLIF images however had significant interference from flame luminosity. The PLIF signal magnitude was generally on the same order as the flame luminosity signal magnitude over the filtered wavelength range and camera gate time. The camera gate time was set to the minimum value necessary to reliably capture the arrival of the laser pulse, and so could not be further reduced. Therefore much of the formaldehyde PLIF signal could not be distinguished from the flame luminosity. Luminosity subtraction could not be performed as in the case of CH-PLIF because the other camera and window was used to acquire the OH-PLIF signal. Therefore calculation of the OH and CH_2O overlap was not possible. However, the upstream part of the formaldehyde was found to exist well away from any flame luminosity. Therefore the outer contour of the signal measured by the CH_2O camera gives a good indication of the border of the CH_2O region, particularly upstream of the OH region. The formaldehyde images were filtered with median (5 pixel width) and Gaussian (2.5 pixel standard deviation, 9 pixel width) filters to reduce the noise before obtaining the outer contour.

Figure 2.18 shows representative instantaneous images for case 1B and 2B from the CH_2O and OH cameras with the outer contour of the CH_2O-PLIF signal overlaid. The OH-PLIF is a good marker of regions where there is flame luminosity in the combustor. Some signal can be seen behind the rear edge of the laser sheet in both CH_2O images indicating that flame luminosity is significant. Figure 2.18(a)(i) shows a large region near the top of the image where the signal drops off abruptly at the rear edge of the laser sheet. This was a common feature among all case 1B images where the CH_2O was well above the OH at the rear edge of the laser sheet. This abrupt drop off in intensity at the edge of the laser sheet indicates that the signal in this region is due to CH_2O LIF rather than flame luminosity. Thus the upper contour for all case 1B images is considered to be a reliable marker of the formaldehyde border. For case 2B conditions, the signal imaged by the CH_2O camera well upstream of the OH-PLIF must be due to formaldehyde LIF since no flame luminosity exists in this region. This was verified by additional runs in which the flame luminosity was imaged without the laser. Toward the rear edge of the laser sheet, the source of the signal recorded by the CH_2O camera was generally ambiguous. All that can be said about this region is that no formaldehyde exists outside the recorded contour.

For the PLIF imaging of the combustor cross sections ($y - z$ planes), the laser sheet passes out of the combustor through a side window as shown in Fig. 2.16(b). Therefore the reflections from a high power laser sheet cause less of a concern for this configuration than for the centerline imaging. The flame luminosity is expected to be more a concern, however, because the cameras must view the imaging plane at the stereo angles shown in Fig. 2.16(b). It is much more difficult to distinguish the PLIF signal from regions of flame luminosity along the optical path viewed by cameras in this arrangement. Therefore 355 nm excitation from the third harmonic

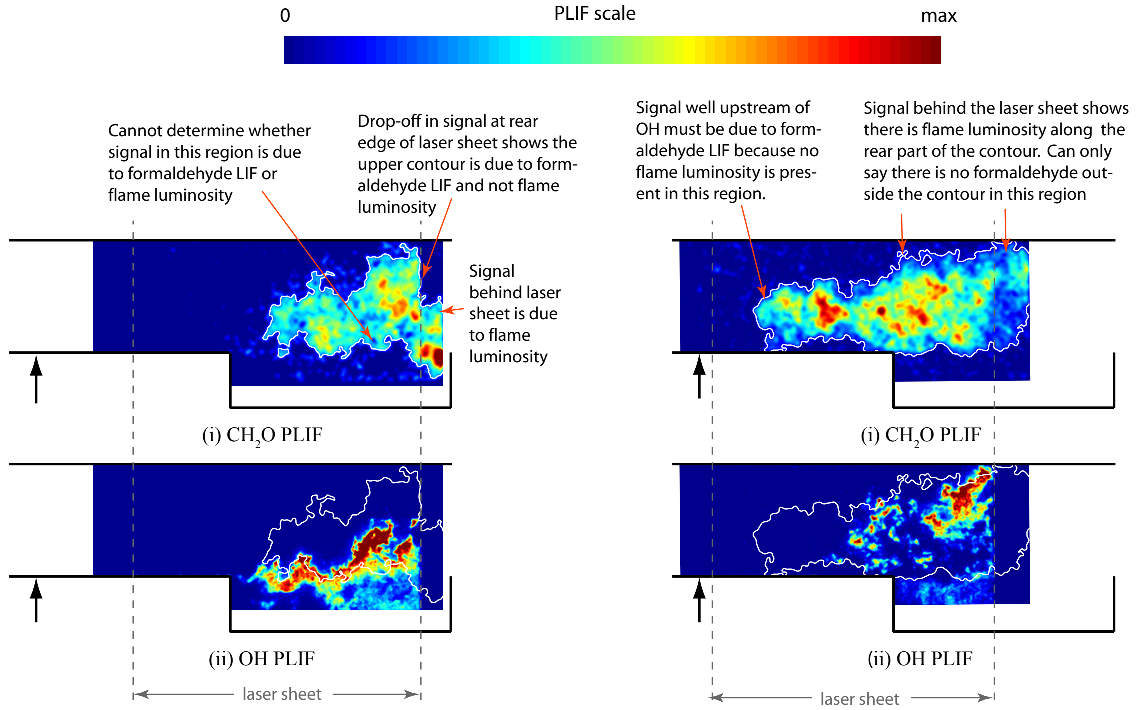

Cannot determine whether signal in this region is due to formaldehyde LIF or flame luminosity

Drop-off in signal at rear edge of laser sheet shows the upper contour is due to formaldehyde LIF and not flame luminosity

Signal behind laser sheet is due to flame luminosity

Signal well upstream of OH must be due to formaldehyde LIF because no flame luminosity is present in this region.

Signal behind the laser sheet shows there is flame luminosity along the rear part of the contour. Can only say there is no formaldehyde outside the contour in this region

(a) case 1 conditions

(b) case 2 conditions

Figure 2.18: Example instantaneous formaldehyde and OH PLIF images with iso-contour from CH_2O image overlaid. Shows flame luminosity interference with CH_2O-PLIF signal.

of an Nd:YAG laser was used for the combustor cross-section formaldehyde PLIF. This allowed much higher laser power to be used (up to 200 mJ/pulse available) to increase the PLIF signal to significantly above that of the flame luminosity. Only 70 mJ/pulse were used in the current study due to the local reflections shown in Fig. 2.20(a).

The intensified cameras viewed the imaging plane through the side windows at an angle of 25 degrees from the laser sheet normal direction. Schiempflug adapters where used to achieve uniform focus across the field of view. The cameras were fitted with the same lenses and filters as for the centerline imaging. Images of a target and DaVis software were used for mapping the distorted camera images onto the imaging plane with the same Cartesian coordinates. Very high local signal was observed by the formaldehyde camera where the laser sheet passed through the windows. This signal was caused by reflections off tiny bubbles and other imperfections in the side windows. To prevent damage to the camera intensifier, metal tabs were affixed to the window frame to block the formaldehyde camera's view of these areas as illustrated in Fig. 2.19. Therefore the formaldehyde camera did not image the regions within approximately 6 mm of the side walls. The entire height of the combustor (y-direction) was visible. Window reflections were not a problem for the OH camera since the 283 nm sheet had a much lower power than the 355 nm sheet and a narrow bandpass filter was used. Therefore the OH camera was able to view the entire combustor cross-section.

The cross-section PLIF imaging was performed with the same camera timing as the centerline PLIF. A -100 mm focal length cylindrical lens and 500 mm focal length spherical lens were used to create a sheet than spanned the height of the test section. The sheet power varied by approximately 30 % across the test section height. No

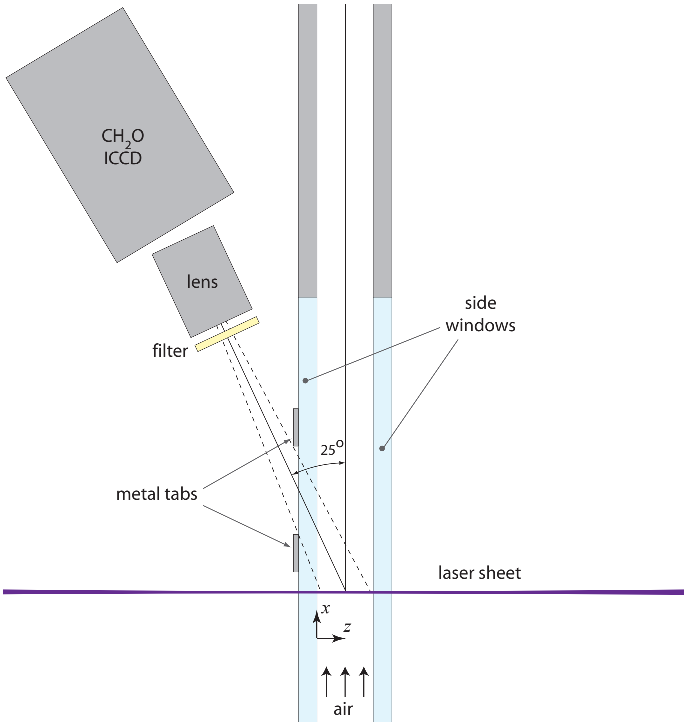

Figure 2.19: Diagram of the cross-section formaldehyde PLIF camera and the placement of the metal tabs used to block direct reflections of the laser sheet off window imperfections.

correction was made for the variation in sheet intensity due to the qualitative nature of the study. The sheet thickness and alignment was the same as for the centerline imaging.

Image processing was done the same way as the centerline PLIF except that the formaldehyde Gaussian filter had a width of 5 pixels and a standard deviation of 2 pixels. The OH-PLIF images again had a good signal to noise ratio of approximately 20 to 1. The formaldehyde PLIF signal was up to an order of magnitude higher than the flame luminosity. All cross-section formaldehyde PLIF images shown in Sec. 4.3 are thresholded at 1000 counts and shown on a false color scale with an 8000 count maximum. This thresholding virtually eliminated any flame luminosity contribution in these images.

The greatest source of noise came from the laser sheet reflections off window

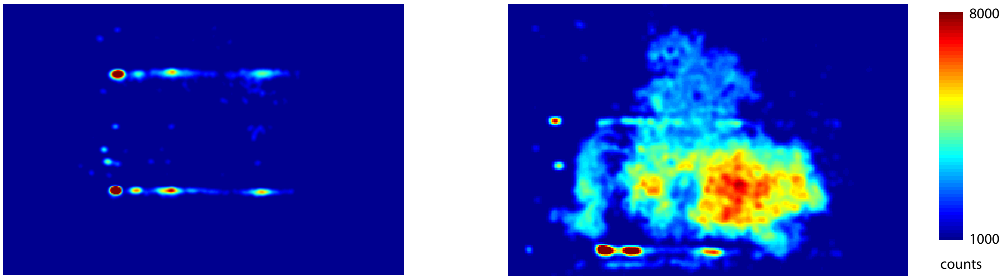

(a) Example high noise image with no combustion. Signal is due to laser scattering off window imperfections.

(b) Example PLIF image. Significant formaldehyde LIF is seen along with along with some high noise spots near the bottom of the image.

Figure 2.20: Example processed cross-section PLIF and noise images from formaldehyde camera. Images cover the 25.4 mm by 38.1 mm cross-section of the combustor at $x/H = 0.0$.

imperfections. Even with the blocking tabs in place, there were some localized areas of high noise from secondary reflections. An example PLIF image and example noise image with no combustion are shown in Fig. 2.20. The noise showed up as spots and lines of very high signal. It was easy to visually distinguish the noise from the LIF signal as it was consistent in location from image to image during the same run. It could not be eliminated by background subtraction due to its varying intensity between images. This noise and the requirement for thresholding the images prevented detailed interpretation of the OH and formaldehyde overlap in the cross-section images.

2.6 Computational Fluid Dynamics Approach

2.6.1 Method

Simulations of the combustor used in the current study were performed by Dr. C.-J. John Tam from Taitech/AFRL using the commercial code CFD++. The modeling approach used is based on the standard practice employed for scramjet combustor design and analysis at the Air Force Research Laboratory.

The computational domain extended from the nozzle entrance to the exit of the combustor. Zero back pressure was considered at the exit. Symmetry was assumed along the combustor centerline ($x - y$ plane) so only half the combustor flowfield was computed. The computational grid consisted of 383,000 hexahedral cells. Grid points were clustered in the region of the main fuel injector, the combustor walls, and the cavity leading and trailing edges. A k-ϵ model was used for modeling the turbulence. Only the steady state solution was computed.

The chemistry was computed by Arrhenius finite rate reactions. No turbulence chemistry interactions were modeled. Only hydrogen fuel was considered in the simulations due to the availability of validated reduced order chemical mechanisms. The chemical mechanism from Drummond et al [32] was chosen for the current study. It included 9 species and 18 reactions and was developed for modeling the combustion of hydrogen in supersonic flows.

Simulations were also performed at the University of Michigan using the 11 species and 33 reaction mechanism given by Jachimoski [56]. This mechanism does a good job of predicting the auto-ignition delay time in hydrogen-air mixtures at scramjet combustor conditions. Only minor differences were found between the solutions using the two different mechanisms. Therefore only the results from the mechanism of Drummond [32] are reported.

2.6.2 Conditions

Simulations were performed for the two cases listed in Table 2.6. These cases are very similar to the hydrogen fuel baseline cavity and jet-wake stabilized cases 1H and 2H. No direct cavity fueling was used for the CFD combustion cases. The combustion stabilization location was found to be independent of the cavity fueling rate in Sec. 3.1. Therefore the added complexity and increased computational time required for clustering grid points around the cavity fuel injectors was not deemed worthwhile. The mass flow of main fuel injected through the wall port is approximately the

Parameter	Case 1C	Case 2C
$P_{0,i}$	590 kPa	590 kPa
$T_{0,air}$	1100 K	1400 K
main flow composition	vitiated air	vitiated air
fuel composition	H_2	H_2
ϕ	0.25	0.25
$\dot{m}_{cavfuel}/\dot{m}_{totalfuel}$	0.0	0.0
fuel injection diameter	0.25	0.25
fuel P_0	845 kPa	755 kPa
fuel T_0	288 K	288 K

Table 2.6: Run conditions for CFD++ simulations.

Major Species	Case 1C	Case 2C
X_{O_2}	0.21	0.21
X_{N_2}	0.66	0.58
$X_{\mathrm{H}_2\mathrm{O}}$	0.13	0.21

Table 2.7: Major species mole fractions of vitiated air used in CFD simulations.

same between the experimental cases 1H and 2H and the computational cases 1C and 2C respectively. The lack of direct cavity fueling makes the overall equivalence ratio slightly less for the computational cases. The air temperature used for the computational cases was also slightly different than the baseline experimental cases. $T_{0,air}$ was 30 K lower for case 1C than for case 1H and 30 K larger for case 2C than case 2H. This greater temperature separation for the computation cases was used in an attempt to force the computational solutions to the two different stabilization modes found experimentally.

The vitiated air composition for the two CFD cases is listed in Tables 2.7 and 2.8. The major species concentrations were taken from the vitiator exit information given in Fig. 2.4. The minor species were calculated from equilibrium chemistry at the settling chamber stagnation conditions. NO and NO_2 were not included because their formation depends on the details of the vitiator flame and they do not have a large effect on the chemistry.

Solutions for cases 1C and 2C were computed assuming an isothermal wall at 450 K (the upper limit for wall heat transfer) and an adiabatic wall (the lower limit

Minor Species	Case 1C	Case 2C
X_{OH}	6.2e-7	3.4e-5
$X_{\mathrm{H_2}}$	1.4e-10	8.2e-8
X_{O}	4.8e-10	1.8e-7
$X_{\mathrm{HO_2}}$	7.7e-9	2.0e-7
$X_{\mathrm{H_2O_2}}$	1.2e-9	2.5e-8

Table 2.8: Minor species mole fractions of vitiated air used in CFD simulations.

for wall heat transfer). Only minor differences were found in the flame stabilization location and structure between these two cases. The pressure field more closely matched the experiments for the isothermal wall cases. Only the results from the isothermal wall cases are reported in Secs. 3.1.4 and 5.5.

CHAPTER III

Combustion Stabilization and Dynamics

Combustion stabilization was studied experimentally using high speed movies of the flame luminosity (at frame rates of 4000 Hz) and wall pressure measurements. The combustor was operated in the ramjet mode. The dynamics encountered at the ram-to-scram transition are examined as well. The objective of the investigation was to determine the locations, mechanisms, and practical implications of the combustion stabilization over a range of conditions in a generic dual-mode scramjet combustor. The experimental results are compared with a CFD simulation of the combustor.

3.1 Upstream Fuel Injection

Ramjet mode combustion with fuel injection through the upstream port (at $x/H = -1.75$) was studied for the range of conditions shown in Table 3.1. Hydrogen fuel equivalence ratios (ϕ) were $0.20 - 0.27$. Higher values of ϕ led to the shock train occasionally moving into the nozzle and lower values led to ram-to-scram oscillations at low values of $T_{0,air}$. Only results for ramjet mode combustion with a pre-combustion shock train fully contained in the isolator are presented in this section.

The blended ethylene-hydrogen fuel was studied for $\phi = 0.42$. This larger value of equivalence ratio was necessary to thermally choke the flow and cause ramjet mode operation for the blended fuel due to its different heat release distribution (discussed

Parameter	H_2 Fuel Conditions	50% H_2, 50% C_2H_4 Fuel (by mole) Conditions
$P_{0,i}$	590±10 kPa	590±10kPa
$T_{0,air}$	1050 - 1500K	1250 - 1500K
ϕ	0.20-0.27	0.42
$\dot{m}_{cavfuel}/\dot{m}_{totalfuel}$	0 - 0.12	0.05
main fuel injector diameter	2.18, 2.49mm	2.49mm
cavity fuel injection location	rear wall, floor, both	rear wall

Table 3.1: Test conditions for upstream main fuel injection ($x/H = -1.75$) tests. High speed chemiluminescence imaging and wall pressure measurements performed.

in Chap. V). Only one equivalence ratio was studied because the operating margin in the current combustor was small for this fuel. Ram-to-scram oscillations occurred for low values of ϕ, and isolator unstart occurred for high values of ϕ. Only results for ramjet mode combustion with a fully contained shock train are presented in this section. The isolator exit Mach number varied between 0.66 and 0.85 for the blended fuel. The higher values of $T_{0,air}$ led to lower values of isolator exit Mach number due to the changes in the heat release distribution.

3.1.1 Combustion Stabilization Modes

For the range of operating conditions shown in Table 3.1, two distinct combustion stabilization modes were found to occur. These two modes will be referred to as the cavity stabilized combustion mode and the jet-wake stabilized combustion mode. Figures 3.1 and 3.2 show an example of the average combustion luminosity for each stabilization mode for hydrogen and for blended fuel. Between each stabilization mode, there is a step change in the combustion stabilization location and the reaction zone structure. For each set of conditions studied, the combustion was steady in either the cavity or jet-wake stabilization mode, or it oscillated between the two modes. There was no set of conditions that produced a steady, intermediate reaction zone structure. The oscillation between modes is discussed in section 3.1.2.

The bimodal nature of the combustion is illustrated by Figs. 3.3 and 3.4. Figure

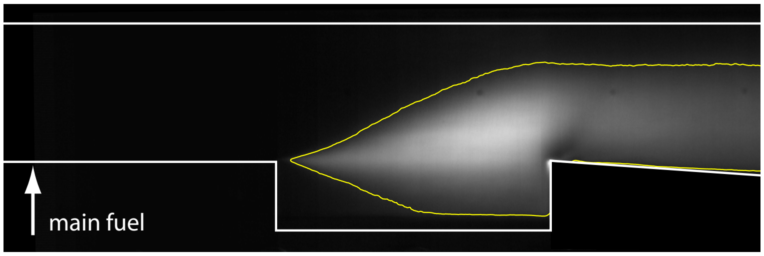

(a) Cavity stabilized combustion.

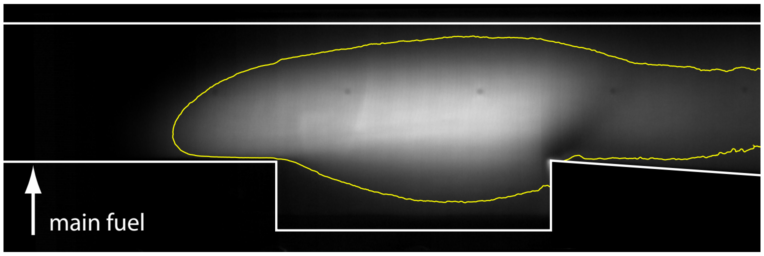

(b) Jet-wake stabilized combustion.

Figure 3.1: Combustion luminosity images averaged over 75 ms for upstream injection of hydrogen fuel. $T_{0,air} = 1250$ K, $\phi = 0.23$, no cavity fueling. Yellow line is an iso-luminosity contour.

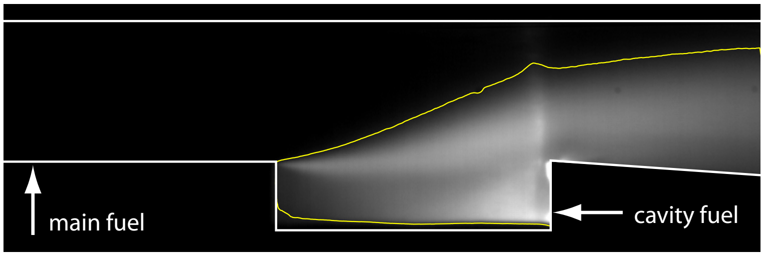

(a) Cavity stabilized combustion.

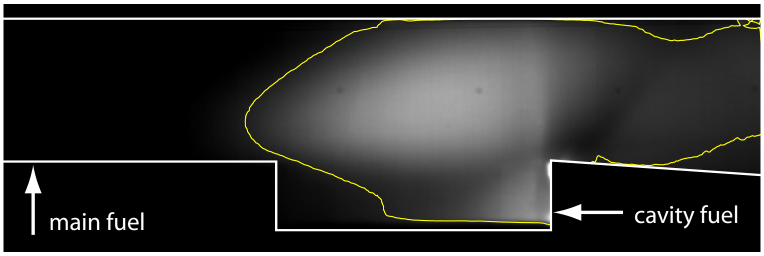

(b) Jet-wake stabilized combustion.

Figure 3.2: Combustion luminosity images averaged over 40 ms for upstream injection of blended fuel (50% ethylene 50% hydrogen). $T_{0,air} = 1370$ K, $\phi = 0.42$, $\dot{m}_{cavfuel}/\dot{m}_{totalfuel} = 0.05$. Yellow line is an iso-luminosity contour.

3.3 shows a histogram of the reaction zone leading edge for 5 runs of hydrogen fuel with $T_{0,air} = 1130 - 1400K$. To create this figure the reaction zone leading edge location was obtained for each frame of the high speed movies. First, an iso-luminosity contour characteristic of the reaction zone border was defined. The average upstream axial location of this contour was then calculated for $y/H = 0.15 - 0.50$ above the cavity. In Fig. 3.3 it can be seen that there are two distinct regions where the combustion can be stabilized. The upstream peak represents the jet-wake stabilized location and the downstream peak represents the cavity stabilized location.

Figure 3.4 shows a plot of the reaction zone leading edge as a function of time for conditions at which the combustion oscillates between the stabilization modes. It can be seen that the reaction zone is generally instantaneously stable in either the jet-wake or cavity stabilized mode, or it is very quickly moving between the two modes.

3.1.1.1 Dependence on Operating Conditions

For each set of conditions studied, the fraction of time the reaction zone spent in each stabilization mode was calculated from the high speed movies. To obtain this data, the same definition of reaction zone leading edge illustrated in Fig. 3.3 was used. Then a critical axial location which separated the two modes was set to $(x/H)_{crit} = 0.6$ (as seen in Fig 3.4). Each image where the reaction zone leading edge was upstream of this value was considered to be in the jet-wake stabilized mode (and downstream in the cavity stabilized mode). The calculated fraction of time in each mode was not very sensitive to the selection of the $(x/H)_{crit}$ value due to the small percentage of time spent in transition.

The influence of $T_{0,air}$, ϕ, cavity fueling rate, and fuel type on the flame stabilization mode was examined by calculating the percentage of time in each mode for the

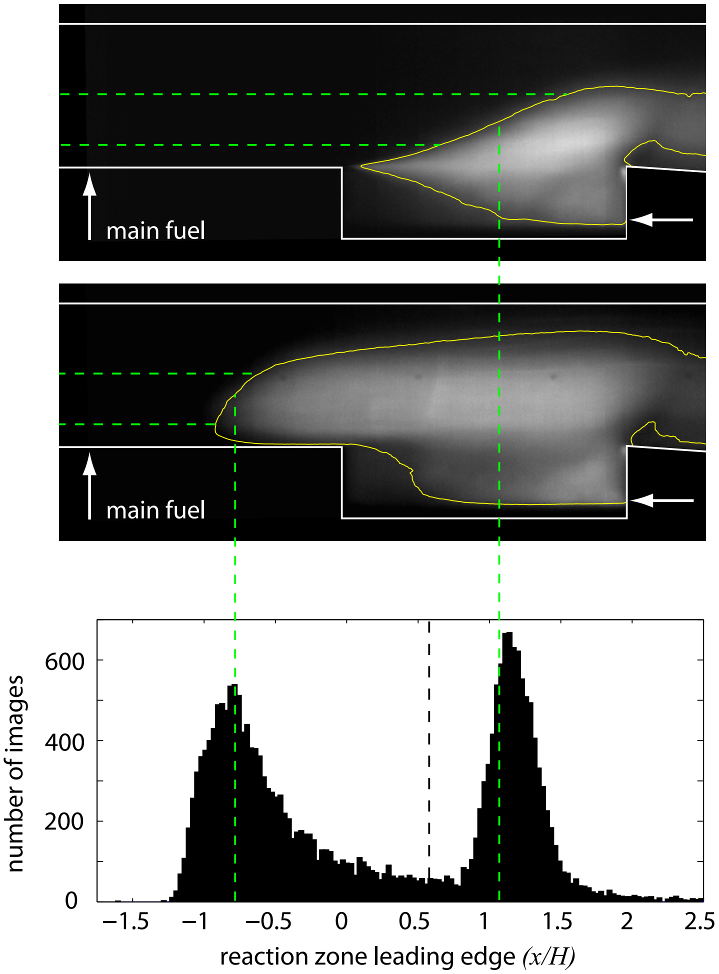

Figure 3.3: Histogram of the reaction zone leading edge location based on 22,500 images. Upstream injection of hydrogen with $T_{0,air} = 1130-1400$ K, $\phi = 0.21$, $\dot{m}_{cavfuel}/\dot{m}_{totalfuel} = 0.02$. Luminosity images show example instantaneous cavity and jet-wake reaction zones. Dashed lines illustrate how the reaction zone leading edge is calculated.

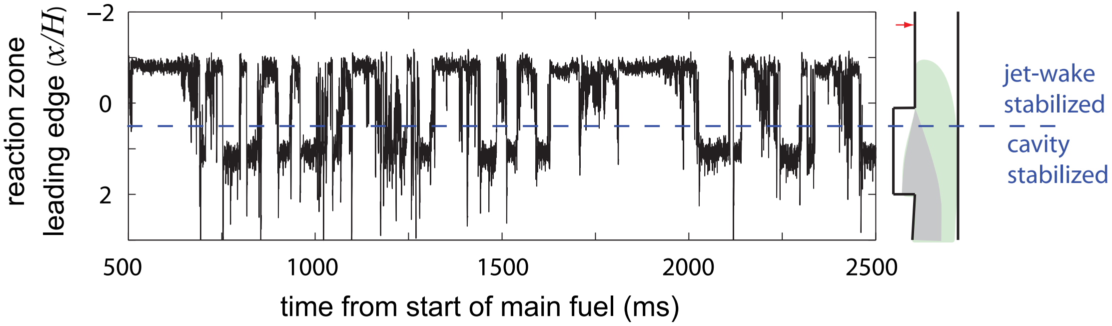

Figure 3.4: Reaction zone leading edge signal for a case of oscillation between modes. Upstream injection of hydrogen with $T_{0,air} = 1220$ K, $\phi = 0.27$, $\dot{m}_{cavfuel}/\dot{m}_{totalfuel} = 0.05$. Dashed line represents the division between jet-wake and cavity stabilized combustion.

	fuel type	ϕ	$\frac{\dot{m}_{cavfuel}}{\dot{m}_{totalfuel}}$	d_{inj} (mm)	$T_{0,air}$ (K)
set A	H_2	0.21	0.02	2.19	1130-1400
set B	H_2	0.21	0.12	2.19	1040-1410
set C	H_2	0.26	0.0	2.49	1050-1370
set D	50-50 H_2,C_2H_4	0.42	0.05	2.49	1250-1500

Table 3.2: Test conditions for determining fraction of time spent in each stabilization mode for upstream main fuel injection ($x/H = -1.75$).

cases given in Table 3.2. The results for hydrogen fuel are plotted in Fig. 3.5. It can be seen that the results for all three data sets collapse relatively well to a single line. Thus $T_{0,air}$ is the dominant variable for determining the combustion stabilization mode. The overall equivalence ratio and cavity fueling rate play little to role for the range of conditions studied. At high $T_{0,air}$ ($\gtrsim$1350 K), the combustion was virtually always stabilized in the jet-wake mode. For low $T_{0,air}$ ($\lesssim$1150 K), the combustion was virtually never stabilized in the jet-wake mode, i.e. it was always stabilized in the cavity mode. For intermediate temperatures (1150 K$\lesssim$ $T_{0,air}$ $\lesssim$ 1350 K) the combustion oscillated between the two stabilization modes. The fraction of time in the jet-wake stabilized mode (f) may be approximated by Eq. 3.1 for all conditions. Eq. 3.1 is plotted as a dashed line in Fig. 3.5.

$$f = \frac{1}{2} + \frac{1}{2}\,\mathrm{erf}\left(\frac{T_{0,air} - 1250K}{75K}\right) \tag{3.1}$$

The results for the blended fuel (50% H_2, 50% C_2H_4 by mole) are shown in Fig. 3.6. The blended fuel exhibits the same behavior seen for the hydrogen fuel, but the transition from cavity to jet-wake combustion occurs at a higher temperature. The error function approximation shown for the blended fuel is simply shifted to the right by 120 K compared with Eq. 3.1.

This temperature and fuel type dependence of the combustion stabilization mode suggests that the speed of the chemistry is controlling which stabilization mode is

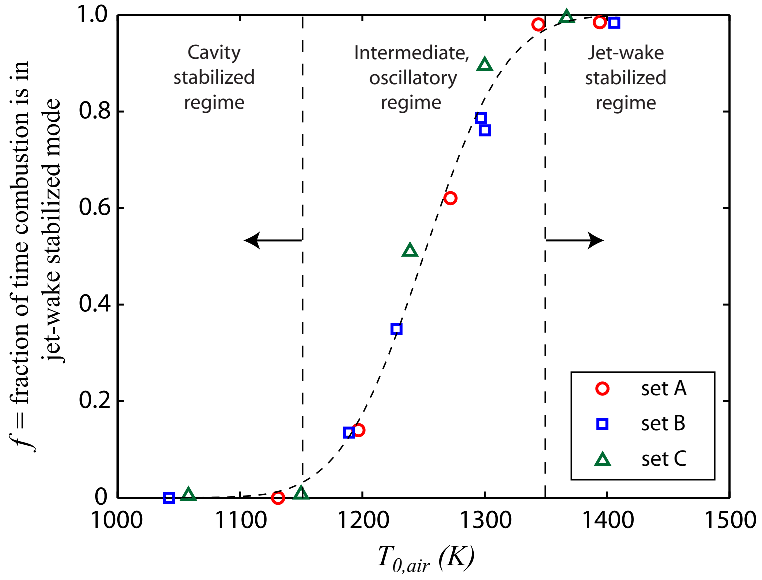

Figure 3.5: Combustion stabilization mode vs. $T_{0,air}$ for hydrogen fuel. Upstream main fuel injection, cavity rear wall fueling.

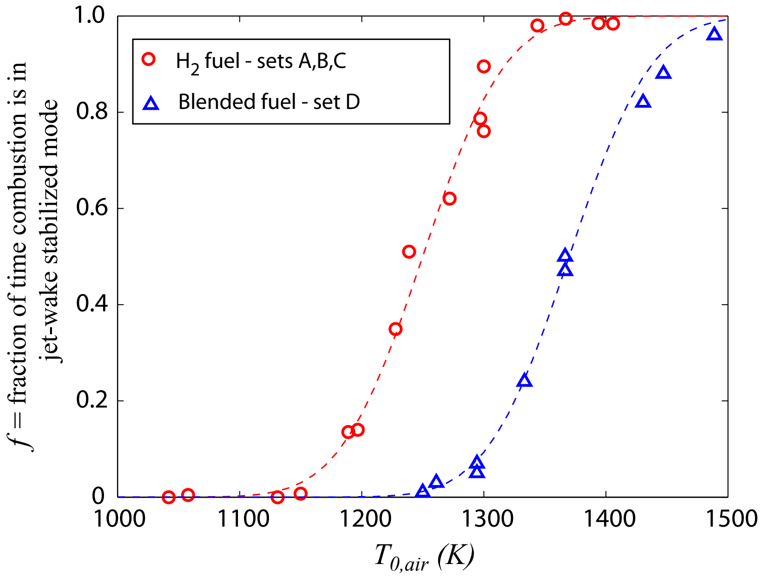

Figure 3.6: Combustion stabilization mode vs. $T_{0,air}$ for hydrogen fuel and blended fuel with upstream main fuel injection.

present. When the chemistry is slower, due to the presence of hydrocarbon fuel or a lower temperature, the combustion is cavity stabilized. When the chemistry is faster, the combustion is jet-wake stabilized. Additionally, these results give support to the concept of using hydrogen fuel to mimic the behavior expected from more practical hydrocarbon fuels at higher temperatures.

Fig. 3.6 shows why a blend of 50% ethylene, 50% hydrogen was chosen as a surrogate hydrocarbon fuel. This fuel composition allowed both steady cavity and steady jet-wake stabilized combustion to be obtained for the range of experimentally achievable temperatures. Ethylene is one of the most reactive hydrocarbon fuels which can be used over wide range of pressures in the gaseous state. Acetylene, which is more reactive, cannot. With pure ethylene, steady jet-wake stabilized combustion could not be obtained at even the highest achievable $T_{0,air}$. Furthermore, with pure ethylene, ignition was unreliable at temperatures which would yield steady cavity stabilized combustion.

3.1.1.2 Cavity Stabilized Combustion

For the cavity stabilized combustion mode, the upstream edge of the reaction zone always was located in the cavity shear layer near the leading edge of the cavity. This stabilization location was fixed, even though there were variations in $T_{0,air}$, ϕ, and fuel composition. Therefore it is apparent that the cavity is functioning as a flameholder in this mode. From the fixed stabilization location, the reaction zone spreads into the flow at an approximately constant angle. Mathur [69] and Lin [65] found a very similar reaction zone for angled ethylene injection upstream of a wall cavity, shown in Fig. 3.7.

The angle of spreading depended on the specific operating conditions. To investigate these effects, the spreading angle was calculated for the conditions shown in

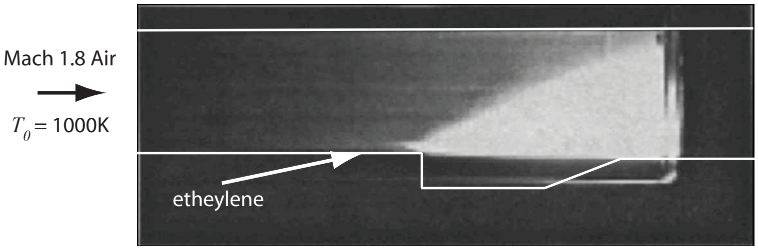

Figure 3.7: Image from Mathur et al [69] showing a cavity stabilized reaction zone structure in a dual-mode combustor.

Table 3.2 which resulted in significant cavity stabilized combustion. For each average cavity stabilized combustion luminosity image obtained, a combustion iso-luminosity contour characteristic of the reaction zone outline was defined. Then the spreading angle was defined from the slope of the line tangent to this contour which passes through the top of the cavity leading edge.

Figure 3.8 shows an example of the spreading angle calculation for two different iso-luminosity contours. It can be seen, that the calculated spreading angle is a function of the chosen value of the iso-luminosity contour. Thus the specific spreading angle for each set of conditions is of less interest than the trends for changes in temperature and fuel type. It can also be seen from Fig. 3.8 that luminosity first spreads at a shallow angle (for $0 \lesssim y/H \lesssim 0.15$), then becomes steeper (for approximately $0.15 \lesssim y/H \lesssim 0.6$) before turning again and becoming nearly parallel to the flow (approximately $y/H \gtrsim 0.6$). This basic structure was present in all average cavity stabilized combustion images.

Figure 3.9 shows the measured reaction zone spreading angles vs. $T_{0,air}$ for the conditions in Table 3.2 for the two critical iso-luminosity values shown in 3.8. The data for hydrogen fuel collapses relatively well to one line, while the blended fuel data collapses to another. The spreading angle increases for increasing $T_{0,air}$ regardless of fueling conditions or the critical luminosity intensity used. Additionally, the

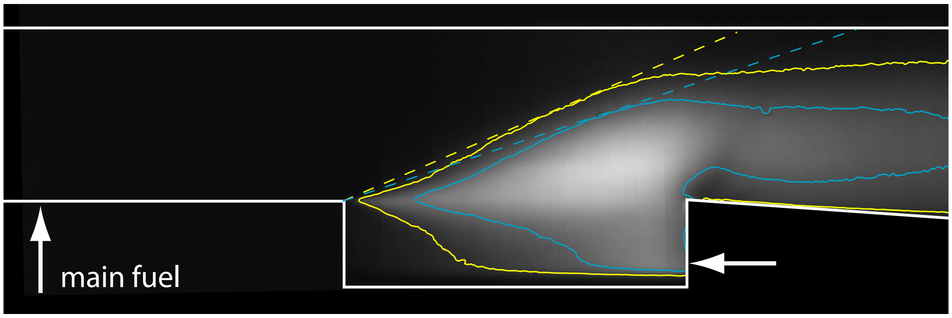

Figure 3.8: Average cavity stabilized combustion luminosity for data set A, $T_{0,air} = 1130$ K. Yellow and blue solid lines are iso-luminosity contours of 30 and 50 counts respectively. Dashed lines show the spreading angles determined from each iso-luminosity contour.

spreading angle is less for the mixed fuel than for the hydrogen fuel at the same temperature.

3.1.1.3 Jet-Wake Stabilized Combustion

For the jet wake stabilized combustion mode, the reaction zone leading edge always was upstream of the cavity leading edge. The stabilization location was not fixed, but varied with the operating conditions. Figure 3.10 shows an example top view combustion luminosity image of jet-wake stabilized combustion. It can be seen that the reaction zone is stabilized in the wake of the fuel injection jet. Although the limited window size prevented directly imaging the sidewall regions from this angle, it does not appear that these regions play a significant role in the stabilization. Therefore this combustion mode is different from that observed by Mathur et al [69] for angled ethylene injection upstream of a wall cavity. This study found reaction upstream of the cavity only along the sidewalls, in the separated boundary layer.

The distance between the fuel injection location and the stabilization zone (l_{ign}) was dependent on the air stagnation temperature and the fuel type. This lift-off distance is plotted as a function of temperature in Fig. 3.11 for all applicable cases at the conditions in Table 3.2. This figure was created using the method for calculating

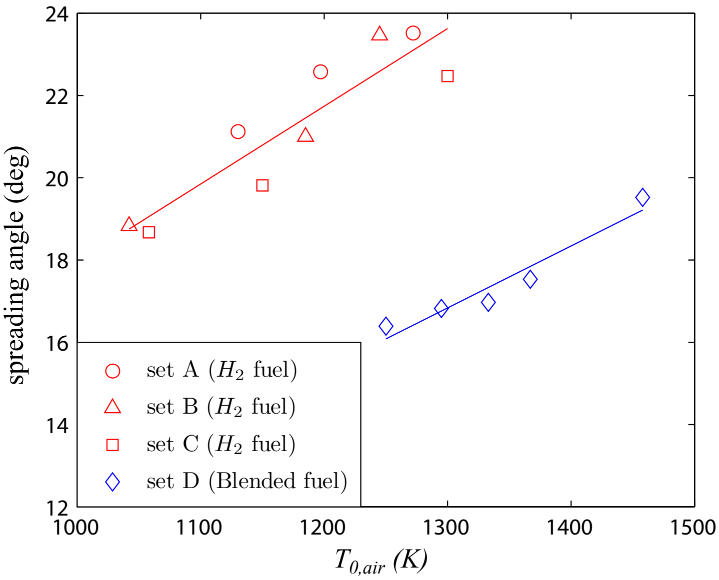

(a) Critical iso-luminosity contour = 30 counts.

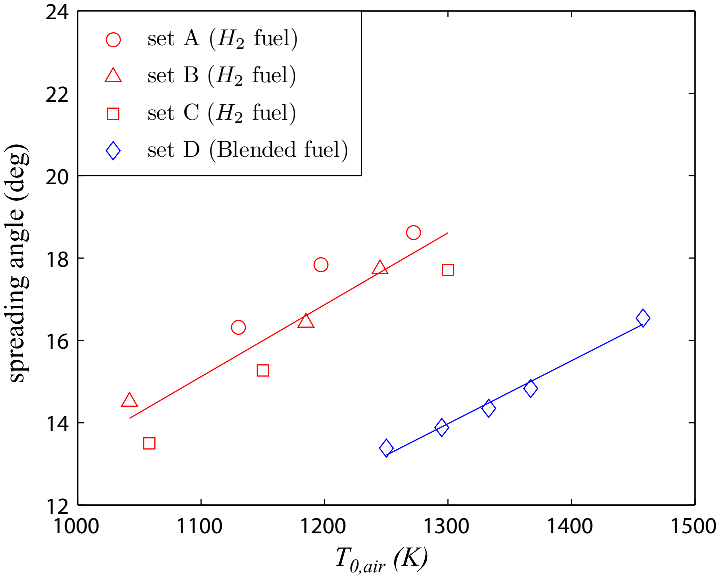

(b) Critical iso-luminosity contour = 50 counts.

Figure 3.9: Measured reaction zone spreading angles for cavity stabilized combustion mode vs. $T_{0,air}$ for the two values of the critical iso-luminosity contour shown in Fig. 3.8. Solid lines are linear regression fits to the data.

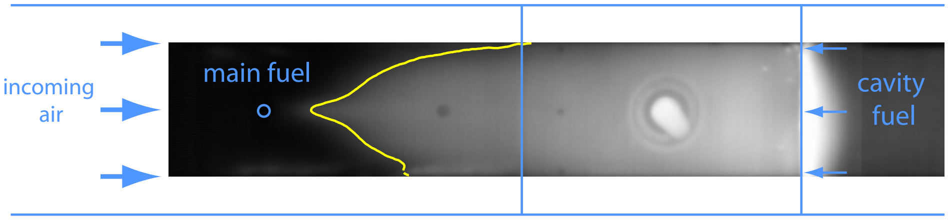

Figure 3.10: Top view, jet-wake stabilized, average combustion luminosity. H_2 fuel, $T_{0,air} = 1370$ K, $\phi = 0.27$, $\dot{m}_{cavfuel}/\dot{m}_{totalfuel} = 0.07$.

the reaction zone leading edge location described in Sec. 3.1.1.1. It can be seen that the lift-off distance l_{ign} decreases with increasing $T_{0,air}$. The hydrogen fuel data collapses relatively well to one line, while the blended fuel data collapses to another.

3.1.2 Ramjet-mode Dynamics

There is a large difference in the steadiness of the combustion between the different stabilization modes. The pressure fluctuations are a good marker of the steadiness of the combustion in a thermally choked flow, because any change in the heat release rate or heat release distribution will cause a change in the entire combustor pressure field and pre-combustion shock train. Figure 3.12 shows the standard deviation of the non-dimensional wall pressure ($\sigma_{P_w/P_{0,i}}$) and the average pressure for a case of each combustion stabilization mode for set A and set C conditions. Pressure measurements were acquired at a 40 Hz sampling at eight wall locations in the combustor and isolator.

The highest pressure fluctuations are observed to occur in the isolator near the start of the pre-combustion shock train. This is due to fluctuations in the pre-combustion shock train length and the large pressure gradient at the shock train leading edge. The cavity stabilized mode has the lowest pressure fluctuations, while those of the jet-wake stabilized mode were larger. Not surprisingly, the largest pressure fluctuations occurred for the cases that undergo oscillations between the two

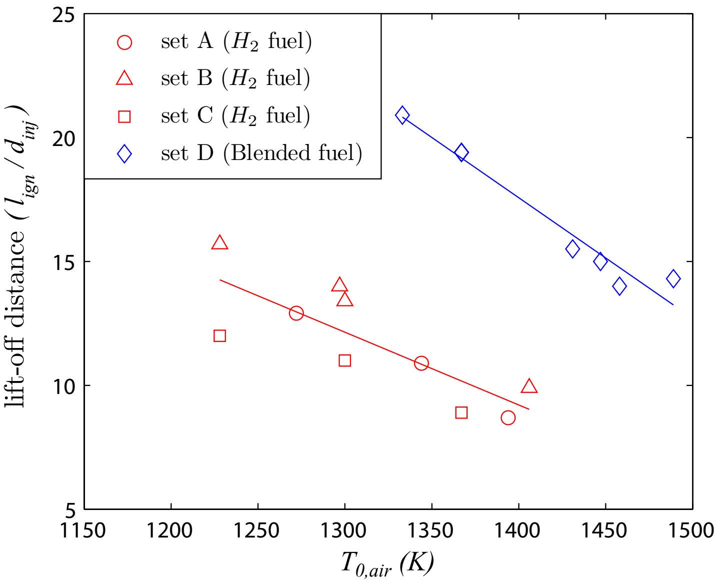

(a) Lift-off distance (l_{ign}) non-dimensionalized by injection orifice diameter (d_{inj}).

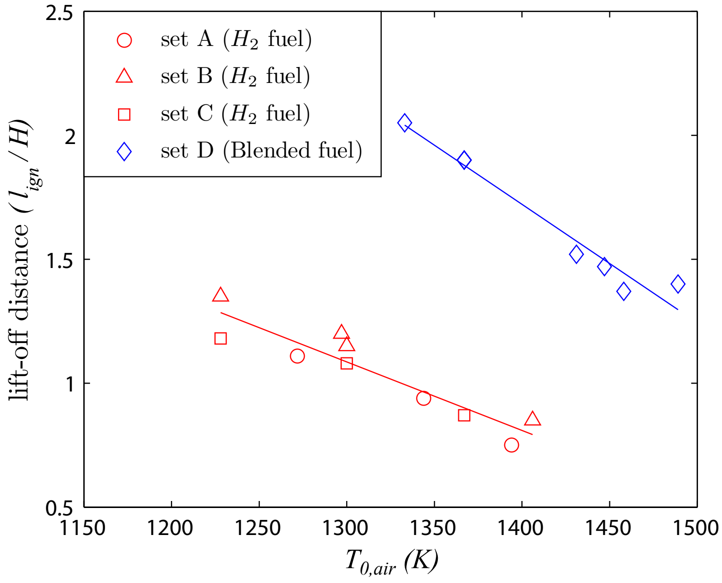

(b) Lift-off distance (l_{ign}) non-dimensionalized by combustor height (H).

Figure 3.11: Lift-off distances (l_{ign}) for jet-wake stabilized combustion vs. $T_{0,air}$. Conditions for each set given in Table 3.2. Solid lines are linear regression fits to the hydrogen and blended fuel data.

combustion stabilization modes. Because these large fluctuations are undesirable in a flight vehicle, it is important to understand the mechanism behind the combustion oscillation at intermediate temperatures.

Two common causes of combustion instabilities are acoustic waves and periodic fluid dynamic instabilities [70]. Thermoacoustic combustion instabilities occur when there is coupling between the acoustic pressure waves and heat release fluctuations. Thermoacoustic instabilities have been observed in a wide variety of devices utilizing premixed or partially premixed combustion [116, 54, 64]. These instabilities result in pressure fluctuation magnitudes that are highly peaked at one or more frequencies, which correspond to acoustic modes of the combustor. Lin et al [64] performed an experimental and theoretical analysis of the acoustic modes and combustion instabilities in a dual-mode scramjet combustor. Lin identified two primary acoustic-convective feedback loops in such combustors, which are shown in Fig. 3.13. The associated frequencies are given by Eq. 3.2 for the reaction zone to fuel-injection instability and by Eq. 3.3 for the reaction zone to pre-combustion shock train instability.

$$f_{if} \approx \frac{\bar{a}\bar{M}\left(1-\bar{M}\right)}{nL_{if}}, \quad n = 1, 2, 3, ... \tag{3.2}$$

$$f_{sf} \approx \frac{\bar{a}\left(1-\bar{M}\right)}{2nL_{sf}}, \quad n = 1, 2, 3, ... \tag{3.3}$$

In the above equations L_{if} is the distance between the flame and the fuel injection location, L_{sf} is the distance between the flame and the shock train leading edge, and $\bar{a}$ and $\bar{M}$ are the average speed of sound and convective Mach number over L_{if} and L_{sf}. For the University of Michigan scramjet combustor, this analysis leads to predicted instability frequencies of 150-2000 Hz. For the similar combustor studied

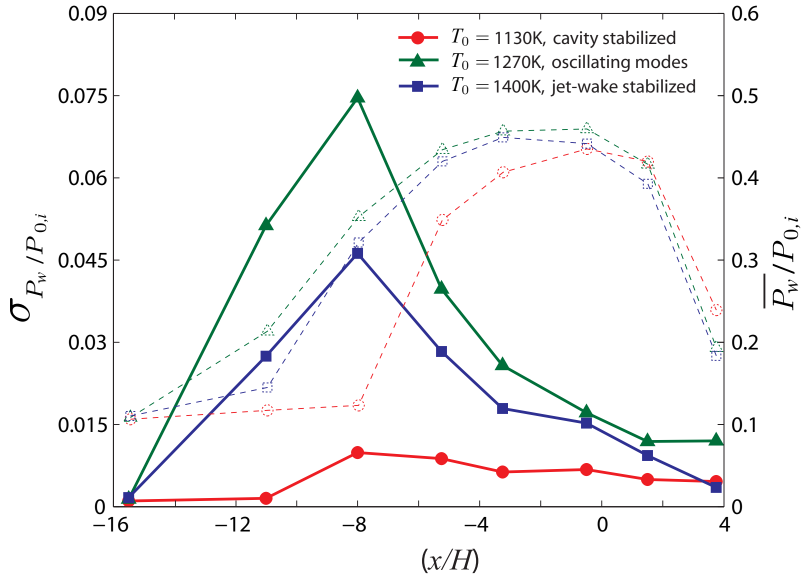

(a) Data set A conditions : Table 3.2.

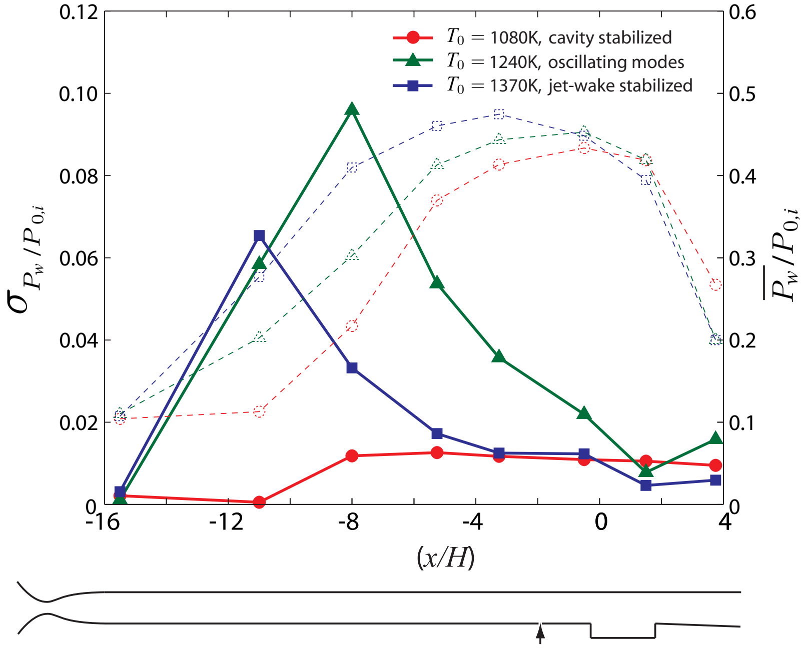

(b) Data set C conditions : Table 3.2.

Figure 3.12: Wall pressure standard deviation (solid symbols) and average (open symbols) for upstream injection of hydrogen fuel with different stabilization modes.

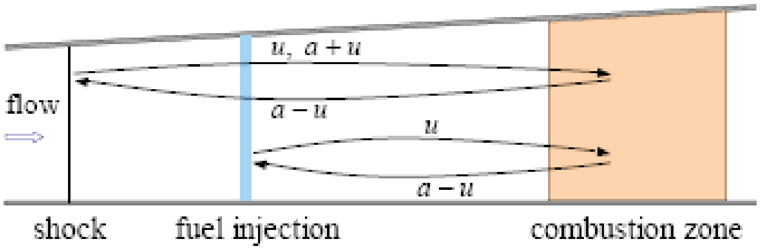

Figure 3.13: Figure from Lin et al [64] showing acoustic-convective feedback loops in a scramjet combustor.

by Lin, the predicted acoustic modes were 70-650 Hz and the measured instability frequencies were 120-380 Hz [64].

Choi, Ma, and Yang performed computations to simulated instability mechanisms in scramjet combustors with transverse jet fuel injection [16, 17]. They found that Richtmyer-Meshkov instability occurs in the shear layer of the fuel injection jet. They also found coupling between the cavity acoustics and the fuel injection jet. Ben-Yakar and Hanson discuss this coupling[6] as well. For the present combustor, these instabilities are in the kHz range due to the high velocities and relatively short length scales.

The measured reaction zone leading edge location (obtained from the 4000 Hz movies) was analyzed to determine if thermoacoustic or periodic fluid dynamic instabilities can explain the large fluctuations observed at intermediate temperatures. Additionally, a high frequency wall pressure signal was acquired at $x/H = -5.5$ and synchronized with the high speed movie data for 4 runs at conditions leading to oscillatory combustion. Figure 3.14 shows an example reaction zone leading edge and synchronized wall pressure signal. The reaction zone is generally clearly stabilized in either the cavity or jet-wake location, with movement between the two locations happening very quickly. The largest pressure fluctuations in the isolator are associated with the movement of the flamefront between modes. The oscillation between modes does not happen at a set frequency. Movement between momentarily stable combustion modes occurs approximately 5-20 times per second.

The lack of a fixed frequency and the relatively low rate of oscillation shows that the oscillation between combustion modes is not caused by thermacoustic or periodic fluid dynamic instabilities. Figure 3.14(b) and 3.14(c) shows the details of a flash-forward (cavity to jet-wake stabilized location) and flash-back (event). The movement of the flamefront between stabilization modes takes approximately 1 ms. The large pressure change in the isolator begins approximately 15 ms after the flamefront movement, and takes approximately 10 ms to complete. Since the flamefront movement precedes the pressure change, the large pressure fluctuations are caused by the movement of the flamefront, and not vice versa.

Some of the flamefront movements happen abruptly with no oscillation, such as the flash-back event shown in Fig. 3.14(c). For other flamefront movements, such as the flash-forward event show in Fig. 3.14(b), there are a few oscillations at high frequency ($\mathcal{O}$(1 kHz))before the new momentarily stable position is established. This high frequency oscillation, which is sometimes encountered during flash-back or flash-forward events, does not couple with the large pressure oscillations due to the relatively long time lag involved.

Figure 3.15 shows the frequency power spectra of the flamefront and pressure signal from Fig. 3.14. The are no sharp peaks in either signal indicating a strong thermoacoustic or fluid-dynamic instability mode. The pressure signal does show a broad range of elevated fluctuations in the range of 300-1000 Hz. These are in the range of expected frequencies for thermoacoustic modes such as those studied by Lin [64]. The flamefront signal does not show elevated fluctuations in this range, showing that coupling with the large flamefront movements is rare.

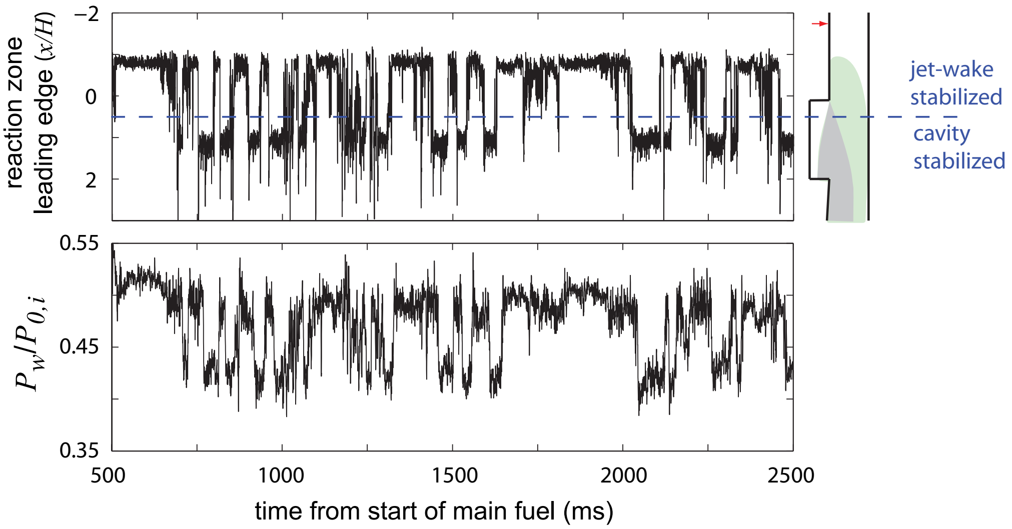

(a) Example 2 s of synchronized reaction zone leading edge and wall pressure

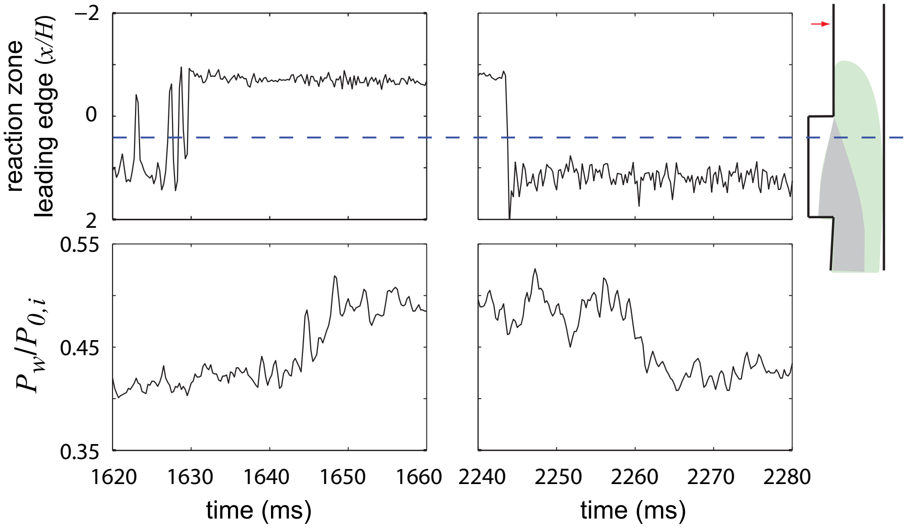

(b) Detail of flash-forward (cavity to jet-wake) event

(c) Detail of flash-back (jet-wake to cavity) event

Figure 3.14: Synchronized reaction zone leading edge location and wall pressure data. Upstream hydrogen fuel injection with $\phi = 0.27$, $\dot{m}_{cavfuel}/\dot{m}_{totalfuel} = 0.05$, $T_{0,air} = 1220$ K.

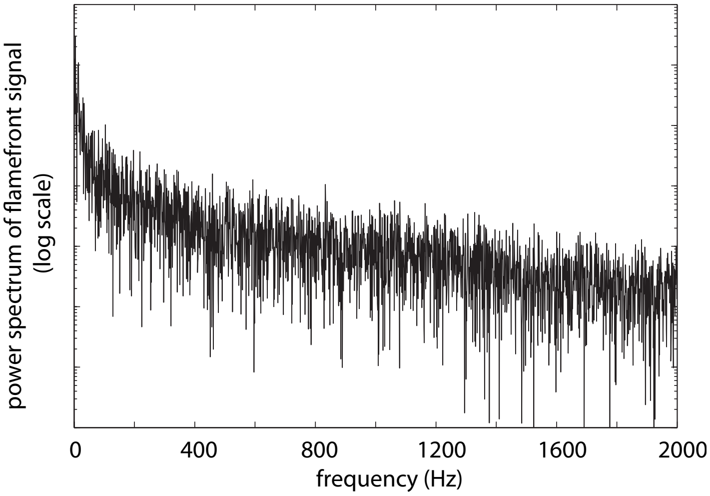

(a) Flamefront axial location data.

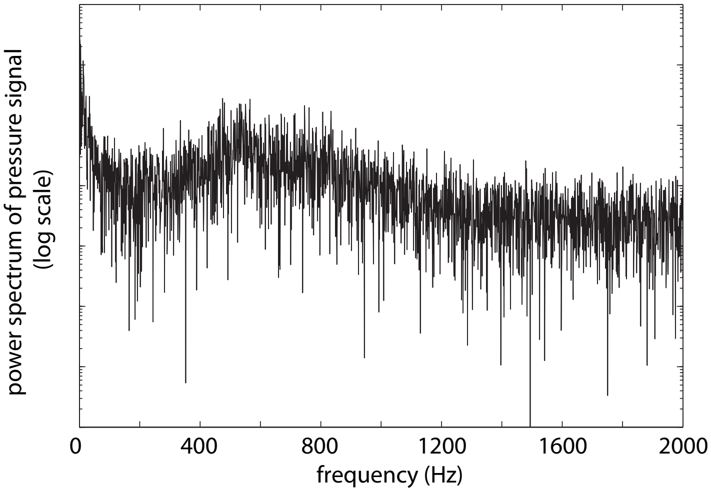

(b) Wall pressure data.

Figure 3.15: Power spectra of the flamefront location and pressure signal shown in Fig. 3.14. There is no spike due to a resonant mode.

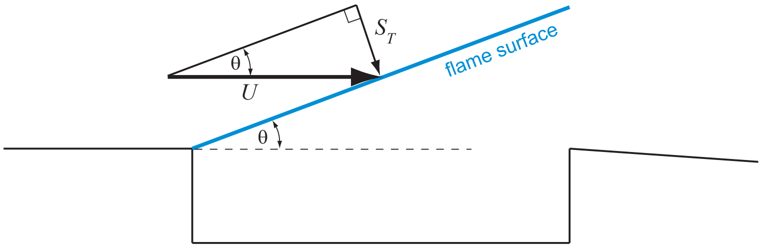

Figure 3.16: Diagram showing relationship between the turbulent flame speed (S_T), the flow velocity (U), and the flame spreading angle θ.

3.1.3 Discussion of Mechanisms

3.1.3.1 Cavity Stabilized Combustion Mechanism

The shape of the cavity stabilized reaction zone strongly suggests that it is a premixed flame. The flame base is anchored in a low speed region near the upstream boundary of the cavity shear layer. A premixed flame sheet then spreads into the flow at an angle which corresponds to the local turbulent flame speed (S_T) equalling the normal flow velocity as illustrated in Fig. 3.16. The relatively constant spreading angle from a fixed location is not consistent with a pure auto-ignition process.

The measured dependence of the spreading angle on $T_{0,air}$, as seen in Fig. 3.9, is expected for premixed flame spreading. Increasing the reactant mixture temperature increases the flame speed, and thus the spreading angle. The flame speed is smaller for the mixed fuel case than for the hydrogen fuel at the same temperature, so the spreading angle is smaller.

The measured temperature dependence of the spreading angle can be compared with the expected temperature dependence of a premixed flame using CHEMKIN. CHEMKIN was used to calculate the laminar flame speed (S_L) for hydrogen-air flames with $\phi = 0.5 - 2.0$ and $T_{mixture} = 700 - 1200K$. The flame spreading angle (θ) was calculated for each set of conditions from the flow velocity U and the turbulent to laminar burning velocity ratio (S_T/S_L) using the geometry shown in Fig. 3.16. The flow Mach number was assumed to be constant and was set equal to 0.75. This was approximately equal to the isolator exit Mach number for all cavity stabilized cases based on the wall pressure and constant impulse function analysis [21]). To facilitate comparison with the measured values, the static mixture temperatures ($\overline{T}$) used for the CHEMKIN simulations were converted to equivalent air stagnation temperatures ($T_{0,air}$) using the equivalence ratio and the assumed Mach number according to Eqs. 3.4 and 3.5. The mixture average properties are denoted by the $\bar{\cdot}$ symbol in these equations.

$$\overline{T_0} = \left(1 + \frac{\overline{\gamma} - 1}{2} M^2\right) \overline{T} \tag{3.4}$$

$$T_{0,air} = \frac{(\dot{m}_{air} + \dot{m}_{fuel})\overline{c_p}\overline{T_0} - \dot{m}_{fuel} c_{p,fuel} T_{0,fuel}}{\dot{m}_{air} c_{p,air}} \tag{3.5}$$

Some calculated flame spreading angles vs. $T_{0,air}$ are shown Fig. 3.17. If the ratio of turbulent to laminar burning velocities of (S_T/S_L) has values of 11 and 9, then calculated spreading angles which agree reasonably well with the measured values for critical iso-luminosity contours of 30 and 40 counts respectively. While S_T/S_L is not known, these value both are physically reasonable. The predicted spreading angle dependence on temperature agrees quite well with the measured values for rich flames with a local equivalence ratio of 1.4. For stoichiometric and lean flames, the predicted spreading angle dependence on temperature is somewhat stronger than measured. Overall, this CHEMKIN analysis suggests that premixed flame propagation is a reasonable explanation for the cavity stabilized combustion spreading angle.

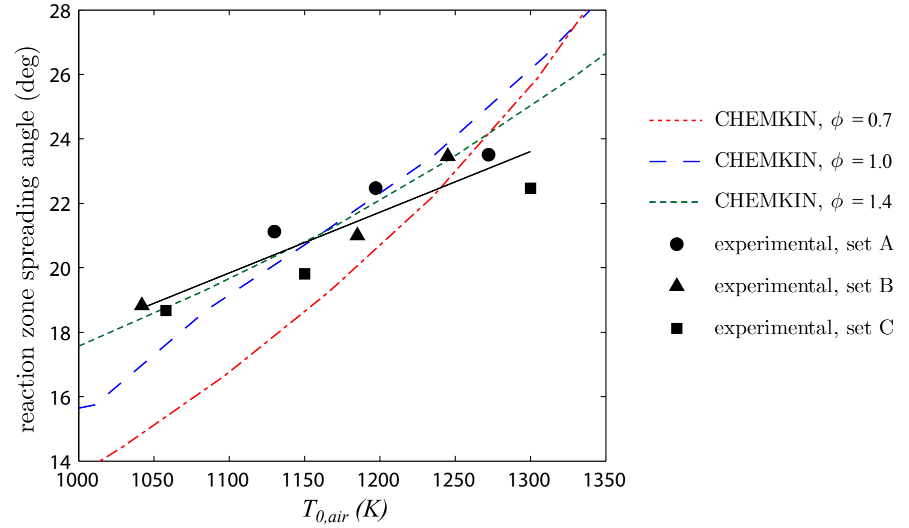

(a) Critical intensity=30 counts for experimental data, $S_T/S_L = 11$ for CHEMKIN analysis.

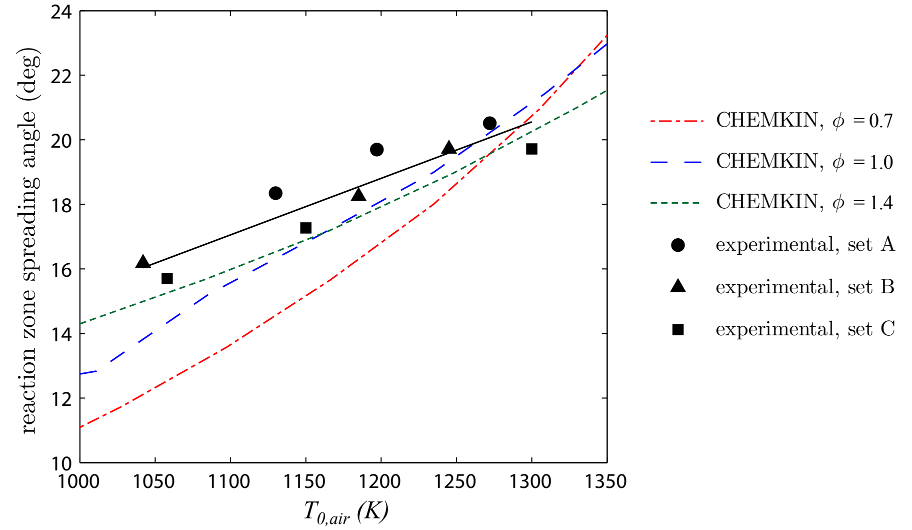

(b) Critical intensity=40 counts for experimental data, $S_T/S_L = 9$ for CHEMKIN analysis.

Figure 3.17: Temperature dependence of CHEMKIN calculated flame spreading angles and the measured spreading angles.

The other possible mechanism for the cavity stabilized combustion is that reactants mix with the hot combustion products in the cavity, and that the combustion is confined to the shear layer above the cavity. This mixing replaces diffusion as a means of raising the reactant temperature sufficiently for ignition. The fact that the angles seen in Fig. 3.9 are much larger than the expected shear layer spreading angles would seem to preclude the possibility that this mechanism occurs. The method of Slessor et al [89] was used to obtain an estimate of the spreading rate of the compressible shear. Rasmussen [82] found that Slessor's free shear layer method agreed well with the measured shear spreading rate over a cavity for a non-reacting, supersonic freestream. Heat release has been found to decrease the shear layer spreading rate compared with non-reacting flow [23]. For the current case, the cavity side was assumed to consist of stoichiometric combustion products at zero velocity. The shear layer spreading half-angle (the angle from the centerline) was calculated to be approximately 6 degrees. The reaction zone spreading angles measured in the current work are far greater than this value.

3.1.3.2 Jet-wake Stabilized Combustion Mechanism

The cavity does not appear to play a significant role in the jet-wake stabilization mode since the reaction zone is observed to begin upstream of the leading edge. The shape and location of the reaction zone leads to two possible explanations for the combustion mechanism: 1) the combustion occurs as a lifted jet flame or 2) the combustion occurs due to auto-ignition. For a lifted jet flame, the stabilization mechanism is generally explained by premixed flame propagation [105, 59, 62]. The fuel and air premix in the lift-off distance, and the base of the reaction zone is a premixed flame. The flame base will be stabilized where the local flame speed is equal to the local flow speed (on average). The fact that the jet-wake stabilized combustion mode

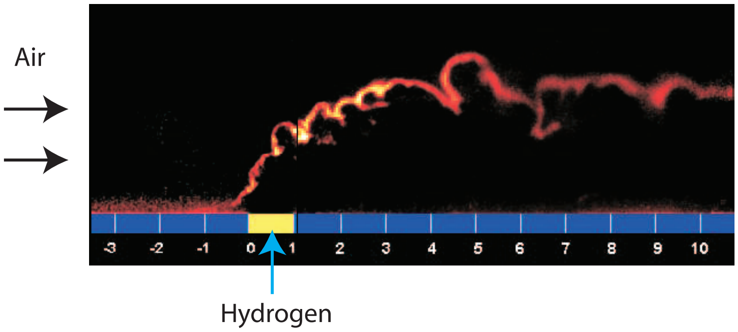

Figure 3.18: Image from Ben-Yakar [4] showing an example reaction zone for pure auto-ignition with a negligible ignition delay time. OH-PLIF signal for hydrogen injection into a Mach 3.4 air crossflow with $T_{0,air} = 3750$ K.

occurs at high stagnation temperatures makes auto-ignition a plausible explanation for the combustion mechanism. For an auto-ignition controlled reaction, the lift-off distance is controlled by the auto-ignition delay time. The local conditions at the reaction zone base are not important, since there is no propagating flame. Instead, the entire time history of the velocity, temperature, and equivalence ratio of a fluid packet controls the auto-ignition delay time and distance.

Previous studies with very high temperature air have found combustion in the fuel-jet wake that was attributed to auto-ignition. Ben-Yakar and Hanson [5, 4] used a shock tunnel to study transverse hydrogen injection into a Mach 3.46 and 4.6 crossflow of air with $T_{0,air} = 3750$ K and 7200 K respectively. These conditions simulate flight Mach numbers of 10 and 13. For such high temperatures, the auto-ignition delay time is negligible, and the fuel burns as soon as it mixes with the air. As Fig. 3.18 shows, the reaction zone is attached to the fuel injection jet.

Yu, Wilson, and Schadow [117] studied angled injection of vitiated ethylene fuel ($T_{0,fuel} = 2100 - 2600$ K) into unheated Mach 2.0 ($T_{0,air} = 288$ K) air and found a reaction zone similar to the current jet-wake stabilized combustion mode. Figure 3.19 shows an example schematic of this reaction zone which began approximately 10

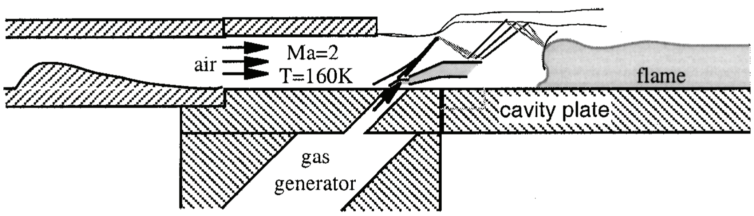

Figure 3.19: Schematic from Yu, Wilson, and Schadow [117] showing a reaction zone similar to jet-wake stabilized combustion. Vitiated fuel ($T_{0,fuel} = 2600$) K consisted of 28% C_2H_4, 36% CO_2, and 36% H_2O.

injection orifice diameters downstream of the injection location. Although Yu refers to the reaction zone as a flame, there is no discussion of whether the stabilization mechanism is auto-ignition or flame propagation.

Gordon et al [40, 39, 38] has examined the lifted combustion of a fuel jet issuing into a vitiated co-flow experimentally and computationally. He proposed that the combustion mechanism (premixed flame propagation or auto-ignition) can be identified based on the species transport budgets at the stabilization location. Auto-ignition stabilized reactions are marked by a convection-reaction balance, while the role of diffusion is negligible. In contrast, premixed flame propagation is identified by a flame preheat layer that contains a diffusion-convection balance with little reaction. Such detailed transport information generally cannot be measured experimentally. In addition, the CFD simulation of the current experiment discussed in Sec. 3.1.4 does a poor job of predicting the stabilization location. Therefore this solution is unlikely to yield insight into the correct stabilization mechanism.

CHEMKIN was used to estimate the expected lift-off distances assuming auto-ignition is the dominant combustion mechanism. These calculated auto-ignition delay distances then were compared with the measured data. CHEMKIN homogeneous reactor simulations of the auto-ignition delay time were performed for both hydrogen fuel and blended fuel for mixture temperatures of 900-1500 K and equivalence ratios of 0.05-20. For hydrogen fuel the chemical mechanism of Ò Conaire et al [19] was used. For the blended fuel the mechanism of Wang and Laskin [106] was used. The calculated distances are crude estimates because the local flow velocity and equivalence ratio must be approximated. Additionally, homogeneous reactor simulations do not account for scalar dissipation which increases the ignition delay time for non-uniform flow fields [39].

Figure 3.20(a) shows the calculated ignition delay distance for hydrogen fuel vs $T_{0,air}$ for four local equivalence ratios. To convert the CHEMKIN calculated ignition delay time to distance, convective Mach numbers of 0.4 and 0.6 were assumed. These numbers are estimates of the average convective Mach number of a fuel-air packet between the injection and ignition locations. They are less than the bulk flow Mach number of 0.65-0.75 near the injection location for these conditions (see Sec. 5.2). Additionally, the static mixture temperatures from the CHEMKIN simulations were converted to equivalent air stagnation temperatures using the equivalence ratio and Mach number according to Eqs. 3.4 and 3.5.

In the actual combustor, no fluid packet remains at a constant equivalence ratio, temperature, and Mach number from the initial injection to the auto-ignition time as is assumed in the CHEMKIN calculation. Thus the results give only an approximate estimate of the expected auto-ignition delay distance. Figure 3.20(a) shows that the calculated auto-ignition delay distance is sometimes shorter and is sometimes longer than the measured distance, depending on the assumed values of ϕ and Mach number. It is concluded that auto-ignition could be a plausible explanation for the observed jet-wakes stabilized combustion. It is important to note that the equivalence ratios in the CHEMKIN analysis are local equivalence ratios. They are not global values of ϕ. Auto-ignition is predicted to occur first in fuel lean regions because the air is heated while the fuel is not. The minimum ignition delay time for a given $T_{0,air}$ was found to occur for $\phi \approx 0.1 - 0.2$.

It is also helpful to examine the temperature dependence on the calculated and measured ignition delay distance l_{ign}. Figure 3.20(a) shows that for all modeling assumptions, the slope dl_{ign}/dT_0 calculated by CHEMKIN is significantly larger than the measured slope. The result is independent of the assumed local equivalence ratio and Mach number of the fluid packet. This is strong evidence that the jet-wake stabilized combustion observed is not controlled primarily by auto-ignition reactions. For an auto-ignition controlled reaction, the ignition delay distance would vary much more quickly with changes in $T_{0,air}$ than the trend that is observed.

The results for the blended hydrogen and ethylene fuel are shown in Fig. 3.20(b). For the blended fuel, the minimum ignition delay distance calculated by CHEMKIN for a given $T_{0,air}$ was found to occur for $\phi \approx 0.2 - 0.4$. This value is larger than that of hydrogen fuel due to the significantly lower specific heat of ethylene. The same conclusions regarding the role of auto-ignition can be drawn from Fig. 3.20(b) as for the hydrogen fuel. The flow conditions alone do not eliminate the possibility of auto-ignition. However, the measured dependence of the ignition delay distance on temperature is far different for the CHEMKIN auto-ignition calculations. This shows that auto-ignition is most likely not controlling the stabilization location.

The tendency of the reaction zone to oscillate between two distinct, relatively stable locations is evidence that the combustion most likely is a flame, and is not auto-ignition, for both the cavity and jet-wake stabilized modes. If the combustion was primarily due to auto-ignition in the jet-wake stabilized mode, the reaction zone leading edge would not be expected to be located only in the small stable region seen in Fig. 3.14(a) and illustrated in Fig. 3.21. Instead, any fluctuations which

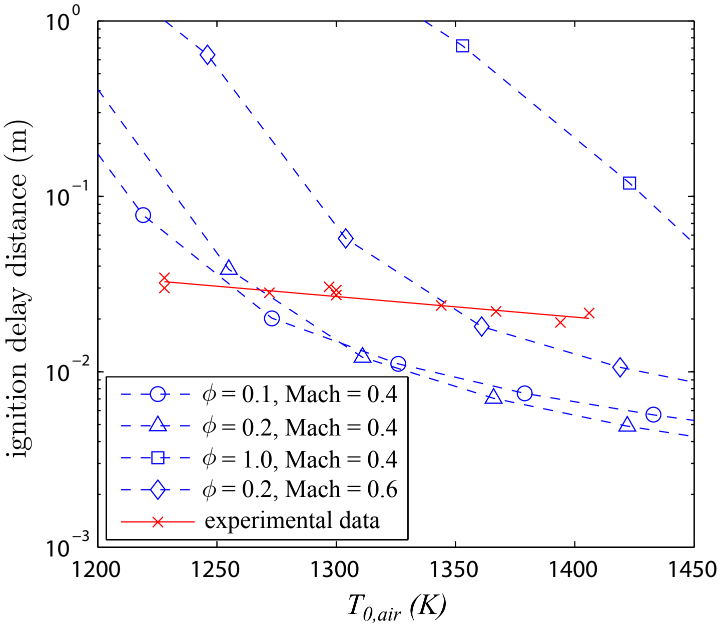

(a) Hydrogen fuel results.

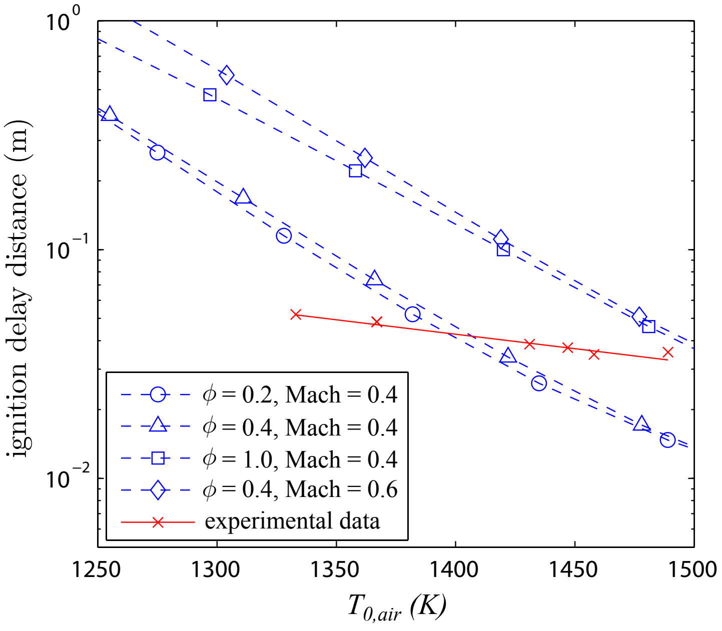

(b) Blended ethylene and hydrogen fuel results.

Figure 3.20: Calculated ignition distances assuming the combustion is controlled by auto-ignition compared with the measured lift-off distances of jet-wake stabilized combustion. Calculated distance is obtained with CHEMKIN assuming that the local equivalence ratio, static temperature, and Mach number remain constant from injection to ignition.

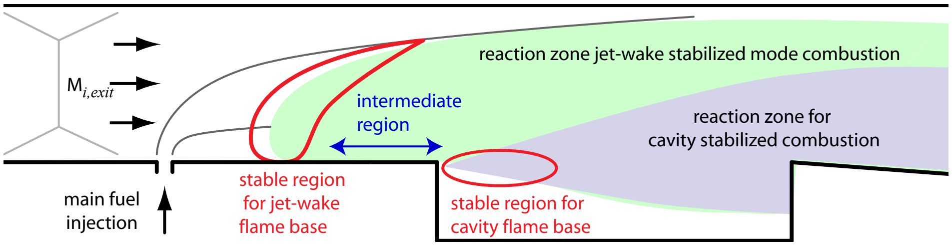

Figure 3.21: Flame base stabilization locations.

pushed the reaction zone downstream of its average location would give the fuel/air mixture more time to react, and thus make it more likely to auto-ignite. Additionally, an auto-ignition controlled reaction zone would be expected to immediately return to the average stable location after any fluctuations which pushed it downstream. Instead, Fig. 3.14(a) shows that the reaction zone remains in the cavity stabilized location for $\mathcal{O}$(10-100 ms) after flash back events.

3.1.3.3 Discussion of Ramjet-mode Dynamics

The cavity stabilized mode is the steadiest mode because the base of the premixed flame is located in a low speed region of the cavity shear layer. This part of the shear layer is relatively steady because its location is fixed by the cavity geometry [82]. Lower speed regions exist deeper in the cavity which provide an additional margin for stability. Cavity fueling rate was varied and measurements indicate that it does not play a role in the stabilization location. This is because sufficient main fuel is entrained into the cavity for the cavity reaction to stabilize the main flame at all conditions studied.

In the jet-wake stabilized mode the present data indicate that the combustion occurs as lifted jet-flame. A lifted jet flame consists of a premixing region, a premixed flame base, and a downstream mixing-limited diffusion flame. The premixed flame base must be located in a region of the jet-wake that has favorable velocity, equivalence ratio, and strain rate where the flame speed equals the flow speed (on average). Upstream of the stabilization location illustrated in Fig. 3.21, the strain rate in the fuel-air mixing layer is likely to be too large for flame propagation [79]. This high strain rate would also serve to delay auto-ignition reactions through high scalar dissipation. Moving downstream, the velocity at the stoichiometric contour is believed to increase due to mixing with the high speed co-flow. Therefore the stable region for the jet-wake stabilized flame base is believed to be limited in both the upstream and downstream directions as illustrated in Fig. 3.21. The base of such lifted jet flames are not located at a fixed position, but have some dynamics associated with the large scale turbulent structures of the jet [13]. This is believed to explain why the pressure fluctuations are larger for the jet-wake stabilized case than for the cavity stabilized case.

The observed reaction zone oscillations occur because the two flame stabilization locations shown in Fig. 3.21 are separated by an intermediate region which is unsuitable for stabilization. At the lowest $T_{0,air}$, only cavity stabilized combustion exists because the jet-wake stabilization is not possible due to the relatively low flame speeds. As $T_{0,air}$ (and thus the local flame speed everywhere) is increased, the jet-wake stabilization becomes possible, but the flame cannot propagate through the intermediate region to the stable location. As $T_{0,air}$ is increased further, some large fluctuations in the flow allow the flame to momentarily propagate through the intermediate region to the jet-wake stabilization location. The flame then remains in the jet-wake stabilization location until another fluctuation pushes the flame base downstream of the stable region, and it flashes back to the cavity stabilized location. As $T_{0,air}$ increases further, magnitude of the fluctuations required for the flame to flash forward to the jet-wake location become smaller, and the magnitude of the fluctuations which cause flash-back become larger. The flame then spends a larger percentage of the time in the jet-wake stabilized location as $T_{0,air}$ increases. At a high enough $T_{0,air}$, there are no fluctuations present in the flow which are sufficient to cause the jet-wake location to become unstable. The flow fluctuations which cause the flame to flash forward to the jet-wake position or back to the cavity position may be related to fluid dynamic, acoustic, or facility dependent fluctuations (or freestream fluctuations in a flight vehicle). The lack of a dominant frequency and relatively low frequencies at which this oscillation occurs, however, shows that any periodic shed vortices or acoustic modes do not couple with the reaction zone location oscillations.

The large pressure fluctuations observed when the combustion oscillates between modes is due to the different heat release distributions for cavity and jet-wake stabilized combustion. This causes the thermal choking point, and thus the entire combustor and isolator pressure field to be different for cavity and jet-wake stabilized combustion, even with the same total heat release. The heat release distribution for jet-wake and cavity stabilized combustion, and its effect on the pressure distribution, is discussed in depth in Chapter V.

The images from the high speed movies suggest that the propagation of the flame from the cavity to the jet wake occurs in the main flow, not just the boundary layer. Figure 3.22 shows a typical cavity to jet-wake transition. Figure. 3.22(a) shows the reaction zone for the cavity stabilized mode. Figures 3.22(b) shows a change in the structure of the reaction zone. The flame base moves upstream of the cavity stabilized flame (which has a constant spreading angle) into the wake of the fuel jet. This flame base then propagates upstream in the fuel jet wake (Figs. 3.22(c)-3.22(e)) until it reaches the jet-wake stabilized location (Fig. 3.22(f)).

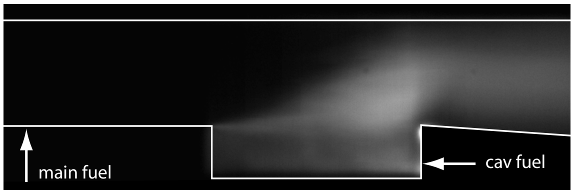

(a) t=0 μs. Cavity stabilized mode.

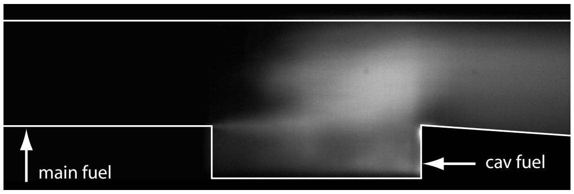

(b) t=250 μs. Reaction zone structure changes, flame base starts propagating into jet-wake.

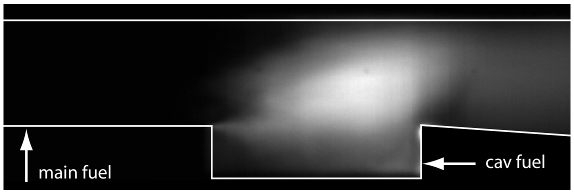

(c) t=500 μs. Flame base in jet-wake propagating forward.

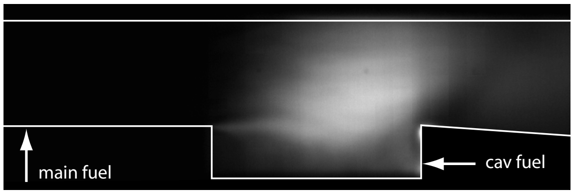

(d) t=750 μs. Flame base in jet-wake propagating forward.

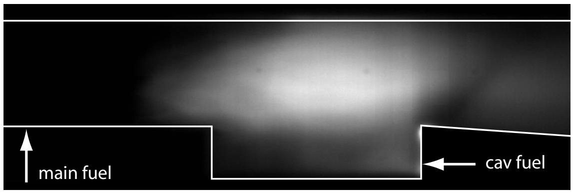

(e) t=1000 μs. Flame base in jet-wake propagating forward.

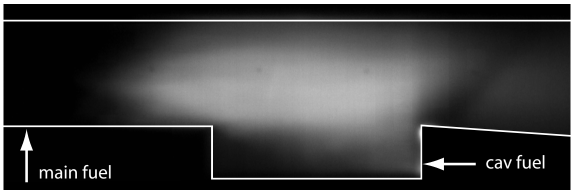

(f) t=1250 μs. Jet-wake stabilized mode. Transition complete.

Figure 3.22: Typical flash-forward event from cavity stabilized location to jet-wake stabilized location. Hydrogen fuel injection with $\phi = 0.27$, $\dot{m}_{cavfuel}/\dot{m}_{totalfuel} = 0.05$, $T_{0,air} = 1220$ K. High speed movie of combustion luminosity acquired at 4000 frames/sec.

3.1.4 Comparison with CFD solution

The combustor centerline static temperature and OH mass fraction (Y_{OH}) computed by the CFD++ code for case 1C and 2C are shown in Figs. 3.23 and 3.24. The experimentally measured average OH* luminosity for case 1H and 2H also is shown. As discussed in Sec. 2.2, the conditions for the experimental cases 1H and 2H are very similar to the conditions for the CFD cases 1C and 2C respectively. It can be seen that reaction zone computed by CFD++ is stabilized upstream of the measured reaction zone in both cases.

For case 2C the computed reaction zone is completely attached the both the upstream and downstream sides of the fuel injection jet. The downstream computed OH contours are located along the upper and lower edges of the fuel jet. This structure is consistent with a mixing limited auto-ignition reaction or an attached diffusion flame. The measured reaction zone is stabilized downstream of the fuel injection jet in the jet-wake stabilized mode. The measured downstream OH* contours are consistent with the computed downstream OH contours.

For case 1C the computed reaction zone is no longer attached to the fuel injection jet. The reaction zone begins along the lower edge of the fuel jet approximately 8 mm downstream of the fuel injection. The reaction zone along the upper edge of the fuel jet begins approximately 23 mm downstream of the fuel injection. The downstream OH again is located along the perimeter of the fuel jet which is similar to a diffusion flame. The measured reaction zone for case 1H is in the cavity stabilized mode. Thus the reaction is stabilized at the cavity leading edge and spreads into the flow at an approximately constant angle, which is consistent with a premixed flame sheet.

Both the cavity and jet-wake combustion stabilization has been explained by premixed flame propagation. It is not surprising then that the CFD++ solution does

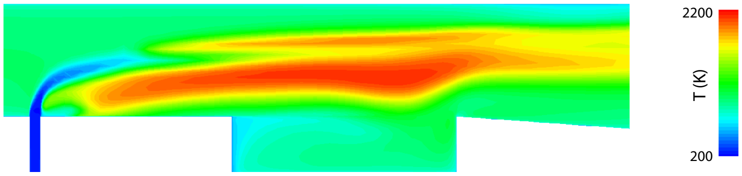

(a) CFD++ solution centerline static temperature for case 1C.

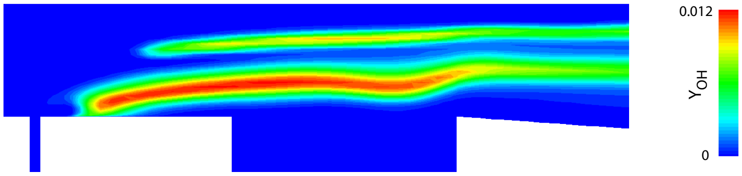

(b) CFD++ solution centerline OH mole fraction (Y_{OH}) for case 1C.

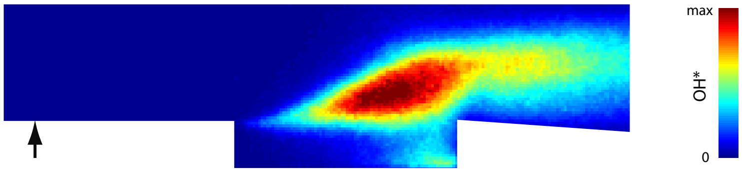

(c) Experimentally measured average OH* luminosity for case 1H.

Figure 3.23: Comparison of the upstream reaction zone computed by CFD++ at case 1C with the experimentally observed reaction zone at case 1H.

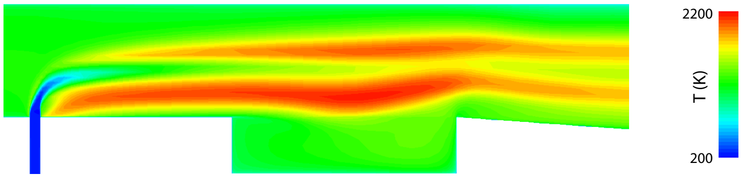

(a) CFD++ solution centerline static temperature for case 2C.

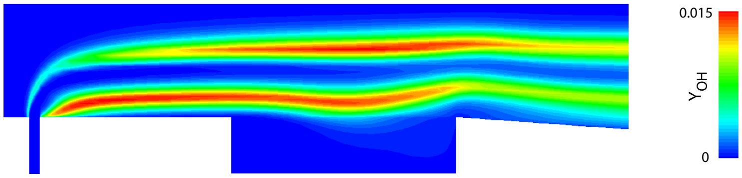

(b) CFD++ solution centerline OH mole fraction (Y_{OH}) for case 2C.

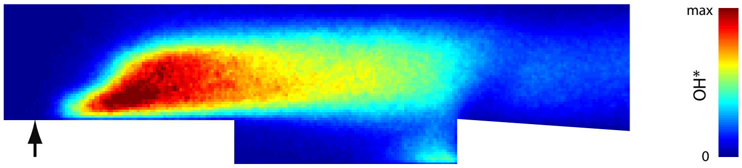

(c) Experimentally measured average OH* luminosity for case 2H.

Figure 3.24: Comparison of the upstream reaction zone computed by CFD++ at case 2C with the experimentally observed reaction zone at case 2H.

a poor job predicting the stabilization location. The finite rate chemistry formulation used by the model may be useful for prediction of auto-ignition, but it is ill-suited for the calculation of premixed flames. The computational grid cannot resolve the thin structures and large gradients that control the flame propagation. Thus the reaction zone is artificially thickened. Such a thickened reaction zone will have a larger flame speed than a thin zone if the reaction rate is not suppressed [24].

A flame model is expected to do a better job predicting the combustion stabilization than the current chemistry treatment. Coherent flamelet models and the G-equation method simulate the turbulent flame speed instead of the finite rate chemistry at each grid point. The strain rate will need to be accounted for in the flame model, since it likely plays a large role in the lift-off distance and flame speed.

3.2 Downstream Fuel Injection

The large pressure fluctuations encountered at intermediate $T_{0,air}$ are undesirable for an operational engine. For a flight vehicle, the conditions leading to these oscillations are encountered as the engine accelerates from low to high flight Mach number. One way to minimize these fluctuations is to move the main fuel injection location to cause the reaction zones for the two stabilization modes to overlap in space. This is illustrated in Fig. 3.25. An iso-luminosity contour showing the outline of jet-wake stabilized combustion for hydrogen fuel injection from the upstream location ($x/H = -1.75$) is shown in red. Moving the fuel injection to the downstream location ($x/H = -0.55$) is expected to move the jet-wake stabilized reaction zone location downstream by the same amount. This hypothetical structure is shown in blue. An outline of the cavity stabilized reaction zone structure is shown in purple. This is expected to occur at the same location regardless of the fuel injection location since

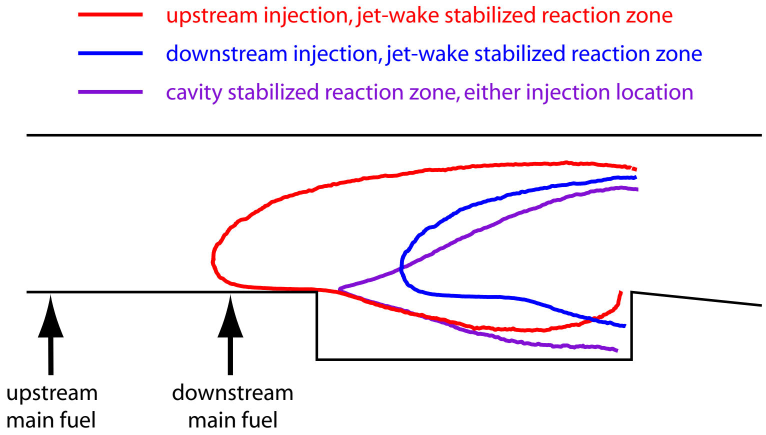

Figure 3.25: Reaction zone locations for upstream and downstream injection.

Parameter	Value
fuel type	H_2
$T_{0,air}$	1250 ± 30 K
ϕ	0.18, 0.27
$\dot{m}_{cavfuel}/\dot{m}_{totalfuel}$	0.0, 0.10
cavity fueling location	rear wall, floor

Table 3.3: Test conditions for downstream main fuel injection ($x/H = -0.55$).

it is determined by the cavity flowfield.

To test this theory, the location of the main fuel injection was moved downstream for the range of conditions shown in Table 3.3. The air stagnation temperature selected caused the most unsteady, oscillatory combustion for upstream main fuel injection. Overall equivalence ratios of 0.18 and 0.27 were studied with and without cavity fuel injection through the rear wall and cavity floor locations.

The average and standard deviation of the wall pressure for all cases in Table 3.3 are shown in Fig. 3.26. The average combustion luminosity images are shown in Figs. 3.27 and 3.28. The reaction zone did not oscillate between two distinct structures as in the case of upstream fuel injection ($x/H = -1.75$), so only the average luminosity images are shown.

For the $\phi = 0.27$ cases of downstream main fuel injection, it can be seen that

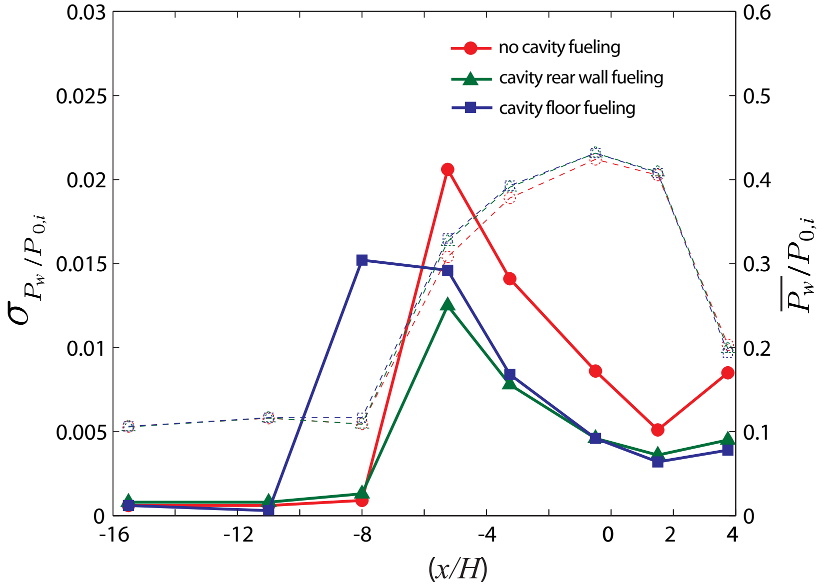

(a) $\phi = 0.18$

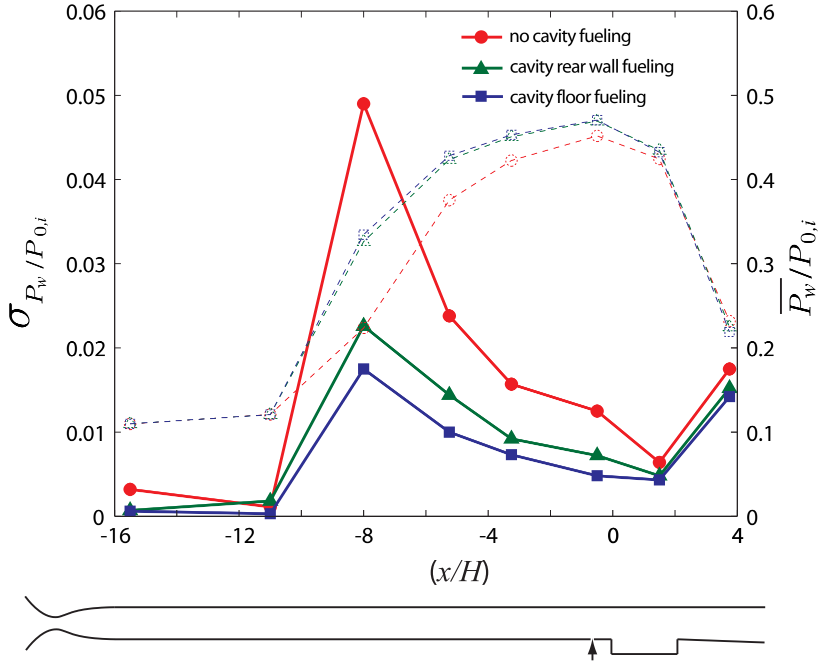

(b) $\phi = 0.27$

Figure 3.26: Wall pressure standard deviation (solid symbols) and average (open symbols) for downstream injection of hydrogen fuel for no cavity fueling and $\dot{m}_{cav\,fuel}/\dot{m}_{total\,fuel} = 0.10$.

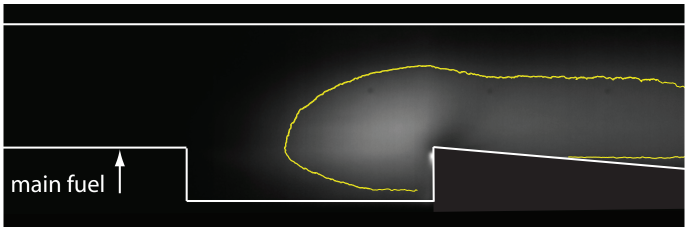

(a) No cavity fueling.

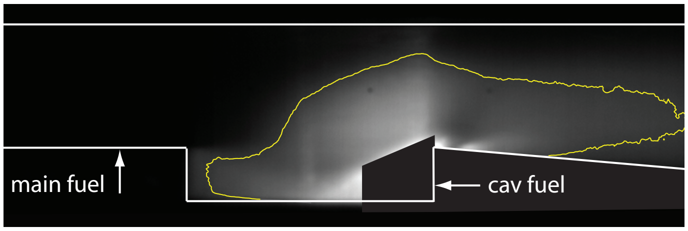

(b) Cavity rear wall fueling.

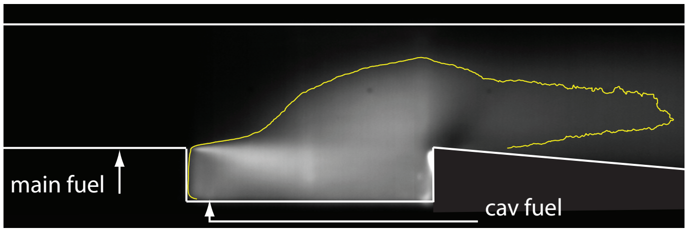

(c) Cavity floor fueling.

Figure 3.27: Flame luminosity images averaged over 1000 ms for downstream main fuel injection of hydrogen. $T_{0,air} = 1250$ K, $\phi = 0.27$, $\dot{m}_{cavfuel}/\dot{m}_{totalfuel} = 0.10$ for cases with cavity fueling. Yellow line is an iso-luminosity contour. Image (b) is blacked out in the rear corner of the cavity due to buildup on the window which was glowing brightly.

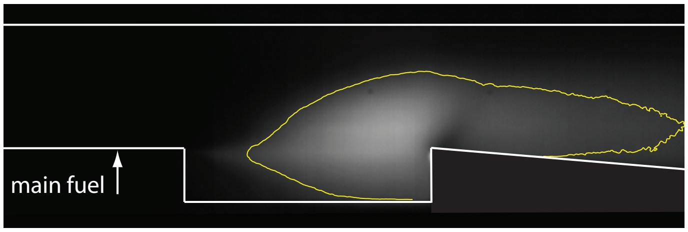

(a) No cavity fueling.

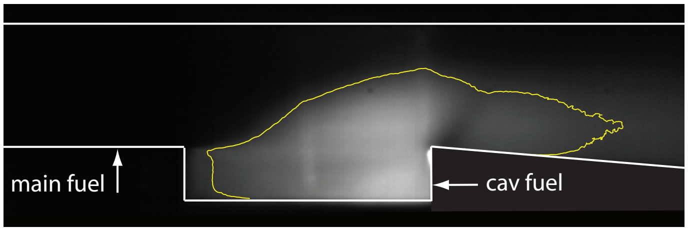

(b) Cavity rear wall fueling.

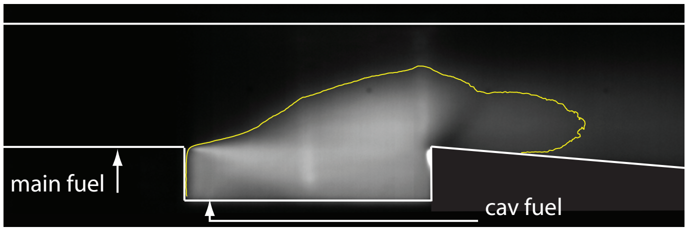

(c) Cavity floor fueling.

Figure 3.28: Flame luminosity images averaged over 1000 ms for downstream main fuel injection of hydrogen. $T_{0,air} = 1250$ K, $\phi = 0.18$, $\dot{m}_{cavfuel}/\dot{m}_{totalfuel} = 0.10$ for cases with cavity fueling. Yellow line is an iso-luminosity contour.

cavity fueling from either the floor or rear wall makes the flow significantly steadier. For no cavity fueling, the combustion appears to be in the jet-wake stabilized mode. The shape and location of the reaction zone with respect to the fuel injector is similar to that seen for the upstream main fuel injection, jet-wake stabilized case shown in Fig. 3.1(b). Additionally, the magnitude of the pressure fluctuations are similar to the jet-wake stabilized cases shown in Fig. 3.12.

With cavity fueling, shown in Figs. 3.27(b) and 3.27(c), the reaction zone extends into the upstream part of the cavity. As noted in Sec. 3.1.2, this is a relatively steady area of low speed flow [82]. Thus the steady combustion in this area provides heat and radicals to the main flow reaction, which appears to be primarily jet-wake stabilized. This hybrid stabilization is steadier than pure jet-wake stabilization, but not quite as steady as pure cavity stabilization. The cavity shear layer reaction is significantly stronger for cavity fueling through the floor injectors than for cavity fueling through the rear wall injectors. This is likely why the floor fueling produced a slightly steadier flow-field.

A reaction zone similar to this hybrid stabilization mode was reported by Sun et al [91] for hydrogen fuel injection a short distance upstream of a wall cavity. They postulated that the cavity flame spreads to the jet-wake flame through the center of the counter-rotating vortex pair in the wake of the fuel injection jet. This is shown in Fig. 3.29.

Pure cavity stabilized combustion, which was observed for upstream main fuel injection, was not observed for downstream main fuel injection. It appears that cavity stabilized combustion occurs as a premixed flame sheet. With downstream fuel injection there is insufficient distance between the injection location and the cavity leading edge to allow enough mixing for this premixed flame sheet to occur.

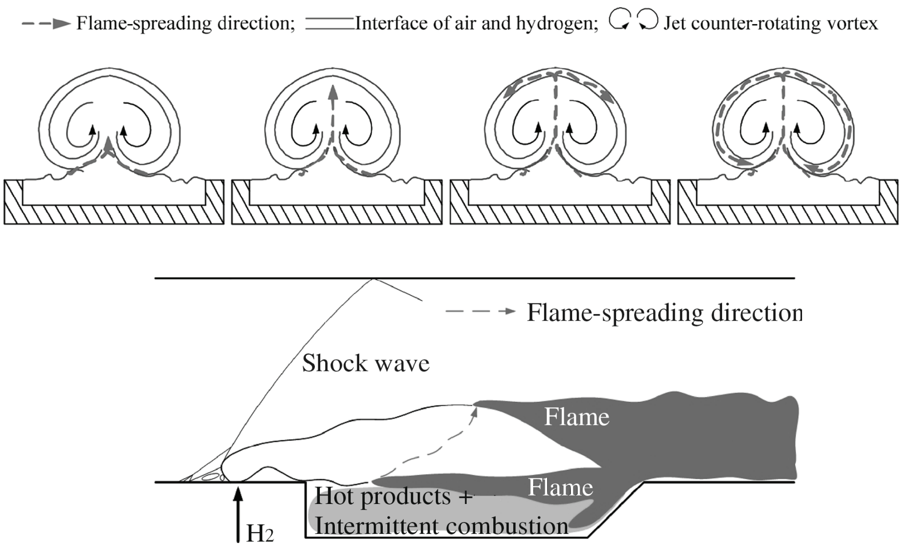

Figure 3.29: Figure from Sun et al [91] showing the mechanism of flame spreading for hybrid cavity/jet-wake stabilized combustion with downstream main fuel injection.

The same basic trends in combustion stabilization and steadiness were seen for $\phi = 0.18$. For the lower equivalence ratio though, the difference in pressure fluctuations between cases with and without cavity fueling was less. Figures 3.27(a) and 3.28(a) shows that for no cavity fueling the reaction extends farther upstream in the cavity shear layer for $\phi = 0.18$ than for $\phi = 0.27$. Thus the cavity is playing a role in stabilizing the lower equivalence ratio combustion and making it steadier. For this lower equivalence ratio the main fuel jet penetration is reduced, so there is likely to be more main fuel entrained into the cavity in this case. With direct cavity fueling, the reaction zone again extends into the upstream, steadiest part of the cavity shear. The pressure fluctuations are then moderately reduced as shown in Fig. 3.26(a).

3.3 Ram-to-Scram Mode Transition

Although the focus of the current study is ramjet mode operation, the behavior of the combustor during the transition from ramjet to scramjet operation is of interest as well. The transition to scramjet mode operation was achieved by reducing the equivalence ratio used for steady ramjet mode operation. Ram-to-scram mode fluctuations were observed for $\phi < 0.20$ for hydrogen fuel and for $\phi < 0.40$ for the blended fuel. The precise equivalence ratio where the combustor transitioned from steady ramjet mode operation was also dependant on the fuel injection location and $T_{0,air}$. Steady scramjet mode combustion was not observed because flame blowout occurred first as the equivalence ratio was reduced. Obtaining steady scramjet mode combustion in this combustor would required raising $T_{0,air}$, reducing ϕ, or moving the heat release further downstream in the diverging section.

The ram-to-scram oscillations encountered were generally slow (2-10 Hz) and were not at a fixed frequency. The transition time was between 1 to 10 ms, while the quasi-steady time in each mode was between 10 to 500 ms. Figure 3.30 shows the average wall pressure distribution in the combustor during quasi-steady ramjet mode and scramjet mode operation for one case where this oscillation occurred. Figure 3.31 shows the average flame luminosity for each mode. As expected, there is a step change in the isolator exit Mach number ($M_{i,exit}$) during the mode transition. For the example shown, $M_{i,exit}$ increases from 0.90 to 1.89 during the ram to scram transition. The isolator exit Mach number was computed from the wall pressure using the 1-D method given by Curran, Heiser, and Pratt [21]. The reason why a step change must occur is explained in Sec. 1.1.2. This can lead to an instability with large pressure fluctuations during the ram-to-scram transition, which occurs during the acceleration of a flight vehicle. To avoid the instability, it may be advisable to alter the fuel injection location before the ram-to-scram transition occurs. This would quickly change the heat release distribution and force the transition to the scramjet mode with a margin that is sufficient to prevent any oscillations. Such staged fuel injection ideas have also been proposed to avoid isolator unstart at low

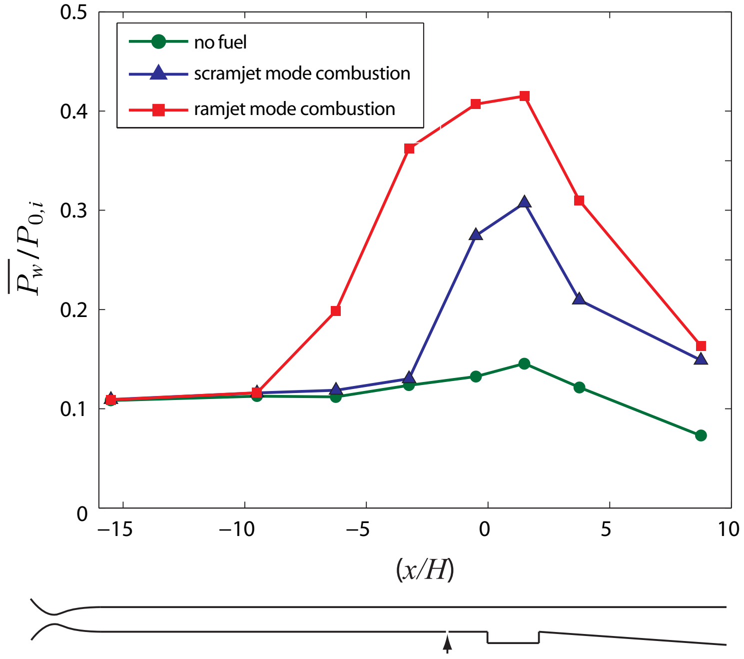

Figure 3.30: Average wall pressure for ramjet mode combustion, scramjet mode combustion, and the no fueling case. Upstream injection of blended fuel at $T_{0,air} = 1270$ K, $\phi = 0.40$, $\dot{m}_{cavfuel}/\dot{m}_{totalfuel} = 0.05$.

flight Mach numbers [98].

The reaction zone was found to only appear in the cavity stabilized mode in the scramjet mode, even for conditions where the ramjet mode was jet-wake stabilized. This is due to the higher velocity and lower static temperature of the main flow for supersonic isolator exit conditions, which make the jet-wake location unsuitable for flame stabilization. Figure 3.31 shows that the spreading of the cavity stabilized scramjet mode combustion is significantly less than that of the ramjet mode. This behavior would be expected for premixed flame spreading due to the lower flame speed and larger flow speed in the scramjet mode. The mixing limited combustion mechanism discussed in Sec. 3.1.3.1 is also a plausible mechanism in the scramjet mode due to the much lower spreading angle.

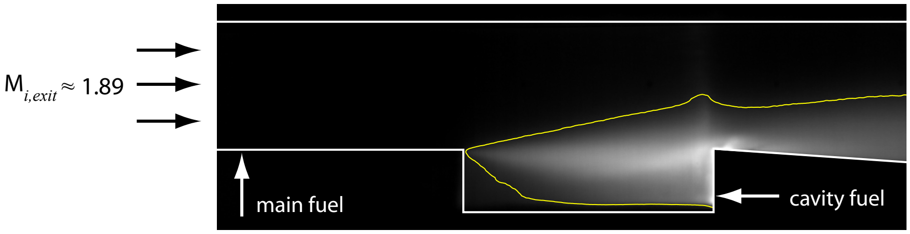

(a) Scramjet mode combustion.

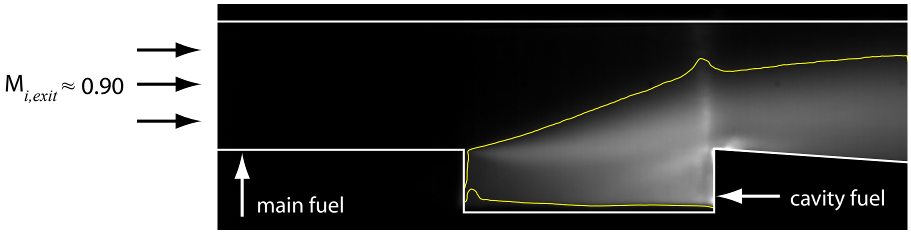

(b) Ramjet mode combustion.

Figure 3.31: Flame luminosity images of scramjet and ramjet mode operation averaged over 50 ms. Upstream injection of blended fuel, $T_{0,air} = 1270$ K, $\phi = 0.40$, $\dot{m}_{cavfuel}/\dot{m}_{totalfuel} = 0.05$. Yellow line is an iso-luminosity contour. The vertical line of increased intensity near the cavity trailing edge is due to camera over-exposure from glowing metal at the rear wall, and is not due to increased combustion in this region.

CHAPTER IV

Reaction Zone Structure

The structure of both the cavity stabilized and jet-wake stabilized reaction zones were studied. Images of the intermediate combustion species of CH, OH, and formaldehyde provide different information about the structure of the reaction zone. These images were obtained from planar laser-induced fluorescence (PLIF).

4.1 Run Conditions

The run conditions used for the PLIF reaction zone structure imaging are given in Table 4.1. Only the blended fuel (50% ethylene, 50% hydrogen by mole) was used since some carbon content in the fuel was necessary for CH and formaldehyde (CH_2O) to be produced in the reaction zone. Conditions for case 1B were chosen to yield steady cavity stabilized combustion, while conditions for case 2B were chosen to yield steady jet-wake stabilized combustion. Figure 4.1 shows the mean thermally excited CH* emissions for cases 1B and 2B. Figure 4.2 shows the average combustion pressure distribution in each case. The pressure distributions are significantly different between 1B and 2B due to the differing heat release distributions for the two combustion stabilization modes. This is discussed in depth in Chapter V.

Parameter	Case 1B - cavity stabilized	Case 2B - jet-wake stabilized
$P_{0,i}$	590 ±10 kPa	590 ±10 kPa
$T_{0,air}$	1270 ±20 K	1470 ±20 K
$\phi_{overall}$	0.42	0.42
$\dot{m}_{cavfuel}/\dot{m}_{totalfuel}$	0.05	0.05
fuel composition	50% H_2, 50% C_2H_4	50% H_2, 50% C_2H_4
main fuel injector diameter	2.49 mm	2.49 mm
main fuel injection location	$x/H = -1.75$	$x/H = -1.75$
cavity fuel injection location	rear wall	rear wall
$M_{i,exit}$	0.73	0.62

Table 4.1: Test conditions for PLIF imaging of the reaction zone structure.

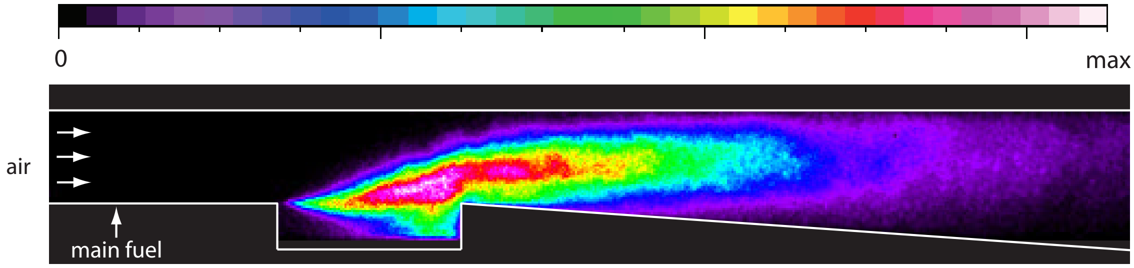

(a) Case 1B.

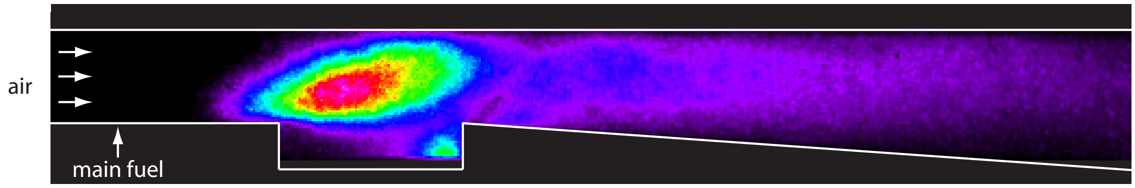

(b) Case 2B.

Figure 4.1: Mean CH* luminosity for case 1B (cavity stabilized) and case 2B (jet-wake stabilized) conditions shown in false color.

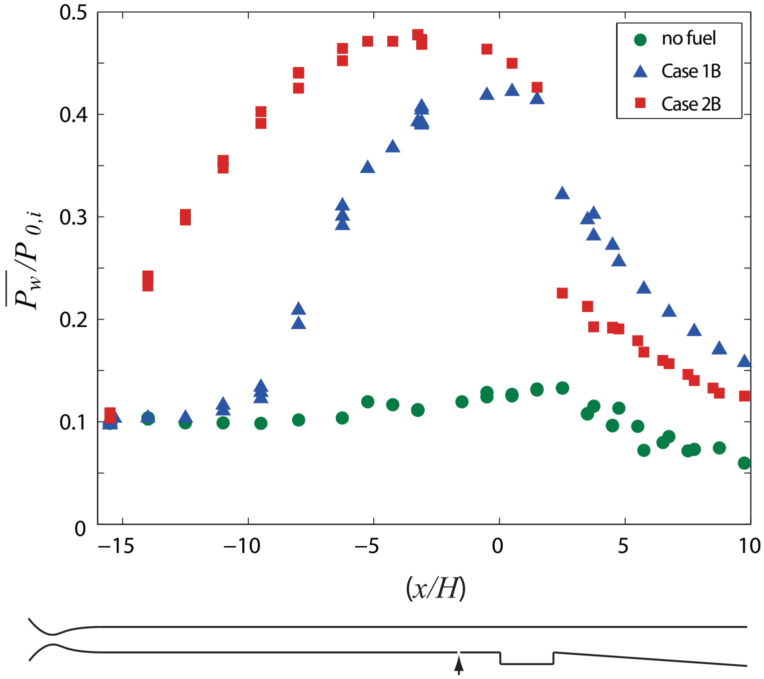

Figure 4.2: Mean wall pressure for case 1B (cavity stabilized), case 2B (jet-wake stabilized), and the no fueling case. The cavity leading edge is at $x/H = 0$ and the fuel injection is at $x/H = -1.75$.

4.2 CH-PLIF Results

All CH-PLIF images were acquired on the centerline of the combustor. Images were acquired at four fields of view (FOVs) spanning the axial range of $-0.45 \leq x/H \leq 9.0$. A smaller field of view was imaged at the most upstream location for case 1B than for case 2B to allow faster image acquisition. All mean PLIF images shown in Sections 4.2.1 and 4.2.2 are displayed with a false color scale ranging from 0 to 2500 counts, and all instantaneous images are displayed with a false color scale ranging from 1500 to 8000 counts. As was discussed in Sec. 2.5, CH is very short lived radical that exists only in areas of local heat release. Therefore any region where CH exists marks the primary reaction zone.

4.2.1 CH-PLIF of Cavity Stabilized Combustion

The case 1B mean and sample instantaneous CH-PLIF images for FOVs 1-4 are shown in Figs. 4.3-4.6. Each of the mean images is the average of approximately 40 instantaneous images. Only pixels with an intensity greater than 1000 counts in the instantaneous images were used in creating the mean in order to minimize the background flame luminosity. The mean centerline CH-PLIF images are very similar to the mean CH* chemiluminescence image shown in Fig. 4.1(a). The reaction zone starts at the cavity leading edge and initially spreads into the flow at an approximately constant angle. Near the cavity trailing edge the spreading angle begins to decrease and the reaction region eventually becomes nearly parallel to the flow. The strength of the CH-PLIF signal decreases significantly at the most downstream location imaged (FOV 4), but it is never equal to zero.

The instantaneous CH-PLIF images give further insight into the reaction zone structure. In all cases the base of the reaction zone is located in the upstream part of the cavity shear layer. The reaction zone spreads from this location as a nearly continuous layer as seen in Figs. 4.3(a)-(h). There are small gaps in the layer and regions of reduced intensity. Farther downstream in the rear half of the cavity and in FOV 2 (which is shown in Fig. 4.4), the reaction layer spreads farther into the flow and becomes more wrinkled and/or thickened.

Downstream of x/H=3, large gaps appear in the CH reaction layer in some images. This can be seen in Figs. 4.4(f)-(h) and 4.5(e)-(g). By FOV 3, there are no images which have a mostly continuous reaction layer across the entire width. The downstream end of the reaction zone appears to be highly variable in time. Approximately 10% of the images acquired at FOV 3 contained little or no CH as shown in Fig. 4.5(h). Thus the end of the reaction zone is likely to be upstream of x/H=4.25

(which is the upstream edge of FOV 3). Figure. 4.4(e) appears to show the end of the reaction zone at such a time. At FOV 4, a little more than half the images showed little or no CH. Thus the reaction zone usually ends within the region covered by FOV 3 ($x/H = 4.25 - 6.7$). A few images show some CH near the end of FOV 4 ($x/H = 9.0$).

The instantaneous CH images show that there is a mostly continuous reaction layer spreading from a fixed base location. This is the structure that is expected for a premixed flame. The structure is not consistent with an auto-ignition controlled reaction for which ignition of each fuel-air fluid packet occurs independently. The small gaps and reduced CH intensity in the upstream part of the reaction layer can be explained by turbulence. The strain exerted on the flame by turbulent eddies can cause local extinction or decreased reaction rate. The small gaps and decreased CH in the upstream part of the reaction layer (1-2 mm) suggest that small eddies are playing a dominant role in this region. The structure indicates the flame is in the broken reaction regime in the premixed flame diagram given by Guttenfelder et al [43]. The large gaps that appear in the reaction layer starting in FOV 2 are most likely due to interaction of the flame with vortices from the shear layer. The largest vortical structures in the shear layer increase with downstream distance, so the gaps in the reaction layer become larger with increasing x.

The apparent thickness of the CH layers was 0.7 to 3 mm on average. Some clumps of CH were even thicker than 3 mm such as the one shown in Fig. 4.4(d). The layers tended to be thin over the upstream half of the cavity, and became thicker as the flame spread into the main flow and moved downstream. These values are much larger than the laminar flame CH thickness of a stoichiometric 50% H_2, 50% C_2H_4 flame which is 60 μm at case 1B conditions. Therefore it is useful to examine the possible reasons for the reaction zone broadening.

Studies have shown that the preheat zone of turbulent premixed flames may be thickened at high turbulence levels [15, 67, 14, 30]. These preheat layers have been observed to be up to 4 times the thickness of those in an unstretched laminar flame [30]. The cause of this broadening is theorized to be due to either the fluid dynamic strain rate or due to small turbulent eddies which enter the preheat layer and increase the rate of diffusion of heat. However, there is no strong experimental evidence which confirms either of these ideas [30]. The eddies which are smaller than the heat release layer thickness tend to be relatively weak. The heat release in the reaction layer causes a strong acceleration due to the decrease in density across it. Thus the effect of these small eddies on the reaction layer is attenuated. There is some debate about whether reaction layers will be extinguished due to high strain rate before they broaden at very high turbulence levels.

The thickness of an unstretched laminar flame for case 1B conditions was estimated using CHEMKIN. Calculations were performed for equivalence ratios of 0.5, 1.0, and 2.0 for an assumed Mach number of 0.75. The mixture temperatures for CHEMKIN then were calculated from Eqs. 3.4 and 3.5. Fig. 4.7 shows the calculated temperature and CH profiles for the $\phi = 1.0$ and $\phi = 2.0$ flames. The $\phi = 0.5$ flame had profiles with similar thickness to the $\phi = 1.0$ case. For the rich flame, the CH decreases more slowly on the products side leading to a significantly thicker CH region. The full width at 10% maximum of the unbroadened CH layers are 60 μm for $\phi = 1.0$ and 380 μm for $\phi = 2.0$. Thus the measured CH layers are up to 10 times thicker than the unbroadened layers.

One possible explanation for the apparently thickened CH-layers are resolution limitations. Very thin CH-layers may be tightly wrinkled on a scale which is below the resolution of the imaging system (220 to 440 μm), making them appear thickened. Also layers which are in the process of merging, or are virtually parallel to the laser sheet, will appear thickened. Such artificially thickened structures would be expected to appear as clumps, and not layers with a consistent thickness. The large clump of CH seen in Fig. 4.4(d) is likely due to one or more of these phenomena. However there are many more cases of consistently thick layers, such as Figs. 4.4(b), 4.4(c), and 4.3(g), which are not easily explainable as experimental artifacts.

The most plausible explanation for the thickened CH layers is turbulence. Small turbulent eddies are entering the reaction layer and are increasing the rate of diffusion, causing the layers broaden. The highly preheated flow conditions allow reaction layers to be thickened without being completely extinguished. As stated earlier, the gas acceleration through the reaction layer attenuates the vorticity of small vortices. The velocity ratio across the reaction layer ($u_{burned}/u_{unburned}$) is almost directly proportional to the temperature ratio ($T_{burned}/T_{unburned}$) if the molecular weight difference between the reactants and products is neglected. For highly preheated reactants this temperature ratio is greatly reduced. For stoichiometric combustion of the blended fuel tested, $T_{burned}/T_{unburned}$ is reduced from approximately 8 to 2.5 between reactant temperatures of 300 K and 1005 K (case 1B conditions). Thus, the attenuating effect of the acceleration is less for flames with highly preheated reactants. The high preheating also increases the extinction strain rate of the flame. Thus there may be some vortices which are able to enter the reaction layer and broaden it without causing extinction.

4.2.2 CH-PLIF of Jet-Wake Stabilized Combustion

For case 2B the mean and instantaneous CH-PLIF images for FOVs 1-4 are shown in Figs. 4.8-4.11. Each of the mean images is the average of approximately 40

Mean CH-PLIF and FOV location.

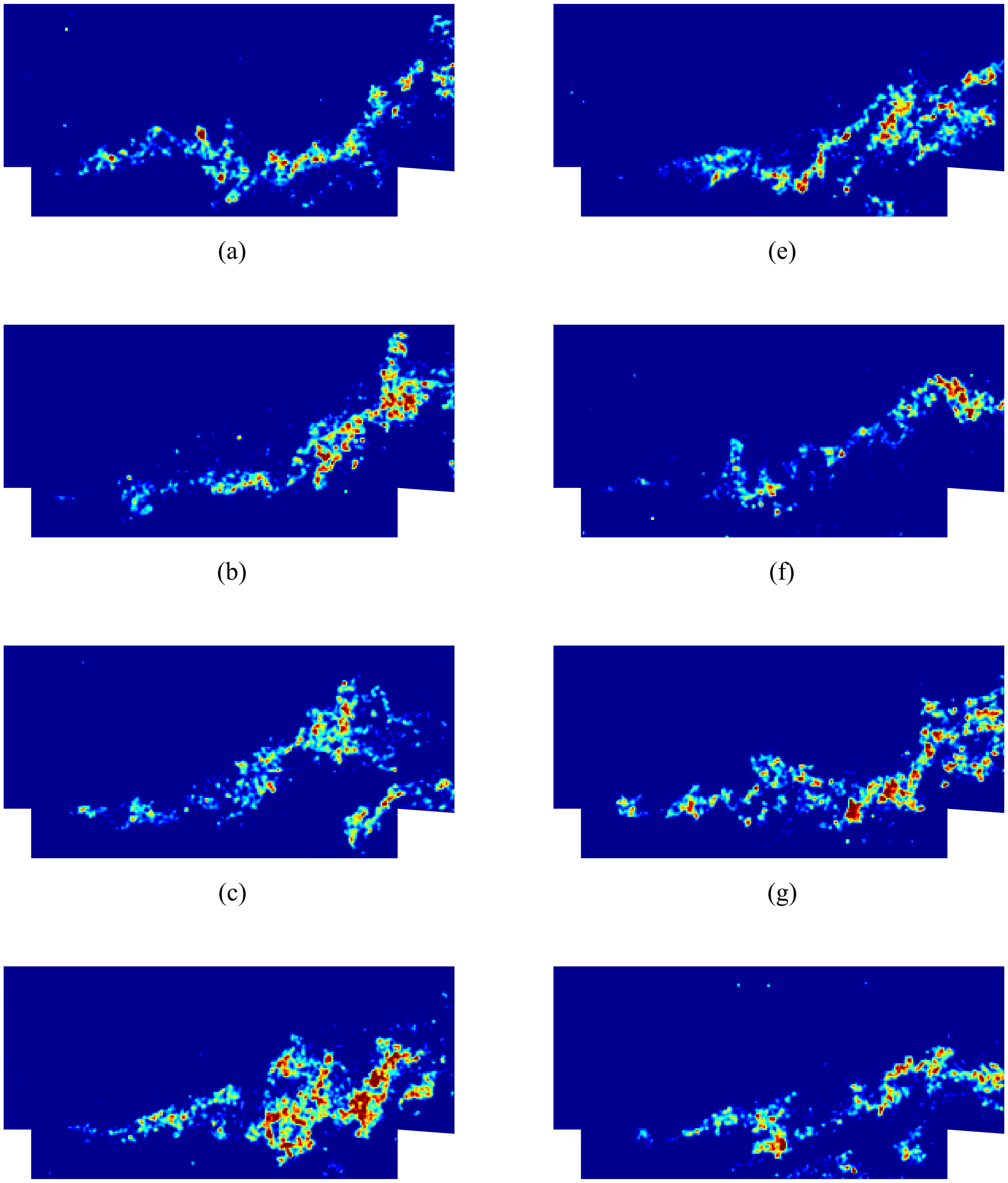

(a)

(e)

(b)

(f)

(c)

(g)

(d)

(h)

Figure 4.3: Mean and instantaneous CH-PLIF images for cavity stabilized case 1B at field of view (FOV) 1. $x/H = -0.15$ to 2.3.

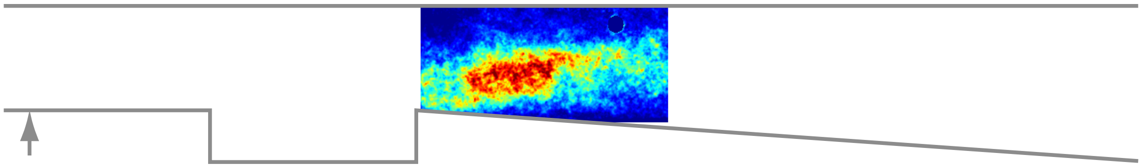

Mean CH-PLIF and FOV location.

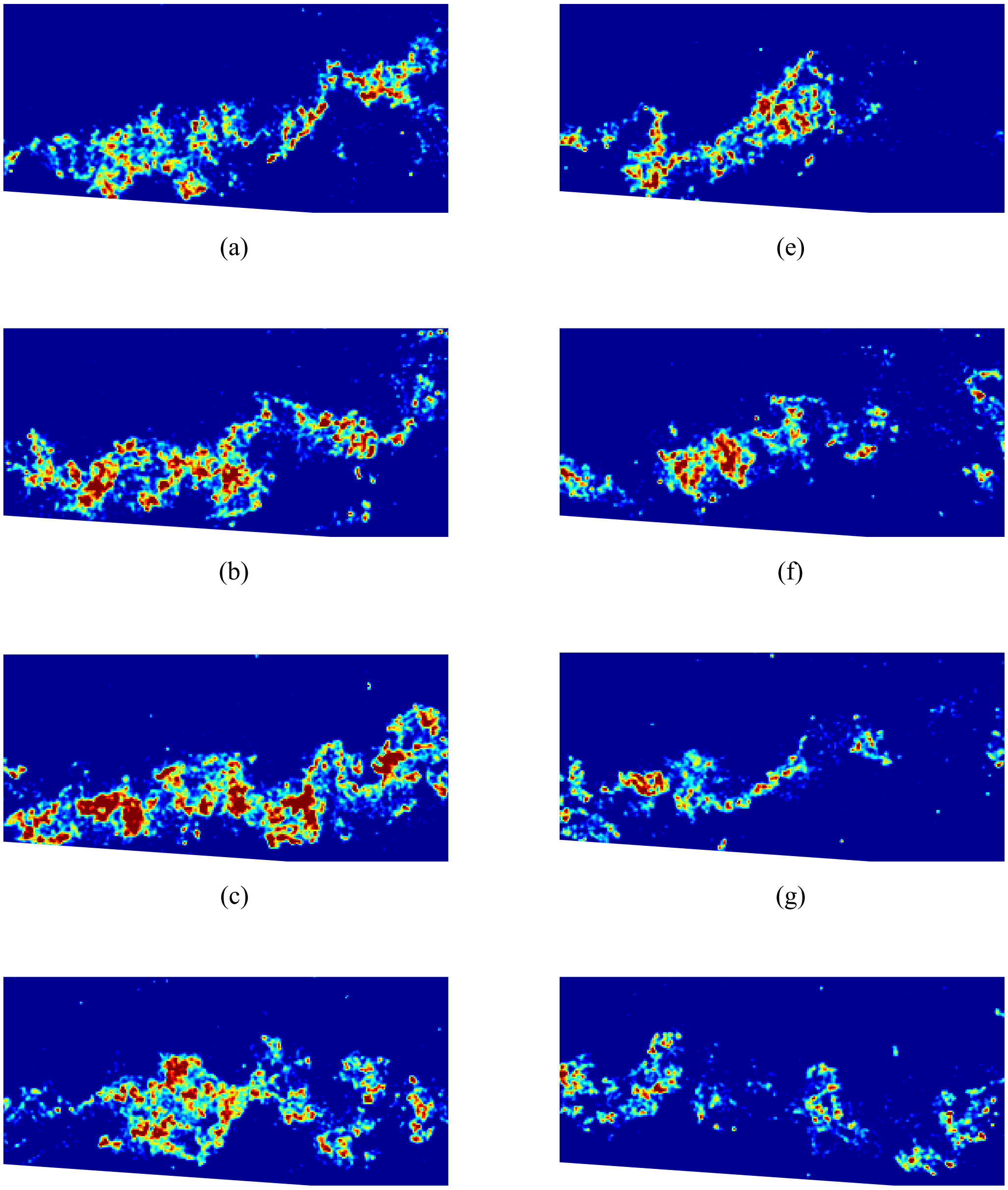

(a) (e)

(b) (f)

(c) (g)

(d) (h)

Figure 4.4: Mean and instantaneous CH-PLIF images for cavity stabilized case 1B at field of view (FOV) 2. $x/H = 2.05$ to 2.5.

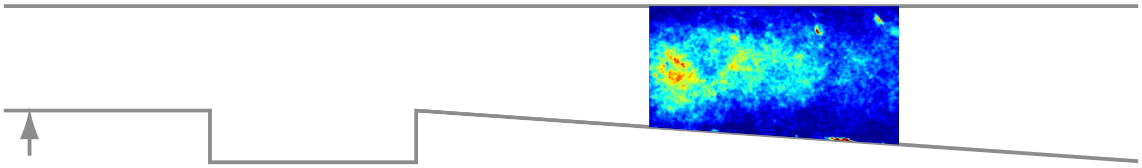

Mean CH-PLIF and FOV location.

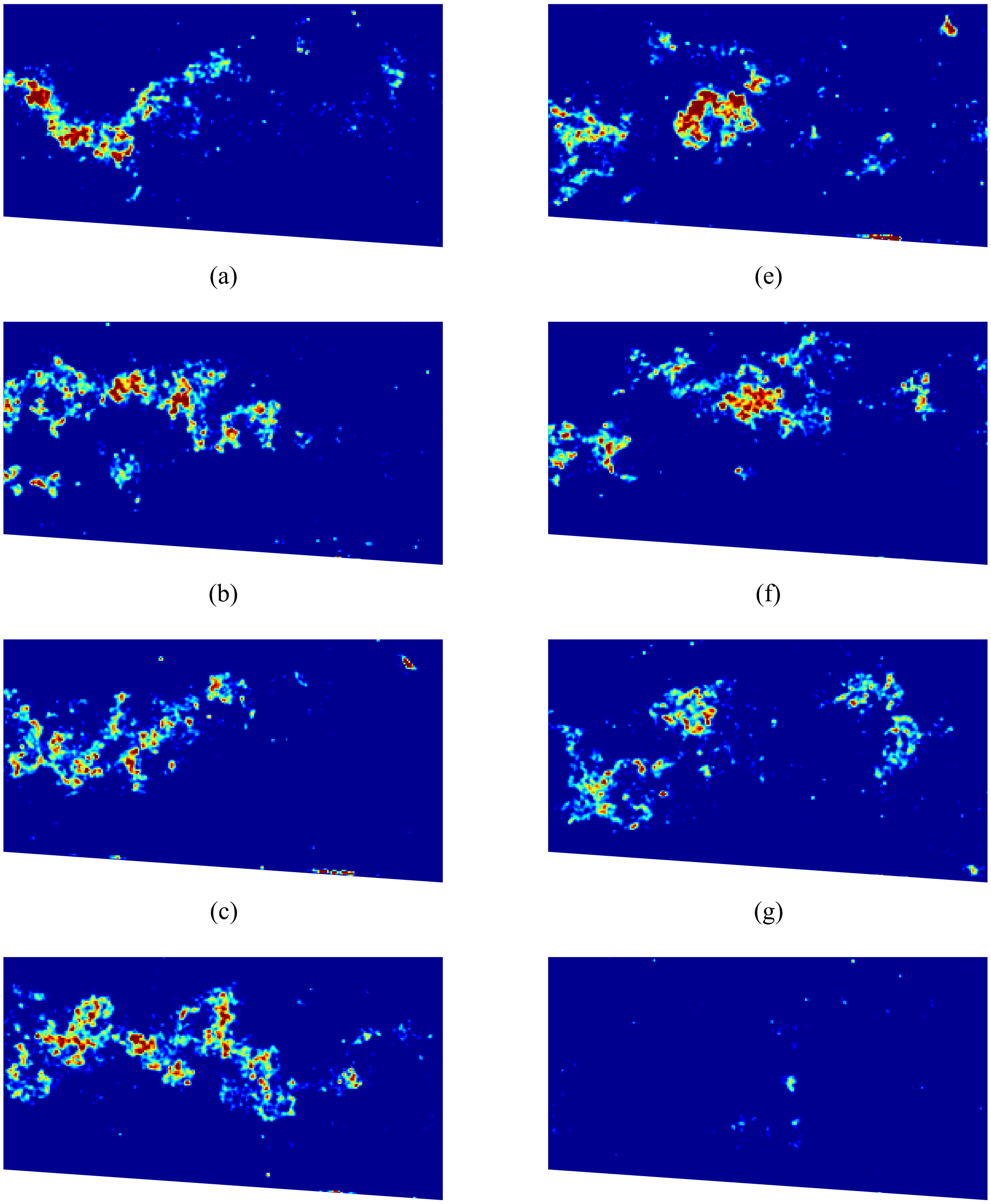

(a) (e)

(b) (f)

(c) (g)

(d) (h)

Figure 4.5: Mean and instantaneous CH-PLIF images for cavity stabilized case 1B at field of view (FOV) 3. $x/H = 4.25$ to 6.7

Mean CH-PLIF and FOV location.

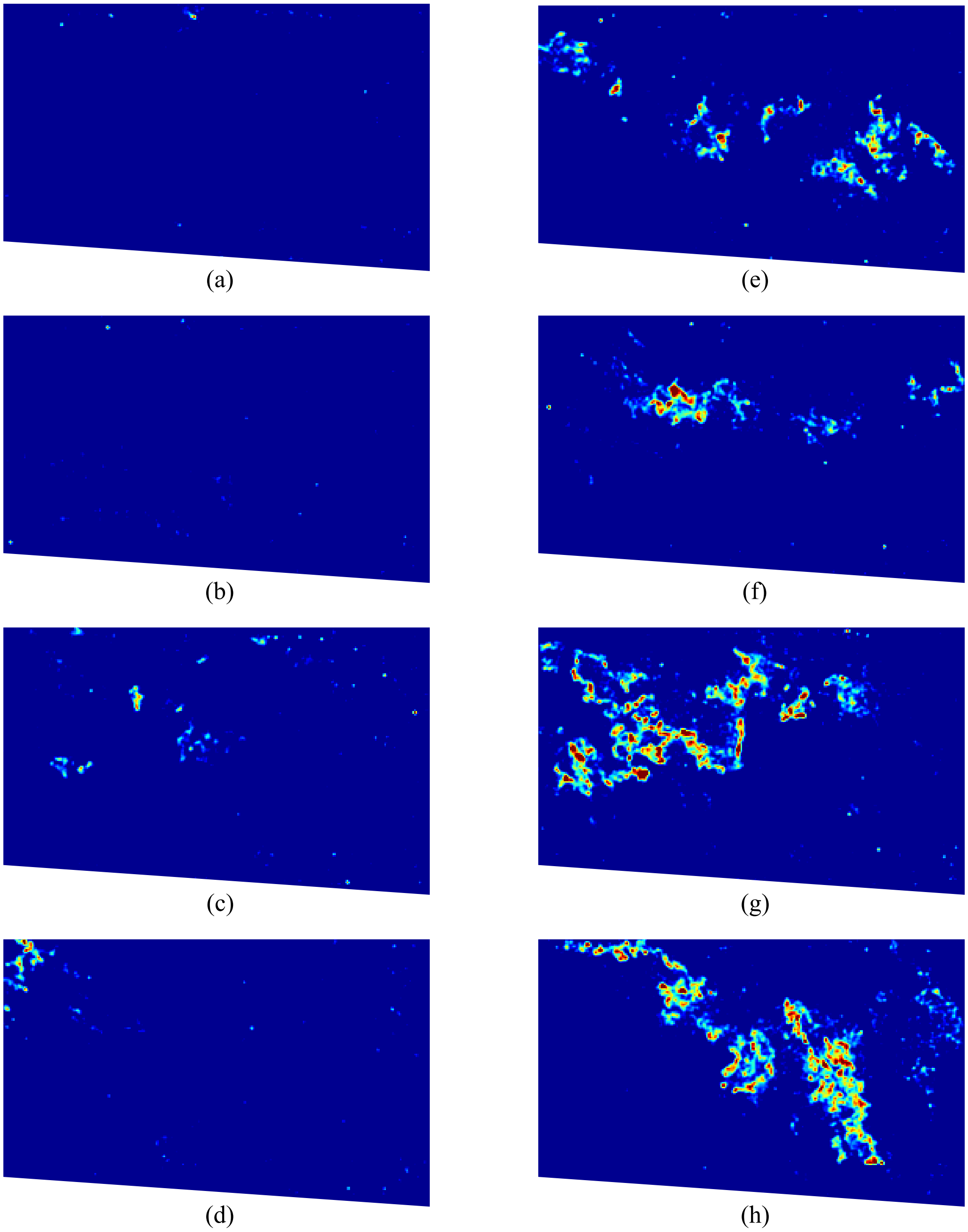

(a) (e)

(b) (f)

(c) (g)

(d) (h)

Figure 4.6: Mean and instantaneous CH-PLIF images for cavity stabilized case 1B at field of view (FOV) 4. $x/H = 6.55$ to 9.0.

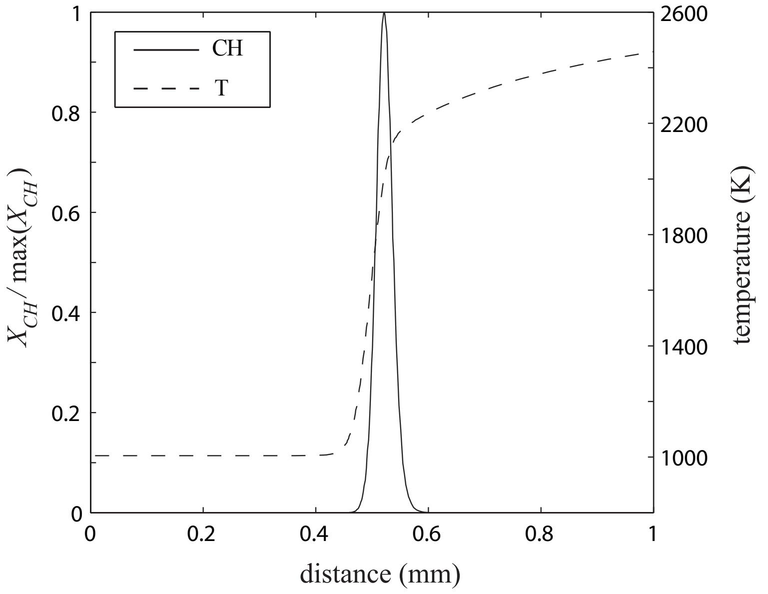

(a) $\phi = 1.0$

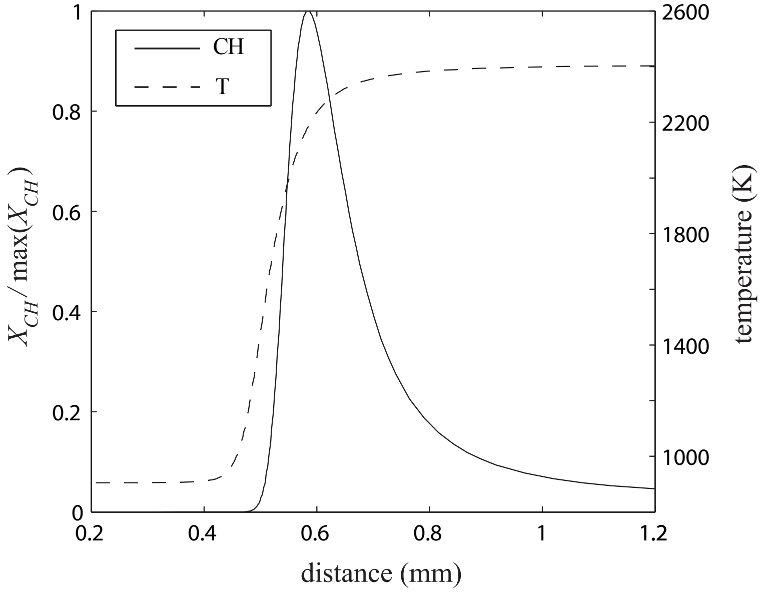

(b) $\phi = 2.0$

Figure 4.7: Profiles of CH mole fraction (X_{CH}) and gas temperature in a laminar premixed flame at case 1B (cavity stabilized) conditions computed using CHEMKIN.

instantaneous images. Only pixels with an intensity greater than 1000 counts in the instantaneous images were used in creating the mean, in order to minimize the background flame luminosity. The mean centerline CH-PLIF images again are similar to the mean CH* image shown in Fig. 4.1(b). The reaction zone starts upstream of the cavity and quickly spreads upward across the majority of the test section height. The PLIF signal intensity is highest at locations directly over the cavity and decreases at downstream locations. However the decrease in the PLIF signal downstream of the cavity is less than the decrease in the CH* signal. As with case 1B, the PLIF signal does not decrease to zero by the last field of view (FOV 4). The reaction zone is spread across most of the test section height for all FOVs, but is biased toward the top of the test section in the downstream region (FOV 3 and 4).

The instantaneous CH structure is very different for the jet-wake stabilized combustion mode (case 2B) than for the cavity stabilized combustion mode (case 1B). Figures 4.8(a)-(h) show example instantaneous CH-PLIF images for case 2B at FOV 1. It can be seen that the CH is confined to relatively small structures as opposed to being distributed evenly over wide regions. Mostly continuous reaction layers are rare however. The reaction zone is instead highly shredded and discontinuous. In some images, such as Figs. 4.8(b)-(d), there are some reaction layers which appear to correspond to the upper and lower edge of the fuel jet. These layers are very discontinuous, however, with many gaps and regions of suppressed CH.

Farther downstream the reaction zone structure remains similar to the upstream structure. In the downstream fields of view (FOV 3 and 4) there are more images where somewhat continuous reaction layers can be identified. Figures 4.10(a)-(d) and 4.11(a),(b) show some of these layers. These downstream locations also have more images with CH clusters, separated by large regions of no CH. Examples of these structures are shown in Figs. 4.10(f),(g) and 4.11(d)-(f).

Approximately 80% of the images acquired at the most downstream location still had measurable CH present. Therefore the reaction zone is longer on average for the jet-wake stabilized combustion mode than for the cavity stabilized mode. Most of the images at FOV 4 have relatively little CH as is seen in Figs. 4.11(d)-(g).

For the jet-wake stabilized combustion mode, the CH structure does not give conclusive information about the combustion mechanism. The relatively discontinuous reaction zone has little spatial structure. This could either indicate that the reactions occur in a highly shredded flame, or are controlled by auto-ignition. The flame-like behavior of jet-wake stabilized combustion discussed in Sec. 3.1 indicates that this case is best described as a lifted jet flame. This structure consists of a premixed flame base followed by a diffusion flame. The CH-PLIF results are consistent with this description, but the diffusion flame is highly shredded and discontinuous. The discontinuities in the reaction layers are most likely caused by local extinction due to high strain rate from flame-vortex interactions. Ratner et al [84] observed local extinction in a highly turbulent diffusion flame, but the spatial extent of the extinction was less than the current case. The reaction zone appears to be more discontinuous for jet-wake stabilized combustion than for cavity stabilized combustion due to the very high strain rate in the near field of the jet-wake.

4.3 Simultaneous OH/Formaldehyde-PLIF Results

Simultaneous OH/formaldehyde-PLIF gives insight into the reaction zone structure that cannot be obtained from CH-PLIF. Formaldehyde (CH_2O) is produced as part of the initial fuel breakdown reactions and is consumed in the reaction layer. OH is produced in the reaction layer, and consumed by slow recombination reactions.

Mean CH-PLIF and FOV location.

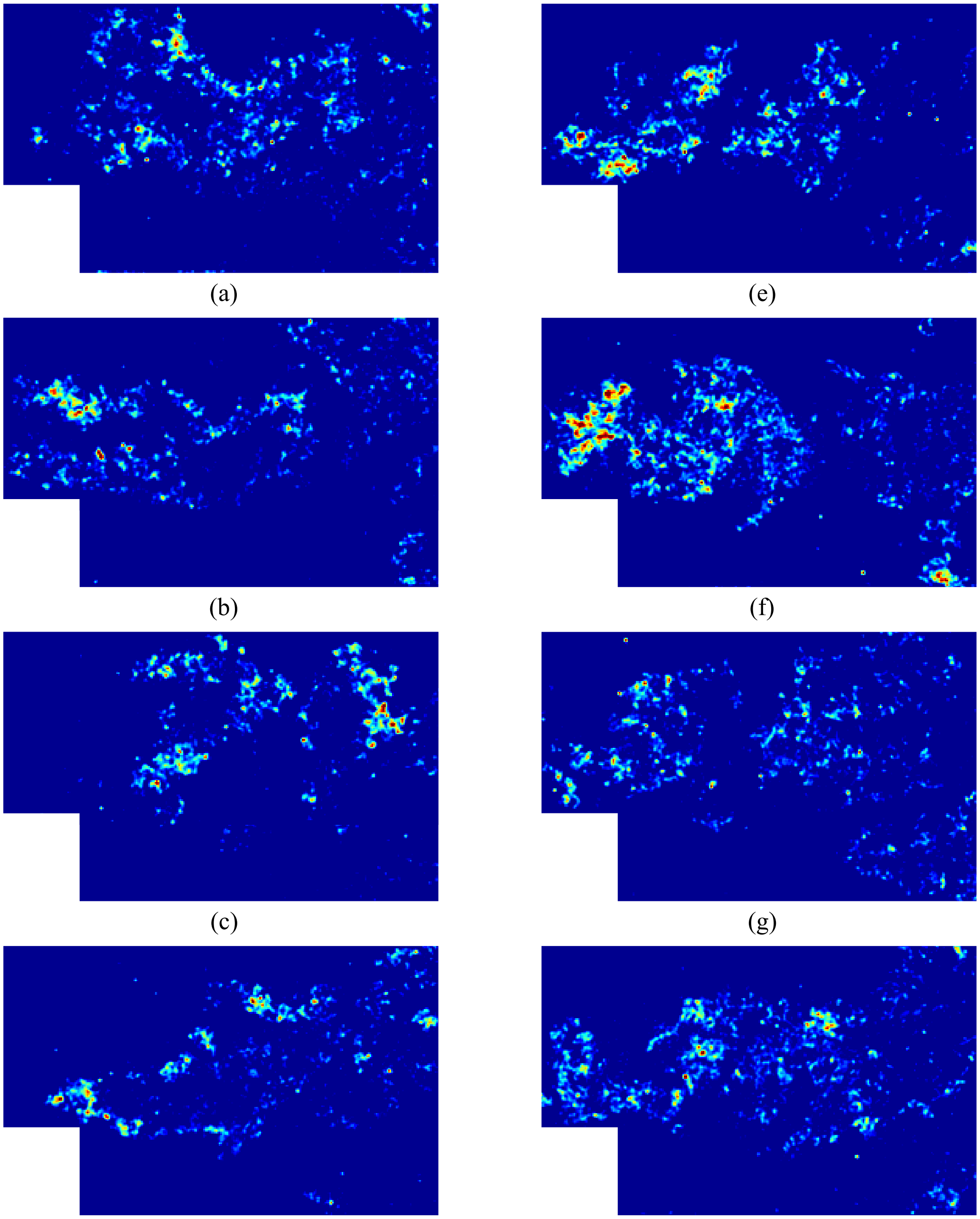

(a) (e) (b) (f) (c) (g) (d) (h)

Figure 4.8: Mean and instantaneous CH-PLIF images for jet-wake stabilized case 2B at field of view (FOV) 1. $x/H = -0.45$ to 2.0.

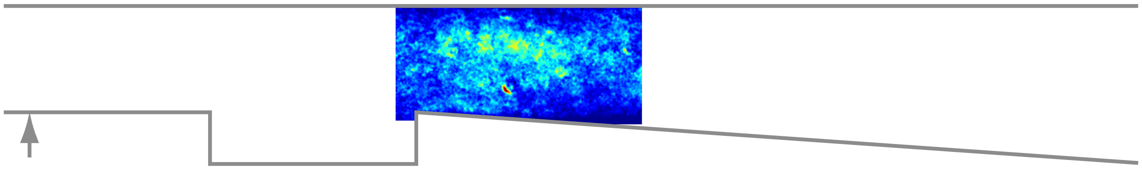

Mean CH-PLIF and FOV location.

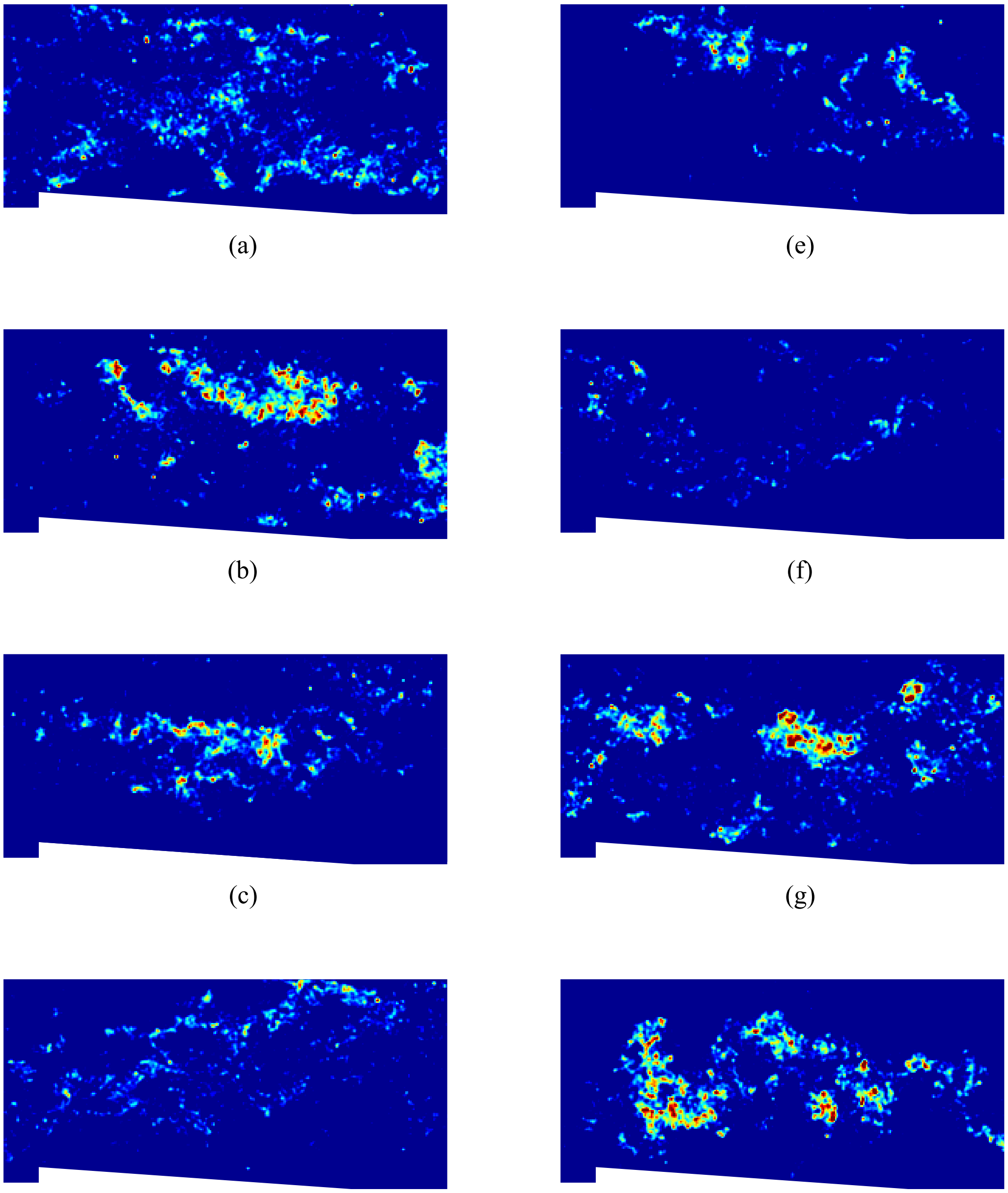

(a) (e)

(b) (f)

(c) (g)

(d) (h)

Figure 4.9: Mean and instantaneous CH-PLIF images for jet-wake stabilized case 2B at field of view (FOV) 2. $x/H = 1.8$ to 4.25.

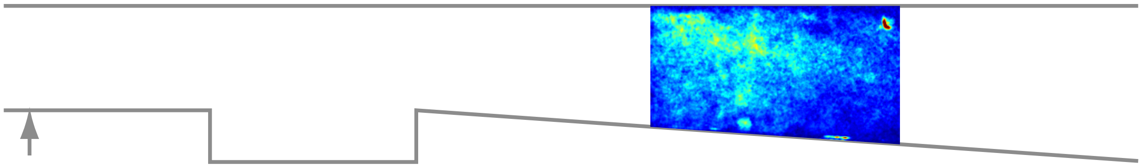

Mean CH-PLIF and FOV location.

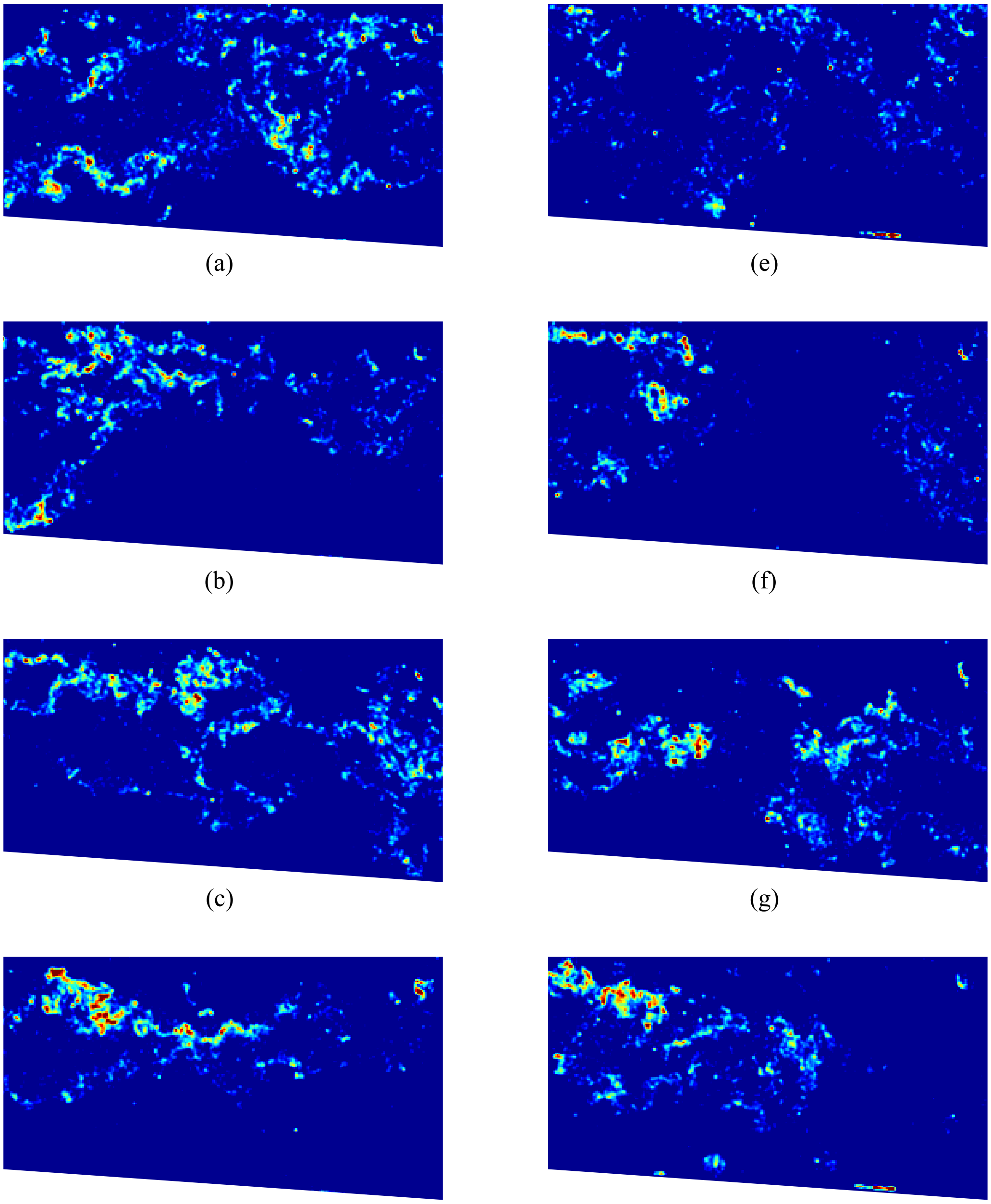

(a)

(b)

(c)

(d)

(e)

(f)

(g)

(h)

Figure 4.10: Mean and instantaneous CH-PLIF images for jet-wake stabilized case 2B at field of view (FOV) 3. $x/H = 4.3$ to 6.75.

Mean CH-PLIF and FOV location.

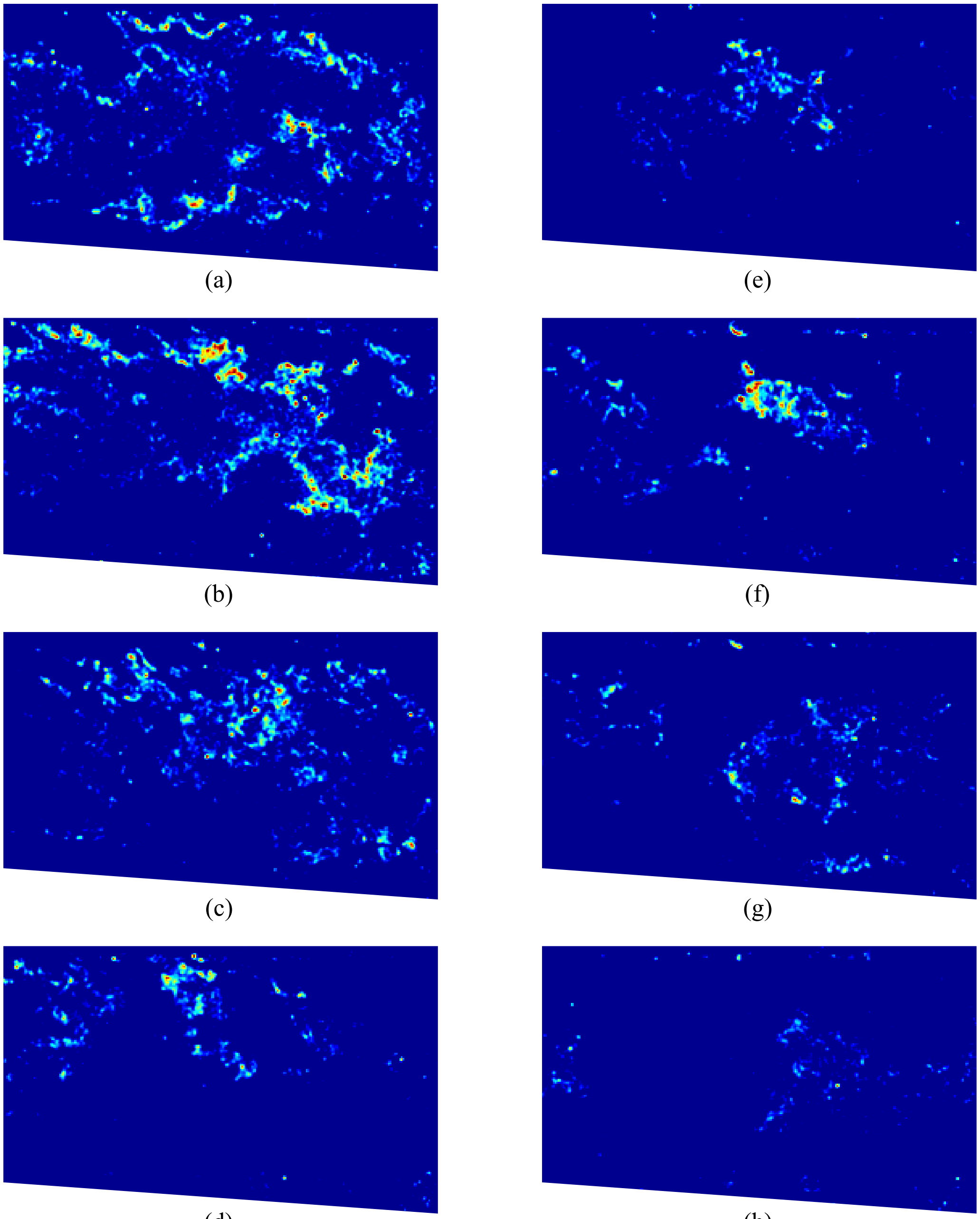

(a)

(e)

(b)

(f)

(c)

(g)

(d)

(h)

Figure 4.11: Mean and instantaneous CH-PLIF images for jet-wake stabilized case 2B at field of view (FOV) 4. $x/H = 6.55$ to 9.0.

Thus OH persists downstream into the hot products. Interpretation of images of either OH alone or formaldehyde alone gives incomplete information due to ambiguities about which edges are due to production, consumption, and mixing. Simultaneous OH/formaldehyde-PLIF allows imaging of both the fuel decomposition region and the hot combustion products which are produced in the primary reaction layer.

Simultaneous OH/formaldehyde-PLIF images were acquired on the test section centerline (x-y plane) and on cross-sections normal to the flow direction (y-z plane). The centerline PLIF images were acquired at one location for each of the two conditions listed in Table 4.1. The location was chosen to capture the most upstream instance of formaldehyde and OH. The cross-section PLIF images were acquired at three axial location for case 1B conditions ($x/H = 1.0$, 1.8, and 3.2), and four axial location for case 2B conditions ($x/H = 0.0$, 1.0, 1.8, and 3.2). As explained in Sec. 2.5.2, the formaldehyde PLIF camera was only able to view the central region that occupies approximately 70% of the combustor cross-section. Therefore any formaldehyde near the left or right walls of the test section was not imaged. This presented little problem since the instantaneous images rarely showed formaldehyde existing up to the edge of the images. The OH-PLIF camera was able to view the entire combustor cross-section. Approximately 40 instantaneous images were acquired at each location.

4.3.1 OH/Formaldehyde-PLIF of Cavity Stabilized Combustion

Figure 4.12(a)-(g) shows several example instantaneous OH/formaldehyde-PLIF images acquired on the test section centerline for cavity stabilized combustion at case 1B conditions. The OH-PLIF signal is displayed as false color while the outer contour of the formaldehyde PLIF signal is shown as a white line. The formaldehyde generally exists in the entire region between this white line and the OH region as discussed in Sec. 2.5.2. In most images the OH region starts near top of the cavity leading edge. A relatively continuous high OH gradient layer then spreads into the flow from this location. A high OH-gradient layer is expected to occur along the surface of a premixed flame. The OH exists in broad regions behind the initial high gradient layer due to the slow recombination reaction which consume the OH in the combustion products.

Figure 4.12(h) shows an example of an instant of jet-wake stabilized combustion at case 1B conditions. As discussed in Sec. 3.1.1.1, at case 1B conditions the combustion is in the cavity stabilized mode more than 90% of the time. For a small percentage of the time it is in the jet-wake stabilized mode. Figure 4.12(h) is included to show the step change in reaction zone structure that occurs between cavity and jet-wake stabilized combustion, which is not solely a function of changing from case 1B to case 2B conditions.

The region between the formaldehyde contour and the OH region in Fig. 4.12 is the fuel breakdown region. In more than half the images, such as Figs. 4.12(a)-(d), the formaldehyde first appears upstream of the cavity leading edge where the OH begins. In these cases, formaldehyde begins up to 20 mm upstream of the cavity leading edge (which is 25 mm downstream of the fuel injection location). In the other images the formaldehyde begins near the cavity leading edge, and exists in thick, 3-20 mm wide regions above the OH. Examples of this structure are shown in Figs. 4.12(e)-(g).

In most premixed flames the formaldehyde is produced in the flame preheat layer where heat from the reaction zone diffuses upstream and causes the initial fuel decomposition. Such preheat layers are generally quite thin. The formaldehyde layer is calculated by CHEMKIN to be 0.1-0.2 mm thick for a laminar premixed flame at case 1B conditions. Turbulent flames have been reported to have preheat layers up to 4 times as thick as laminar flames [30], but this is still more an order of magnitude less than the observed thickness. Rasmussen [83] measured formaldehyde layers that were thick for cases that had hot products which recirculated upstream of the reaction layer. However, the very high axial velocity present in the current configuration would make it highly unlikely that recirculation could create thick formaldehyde regions. Since the observed formaldehyde cannot be produced in the flame preheat layer, it must be produced during initial auto-ignition reactions that are uncorrelated with the heat release from the combustion. This combustion mechanism is further discussed in Sec. 4.4.3.

Figure 4.13 shows a cross-section view of the mean and sample instantaneous OH and formaldehyde PLIF images for case 1B (cavity stabilized combustion) at $x/H = 1$. The formaldehyde PLIF images generally show the regions of premixed fuel and air. Formaldehyde is present where the fuel and air have premixed and the initial fuel breakdown reactions have occurred during the auto-ignition process. In a few images, such as Fig. 4.13(c)(iv), there is little formaldehyde present. This shows that the upstream initial auto-ignition reactions are not steady. It should be noted that the intense streaks that are present in some formaldehyde PLIF images are due to reflections of the laser beam off window imperfections, and are not due to localized high formaldehyde concentrations. Section 2.5.2 discusses this noise source.

The mean OH-PLIF image in Fig. 4.13(b) shows that the flame is relatively flat across the width of the test section on average. The decreasing intensity of the OH signal is the z direction is due to the absorption of the laser sheet energy across the width of the test section. The laser sheet enters from the right side of the images. This should not be interpreted to mean that the reaction is much stronger

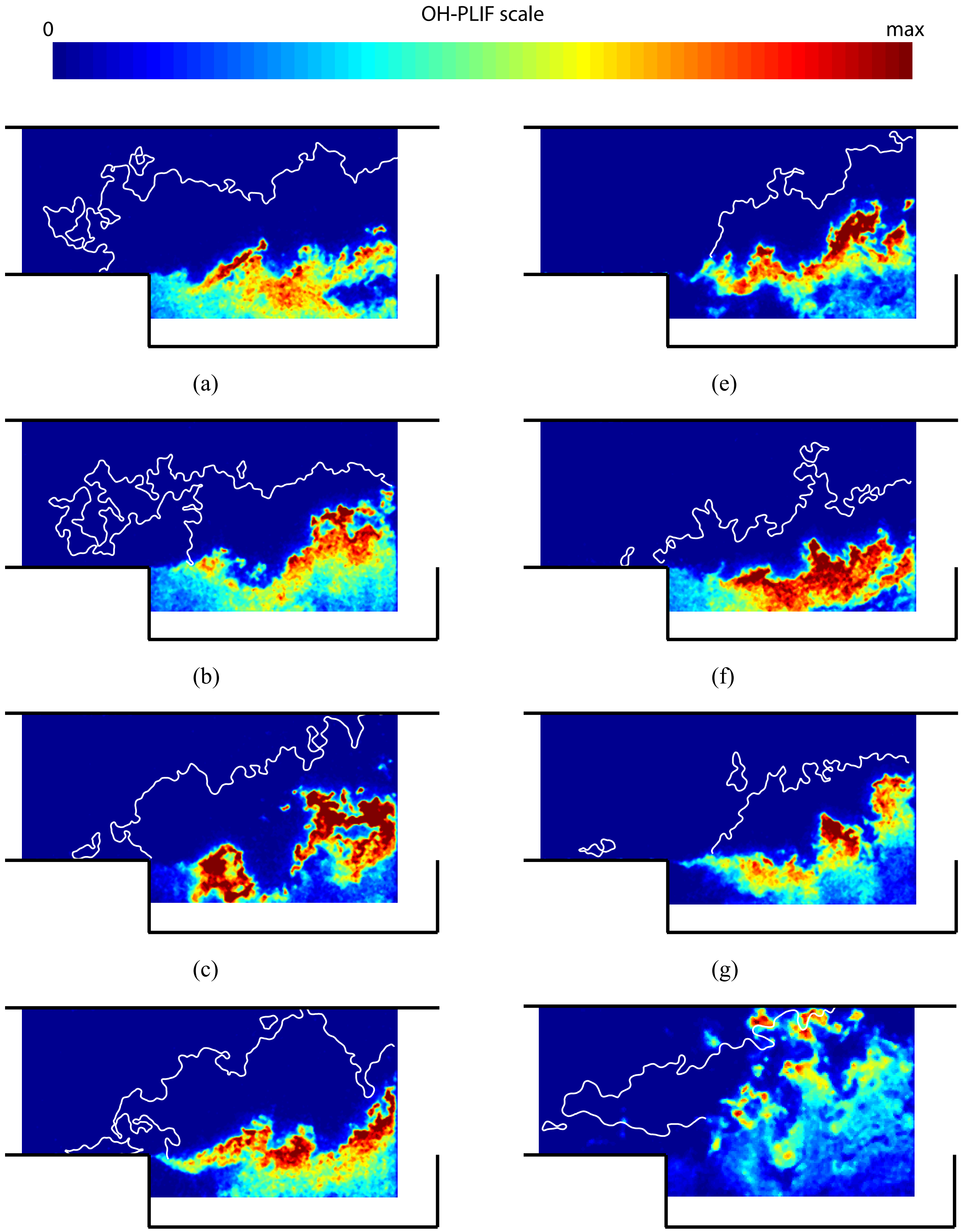

(a) (e)

(b) (f)

(c) (g)

(d) (h)

Figure 4.12: Centerline instantaneous OH/CH_2O-PLIF images for case 1B. The OH-PLIF signal is displayed using a color scale while the outer contour of the simultaneous CH_2O-PLIF signal is shown as the white line. Formaldehyde is generally present in the entire region between the white line and the OH. Images (a)-(g) show examples of cavity stabilized combustion. Image (h) shows an example of jet-wake stabilized combustion at case 1B conditions.

on right side of the test section. The instantaneous images show that the upper border of the OH region is usually approximately coincident with the lower edge of the formaldehyde as seen in Fig. 4.13(d)(i). This is the structure that is expected for a premixed flame sheet that is consuming the fuel-air mixture from the bottom up.

The instantaneous images display a significant wrinkling of the flame sheet across the width of the test section. In many of the instantaneous OH images at $x/H = 1$ there is a gap in the OH near the center of the test section as seen in Figs. 4.13(d)(ii)-(iv). The average OH image also has reduced intensity in the center (compared to the left side where the laser power is lower). A reasonable explanation for this behavior is that the fuel-air mixture is rich near the test section centerline, which is directly behind the fuel injection jet. The flame speed along the centerline therefore is relatively low and so the reaction zone spreads into the flow slowly. The average centerline CH-PLIF image shown in Fig. 4.3 does show slower spreading over the front half of the cavity than the average CH* image (which is averaged over the width of the test section) shown in Fig. 4.1(a). Images such as Figs. 4.13(d)(ii)-(iv) could be instances where the flame sheet is below the cavity leading edge near the centerline. There may also occasionally be a hole in the premixed flame sheet near the centerline due to the high equivalence ratio.

Figures 4.14 and 4.15 display the mean and instantaneous PLIF images at x/H =1.8 and 3.2. In these images the premixed flame sheet spreads further into the flow and consumes the fuel/air mixture (marked by the formaldehyde) from the bottom up. Usually there is no formaldehyde present below the top of the flame sheet (which is indicated by the top of the OH region). At x/H = 3.2, there were a few images in which regions of formaldehyde exist below the top of the flame sheet. Figure

4.15(d)(ii) is one example of this. Such structures could be formed by flame sheet merging or by local extinction.

Figure 4.16 illustrates the 3-dimensional structure of the reaction zone with a representative instantaneous PLIF image at the each of the three measured locations. It can be seen that the fuel-air mixture, represented by formaldehyde, is consumed by a mostly continuous flame sheet that is spreading into the flow as it moves downstream.

4.3.2 OH/Formaldehyde-PLIF of Jet-Wake Stabilized Combustion

Figure 4.17 shows several example instantaneous OH/formaldehyde-PLIF images acquired on the test section centerline for jet stabilized combustion at case 2B conditions. The OH-PLIF signal is displayed as false color while the outer contour of the formaldehyde signal is shown as a white line. The formaldehyde generally exists in the entire region between this white line and the OH as discussed in Sec. 2.5.2. The OH is found in discontinuous clumps which generally start upstream of the cavity leading edge. This structure is consistent with the highly shredded reaction zone imaged by CH-PLIF. The OH begins between 20-45 mm downstream of the fuel injection (x/H=-1.0 to 0). The most upstream appearance of OH is usually near the lower combustor wall.

The formaldehyde is distributed across broad regions which appear to encompass the spreading of the fuel jet. It begins 4-25 mm downstream of the fuel injection (x/H=-1.6 to -0.75). This is well upstream of the heat release zone (signified by the production of OH) in almost all images. A similar structure was imaged by Gordon, Masri, and Mastorakos [38] for lifted methane flames in a vitiated co-flow. This formaldehyde is produced by preliminary auto-ignition reactions that are uncorrelated with the heat release from the combustion.

Figures 4.18-4.21 show the mean and instantaneous cross-section OH and formalde-

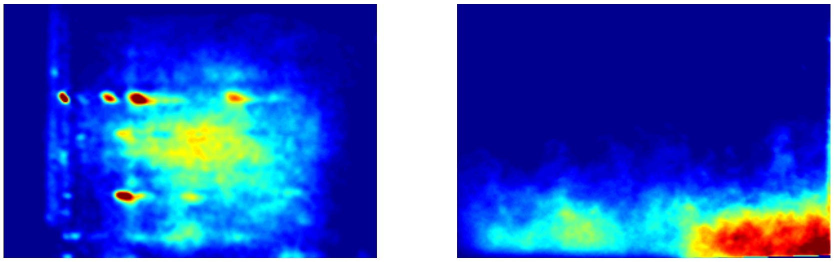

(a) Mean formaldehyde - PLIF

(b) Mean OH - PLIF

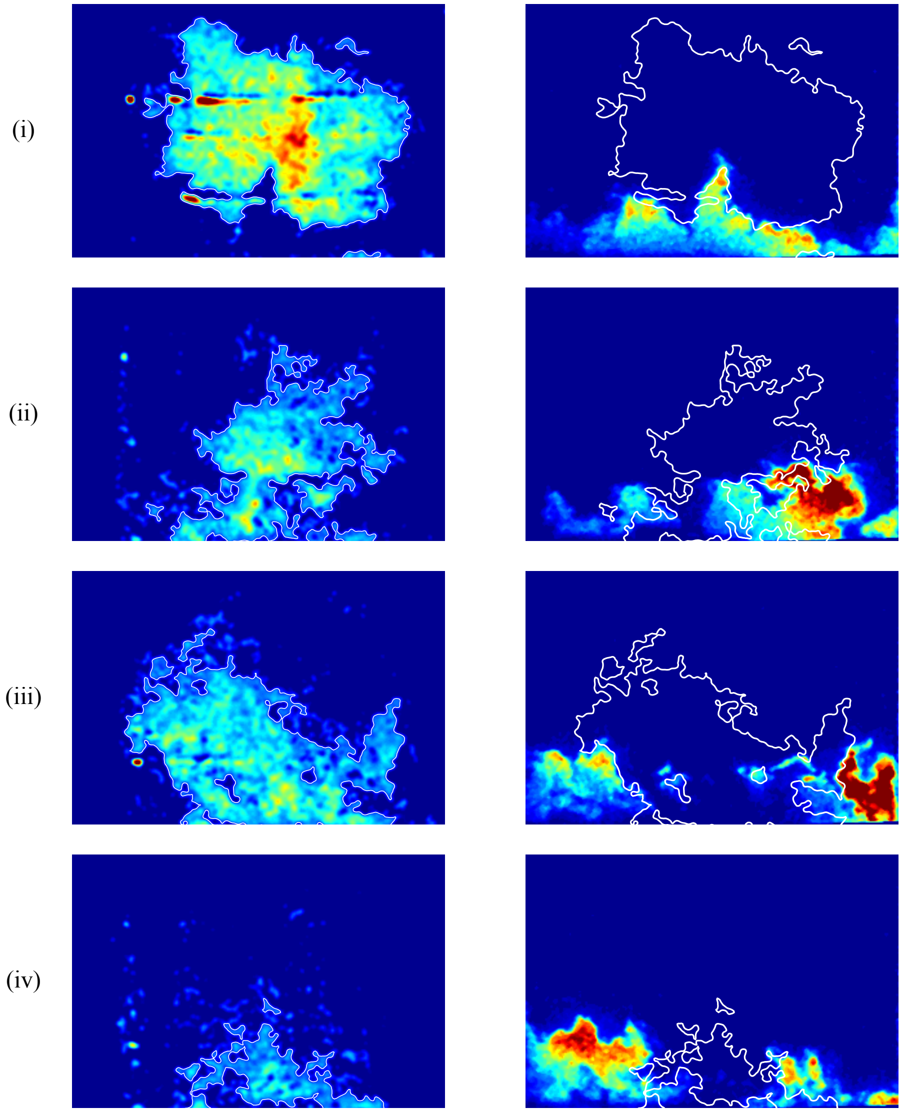

(c) Instantaneous formaldehyde - PLIF

(d) Instantaneous OH - PLIF

Figure 4.13: Cross-section OH/CH_2O-PLIF images at $x/H = 1.0$ for case 1B, cavity stabilized combustion. The outer contour of the CH_2O-PLIF is shown as a white line in the instantaneous PLIF images.

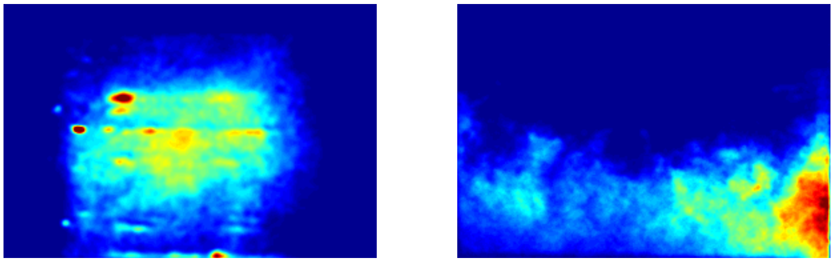

(a) Mean formaldehyde - PLIF (b) Mean OH - PLIF

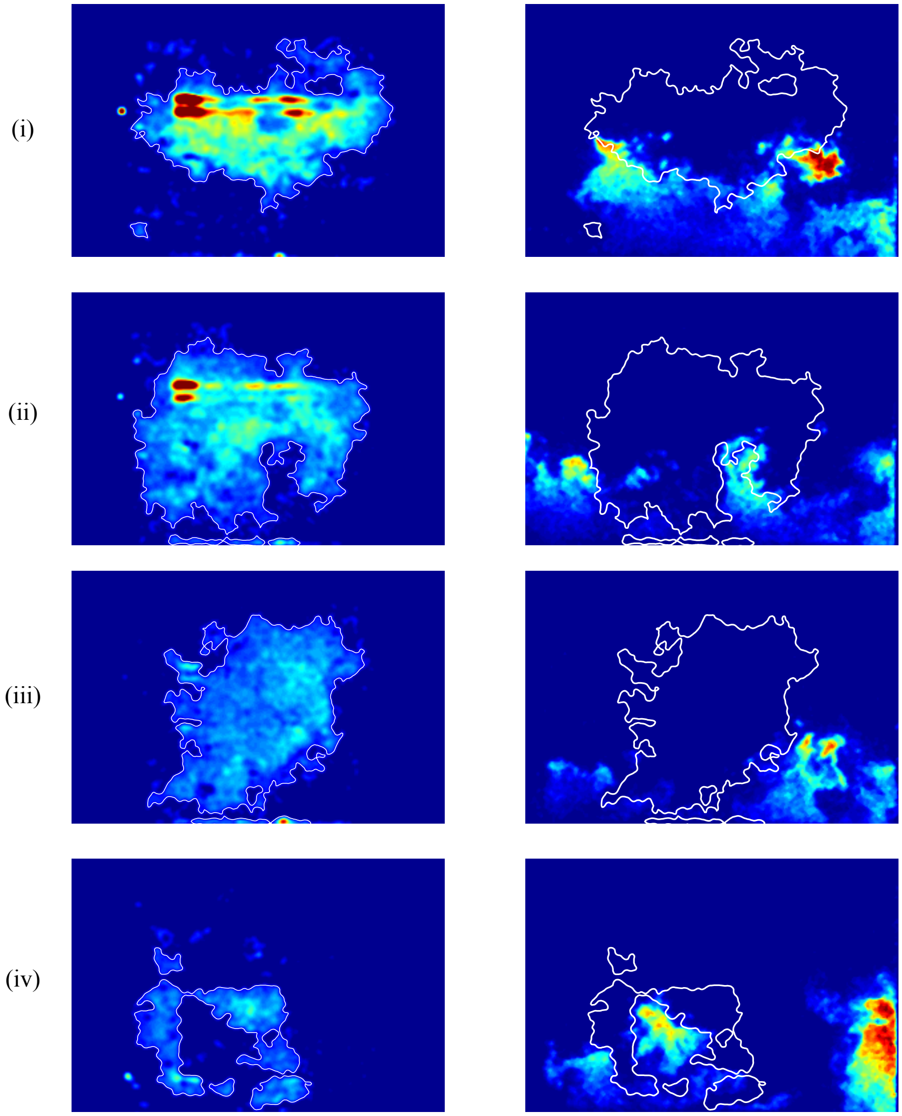

(c) Instantaneous formaldehyde - PLIF (d) Instantaneous OH - PLIF

Figure 4.14: Cross-section OH/CH_2O-PLIF images at $x/H = 1.8$ for case 1B, cavity stabilized combustion. The outer contour of the CH_2O-PLIF is shown as a white line in the instantaneous PLIF images.

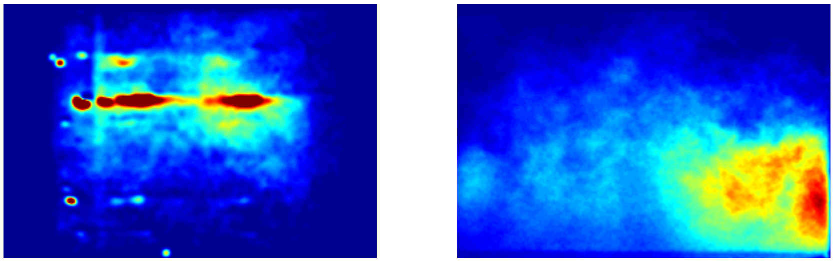

(a) Mean formaldehyde - PLIF

(b) Mean OH - PLIF

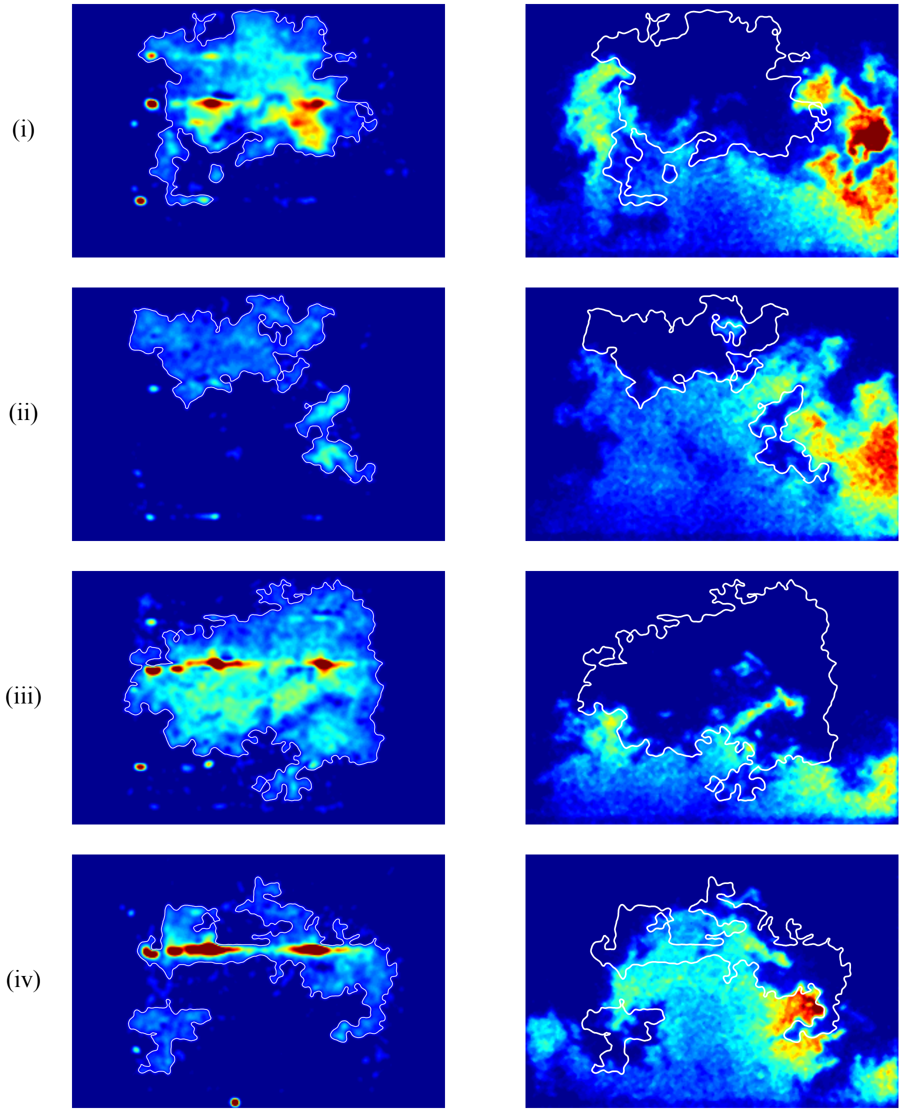

(c) Instantaneous formaldehyde - PLIF

(d) Instantaneous OH - PLIF

Figure 4.15: Cross-section OH/CH_2O-PLIF images at $x/H = 3.2$ for case 1B, cavity stabilized combustion. The outer contour of the CH_2O-PLIF is shown as a white line in the instantaneous PLIF images.

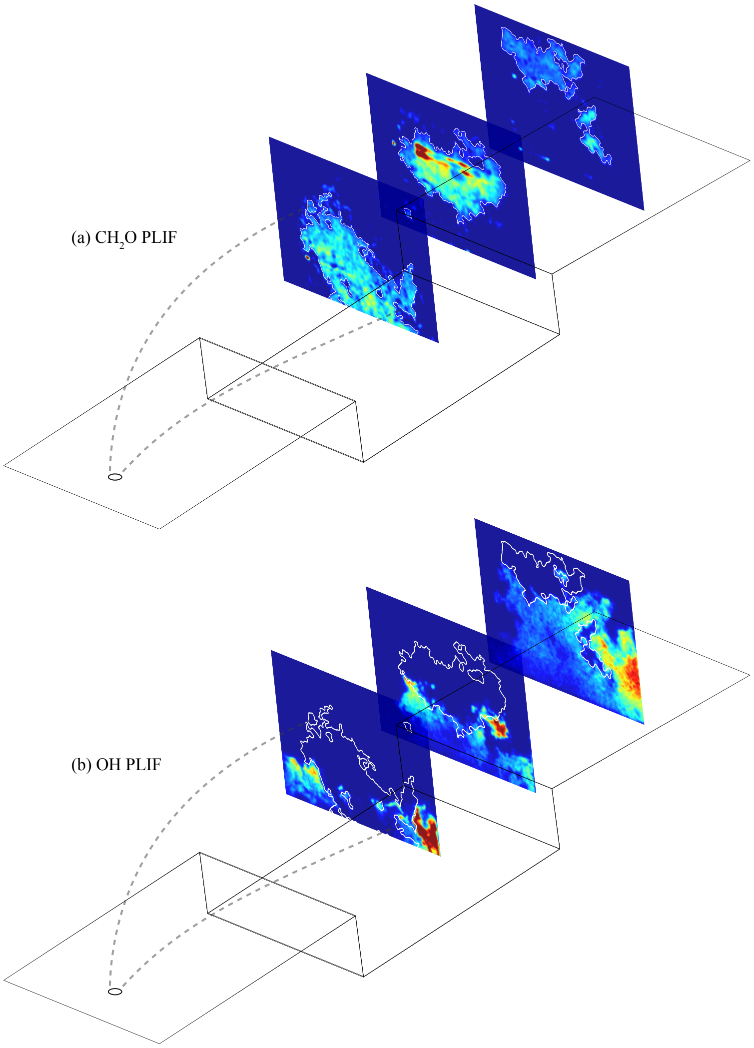

Figure 4.16: Instantaneous PLIF images showing 3D reaction zone structure for case 1B, cavity stabilized combustion. Outer contour of CH$_2$O-PLIF signal is shown as white line. Images in different planes were acquired at different times.

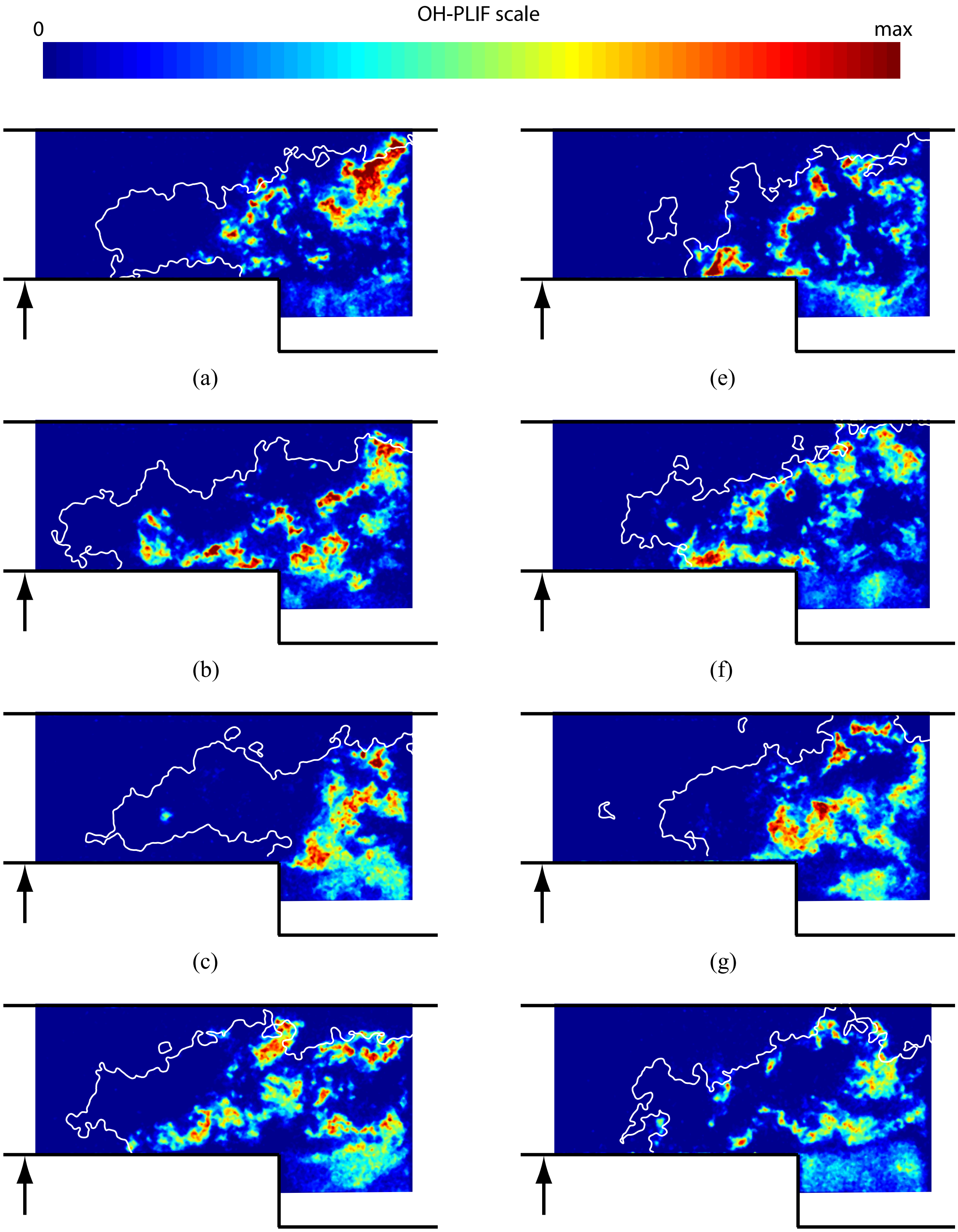

(a) (e)

(b) (f)

(c) (g)

(d) (h)

Figure 4.17: Centerline instantaneous OH/CH_2O-PLIF images for case 2B (jet-wake stabilized combustion). The OH-PLIF signal is displayed using a color scale while the outer contour of the simultaneous CH_2O-PLIF signal is shown as the white line. Formaldehyde is generally present in the entire region between the white line and the OH.

hyde PLIF images for case 2B. At $x/H = 0.0$, the formaldehyde images indicate that the fuel jet usually has not penetrated to the top of the test section. Based on the mean OH-PLIF image in Fig. 4.18(b) the reaction zone is generally confined to the lower half of the test section vertically (y-direction) and the center of the test section horizontally (z-direction). The instantaneous images in Fig. 4.18(d)(i)-(iii) indicate that the reaction zone is usually located on the bottom edge of the premixed fuel jet. In a few instances, such as Fig. 4.18(d)(iv), the reaction has spread around the entire perimeter of the premixed fuel jet.

Moving downstream, Fig. 4.19(a) shows that the fuel jet has penetrated to the top of the test section (on average) by $x/H = 1.0$. Based on the instantaneous OH-PLIF images in Fig. 4.19(d) the reaction zone has generally spread around the entire perimeter of fuel jet. The perimeter of the premixed jet has an equivalence ratio that is more favorable for combustion than the rich interior. The average OH-PLIF image in Fig. 4.19(b) shows that the majority of the OH exists in regions along the sides of the fuel jet.

At $x/H = 1.8$, there is virtually no formaldehyde present in Figs. 4.20(a) and (c). However the CH-PLIF and CH* imaging showed that significant combustion occurs downstream of this location. Therefore it is concluded that the structure of the jet-wake stabilized combustion includes an inner, rich premixed flame. This structure is similar to the bunsen flame that was studied as part of the PLIF system calibration. The bunsen flame consists of a diffusion flame that surrounds a rich premixed flame cone. All of the formaldehyde is destroyed at the surface of the inner, rich flame. No formaldehyde was present between the inner premixed flame and the diffusion flame. A diagram of this jet-wake stabilized reaction zone structure appears in Fig. 4.22. Figure 4.23 illustrates the 3-D structure with a representative instantaneous PLIF image at each imaging plane.

The average OH PLIF image in 4.20(b) shows OH has spread throughout the entire test section cross section by $x/H = 1.8$. A similar image is seen in 4.21(b) at $x/H = 3.2$, but there is a decrease in the OH signal near the center (horizontally) of the upper half of the cross-section. The instantaneous OH-PLIF images generally show areas of low OH signal surrounded by areas of high OH signal. The bunsen flame PLIF images also contained low OH signal in the region between the rich, premixed flame and the outer diffusion flame (Sec. 2.5.2). Thus these low OH regions most likely are products of the rich premixed flame which have not passed through the diffusion flame. The regions where the OH signal is large indicate locations where products of the diffusion flame exists.

4.4 Combustion Mechanisms

The observed reaction zone structure gives some insight into the controlling mechanism of the combustion. In this section, the limiting cases of a pure flame and pure auto-ignition are described and the expected reaction zone structure of each case is illustrated. A hybrid mechanism which best explains the observed reaction zone structure and behavior is also described. The hybrid mechanism is referred to as an auto-ignition assisted flame.

4.4.1 Pure Flame

If the reaction zone base occurs as a flame, it will be a premixed flame since there is significant distance between the fuel injection location and reaction zone for mixing of the fuel and air to occur. A premixed flame is a thin structure consisting of a preheat layer and a reaction layer (or heat release layer) where the majority of the chemical energy is released. In the preheat layer, the premixed reactants are heated

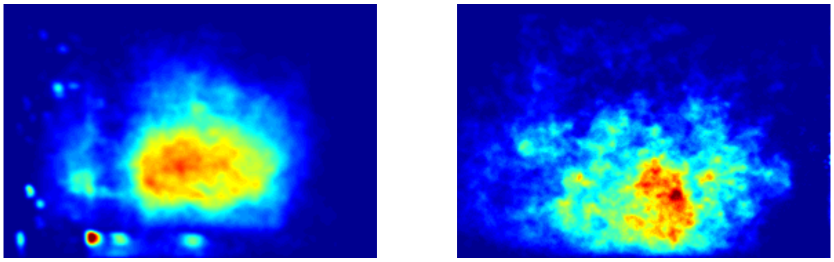

(a) Mean formaldehyde - PLIF

(b) Mean OH - PLIF

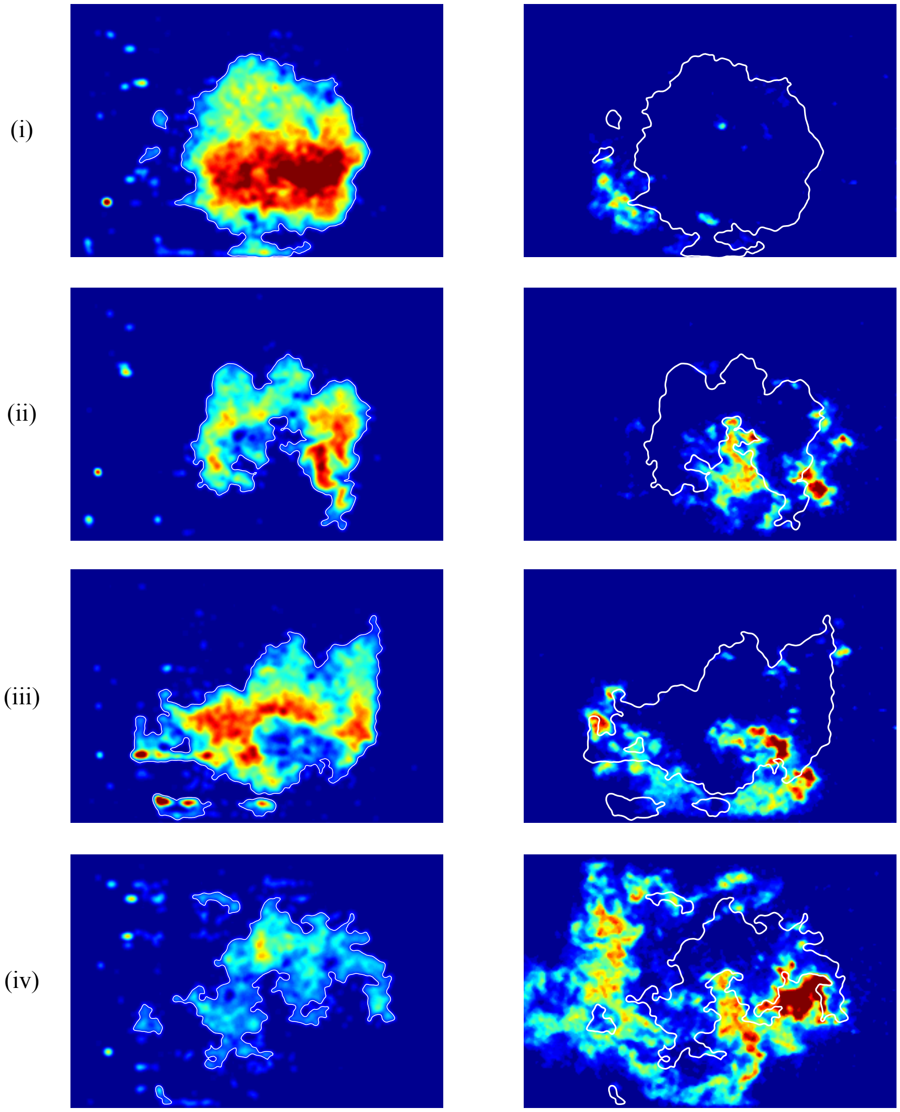

(c) Instantaneous formaldehyde - PLIF

(d) Instantaneous OH - PLIF

Figure 4.18: Cross-section OH/CH_2O-PLIF images at $x/H = 0.0$ for case 2B, jet-wake stabilized combustion. The outer contour of the CH_2O-PLIF is shown as a white line in the instantaneous PLIF images.

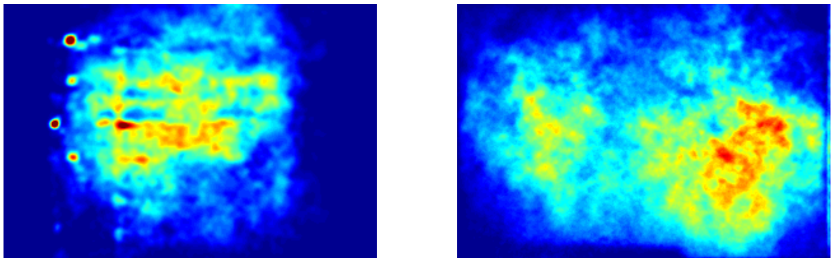

(a) Mean formaldehyde - PLIF

(b) Mean OH - PLIF

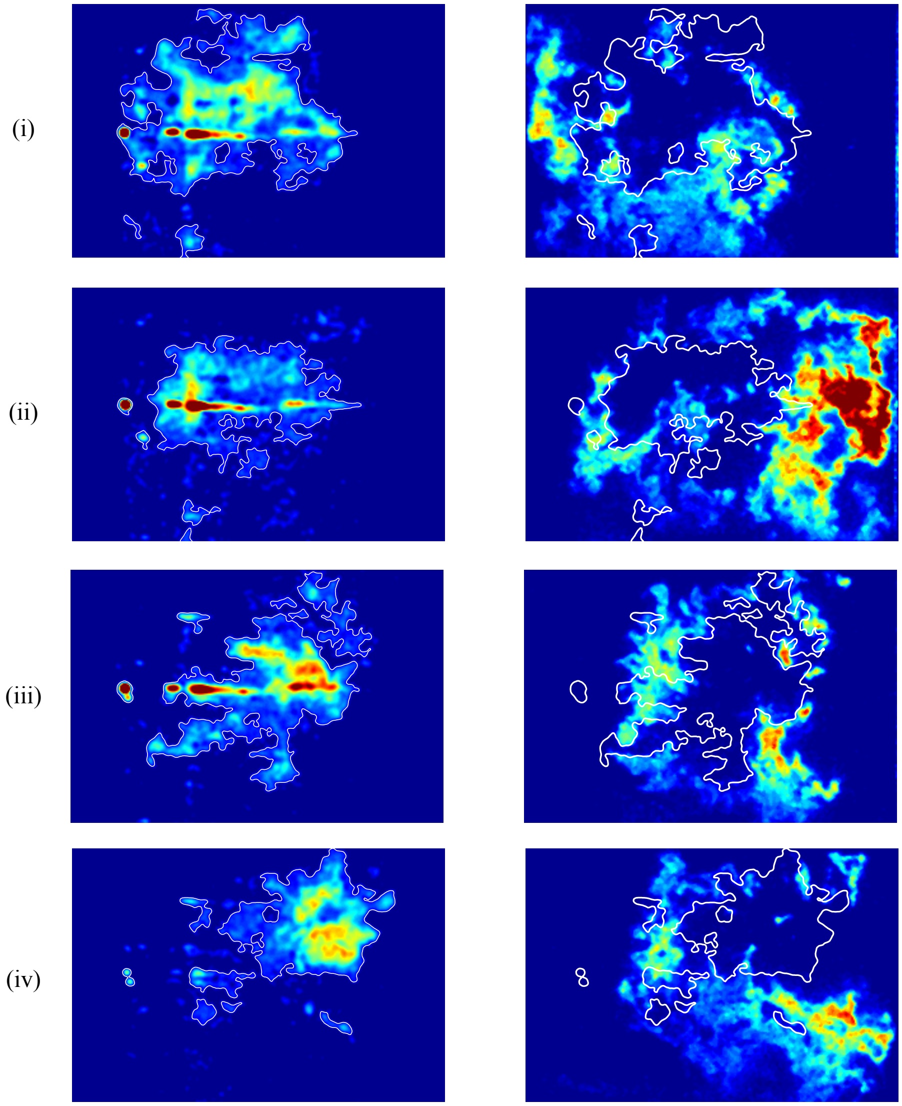

(c) Instantaneous formaldehyde - PLIF

(d) Instantaneous OH - PLIF

Figure 4.19: Cross-section OH/CH_2O-PLIF images at $x/H = 1.0$ for case 2B, jet-wake stabilized combustion. The outer contour of the CH_2O-PLIF is shown as a white line in the instantaneous PLIF images.

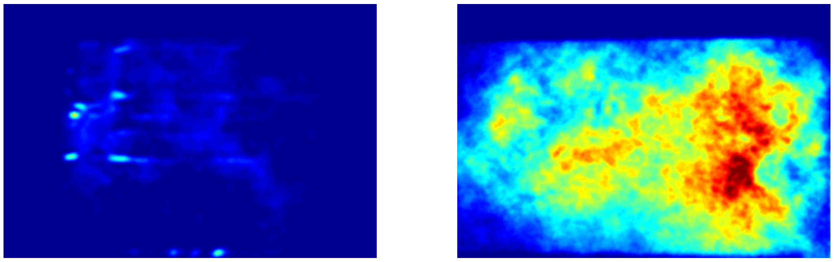

(a) Mean formaldehyde - PLIF

(b) Mean OH - PLIF

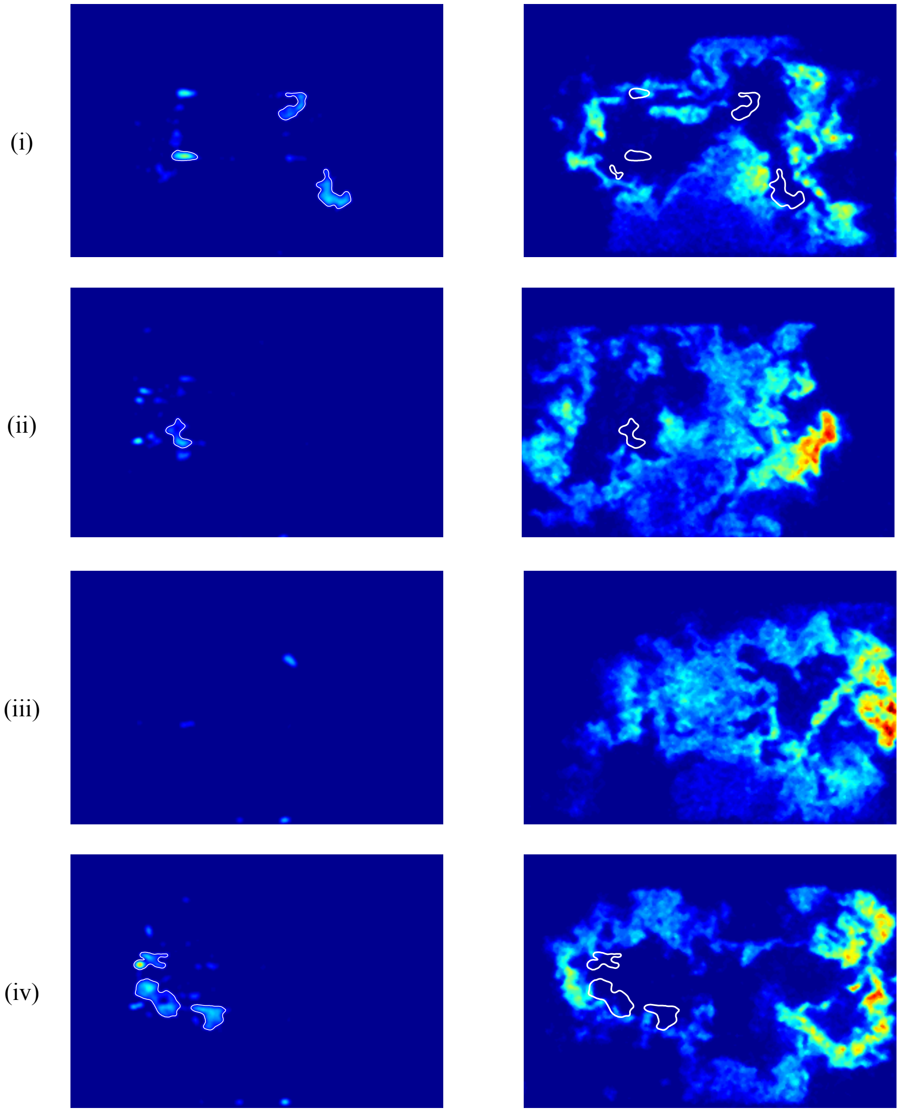

(c) Instantaneous formaldehyde - PLIF

(d) Instantaneous OH - PLIF

Figure 4.20: Cross-section OH/CH_2O-PLIF images at $x/H = 1.8$ for case 2B, jet-wake stabilized combustion. The outer contour of the CH_2O-PLIF is shown as a white line in the instantaneous PLIF images.

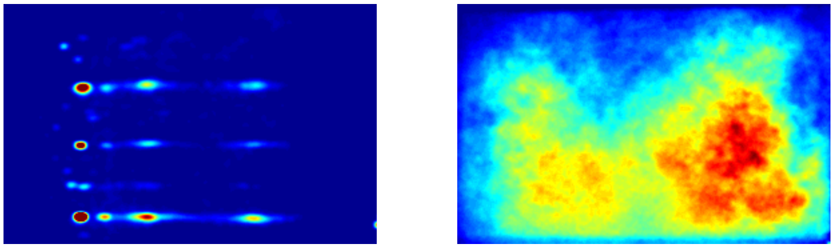

(a) Mean formaldehyde - PLIF (b) Mean OH - PLIF

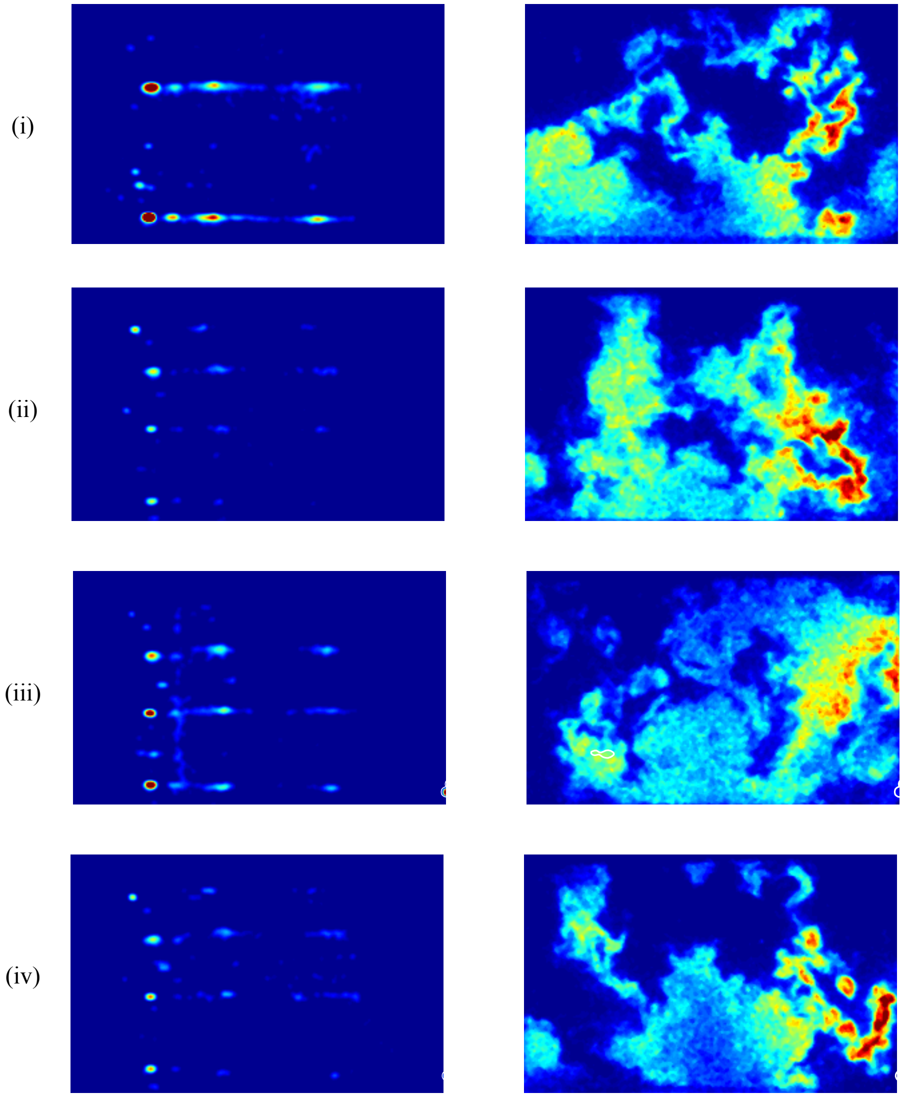

(c) Instantaneous formaldehyde - PLIF (d) Instantaneous OH - PLIF

Figure 4.21: Cross-section OH/CH$_2$O-PLIF images at $x/H = 3.2$ for case 2B, jet-wake stabilized combustion. No formaldehyde is present at this location. Signal seen in formaldehyde images is due to reflections of pump beam off imperfections in the window (see Sec. 2.4.2).

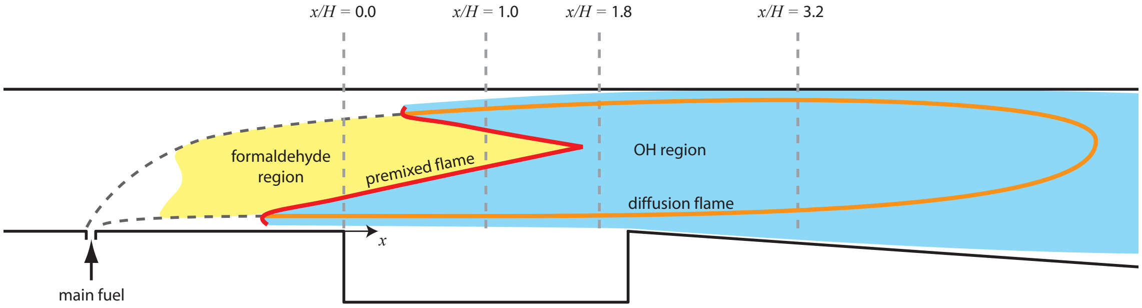

Figure 4.22: Structure of the jet-wake stabilized reaction zone based on the formaldehyde and OH PLIF images. The location of the PLIF imaging planes are labeled.

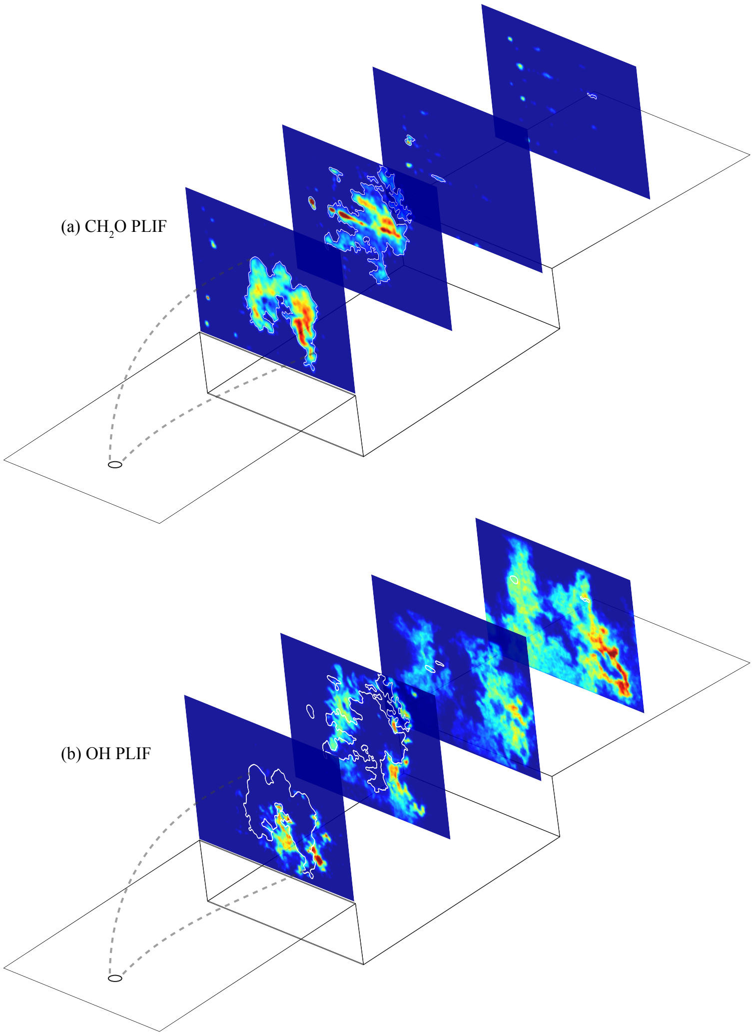

Figure 4.23: Instantaneous PLIF images showing 3D reaction zone structure for case 2B, jet-wake stabilized combustion. Outer contour of CH_2O-PLIF signal is shown as white line. Images in different planes were acquired at different times.

by diffusion of heat and radicals from the reaction layer due to the high temperature gradient across the thin structure. Once the reactants are heated sufficiently above the auto-ignition temperature, the heat release reactions occur in the reaction layer.

The flame speed is an important concept for premixed flames. The flame speed is the speed at which a premixed flame will propagate into reactants. The base of a flame generally must be normal to the flow. Therefore the base of a premixed flame must be stabilized in a location where the flow speed is equal to the flame speed. Away from the flame base, the flame speed controls the angle at which the flame spreads into the reactants. From a modeling perspective then it is important to properly predict the flame speed to predict the flame stabilization locations and spreading. It is computationally prohibitive to directly resolve the high gradients associated with flames for most practical engineering problems. Therefore premixed flame models must be used in CFD simulations where premixed flames are present.

Figure 4.24 shows the expected structure for cavity and jet-wake stabilized combustion occurring as a pure flame. The regions of the initial fuel decomposition, the flame preheat layer, and the reaction zone (or heat release zone) are labeled. In a pure flame there are no chemical reactions occurring upstream of the flame preheat layer. The reactants enter the preheat layer where they are very quickly heated by diffusion of heat from the reaction zone, and the initial fuel breakdown reactions occur. Once the reactants reach a temperature such that the auto-ignition delay time become negligible, the heat release reactions occur in the reaction zone. The PLIF imaging shows that the initial fuel breakdown leading to formaldehyde production is well upstream of the flame preheat layer for both stabilization modes. Therefore the combustion does not occur as a pure flame in either the cavity stabilized or jet-wake stabilized mode for the conditions studied.

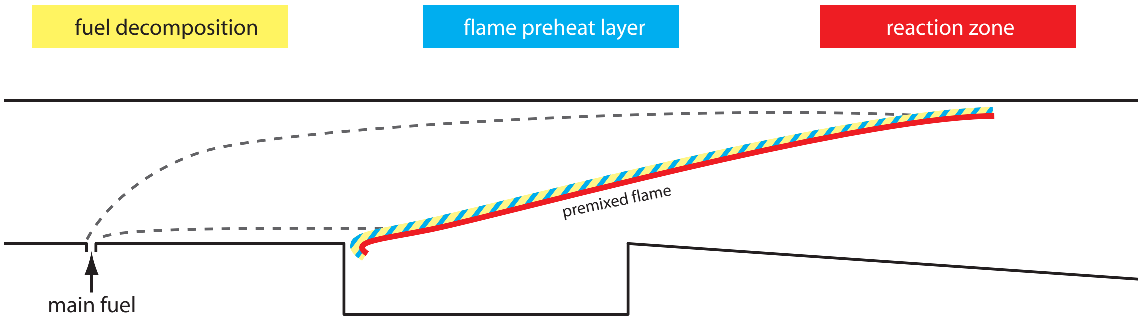

(a) Cavity stabilized combustion.

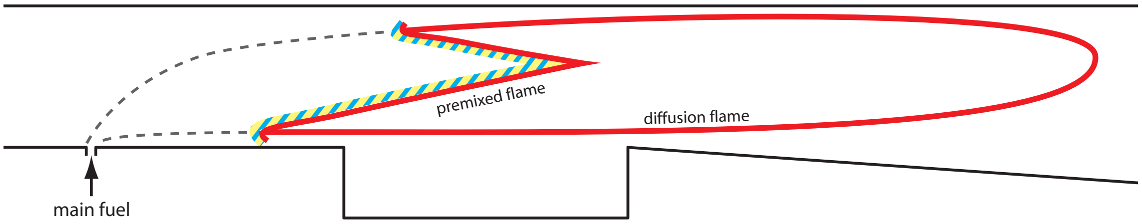

(b) Jet-wake stabilized combustion.

Figure 4.24: Expected reaction zone structure for cavity and jet-wake stabilized combustion occurring as a pure flame (no chemical reactions upstream of the flame preheat zone).

4.4.2 Pure Auto-ignition

In pure auto-ignition reactions, the diffusion of heat from combustion does not play a role in heating the reactants. Instead the reactants are preheated by some external means. In the current case, mixing with the very high temperature air provides the preheating. Because diffusion of heat from the combustion does not play a role, the reaction does not occur as a propagating wave and flame speed has no relevance. Instead, the controlling factor is the auto-ignition delay time of the reactants. The auto-ignition delay time is the time it takes for the rapid temperature rise to begin given a set of initial conditions. The auto-ignition delay time for a reactant mixture is very strongly dependant on the initial temperature (approximately exponentially dependent on $1/T_{initial}$) and weakly dependent on the stoichiometry for a given fuel [66]. For very high temperatures then, the ignition delay time becomes negligible and fuel burns as soon as it mixes with the air. This leads to a reaction zone which is attached to the fuel injector as studied by Ben-Yakar and Hanson [5, 4]. For lower initial temperatures (which are still above the auto-ignition temperature) the ignition delay time controls the distance between the fuel injection location and the start of the reaction zone.

Figure 4.25 shows the expected reaction zone structure for combustion occurring as pure auto-ignition. The fuel mixes with the high temperature air causing the initial auto-ignition reactions leading to fuel decomposition. After the fuel and air have been mixed for the auto-ignition delay time, the heat release reactions occur. The reaction zone will not have a continuous structure (for cases with a non-negligible ignition delay time) because each fluid packet will react independently based on its integrated time history of temperature and equivalence ratio from the injection location. The reaction zone in Figure 4.25 has been drawn downstream of the observed location to emphasize that its location is set by different factors than the case of the flame (time history of velocity, temperature and equivalence ratio vs. local flame speed and local flow speed at the stabilization location). For the proper set of conditions, an auto-ignition reaction could exist at the observed location.

For cavity stabilized combustion, a relatively continuous reaction layer spreading from a fixed location was observed. This is completely inconsistent with a pure auto-ignition reaction. For jet-wake stabilized combustion, it is not so clear. The upstream fuel breakdown reactions are consistent with auto-ignition and there are not thin and continuous reaction layers present. The behavior of the reaction zone leading edge described in Secs. 3.1.1.3 and 3.1.2 is strong evidence that a propagating flame plays a role in the stabilization however. Thus it is unlikely that the jet-wake stabilized combustion is due to pure auto-ignition.

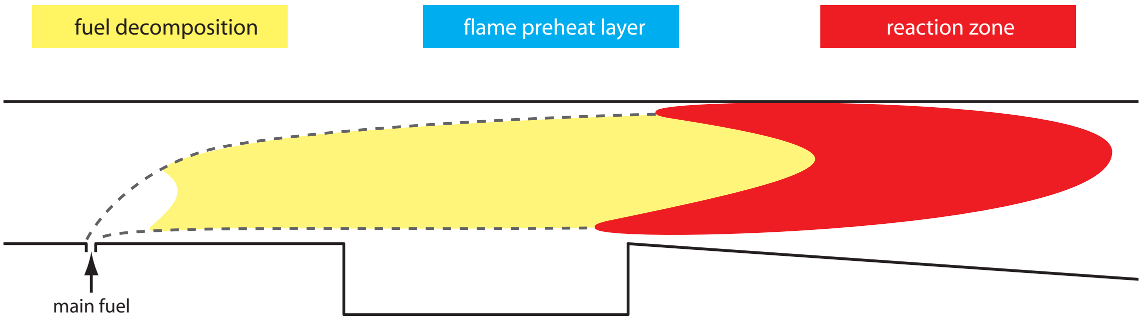

Figure 4.25: Expected reaction zone structure for combustion occurring as pure auto-ignition (no diffusion of heat from the reaction zone).

4.4.3 Auto-ignition Assisted Flame

The best explanation for combustion mechanism in each case is that of an auto-ignition assisted flame. This structure is shown in Fig. 4.26 for cavity and jet-wake stabilized combustion. The fuel mixes with the air at high temperature causing the initial fuel decomposition reactions to occur as part of the auto-ignition process. The pure auto-ignition process does not continue to completion however, because the heat release reactions occur in a flame first. In the flame structure, the diffusion of heat from the reaction zone raises the reactant temperature, causing the ignition delay time to decrease rapidly.

This auto-ignition assisted flame mechanism should be primarily modeled as flame. There is a flame speed which the sets stabilization location and the rate at which the reaction wave can consume reactants. The upstream auto-ignition reactions serve to increase the auto-ignition assisted flame over that of a pure flame. In the pure flame case, the flame speed depends only on the local temperature, ϕ, and turbulence level. In an auto-ignition assisted flame, this speed also depends on the progression of the upstream auto-ignition reactions, which are a function of the distance between the fuel injection location and the flame. To properly model combustion in this auto-

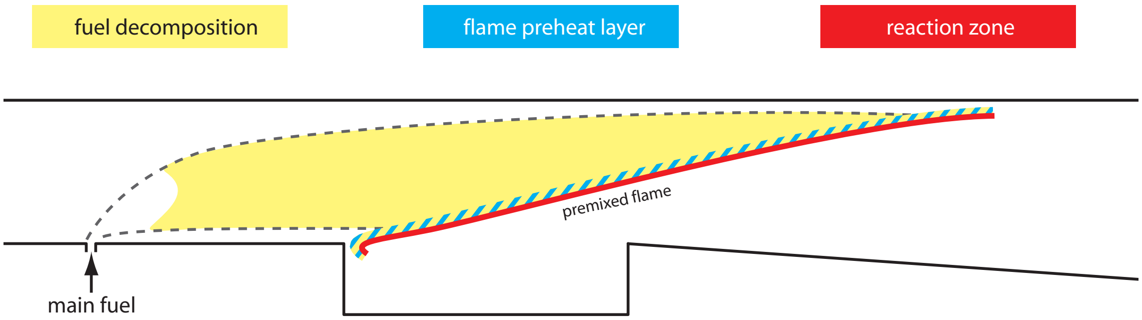

(a) Cavity stabilized combustion.

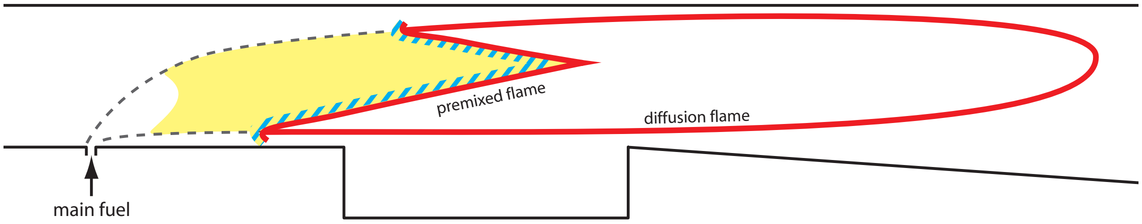

(b) Jet-wake stabilized combustion.

Figure 4.26: Reaction zone structure for cavity and jet-wake stabilized combustion occurring as an auto-ignition assisted flame. Finite rate kinetics occur well upstream of the reaction zone. Diffusion of heat and radicals is important in the flame preheat layer.

ignition assisted flame regime both finite rate kinetics upstream of the reaction zone, and premixed flame properties must be simulated.

CHAPTER V

Heat Release Distribution

5.1 Run Conditions

The axial heat release distribution was estimated from wall pressure measurements and OH* and CH* luminosity for the conditions given in Table 5.1. Cases 1H, 2H, 1B, and 2B are the baseline cavity and jet-wake stabilized combustion for hydrogen and blended fuel. The effects of varying the air stagnation temperature and the overall equivalence ratio was examined in data sets E and F. For all cases given in Table 5.1, the main fuel was injected through the upstream port at $x/H = -1.75$, and the cavity fuel was injected through the rear wall.

5.2 Wall Pressure and Quasi-One-Dimensional Data Analysis Model

Detailed wall pressure distributions were obtained for cases 1H, 2H, 1B, and 2B. These distributions are shown in Figs. 5.1 and 5.2. For both fuel types, the pre-combustion shock train has a greater length and pressure rise for jet-wake stabilized

Case	$T_{0,air}$	fuel composition	ϕ	$\frac{\dot{m}_{cavfuel}}{\dot{m}_{totalfuel}}$
case 1B	1270 K	$50\%H_2, 50\%C_2H_4$	0.42	0.05
case 2B	1470 K	$50\%H_2, 50\%C_2H_4$	0.42	0.05
case 1H	1130 K	$100\%H_2$	0.27	0.05
case 2H	1370 K	$100\%H_2$	0.27	0.05
set E	1220 K - 1500 K	$100\%H_2$	0.26	0.05
set F	1500 K	$100\%H_2$	0.23-0.36	0.05

Table 5.1: Test conditions for OH* and CH* chemiluminescence measurements.

combustion (cases 2B and 2H) than for cavity stabilized combustion (cases 1B and 1H). In all cases the pressure begins to decrease after the start of the reaction zone. There is a sharp decrease in pressure near the cavity trailing edge (which is the beginning of the diverging section) that is more pronounced for jet-wake stabilized combustion than for cavity stabilized combustion. Downstream of the cavity trailing edge the pressure is higher for the cavity stabilized combustion than for jet-wake stabilized combustion.

The wall pressure measurements were used in conjunction with a one-dimensional model to obtain the average flow conditions and heat release rate throughout the combustion and isolator. The model solves the one-dimensional mass, momentum, and energy conservation equations with area change. The wall pressure data is input into the model to solve for the unknown percentage of reacted fuel at each axial location in the combustor. This approach previously has been used by Tomioka et al [98] and Donbar et al [27] to calculate the flow conditions and combustion efficiency in dual-mode scramjet combustors from measured wall pressure data.

For the current study a MATLAB code was created to solve the one-dimensional conservation equations with area change. The isolator entrance conditions, combustor area distribution, and wall pressure distribution $P(x)$ were used as inputs. A continuous function for $P(x)$ was needed to solve the differential conservation equations. This function was obtained from the discrete experimental data by creating spline fits. These spline fits are shown along with the experimental data in Figs. 5.1 and 5.2. Single step chemistry was assumed that included only the major species ($H_2, C_2H_4, O_2, N_2, H_2O$, and CO_2). This allowed all species concentrations to be written as algebraic functions of a single variable, which is the combustion efficiency ($\eta_c(x)$), that was computed by the model. Combustion efficiency is a reaction

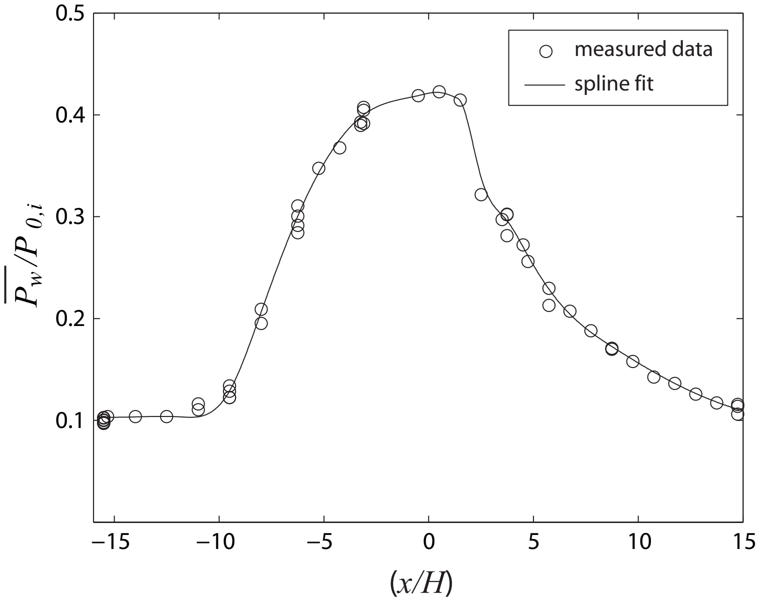

(a) Case 1B.

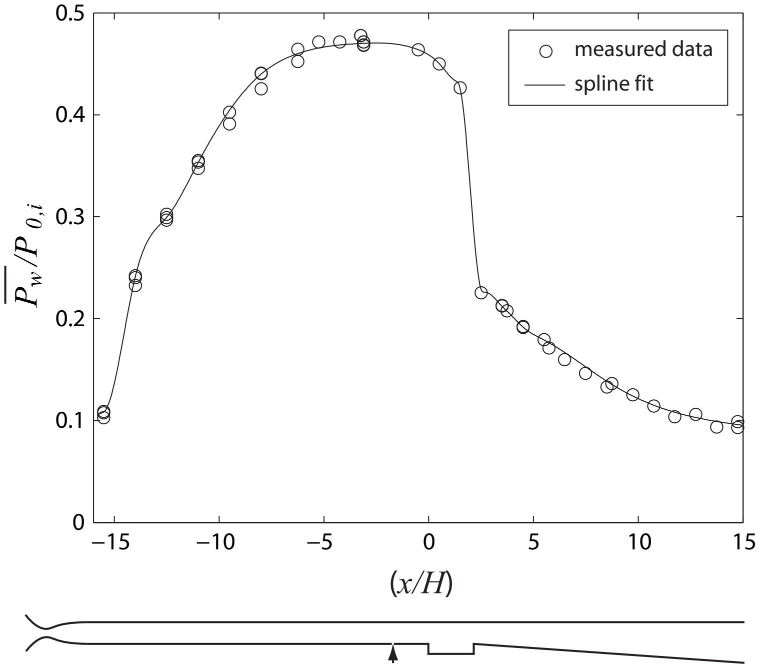

(b) Case 2B.

Figure 5.1: Mean wall pressure distribution for cases 1B (cavity stabilized) and 2B (jet-wake stabilized) with spline fit used in the data analysis model.

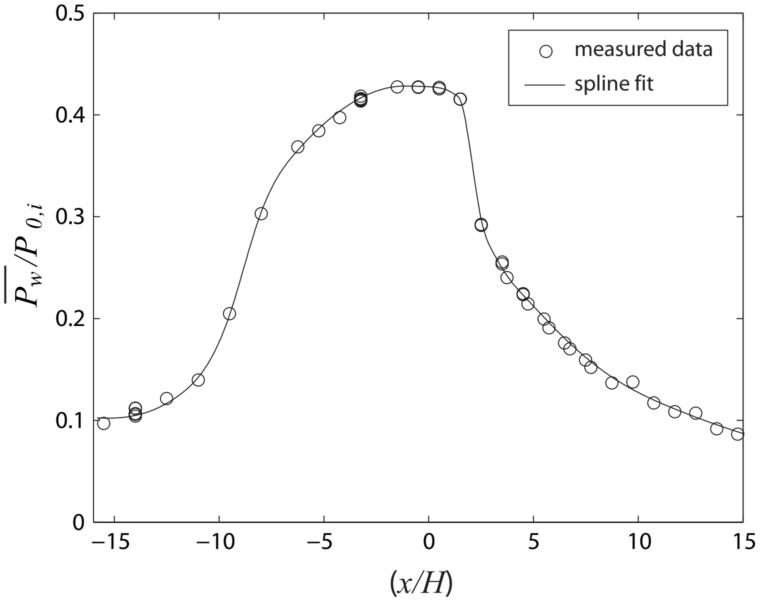

(a) Case 1H.

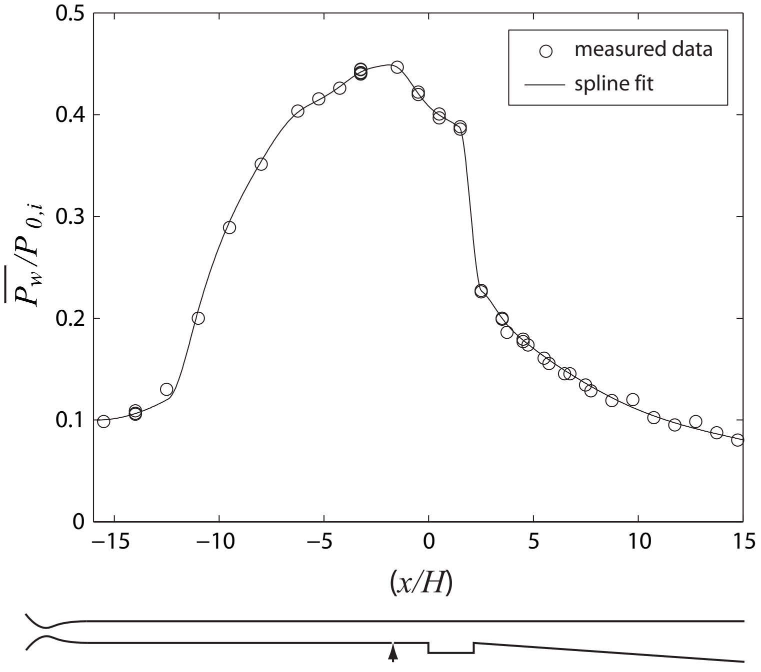

(b) Case 2H.

Figure 5.2: Mean wall pressure distribution for cases 1H (cavity stabilized) and 2H (jet-wake stabilized) with spline fit used in the data analysis model.

progress variable that is defined as:

$$\eta_c(x) = \frac{\dot{m}_{fuel,burned}(x)}{\dot{m}_{fuel,injected}} \tag{5.1}$$

Skin friction and heat transfer to the wall were calculated using the van Driest method and Reynolds analogy. Details of the one-dimensional data analysis model are given in Appendix A.

The biggest source of uncertainty in the one-dimensional data analysis model is due to heat transfer to the wall. There is no data available for the wall temperatures in the combustor. Due to the relatively short runs times, the combustor is not in thermal equilibrium, and the heat transfer is expected to be significant. The overall combustion efficiency calculated by the model is quite sensitive to the heat transfer to the wall. Figures 5.3-5.6 show the calculated combustion efficiency for cases 1B-2H for assumed constant wall temperatures of $T_{0,air} - 100K, T_{0,air}$, and $T_{0,air} + 100K$. It can be seen that the overall combustion efficiency varies significantly over this range of wall temperatures, and thus cannot be reliably calculated by the model with the available information (The calculated values of $\eta_c > 1$ are non-physical results that are allowed by the model solution as discussed in Appendix A).

The axial derivative of the combustion efficiency ($d\eta_c/dx$) is a measure of the heat release rate per unit length. This quantity is also shown in Figs. 5.3-5.6 for cases 1B-2H. It can be seen that this curve is shifted up or down for varying wall temperatures, but the shape remains fixed. There are some general trends from these curves that are consistent with the OH* and CH* distributions discussed in Sec. 5.3. The heat release generally peaks over the cavity and decreases at the trailing edge. Jet-wake stabilized combustion has a more highly peaked heat release distribution than cavity stabilized combustion. The heat release distribution curves shown in 5.3-5.6 are much less smooth than those found from the CH* and OH* in

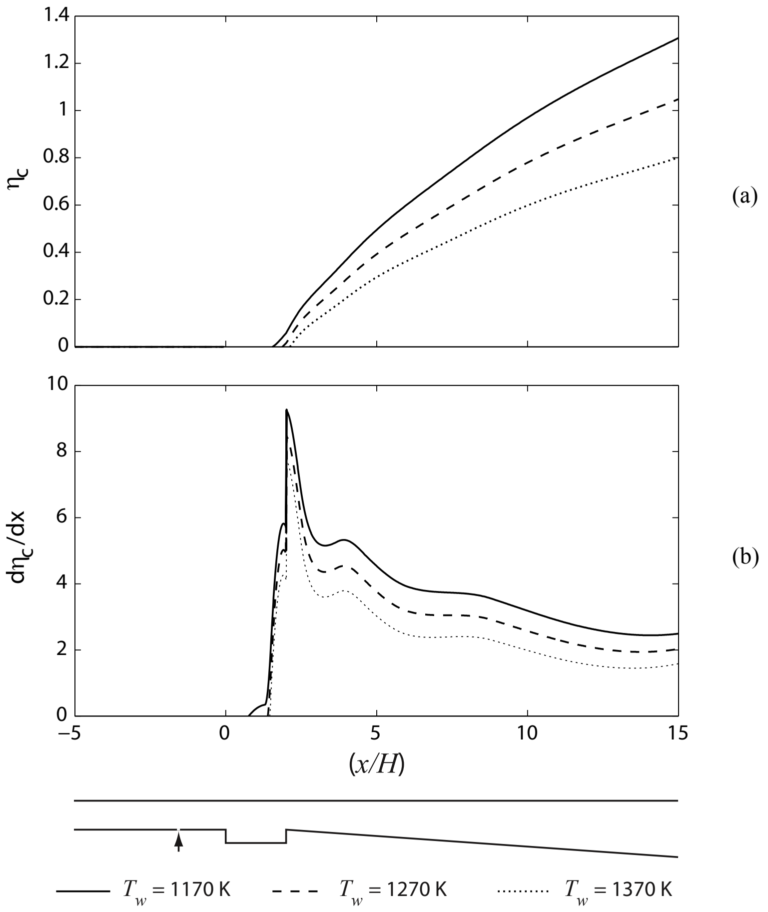

Figure 5.3: Case 1B distribution of combustion efficiency and its axial derivative calculated by the 1-D data analysis model (from the measured wall pressure) with different assumed (constant) wall temperatures.

Sec. 5.3 though. As a derivative quantity, $d\eta_c/dx$ is sensitive to the derivative of the pressure distribution $(dP(x)/dx)$. Due to the discrete nature of the wall pressure data, this quantity is not known accurately in some areas. This is particularly true in regions where the pressure changes quickly, such as near the cavity trailing edge. Additionally, the 1-D model cannot properly account for the sudden changes across shock waves. Both these issues lead to artifacts such as negative values of $d\eta_c/dx$ near the cavity trailing edge in Figs. 5.4 and 5.6.

The distributions of Mach number, velocity, density, and static temperature predicted by the 1-D data analysis model are shown in Figures 5.7 and 5.8 for cases

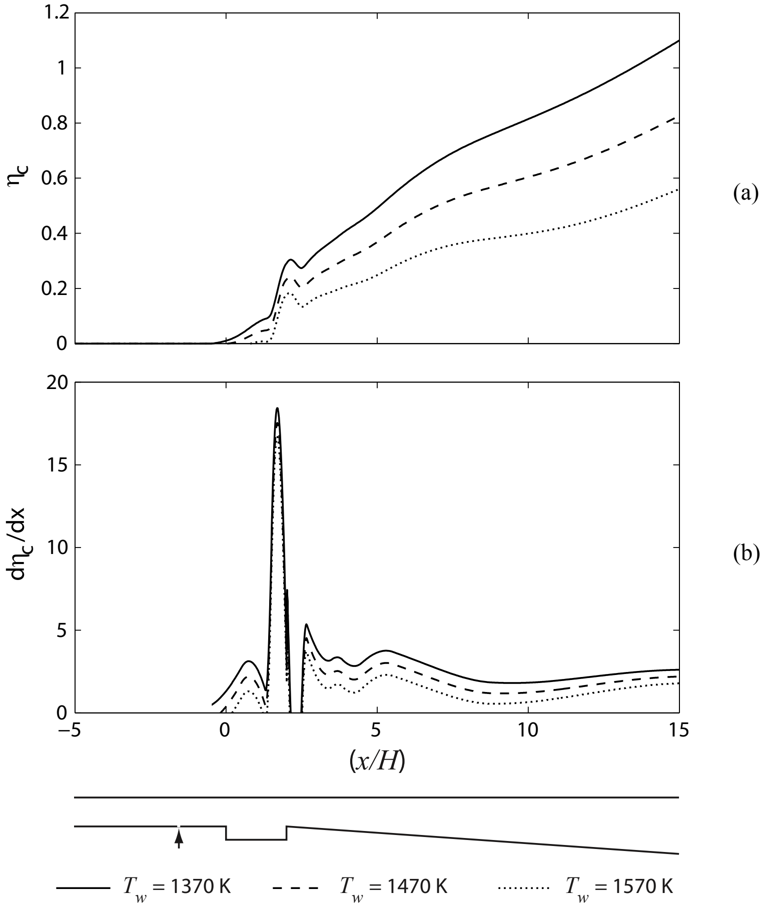

Figure 5.4: Case 2B distribution of combustion efficiency and its axial derivative calculated by the 1-D data analysis model (from the measured wall pressure) with different assumed (constant) wall temperatures.

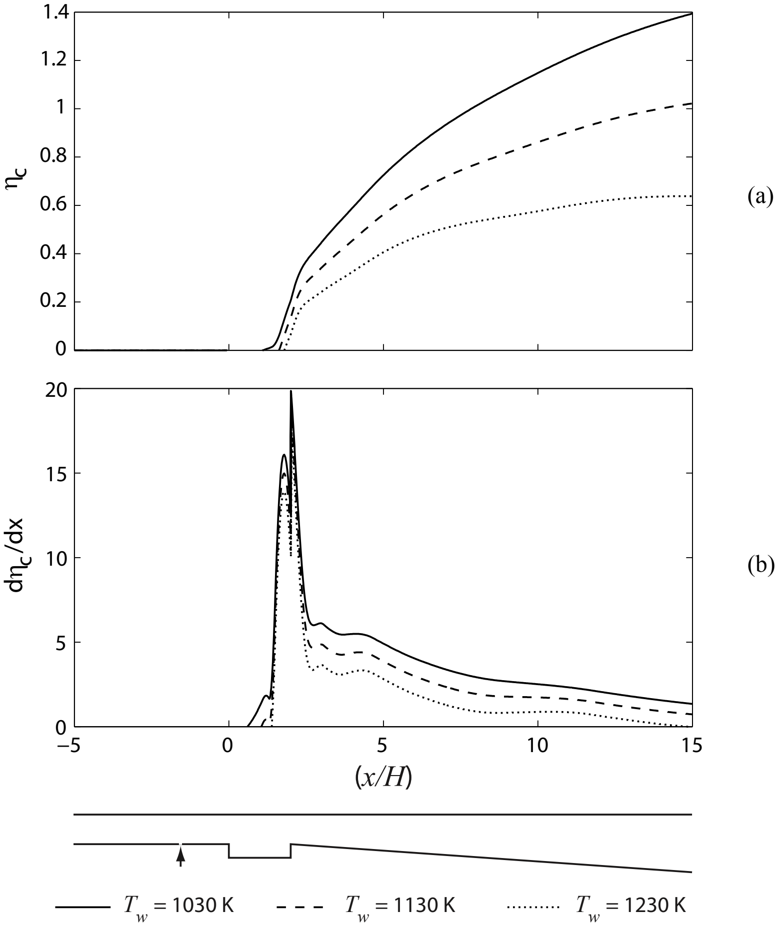

Figure 5.5: Case 1H distribution of combustion efficiency and its axial derivative calculated by the 1-D data analysis model (from the measured wall pressure) with different assumed (constant) wall temperatures.

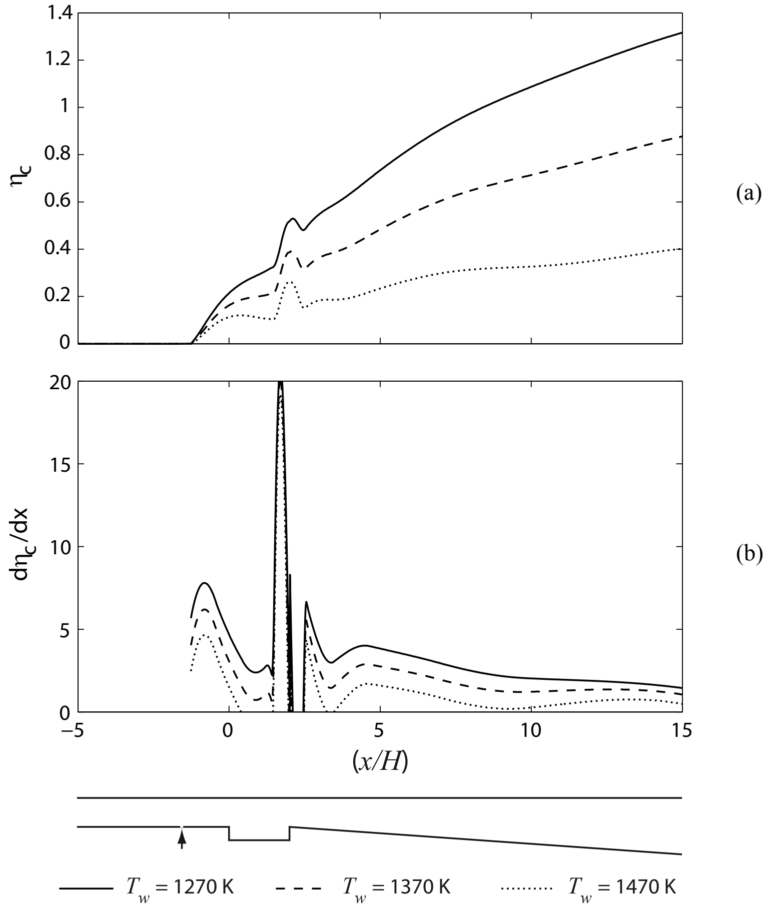

Figure 5.6: Case 2H distribution of combustion efficiency and its axial derivative calculated by the 1-D data analysis model (from the measured wall pressure) with different assumed (constant) wall temperatures.

1B-2H. These distributions are virtually independent of the heat transfer to the wall. The calculated local rate of heat release offsets any change in heat transfer to the wall. The temperature field is nearly independent of the wall temperature (except for very minor differences caused by changes in the average molecular weight). Thus the distribution of these variables can be used with a degree of confidence.

In all cases the thermal throat (M=1 location) is predicted by the 1-D model to be located near the beginning of the diverging section, just behind the cavity trailing edge. For jet wake stabilized combustion (case 2B, and 2H), the thermal throat is located further upstream than for cavity stabilized combustion (case 1B and 1H). The Mach number, velocity, and density change more abruptly at the choked point for jet-wake stabilized combustion. The static temperature is virtually unchanged through the combustion region for the jet-wake stabilized cases, and rises slightly for the cavity stabilized cases. The increase in stagnation temperature from the reaction is mostly offset by the increase in Mach number (which decreases T/T_0). It should be noted that the variables shown in Figs. 5.7 and 5.8 are mixture averaged 1-D results and are not necessarily representative of any local conditions. The step change in static temperature and density observed near the injection location is due to the instantaneous addition and mixing of room temperature fuel in the model. The results shown in Figs. 5.7 and 5.8 are useful for interpreting the OH* and CH* luminosity results in Sec. 5.3.

5.3 OH* and CH* Distributions

As discussed in Sec. 2.4.2, the heat release rate has been shown to be proportional to OH* and CH* luminosity in several previous studies. If this holds true everywhere in the test section, the 1-D OH* and CH* results ($I_{OH^*}(x)$ and $I_{CH^*}(x)$) presented are

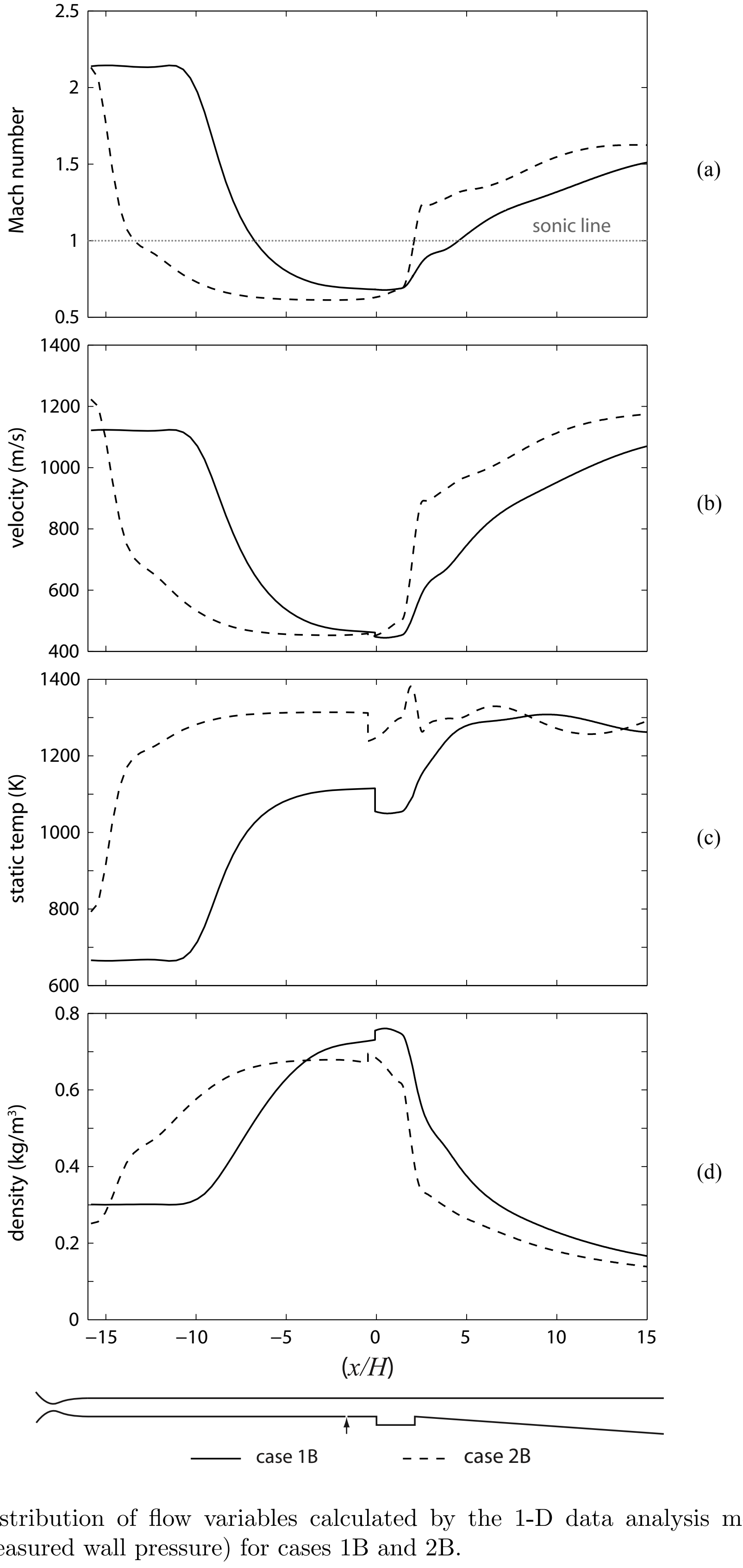

Figure 5.7: Distribution of flow variables calculated by the 1-D data analysis model (from the measured wall pressure) for cases 1B and 2B.

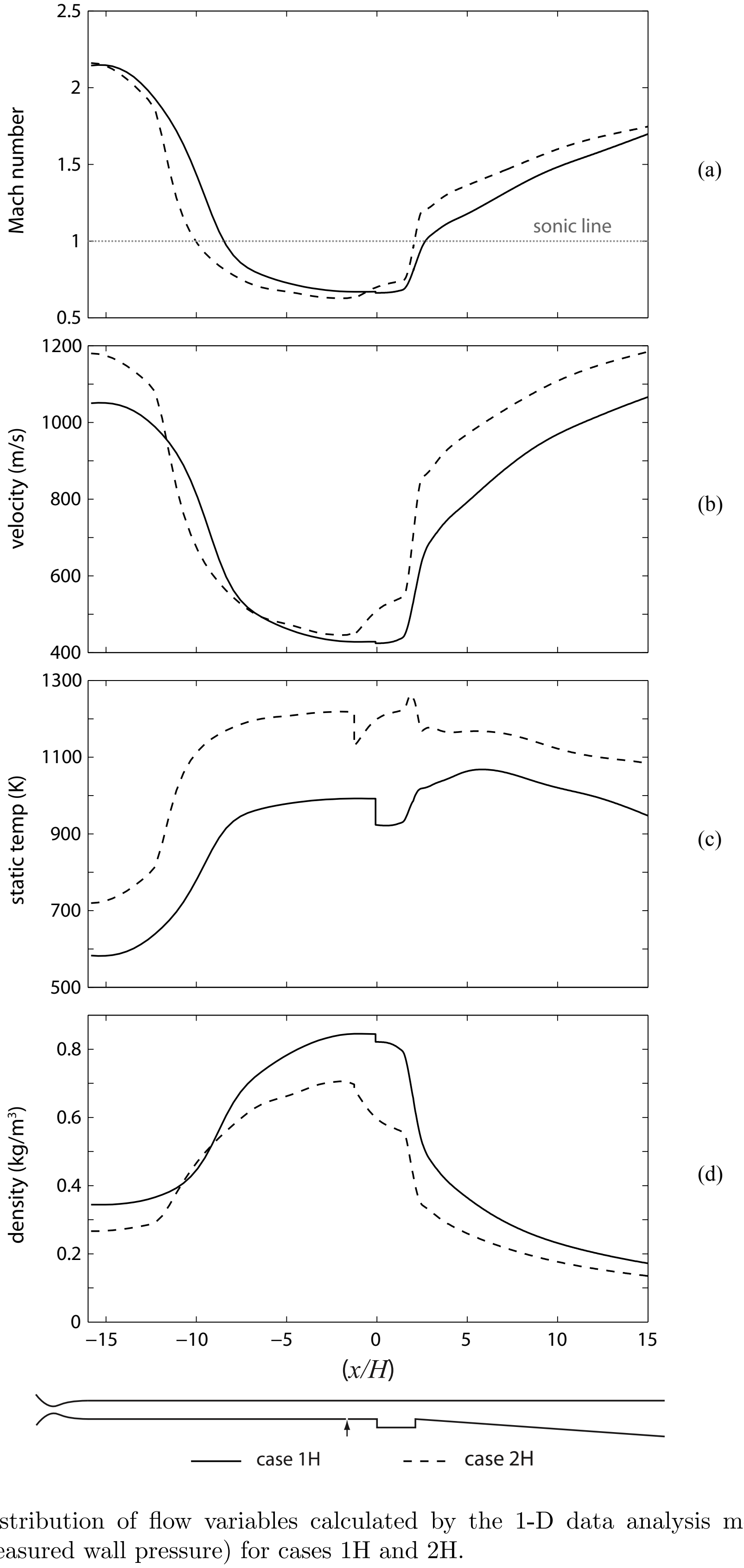

Figure 5.8: Distribution of flow variables calculated by the 1-D data analysis model (from the measured wall pressure) for cases 1H and 2H.

proportional to the 1-D distribution of heat release per unit length, $\dot{Q}(x)$. However care must be taken in interpreting the results quantitatively, since it is unclear how relationship between the intensity of OH* (and CH*) and heat release varies with changes in local temperature, pressure, and strain rate.

5.3.1 Comparison of OH* and CH* Results

The mean CH* and OH* images for cases 1B and 2B are shown in Figs. 5.9 and 5.10. There are no major differences in the shape or size of the reaction zone as indicated by the CH* and OH*. The 1-D signal obtained from these images is shown in Fig. 5.11. The signals are normalized by the area under the curve, which is proportional to the total heat release. There is relatively little difference between the distribution of I_{OH^*} and I_{CH^*} in these figures. As discussed in Sec. 2.4.2, CH exists only in regions of local heat release, and thus is likely to be a good marker of the heat release distribution in this very high speed flow. Ground state OH can persist downstream in the hot products and does not mark the local heat release. Chemiluminescence from hydroxyl, however, from the electronically excited state denoted as OH* [44]. OH* is produced in the heat release layer and has a lifetime based on the collisional quenching rate, which is generally very fast [94]. OH* then is confined to regions of local heat release and does not persist far downstream in the hot products. Figure 5.11 shows relatively minor differences between the distribution of I_{OH^*} and I_{CH^*} for case 1B and 2B. Thus OH* is likely a reasonable marker of the heat release distribution under these conditions.

5.3.2 Cavity Stabilized Combustion

The mean OH* images for cases 1B and 1H are shown in Figs. 5.10(a) and 5.12(a). As discussed in Sec. 3.1.1.2, the cavity stabilized reaction zone begins at

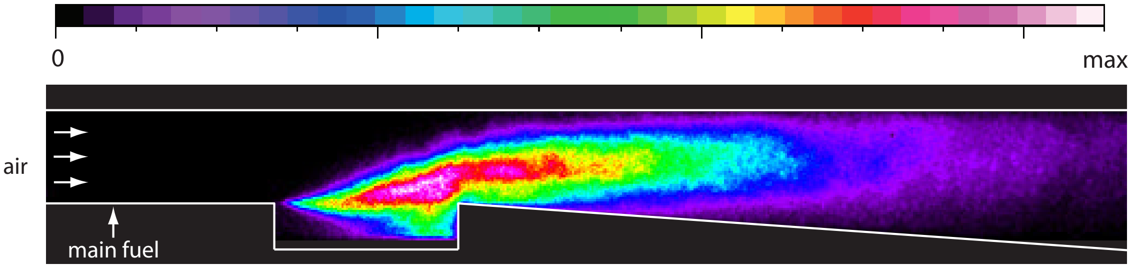

(a) Case 1B.

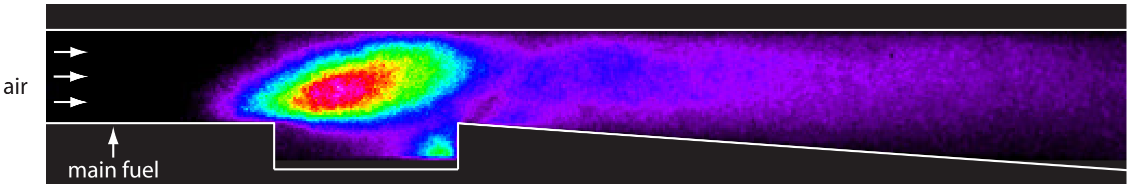

(b) Case 2B.

Figure 5.9: Mean CH* luminosity for case 1B and 2B conditions shown in false color.

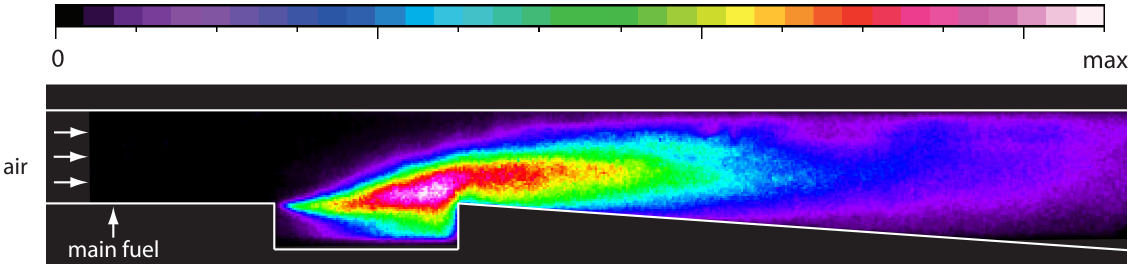

(a) Case 1B.

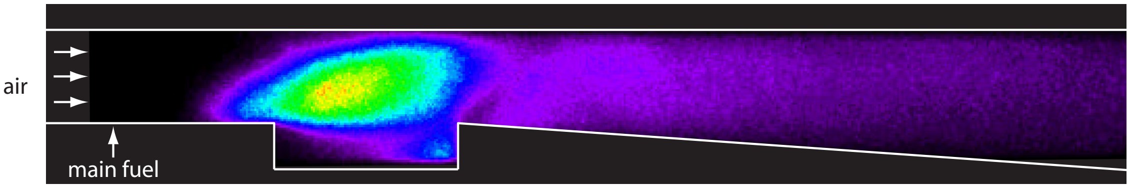

(b) Case 2B.

Figure 5.10: Mean OH* luminosity for case 1B and 2B conditions shown in false color.

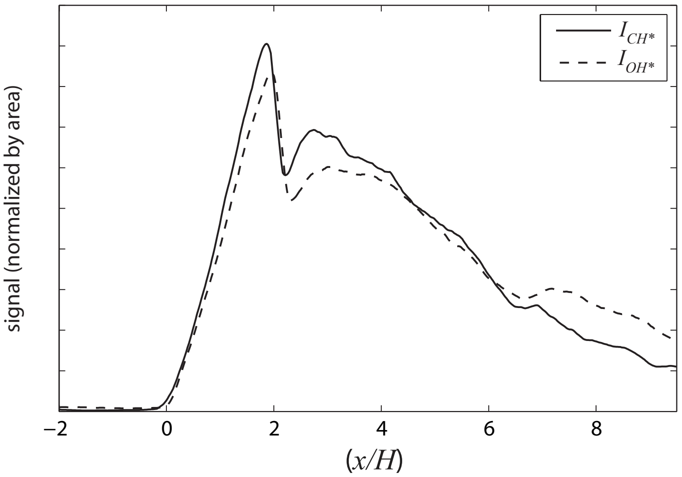

(a) Case 1B.

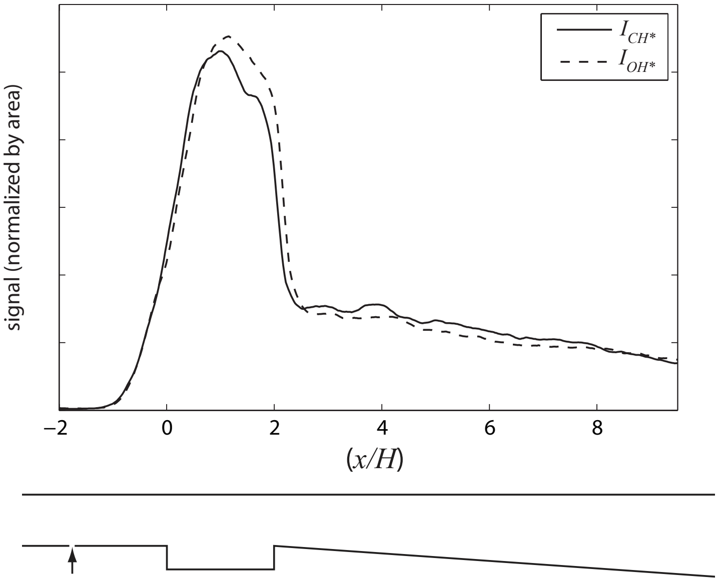

(b) Case 2B.

Figure 5.11: 1-D CH* and OH* signals for cases 1B and 2B. Signals are normalized by the area under the curve ($\int I_{OH^*} dx$ and $\int I_{CH^*} dx$).

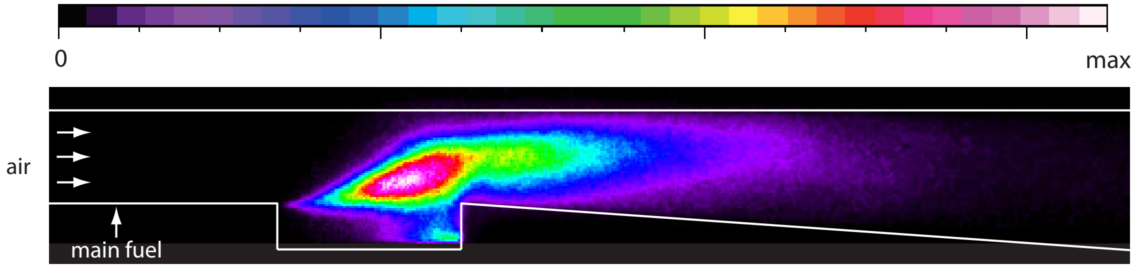

(a) Case 1H.

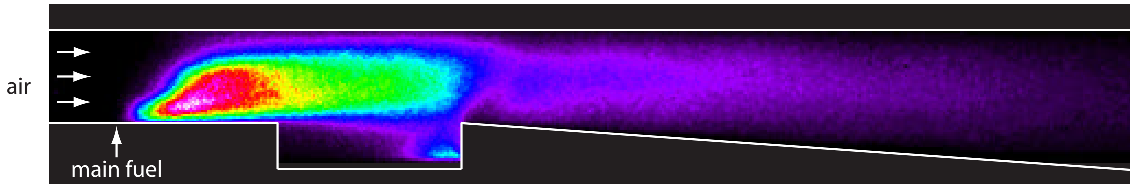

(b) Case 2H.

Figure 5.12: Mean OH* luminosity for case 1H and 2H conditions shown in false color.

the upstream edge of the cavity shear layer and spreads into the premixed reactants at an approximately constant angle (initially). The spreading angle is determined by the flame speed and the flow speed. At downstream locations, the spreading angle decreases as the flow velocity increases (shown in Figs. 5.7 and 5.8).

The 1-D OH* signals are shown in Fig. 5.13. For both cavity stabilized cases, I_{OH^*} increases approximately linearly in the x direction over the cavity. As with the 1-D model results, the decrease in I_{OH^*} starts near the cavity trailing edge. The decrease in the heat release indicated by the I_{OH^*} signal at this location is much less abrupt than that indicated by the model. Near the rear of the window I_{OH^*} from the cavity stabilized mode approaches that of the jet wake stabilized mode. For both cavity stabilized modes, there is a trend of consistent decreasing OH* signal behind the cavity trailing edge. In addition to this consistent trend, there is locally decreased I_{OH^*} signal for $2 \lesssim x/H \lesssim 3$.

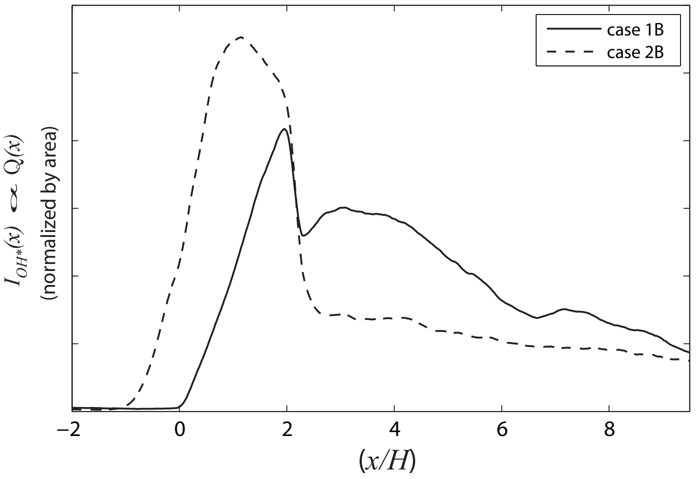

(a) Blended fuel (case 1B and 2B).

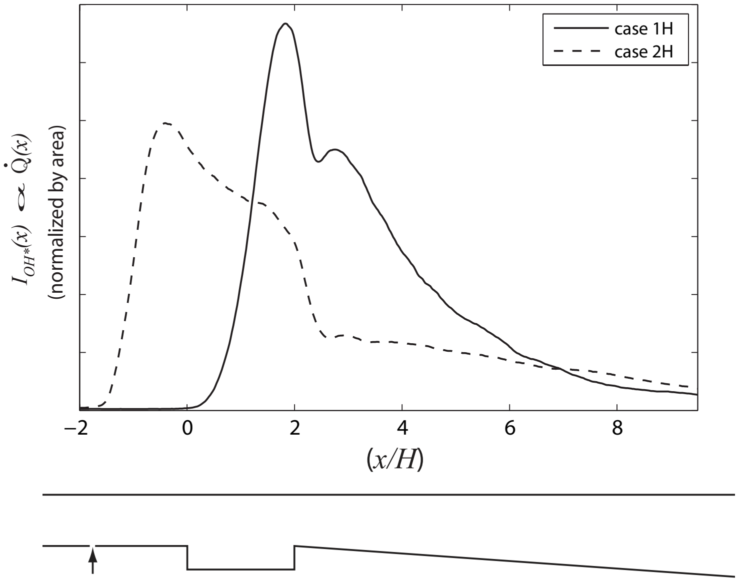

(b) Hydrogen fuel (cases 1H and 2H).

Figure 5.13: 1-D OH* signals for cases 1B, 2B, 1H, and 2H. Signals are normalized by the area under the curve ($\int I_{OH^*} dx$).

5.3.3 Jet-Wake Stabilized Combustion

The mean OH* images for cases 2B and 2H are shown in Figs. 5.10(b) and 5.12(b). The 1-D OH* signals are shown in Fig. 5.13. As seen in the flame luminosity images in Sec. 3.1.1, the jet-wake stabilized reaction zones begin upstream of the cavity stabilized ones. At the start of the reaction zone, I_{OH^*} increases quickly to the peak value. The reaction zone leading edge and the peak I_{OH^*} location occur farther downstream for case 2B than case 2H. Behind the peak I_{OH^*} location, the signal decreases gradually until the cavity trailing edge, where it decreases very sharply. Behind the cavity trailing edge, I_{OH^*} decreases slowly and does not reach zero by the end of the window.

5.3.3.1 Effect of Varying $T_{0,air}$

Figure 5.14 shows the mean OH* images for data set E conditions. For these cases, ϕ remains fixed and $T_{0,air}$ is varied from 1220 K to 1520 K. It can be seen that the lower reaction zone leading edge appears to be attached to the fuel injection jet for all temperatures. The upper side of the reaction zone leading edge moves downstream as $T_{0,air}$ decreases. This is different than the behavior observed during the flame luminosity imaging discussed in Sec. 3.1.1.3, where the entire reaction zone leading edge moved as $T_{0,air}$ was varied. This hysteresis in the stabilization location is most likely due to the wall temperature. The OH* images in set E, were acquired in one day. The first run was at $T_{0,air} = 1520$ K, which is over 100 K higher than any data acquired during the hydrogen fuel high speed flame luminosity imaging discussed in Sec. 3.1.1.3. $T_{0,air}$ was then decreased by approximately 40 K for each subsequent run, but the cooling time between runs was significantly shorter than usual. Thus the wall temperature for the set E OH* imaging was likely much higher than it was for sets A-C in Sec. 3.1.1.3. This allowed the lower edge of the reaction zone to remain attached to the fuel jet.

The 1-D OH* signals for set E are shown in Fig. 5.15(a). The basic shape of the I_{OH^*} distribution is the same as that seen for case 2H. The reaction zone starts in the same location for all cases due to the attached stabilization location. However the I_{OH^*} signal rises more slowly for the lower $T_{0,air}$ cases, causing the peak I_{OH^*} value to occur further downstream. Near the cavity trailing edge, all the I_{OH^*} signals drop sharply. Further downstream the signals for all cases are virtually identical. The highest temperature case does have slightly lower I_{OH^*} signal behind the cavity trailing edge.

The decrease in OH* signal near the cavity trailing edge clearly is a prominent feature of the jet-wake stabilized combustion. Part of this decrease is due to the abrupt end of any reaction in the cavity at this location. It is useful to separate this effect from the decrease in main flow reaction rate. Figure 5.15(b) shows the 1-D OH* data for set E with the contribution from the cavity reaction excluded. In this figure it can be seen that the OH* is already decreasing quickly before the cavity trailing edge, but there is still a pronounced decrease at this location.

5.3.3.2 Effect of Varying ϕ

Figure 5.14 shows the mean OH* images for data set F conditions. For these cases $T_{0,air}$ is fixed and ϕ is varied from 0.23 to 0.36. The shape of the reaction zone has the same general appearance in all cases. Figure 5.17 shows the 1-D OH* signals for each of these cases with and without the cavity reaction included. In the upstream region up to the peak I_{OH^*} value, the profiles are virtually identical for all cases in set F. Downstream of the peak I_{OH^*} location, the I_{OH^*} signal decreases more quickly for the lower ϕ cases. Near the cavity trailing edge, the I_{OH^*} signal drops sharply

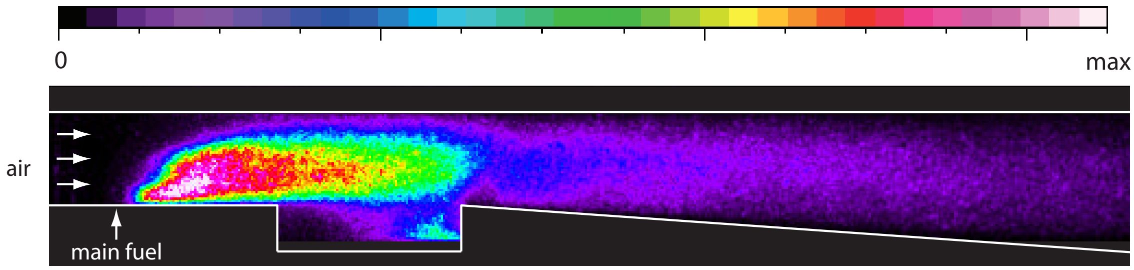

(a) $T_{0,air} = 1520\text{K}$.

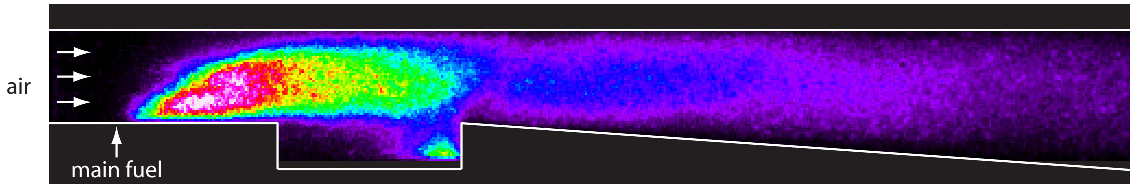

(b) $T_{0,air} = 1410\text{K}$.

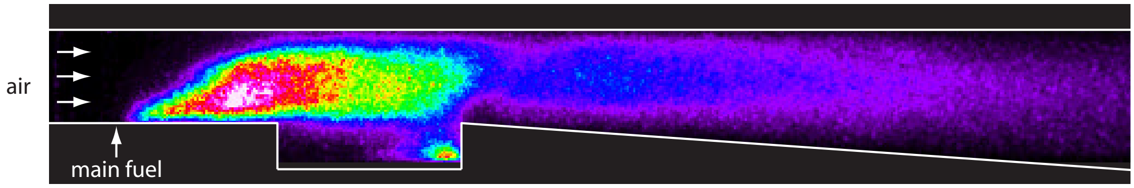

(c) $T_{0,air} = 1270\text{K}$.

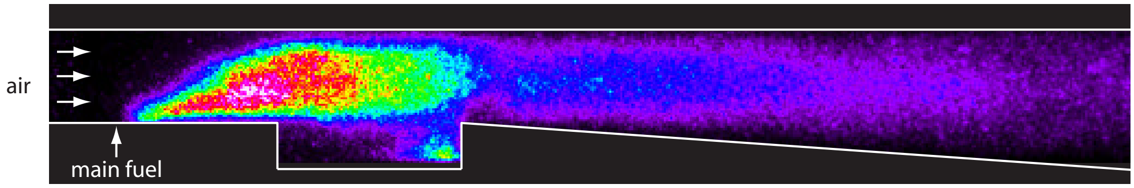

(d) $T_{0,air} = 1220\text{K}$.

Figure 5.14: Mean OH* luminosity for data set E shown in false color. Conditions are listed in Table 5.1.

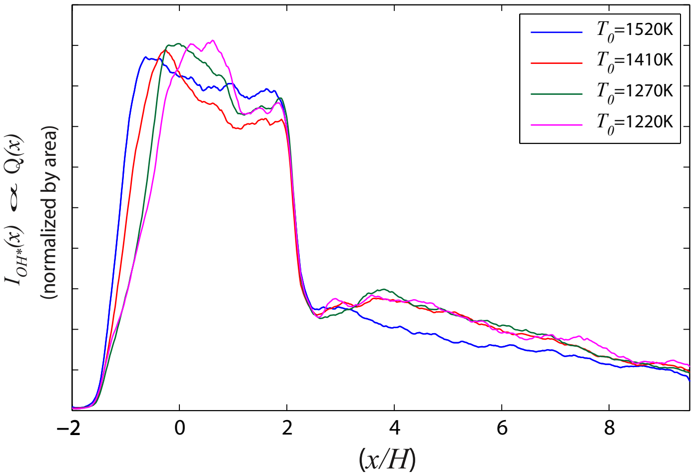

(a) Including cavity signal.

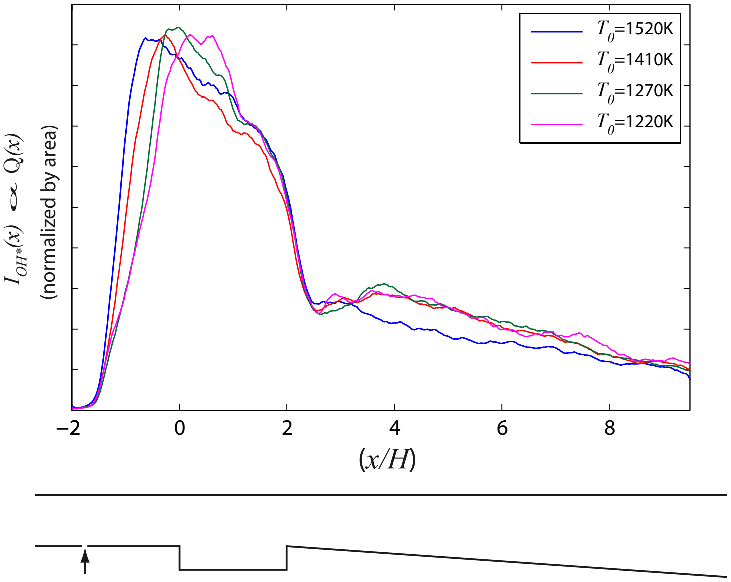

(b) Excluding cavity signal.

Figure 5.15: 1-D OH* signals for data set E with and without the signal from the wall cavity included. $T_{0,air}$ is varied. Signals are normalized by the area under the curve ($\int I_{OH^*}dx$).

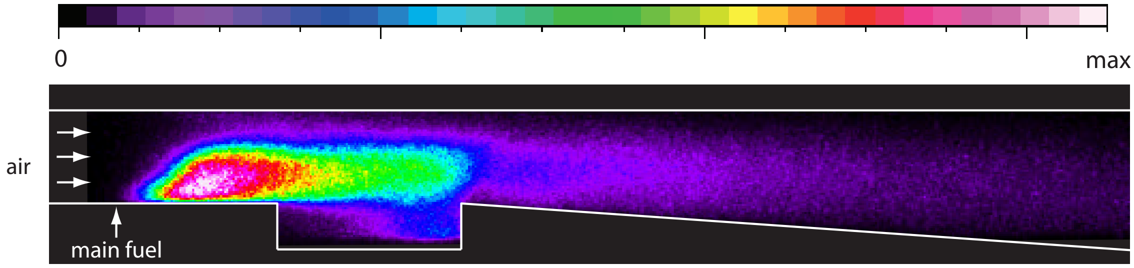

(a) $\phi = 0.23$.

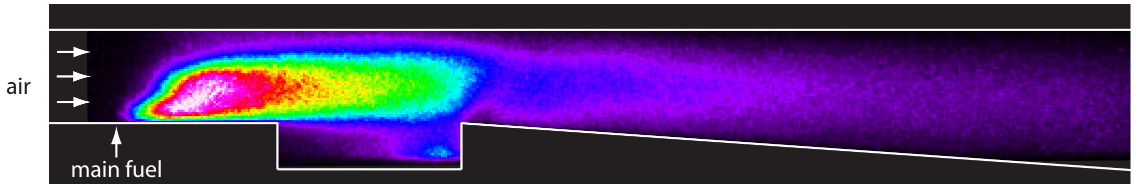

(b) $\phi = 0.26$.

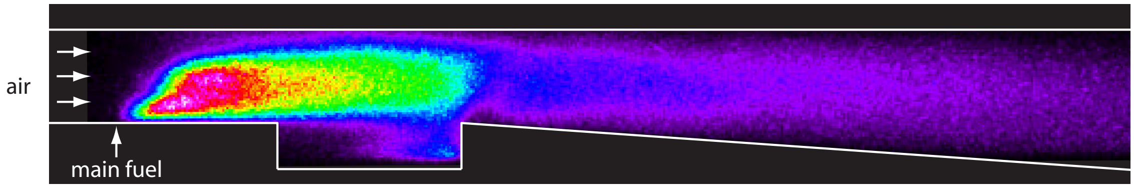

(c) $\phi = 0.30$.

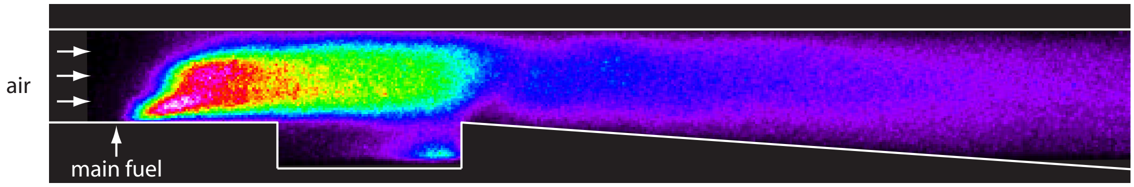

(d) $\phi = 0.36$.

Figure 5.16: Mean OH* luminosity for data set F shown in false color. Conditions are listed in Table 5.1.

for all cases.

The I_{OH^*} signals in Fig. 5.17 were not normalized by the area under the curve as in the previous 1-D OH* figures. The area under the I_{OH^*} curve is proportional to the total heat release rate, assuming that the local heat release rate per unit volume ($\dot{q}$) is proportional to the intensity of OH* emissions per unit volume (e_{OH^*}). The accuracy of this assumption can be evaluated by examining the change in area under the $I_{OH^*}(x)$ curves for set F. Because the end of the reaction zone occurs past the

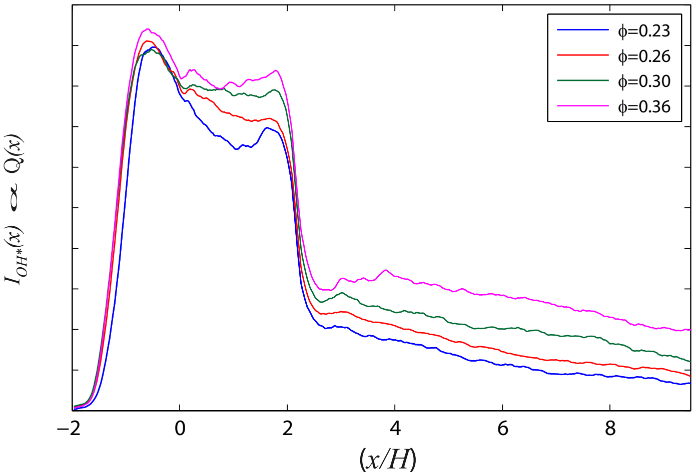

(a) Including cavity signal.

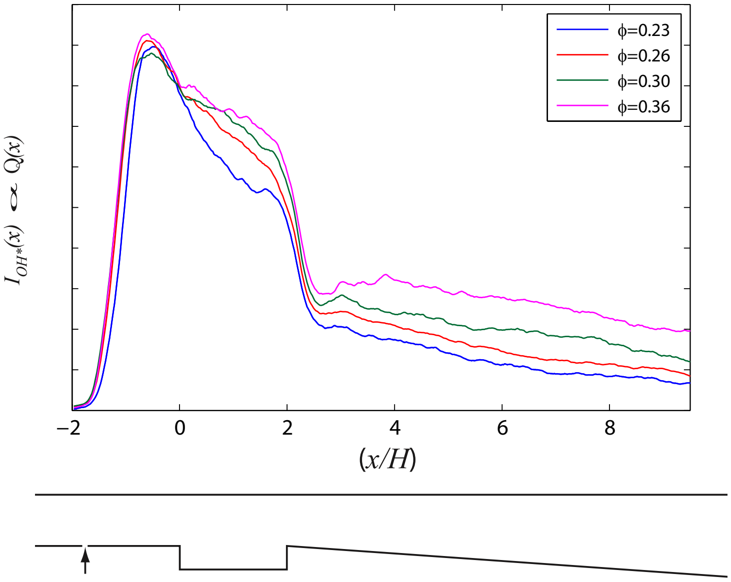

(b) Excluding cavity signal.

Figure 5.17: 1-D OH* signals for data set F with and without the signal from the wall cavity included. Equivalence ratio is varied.

end of the window, the $I_{OH^*}(x)$ data for each case was extrapolated until it reached zero. A linear regression fit was used for this extrapolation since the I_{OH^*} signal decreased roughly linearly behind the cavity trailing edge. The results are shown in Fig. 5.18. The area under these curves ($\int I_{OH^*}dx$) is plotted as a function of ϕ in Fig. 5.19 along with a linear best fit line that passes through the origin. It can be seen that the area under the $I_{OH^*}(x)$ curves increases linearly with ϕ. Thus the assumption of the proportionality of the OH* emissions to heat release rate appears to be relatively good for the current conditions.

The extrapolated OH* curves in Fig. 5.18 also can be used to obtain the flame length as a function of ϕ, which is plotted in Fig. 5.20. The measure of flame length used in this figure ($l_{90\%}$) is the distance between the fuel injection and the location where the area under the extrapolated $I_{OH^*}(x)$ curve is 90% of the total area. This is equal to the distance where 90% of the heat release has occurred if the heat release is proportional to the OH* chemiluminescence.

5.4 Factors Controlling the Heat Release

5.4.1 Jet-Wake Stabilized Combustion

The measured heat release distribution for jet-wake stabilized combustion is consistent with the description of a lifted diffusion flame that appeared in Secs. 3.1.1.3 and 4.4. The initial peak in heat release rate per unit length ($\dot{Q}$) indicated by I_{OH^*} corresponds to the premixed flame base where the fuel that has premixed with air in the lift-off distance is consumed. After the end of the premixed flame base, the combustion is mixing limited. These regions are illustrated in Fig. 5.21.

The changes observed when $T_{0,air}$ and ϕ were varied are consistent with this description. Changes in the temperature affect the stabilization and spreading of the premixed flame base, but have little effect on the mixing field. Therefore the

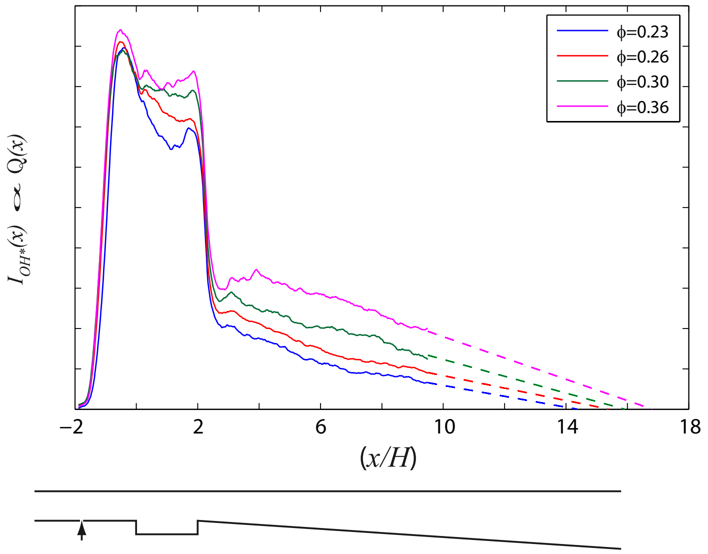

Figure 5.18: 1-D OH* signal for data set F (solid lines) and extrapolated linear best fit lines (dashed lines). Data was acquired up to the end of the window at approximately $x/H = 9.5$. Linear regression lines fit to the data from $x/H = 5.5$ to 9.5 are shown as dashed lines for $x/H > 9.5$.

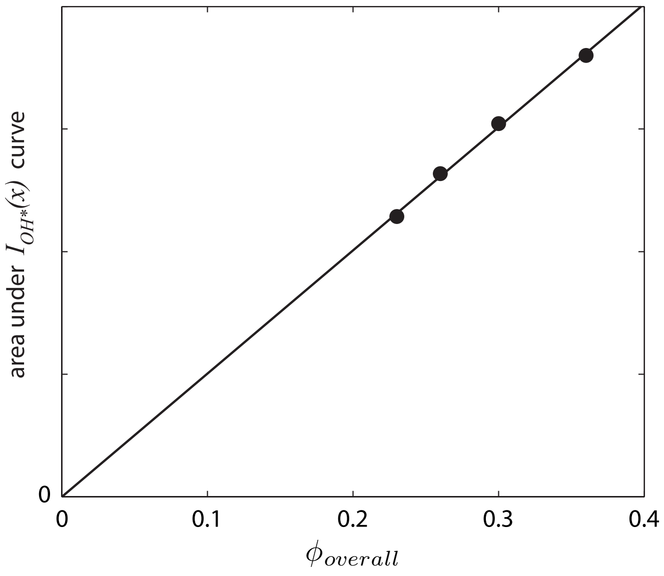

Figure 5.19: Total area under the extrapolated $I_{OH^*}(x)$ curves in Fig. 5.18 vs. the overall equivalence ratio. A linear regression fit which passes through origin is shown as a solid line.

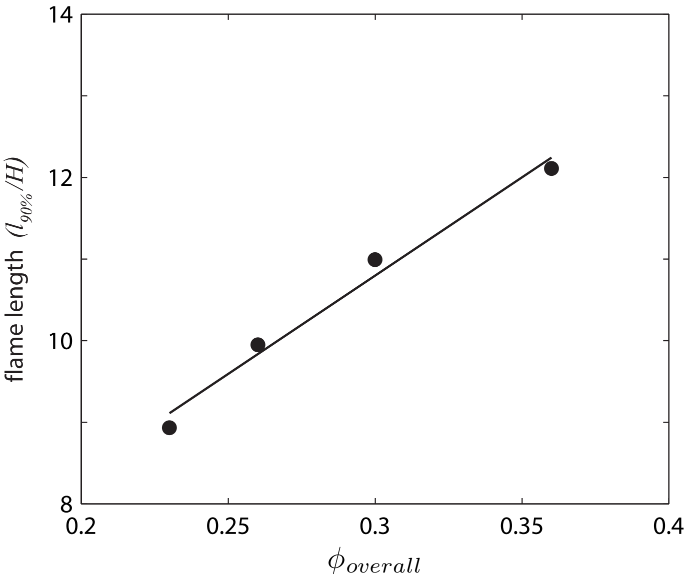

Figure 5.20: Measured flame length vs. ϕ for data set F conditions. The flame length $l_{90\%}$ is the distance between the fuel injection location and the location where the area under the $I_{OH^*}(x)$ curve shown in Fig. 5.18 is 90% of the total area. This is approximately equal to the length it takes for 90% of the heat release to occur. A linear regression fit is shown as a solid line.

upstream part of the heat release distribution is affected by changes in $T_{0,air}$ while the mixing limited downstream region is not. This result is not consistent with the downstream reaction being finite rate kinetics limited. As discussed in Sec. 4.3.2, the premixed flame base consists of a ring around the perimeter of the fuel jet. This ring forms the base of a rich premixed flame cone in the interior of the jet. As $T_{0,air}$ is decreased in data set E, the premixed flame spreading from the stabilization point around the jet perimeter slows. This moves the upper edge of the flame base downstream. The downstream end of the premixed flame region occurs near $x/H = 1.5$ for the lowest temperature case in Fig. 5.15. As ϕ is varied, the overall flame length changes due to changes in the stoichiometric mixing length. Both of these trends are consistent with the physical concept of a lifted diffusion flame.

The sharp decrease in I_{OH^*} signal near the cavity trailing edge in all cases also is explained by the above description. As seen in Figs. 5.7 and 5.8, the thermal throat

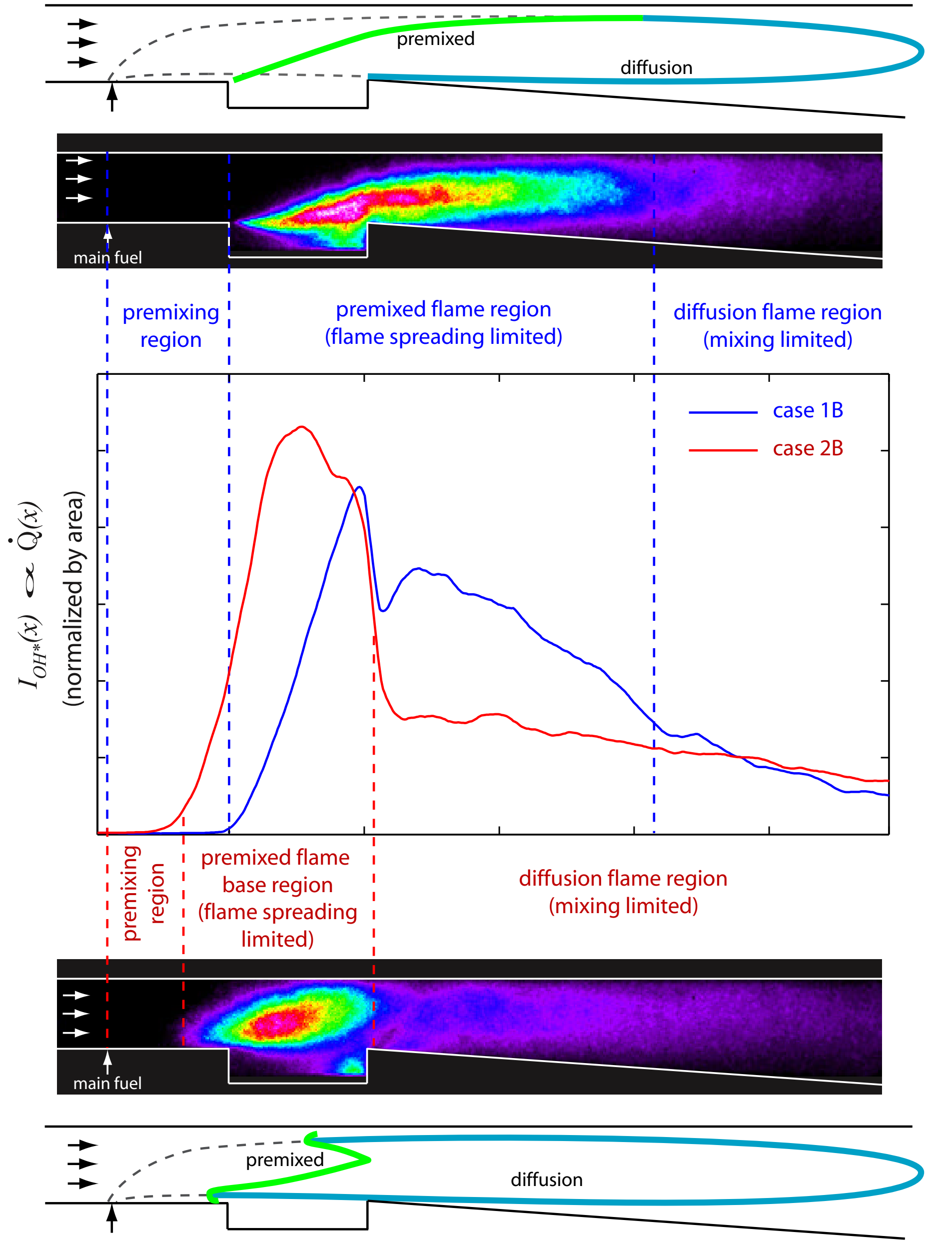

Figure 5.21: Illustration of the factors limiting the heat release rate in different regions for cavity (case 1B) and jet-wake stabilized combustion (case 2B).

is located shortly downstream of the cavity trailing edge in all cases. Across this throat there is a very large increase in velocity, a large decrease in density, and a modest decrease in static temperature for the jet-wake stabilized combustion cases. In a diffusion flame a decrease in reaction rate would be caused by a decrease in the fuel-air mixing rate. An estimate of the change in mixing rate can be obtained from the similarity solution for co-flowing jets since the fuel jet is turned to be nearly parallel to the air stream by the cavity trailing edge. The rate of fuel-air mixing then can be estimated to be proportional to the mass entrainment rate of a co-flowing jet. The mass flow rate contained in a co-flowing jet is given by Han and Mungal [45] as:

$$\dot{m}(x) = C_1 \rho_c u_c \delta^2 + C_2 \rho_c u_\infty \delta^2 \tag{5.2}$$

In the far field, the wake similarity solution applies for which u_c and δ are given by: 5.4.

$$\frac{u_c}{u_\infty} = (C_u)_w \left(\frac{x}{\theta}\right)^{-2/3} \tag{5.3}$$

$$\frac{\delta}{\theta} = (C_\delta)_w \left(\frac{x}{\theta}\right)^{1/3} \tag{5.4}$$

$$\theta^2 = \frac{J_0}{\rho_\infty U_\infty^2 \pi} \tag{5.5}$$

J_0 is the initial momentum mass flux of the co-flowing jet, or drag in the case of the transverse jet. Making the assumption that $u_c = u_\infty$ in the far field yields the following expression for the mass flow rate contained in the jet as a function of x.

$$\dot{m}(x) = C_3 \frac{J_0}{u_\infty} + C_4 \rho_\infty^{1/3} \frac{J_0^{2/3}}{u_\infty^{1/3}} x^{1/3} \tag{5.6}$$

The entrainment rate is obtained by differentiating the mass flow rate with respect to x.

$$\frac{d\dot{m}}{dx} \propto C_5 \left(\frac{\rho_\infty}{u_\infty}\right)^{1/3} J_0^{2/3} x^{-1/3} \tag{5.7}$$

Hasselbrink and Mungal [50, 51] found the same scaling of entrainment rate with respect to ρ_∞ and u_∞ for the far field of a jet in crossflow.

Thus for a fixed jet drag and location, Eq. 5.7 indicates that the mixing rate will decrease as u_∞ increases or ρ_∞ decreases. Therefore the heat release rate for a diffusion flame would be expected to decrease quickly as the gas passes through the thermal throat. We can attempt to account for this decreased mixing rate by multiplying I_{OH*} by $u^{1/3}/\rho^{1/3}$. If the mixing rate is directly proportional to the mass entrainment rate given by 5.7, then this factor should exactly offset the decreased mixing rate that occurs through the thermal throat. Two of these modified $I_{OH^*}(x)$ curves are shown in Fig. 5.22 with $u(x)$ and $\rho(x)$ obtained from the 1-D data analysis model of Sec. 5.2. It can been seen that this mixing correction factor reduces the decrease in signal that is seen at the rear edge of the cavity, but it does not eliminate it. The correction is based on several approximations that do not apply perfectly to the actual combustor flowfield however.

5.4.2 Cavity Stabilized Combustion

The heat release distribution of the cavity stabilized combustion mode is consistent with the premixed flame description from Secs. 3.1.1.2 and 4.4. A flame sheet spreading from the cavity leading edge consumes the premixed fuel-air in the jet-wake from the bottom up. The heat release rate initially increases in the x-direction due to the vertical distribution of fuel in the jet-wake. An example of this fuel distribution may be obtained from the non-reacting CFD++ solution for case 1H conditions. The chemistry was turned off to obtain the non-reacting solution. The fuel concentration in the cross-section of the jet-wake at $x/H = 1.0$ from this solution is shown in Fig. 5.23. The mass flow rate of fuel per unit height through this plane ($\dot{m}_f(y)$) is also shown. $\dot{m}_f(y)$ is calculated by integrating the fuel mass flux through

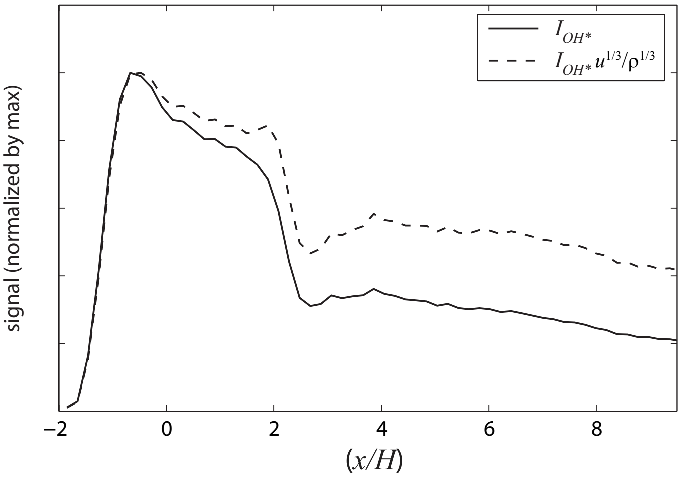

(a) Set E, $\phi = 0.36$.

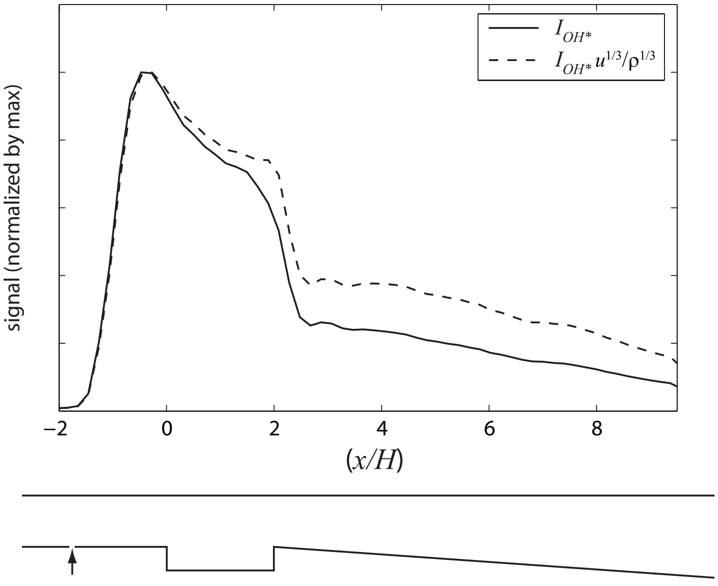

(b) Case 2H.

Figure 5.22: 1-D OH* signals with and without the co-flow mixing correction applied. Cavity reaction excluded.

the plane over the width (z direction) of the combustor. A flame sheet spreading in the y direction into this jet would be expected to have an increasing heat release rate for increasing y in the lower half of the jet. The observed flame sheet location increases in y for increasing x. Thus the initial rise in heat release rate in the x direction is expected.

The heat release rate eventually decreases in the x-direction for two reasons. Once the flame sheet reaches the upper half of the jet shown in Fig. 5.23, the heat release rate will decrease with increasing y (and thus increasing x) due to the decreasing fuel mass flow per unit height ($\dot{m}_f(y)$). Secondly, the static temperature of the reactants decreases through the thermal throat as the Mach number increases. The temperature change causes a decrease in flame speed and thus the flame spreading angle. This explains the drop in heat release rate seen behind the cavity trailing edge in for both cases in Fig. 5.13. For case 1H the spreading angle is relatively high and the flame sheet appears to reach the center of the fuel plume (on average) before the thermal throat. This explains the slow decrease in heat release rate in the x-direction seen upstream of the cavity trailing edge in Fig. 5.13(b). For case 1B the spreading angle is significantly lower than for case 1H. Therefore the heat release rate increases in the x-direction until the sudden change at the thermal throat as seen in Fig. 5.13(a). The effect of the flame sheet reaching the upper part of the fuel jet is delayed until well downstream.

In the far downstream region, the cavity stabilized reaction most likely becomes mixing limited. The center of the premixed flame sheet starts out fuel rich, as shown by the reaction zone images in Secs. 4.2.1 and 4.3.1. Thus there will be unburned fuel that passes through the flame sheet and reacts after mixing with air downstream. The mixing field is not expected to change greatly between the two

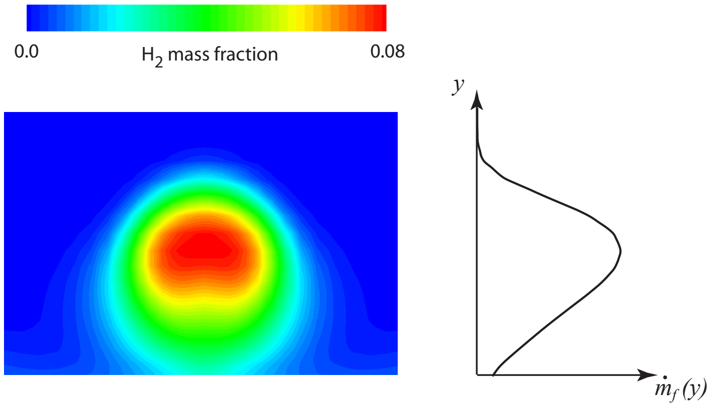

Figure 5.23: Fuel distribution in the jet-wake cross section (y-z plane) at x/H=1.0 as computed by non-reacting CFD++ at case 1H conditions. The fuel mass flow rate per unit height through this plane ($\dot{m}_f(y)$) is also shown.

combustion modes, so the jet wake stabilized results can be used as measure of the mixing limited heat release downstream. The cavity and jet-wake stabilized I_{OH^*} and I_{CH^*} distributions approach the same values for $x/H \gtrsim 6$. This is likely to be the region where the flame spreading limited reaction transitions to a mixing limited reaction. This is consistent with the CH-PLIF results in Sec.4.2.1 which show that the end of the relatively continuous reaction layer usually has ended by this location.

5.5 Comparison with CFD solution

The heat release distribution calculated by CFD++ for cases 1C and 2C is compared to the experimental heat release distribution for cases 1H and 2H in Fig. 5.24. As discussed in Sec. 2.2, the test conditions for cases 1C and 1H are similar. Likewise the case 2C and 2H test conditions are similar. The heat release distribution for the CFD cases was calculated from the change in the enthalpy of formation flux of all species integrated over $y - z$ planes (see Sec. 2.6). The experimental heat release distribution $\dot{Q}(x)$ was assumed to be proportional to the 1-D OH* luminosity signal $I_{OH^*}(x)$. All heat release distributions in Fig. 5.24 are normalized by the area under the curve (which is equal to the total heat release).

Figure 5.24(a) shows that the computational and experimental heat release distribution are significantly different for cases 1C and 1H. This difference is due to the fact that cavity stabilized combustion was measured for these conditions, but jet-wake stabilized combustion was predicted by CFD++ (see Sec. 3.1.4). For cases 2C and 2H, jet-wake stabilized combustion was measured and predicted by CFD++. However figure 5.24(a) shows that the heat release is shifted significantly upstream in the computed case.

The heat release distribution computed by CFD++ at case 1C is similar to the measured distribution at case 2H even though T_0 is 270 K less for case 1C. Both these distributions exhibit a peak in heat release near the start of the reaction zone. The heat release rate decreases very quickly near the cavity trailing edge where the thermal throat exists. This decrease is more pronounced for the computational case than the experimental case. Downstream of the cavity trailing edge the heat release rate is nearly constant for the CFD solution while it continues to decrease with x for the experimental case.

The wall pressure distributions calculated by calculated by CFD++ for cases 1C and 2C are shown with the measured wall pressure distribution for cases 1H and 2H in Fig.5.25. The CFD solution over-predicts the length and pressure rise of the pre-combustion shock train in both cases. This is due to the fact that the reaction zone is shifted upstream in the CFD cases and thus more heat is released upstream of the thermal throat. Therefore the CFD predicts isolator unstart will occur at a lower equivalence ratio than the actual value. Figure 5.25(a) shows that the pre-combustion shock train starts in the diverging part of the nozzle for the CFD case 1C. On a flight vehicle this could be an un-started condition.

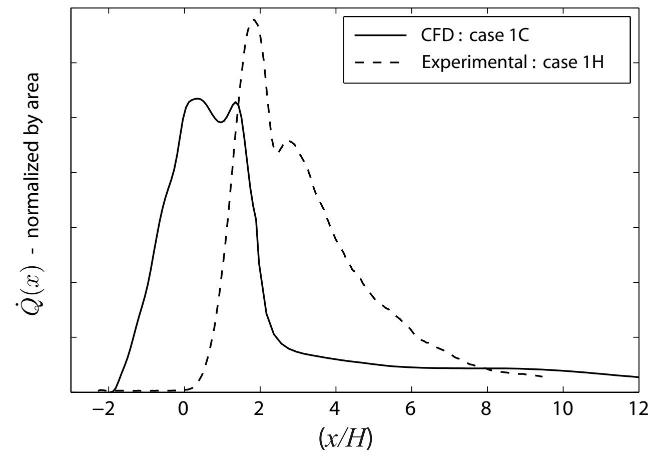

(a) Case 1C and 1H. Experimental and CFD test conditions are approximately equivalent.

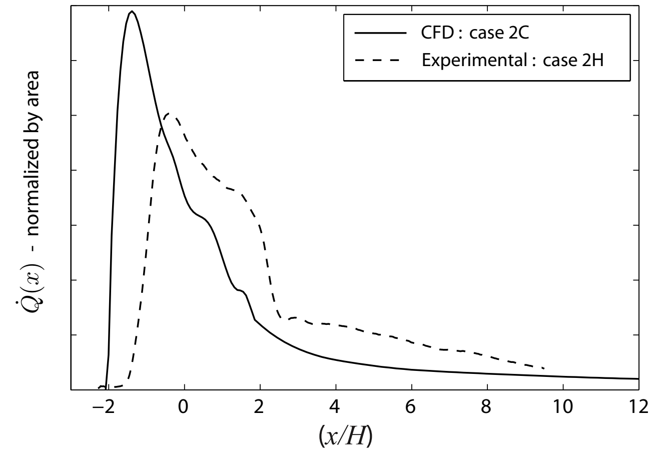

(b) Case 2C and 2H. Experimental and CFD test conditions are approximately equivalent.

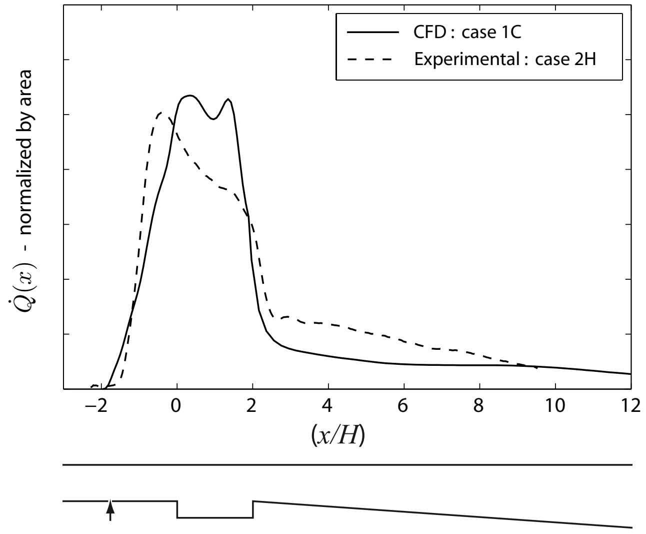

(c) Case 1C and 2H. $T_{0,air}$ is 270 K higher for experimental case 2H than for CFD case 1C.

Figure 5.24: Axial distribution of the heat release rate per unit length ($\dot{Q}(x)$) calculated by CFD++ and measured experimentally. The experimental heat release distribution was obtained from the OH* chemiluminescence.

The pressure downstream of the cavity trailing edge is predicted quite well by the CFD for case 2C. This is likely due to the fact mixing limited combustion occurs in this region for both the experimental and computational cases. As seen in Fig. 5.24(b), the shape of heat release distribution $\dot{Q}(x)$ that is predicted by CFD in this region is quite similar to the experimental profile, although there is some difference in the magnitudes. The agreement between the CFD and the measured pressure downstream of the cavity trailing edge is not as good for case 1C and for case 2C. This is due to the fact that the combustion is mixing limited in the CFD simulation and the combustion is limited by premixed flame spreading in the experiment. While the case 1C and 2H heat release distributions (shown in Fig 5.24) are quite similar, the pressure distributions are not. This can be explained by the previous discussion in Sec. 1.1.2. The factor that governs the effect of heat addition on the flow is $\Delta T_0/T_{0,air}$. Since the ΔT_0 from the combustion is approximately proportional to ϕ for lean mixtures, the effect of the heat release for a fixed ϕ is larger for lower $T_{0,air}$.

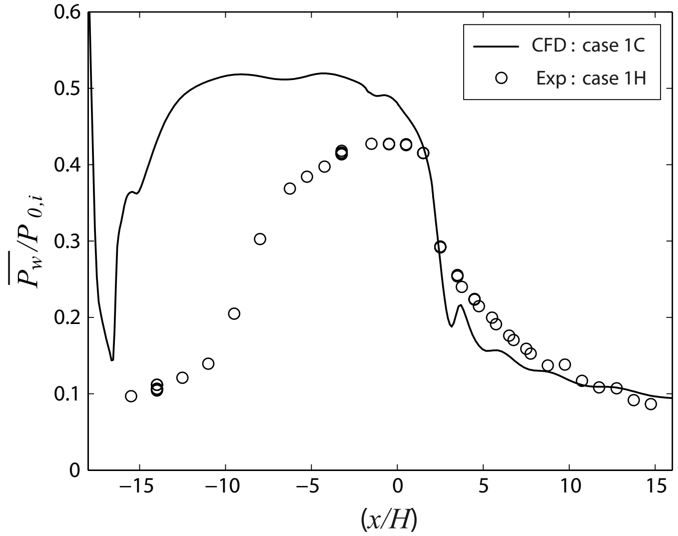

(a) Case 1C and 1H. Experimental and CFD test conditions are approximately equivalent.

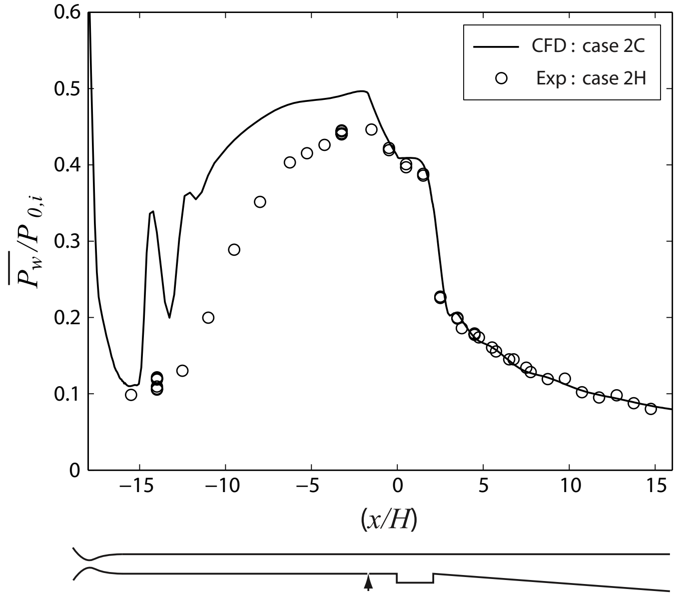

(b) Case 2C and 2H. Experimental and CFD test conditions are approximately equivalent.

Figure 5.25: Mean wall pressure calculated by CFD++ and measured experimentally.

CHAPTER VI

Conclusions and Future Work

6.1 Conclusions

1) The reaction zone structure in a dual-mode scramjet combustor with wall fuel injection and a cavity flameholder was measured for a range of conditions that corresponding to ramjet mode combustion at M_{flight} between 4.3 and 5.5. Two distinct reaction zone structures were observed. One structure corresponds to cavity stabilized combustion and the other corresponds to jet-wake stabilized combustion.

2) In the cavity stabilized combustion mode, the reaction zone structure is that of a premixed flame. The flame base is always stabilized at the same location near the top of the upstream wall of the cavity. The cavity plays a vital role in this flame stabilization mode. It provides a relatively low velocity region for the flame base to exist, as well as providing heat and radicals to this location through the cavity recirculation zone. The flame stabilization location in this mode is determined by the cavity geometry, and therefore does not vary with changes in temperature, fuel, type, or equivalence ratio. CH-PLIF images show that the premixed flame initially spreads from the cavity as a relatively thin and continuous sheet. Downstream the flame sheet becomes more discontinuous as

it is broken up by large turbulent structures.

3) In the jet-wake stabilized combustion mode, the reaction zone structure is that of a lifted, jet diffusion flame. The base region is a premixed flame while further downstream there is a non-premixed, diffusion flame. The premixed flame base is stabilized in the wake of the fuel injection jet where it is believed that the local flame speed is equal to the local flow speed (on average). The location of the flame base is independent of, and unaffected by, the cavity. The flame base moves closer to the injection location as the kinetics are increased (either by $T_{0,air}$ of fuel composition). The diffusion flame downstream of the premixed base is quite shredded and discontinuous. Formaldehyde PLIF images show that the fuel passes through an inner rich premixed flame before entering the outer diffusion flame.

4) The combustion stabilization mode present was primarily dependent on the air stagnation temperature the and fuel composition. For high stagnation temperatures ($T_{0,air} \geq 1350$ K for H_2 fuel), only jet-wake stabilized combustion was found. For low stagnation temperatures ($T_{0,air} \leq 1150$ K for H_2 fuel), only cavity stabilized combustion occurs. The same behavior was found using a mixture 50% H_2 and 50% C_2H_4, but the mode transition temperatures were approximately 120 K higher. The cavity fueling rate, and overall equivalence ratio had little effect on the combustion stabilization mode for the range of conditions studied.

5) The axial heat release distribution was measured from OH* and CH* chemiluminescence. It is an important parameter needed to design and model scramjet engines. This distribution varies significantly between the two stabilization

modes. For jet-wake stabilized combustion, the heat release distribution is mixing limited downstream of the flame base. Finite rate kinetics do not play a role in this region. A peak in the heat release occurs in the flame base region where the fuel that is premixed with the air upstream of this location is quickly consumed. This peak is higher for larger lift-off distances. Heat release for cavity stabilized combustion is consistent with premixed flame spreading the majority of the reaction zone. Far downstream the heat release appears to approach a mixing limited case as fuel is consumed that has passed through rich, or broken areas of the premixed flame.

6) Strong combustion dynamics were observed for intermediate air stagnation temperatures that can have a detrimental effect on the engine performance. For an intermediate range of $T_{0,air}$, the flame base oscillated between the cavity and jet-wake anchoring positions. The movement between flame stabilization modes was fast, $\mathcal{O}$(1 ms), while the relatively steady time in each mode was generally much longer, $\mathcal{O}$(10-100 ms). The oscillation is due to blow-off and flashback events of the premixed flame base that are caused by fluctuations in the freestream or jet-wake. This oscillation did not occur at a fixed frequency and was not coupled with any acoustic mode.

7) Oscillation between the two modes leads to very high pressure fluctuations due to the different heat release distributions associated with the two flame anchoring locations. Synchronized high speed imaging and pressure data confirmed that the flame movement preceded the large pressure fluctuations. These fluctuations were greatly reduced by moving the main fuel injection downstream so that reaction zone location for the two stabilization modes overlapped. This

resulted in a hybrid stabilization mode where the cavity provided heat and radicals to the main jet-wake stabilized combustion. Direct cavity fueling was necessary to realize the full benefits of this hybrid stabilization.

8) The instantaneous CH-PLIF images showed that the reaction zone is not a well stirred, distributed reactor. The reaction zone is consistent with the thickened, highly strained flamelet regime. The heat release indicated by the CH-PLIF is generally confined to layers $0.7 - 3$ mm wide, which is much thicker than the unstrained laminar flame thickness. The thickened regions may be caused by turbulence broadening the reaction layer. Local extinction appears to be prevalent in the reaction layers.

9) The initial fuel breakdown region and hot combustion products were imaged using simultaneous OH/formaldehyde-PLIF. Thick fuel breakdown regions were observed upstream of the primary reaction zone (indicated by the start of OH) for both stabilization modes. This upstream fuel decomposition is caused by preliminary auto-ignition reactions that are uncorrelated with the heat release from the combustion. The combustion occurs as an auto-ignition assisted flame, where the upstream auto-ignition reactions serve to increase the local flame speed. The behavior of the combustion is still flame-like however, due to the need for flame propagation against the incoming flow.

10) A CFD++ simulation of the two experimental cases illustrates the limitations of current engineering models. The simulation predicted combustion stabilization and heat release well upstream of the experimental observations. The chemistry modeling used is ill-suited for predicting the auto-ignition assisted flame propagation controlling the actual stabilization location.

6.2 Future Work

While the current study has yielded new insight into the combustion mechanisms in dual-mode scramjet combustors, many more questions remain. Several directions for future experimental and computational work are suggested.

Combustion efficiency is an important property in scramjet combustors that was not directly treated in the current study. Measurements of the combustion efficiency as the flame moves between stabilization modes would be very useful. Such measurements could be made through exhaust gas sampling rakes or through refinement and calibration of the 1-D wall pressure analysis model. The later method would involve the measurement of wall temperatures throughout the combustor.

While the current study focused on ramjet mode combustion, it is important to understand how the combustion stabilization location and mechanism changes for conditions all the way up to high M_{flight}, scramjet mode combustion. Exploring scramjet mode combustion will require raising $T_{0,air}$ up to 2000 K and above.

The thickened reaction layers imaged by the CH-PLIF raises interesting theoretical questions. Since thin reaction layers are fundamental to much of premixed flame theory and flame modeling, the implications of such thickening is unclear and would be useful to investigate. The precise thickness and structure of these layers may be better resolved in the future through simultaneous OH/formaldehyde-PLIF. This method has the potential for a better signal to noise ratio than CH-PLIF since the laser sheet reflections which hampered the current study are surmountable.

The CFD method examined in the current study is representative of engineering codes which run in a reasonable period of time and have robust convergence over a wide range of conditions. It is not representative of the state of the art in combustion modeling research. More advanced modeling methods may be able to do a better job predicting the combustion stabilization and provide comparisons for the experimental results. One promising approach for the current problem is the compositional PDF turbulence-chemistry modeling used by Gordon et al [40]. The variation in lift-off height for changes in $T_{0,air}$ of a non-premixed jet reaction in a vitiated co-flow was predicted using this method. The combustion in this case is likely similar to the jet-wake stabilized combustion observed in the current study.

Modeling may also be useful for providing insight into the auto-ignition assisted flame mechanism proposed by the current study. It has been theorized that the upstream auto-ignition reactions serve to increase the flame propagation speed. The magnitude of this effect and whether it must be accounted for in combustion models is unclear.

The final step is to use the physical mechanisms revealed by this study to build predictive models. This has been done by Torrez et al [100] in the case of a quasi-1-dimensional model for the heat release distribution in scramjet combustors. More refinement of this model is necessary to obtain good agreement with the experimental results.

APPENDIX

APPENDIX

Quasi-One-Dimensional Data Analysis Model

A model was created to solve for the distribution of all flow variables in the combustor from the measured wall pressure data using the mass, momentum, and energy conservation equations. All flow properties were assumed to be constant across the combustor cross section and only the axial component of the flow velocity was considered. The combustor cross-section area was allowed to vary making the model quasi-one-dimensional. Matlab was used to implement the code and solve the conservation equations. The code consisted of three sections: the isolator, the fuel air mixing section, and the combustion section.

A.1 Appendix Nomenclature

For all symbols an overline $(\bar{\cdot})$ denotes a mixture average property.

Symbols

a	number of carbon atoms in the hydrocarbon fuel molecule
A	flow cross section area
b	number of hydrogen atoms in the hydrocarbon fuel molecule
c	number of moles of H_2 per mole of hydrocarbon in fuel mixture
c_p	constant pressure specific heat
C_f	wall friction coefficient

$C_{f,incomp}$	incompressible flow wall friction coefficient
h	enthalpy
k	thermal conductivity
$\dot{m}$	mass flow
n	number of moles
n_{tot}	total number of moles of all species
M	Mach number
MW	molecular weight
P	static pressure
Pr	Prandtl number
Re_x	Reynolds number
$\Re$	universal gas constant
T	static temperature
T_0	stagnation temperature
T_w	wall temperature
T_{aw}	adiabatic wall temperature
U	axial velocity
x	axial location
X	mole fraction
Y	mass fraction
γ	ratio of specific heats
$\eta_c(x)$	Combustion efficiency up to location x ($\dot{m}_{fuel,burned}(x)/\dot{m}_{fuel,injected}$)
μ	dynamic viscosity
ρ	density
ϕ	overall equivalence ratio ($\dot{m}_{totalfuel}$/stoichiometric $\dot{m}_{totalfuel}$)

Subscripts

i	property for species i
in	inflow conditions for fuel-air mixing section
out	outflow conditions for fuel-air mixing section
vit	vitiator exit property

A.2 Chemistry Treatment

A single step chemistry was assumed that includes only the major species of H_2, C_aH_b, H_2O, CO_2, O_2, and N_2 (C_aH_b is a generic hydrocarbon. Only ethylene with a=2 and b=4 was considered for the current study). This allowed the all the species concentrations to be written as algebraic functions of the combustion efficiency (η_c) which is defined as:

$$\eta_c(x) = \frac{\dot{m}_{fuel,burned}(x)}{\dot{m}_{fuel,injected}} \tag{A.1}$$

The reaction for lean combustion can be written in terms of the fuel composition (a, b, c), the overall equivalence ratio (ϕ), and η_c as:

(A.2)

$$\phi\,(\mathrm{C_aH_b} + c\,\mathrm{H_2}) + \left(a + \frac{b}{4} + \frac{c}{2}\right)\left[\mathrm{O_2} + \frac{X_{\mathrm{H_2O},vit}}{0.21}\,\mathrm{H_2O} + \left(3.76 - \frac{X_{\mathrm{H_2O},vit}}{0.21}\,\mathrm{N_2}\right)\right]$$
$$\rightarrow n_{\mathrm{C_aH_b}}\,\mathrm{C_aH_b} + n_{\mathrm{H_2}}\,\mathrm{H_2} + n_{\mathrm{H_2O}}\,\mathrm{H_2O} + n_{\mathrm{CO_2}}\,\mathrm{CO_2} + n_{\mathrm{O_2}}\,\mathrm{O_2} + n_{\mathrm{N_2}}\,\mathrm{N_2}$$

where

$$n_{\mathrm{C_aH_b}} = (1 - \eta_c)\,\phi \tag{A.3}$$

$$n_{\mathrm{H_2}} = (1 - \eta_c)\,\phi c \tag{A.4}$$

$$n_{\mathrm{H_2O}} = (b + 2c)\frac{\phi\eta_c}{2} + (a + \frac{b}{4} + \frac{c}{2}\frac{X_{\mathrm{H_2O},vit}}{0.21} \tag{A.5}$$

$$n_{\mathrm{CO_2}} = a\eta_c\phi \tag{A.6}$$

$$n_{\mathrm{O_2}} = (a + b/4 + c/2)\,(1 - \phi\eta_c) \tag{A.7}$$

$$n_{\mathrm{N_2}} = \left(a + \frac{b}{4} + c2\right)\left(3.76 - \frac{X_{\mathrm{H_2O},vit}}{0.21}\right) \tag{A.8}$$

where $X_{\mathrm{H_2O},vit}$ is the mole fraction of water vapor in the vitiator products. The mole and mass fractions for each species and the mixture molecular weight and ratio of specific heats are given as:

$$X_i = n_i/n_{tot} \tag{A.9}$$

$$n_{tot} = \sum_i n_i \tag{A.10}$$

$$\overline{MW} = \sum_i X_i MW_i \tag{A.11}$$

$$\overline{\gamma} = \sum_i X_i \gamma_i \tag{A.12}$$

$$Y_i = \frac{MW_i}{\overline{MW}} X_i \tag{A.13}$$

A.3 Isolator

For the purposes of the code, the isolator consists of the region from the nozzle exit, to the start of the combustion. Constant flow area (equal to the combustor cross section), no chemical reactions, and constant T_0 was assumed in the isolator.

The constant area assumption leads to slight under prediction of the Mach number in regions where the boundary layer is separated. However, the primary role of the isolator analysis is to determine the isolator exit conditions. The boundary layer is expected to be re-attached at, or shortly after the isolator exit so the constant area assumption is considered sufficient. The constant T_0 assumption means there is no heat transfer to the wall in the isolator. This assumption can be made because there is low heat transfer in regions where the boundary layer is separated, which is the majority of the length of the isolator.

Mass conservation in the isolator can be written as:

$$\dot{m} = \rho U A \tag{A.14}$$

where

$$\rho = \frac{P\overline{MW}}{\Re T} \tag{A.15}$$

$$U = M\sqrt{\frac{\overline{\gamma}\Re T}{\overline{MW}}} \tag{A.16}$$

$$\frac{T_0}{T} = 1 + \frac{\overline{\gamma}-1}{2}M^2 \tag{A.17}$$

Combining Eqs. A.14-A.17 gives:

$$M = \frac{\dot{m}}{AP}\sqrt{\frac{\Re T_0}{\overline{\gamma}\overline{MW}\left(1+\frac{\overline{\gamma}-1}{2}M^2\right)}} \tag{A.18}$$

All the quantities in Eq. A.18 except the Mach number are known everywhere in the isolator. This allows the Mach number to be solved for algebraically.

A.4 Fuel-Air Mixing Section

The fuel air mixing section is a section of zero length where the fuel and air are mixed. The mass and momentum conservation equations give:

$$\dot{m}_{air}U_{in} = \left(\dot{m}_{air} + \dot{m}_{fuel}\right)U_{out} \tag{A.19}$$

allowing U_{out} to be calculated. The fuel injection provides no axial momentum since it is injected normal to the flow. The energy conservation equation gives:

$$\frac{1}{2}\dot{m}_{air}U_{in}^2 + \sum_i \left(\dot{m}_{air} + \dot{m}_{fuel}\right) Y_{i,out} h_i(T_{in}) = \frac{1}{2}\left(\dot{m}_{air} + \dot{m}_{fuel}\right) U_{out}^2 + \sum_i \left(\dot{m}_{air} + \dot{m}_{fuel}\right) Y_{i,out} h_i(T_{out}) \tag{A.20}$$

The inlet conditions for the air stream are the isolator exit conditions. The inlet conditions for the fuel stream are the known fuel injection conditions. The mixture composition ($Y_{i,out}$) is determined from the equations given in Sec. A.2 with $\eta_c = 0$. The static enthalpy of each species is a function of the temperature ($h_i(T)$). These values are obtained at a given temperature from the tabulated thermodynamic data in the GRI-Mech 3.0 therm.dat file [90]. This allows Eq. A.20 to be solved iteratively for T_{out}.

A.5 Combustion Section

The system of equations for this section were arranged such that the unknown variables were ρ, U, T, $\overline{MW}$, η_c, n_{tot}, Y_i, and X_i. The system of differential equations for these 18 variables (6+2×6 species) is given in Eqs. A.21-A.28 . The ode23 function in Matlab was used to solve this system of equations up to the end of the combustor. The initial conditions are equal to the exit conditions of the fuel-air mixing section. The number of equations could be reduced significantly by elimination of variables at the expense of coding simplicity. This was not done because reducing the run time of the code (which is approximately 1 minute) was not important.

$$\frac{dU}{dx} = -\frac{U}{\overline{\gamma}M^2}\left(\frac{1}{P}\frac{dP}{dx} + \frac{2\overline{\gamma}M^2C_f}{\mathcal{D}}\right) \tag{A.21}$$

$$\frac{d\rho}{dx} = -\frac{\rho}{U}\frac{dU}{dx} - \frac{\rho}{A}\frac{dA}{dx} \tag{A.22}$$

$$\frac{dT}{dx} = -\frac{1}{\overline{c_p}}\left[\sum_i h_i\frac{dY_i}{dx} + \frac{2C_f\overline{c_p}(T_{aw}-T_w)}{Pr^{2/3}A} + U\frac{dU}{dx}\right] \tag{A.23}$$

$$\frac{d\overline{MW}}{dx} = \overline{MW}\left(\frac{1}{\rho}\frac{d\rho}{dx} + \frac{1}{T}\frac{dT}{dx} - \frac{1}{P}\frac{dP}{dx}\right) \tag{A.24}$$

$$\frac{d\eta_c}{dx} = \frac{1}{\phi(b/4 - c/2 - 1)}\frac{dn_{tot}}{dx} \tag{A.25}$$

$$\frac{dn_{tot}}{dx} = \frac{1}{\overline{MW}}\sum_i MW_i\frac{dn_i}{dx} - \frac{n_{tot}}{\overline{MW}}\frac{d\overline{MW}}{dx} \tag{A.26}$$

$$\frac{dY_i}{dx} = \frac{MW_i}{\overline{MW}}\frac{dX_i}{dx} - \frac{Y_i}{\overline{MW}}\frac{d\overline{MW}}{dx} \tag{A.27}$$

$$\frac{dX_i}{dx} = \frac{1}{n_{tot}}\frac{dn_i}{dx} - \frac{X_i}{n_{tot}}\frac{dn_{tot}}{dx} \tag{A.28}$$

Equations A.21-A.24 are forms of the mass, momentum and energy equations given by Torrez et al [99]. The skin friction coefficient (C_f) in Eq. A.21 was determined using the method given by van Driest [103] where:

$$C_f = f(C_{f,incomp}, Re_x, T, T_w, T_{aw}) \tag{A.29}$$

The incompressible skin friction coefficient ($C_{f,incomp}$) was determined by the method given by Schitling [88].

$$\frac{1}{\sqrt{C_{f,incomp}}} \approx 4.15log_{10}(Re_xC_{f,incomp}) + 1.7 \tag{A.30}$$

$$Re_x = \frac{\rho Ux}{\overline{\mu}} \tag{A.31}$$

The viscosity (μ) was calculated from the GRI-Mech 3.0 [90] transport.dat file for each species at the static temperature T. The mixture viscosity ($\overline{\mu}$) was then calculated by the method given by Wilke [109]. The adiabatic wall temperature was given by Eqs. A.32 and A.33.

$$r = \frac{T_{aw} - T}{T_0 - T} \approx \sqrt{Pr} \tag{A.32}$$

$$Pr = \frac{\overline{c_p \mu}}{\overline{k}} \tag{A.33}$$

The mixture thermal conductivity ($\overline{k}$), viscosity ($\overline{\mu}$), and specific heat ($\overline{c_p}$) were obtained at T from the GRI-Mech therm.dat and transport.dat files.

Equation A.25 was derived from the single step chemistry equations given in Eqs. A.3-A.8 and A.10. Equation A.26 was derived from Eqs. A.9 and A.11. Expressions for the terms dn_i/dx can be written as functions of $d\eta_c/dx$ from Eqs. A.3-A.8. Equations A.27 and A.28 were derived from Eqs. A.13 and A.9.

BIBLIOGRAPHY

BIBLIOGRAPHY

[1] R. S. Barlow, R. W. Dibble, J. Y. Chen, and R. P. Lucht. Effect of Damkohler number on superequilibrium OH concentration in turbulent nonpremixed jet flames. *Combust. Flame*, 82:235–251, 1990.

[2] R. A. Baurle. Modeling of high speed reacting flows: established practices and future challenges. *AIAA Aerospace Sciences Meeting*, AIAA-2004-267, 2004.

[3] R. A. Baurle and D. R. Eklund. Analysis of dual-mode hydrocarbon scramjet operation at Mach 4-6.5. *J. Prop. Power*, 18(5):990–1002, 2002.

[4] A. Ben-Yakar. *Experimental investigation of mixing and ignition of transverse jets in supersonic crossflows.* PhD thesis, Stanford University, 2000.

[5] A. Ben-Yakar and R. K. Hanson. Experimental investigation of flame-holding capability of hydrogen transverse jet in supersonic cross-flow. *Proc. Comb. Inst.*, 27:2173–2180, 1998.

[6] A. Ben-Yakar and R. K. Hanson. Cavity flame-holders for ignition and flame stabilization in scramjets: an overview. *J. Prop. Power*, 17(4):869–877, 2001.

[7] M. Berglund and C. Fureby. LES of supersonic combustion in a scramjet engine model. *Proc. Comb. Inst.*, 31:2497–2504, 2007.

[8] A. M. Bonanos, J. A. Schetz, W. F. O'Brien, and G. P. Goyne. Dual-mode combustion experiments with an integrated aeroramp-injector/plasma-torch igniter. *J. Prop. Power*, 24:267–273, 2008.

[9] A. Bryant. *Planar laser-induced fluorescence imaging of fuel mixing and the reaction zone in a supersonic combustor.* PhD thesis, University of Michigan, 1998.

[10] B. T. Campbell, A. Sienbenharr, and T. Nguyen. Strutjet engine performance. *J. Prop. Power*, 17:1227–1232, 2001.

[11] B. Carroll, J. Dutton, and A. Andy. A computer program for the design of continuous slope supersonic nozzles. Technical report, Tech. Rep. UILU ENG 86-4007, University of Illinois at Urbana-Champaign, 1986.

[12] C. D. Carter, J. M. Donbar, and J. F. Driscoll. Simultaneous CH planar laser-induced fluorescence and particle imagine velocimetry in turbulent nonpremixed flames. *Appl. Phys. B*, 66:129–132, 1998.

[13] A. Cessou, C. Maurey, and D. Stepowski. Parametric and statistical investigation of the behavior of a lifted flame over a turbulent free-jet structure. *Combust. Flame*, 458-477:458–477, 2004.

[14] Y.-C. Chen and M. S. Mansour. Topology of turbulent premixed flame fronts resolved by simultaneous planar imaging of LIPF of OH radical and rayleigh scattering. *Exp. in Fluids*, 26:277–287, 1999.

[15] Y.-C. Chen, N. Peters, G. A. Schneenmann, N. Wruck, U. Renz, and M. S. Mansour. The detailed structure of highly stretched turbulent premixed methane-air flames. *Combust. Flame*, 107:223–226, 1996.

[16] J.-Y. Choi, F. Ma, and V. Yang. Combustion oscillations in a scramjet engine combustor with transverse fuel injection. *Proc. Comb. Inst.*, 30:2851–2858, 2005.

[17] J.-Y. Choi, F. Ma, and V. Yang. Dynamics combustion characteristics in scramjet combustors with transverse fuel injection. *AIAA Joint Propulsion Conference*, AIAA-2005-4428, 2005.

[18] Noel T. Clemens. *Encyclopedia of Imaging Science and Technology*, chapter Flow imaging, pages 390–419. John Wiley and Sons, 2002.

[19] M. O Conaire, H. J Curran, J. M. Smmie, W. J. Pitz, and C. K. Westbrook. A comprehensive modeling study of hydrogen oxidation. *Int. J. Chem. Kinet.*, 36:603–622, 2004.

[20] E. T. Curran. Scramjet engines: the first forty years. *J. Prop. Power*, 17:1138–1148, 2001.

[21] E. T. Curran, W. H. Heiser, and D. T. Pratt. Fluid phenomena in scramjet combustion systems. *Annu. Rev. Fluid Mech.*, 28:323–360, 1996.

[22] E. T. Curran and S. N. B. Murthy. Supersonic flow combustors. In E. T. Curran and S. N. B. Murthy, editors, *Scramjet Propulsion*, pages 513–568. AIAA, 2000.

[23] W. J. A. Dahm. Effects of heat release on turbulent shear flows. part 2. turbulent mixing layers and the equivalence principle. *J. Fluid Mech.*, 540:1–19, 2005.

[24] A. De and S. Acharya. Large eddy simulation of premixed combustion with a thickened-flame approach. *J. Eng. Gas Turb. Power*, 131:doi:10.1115/1.3094021, 2009.

[25] O. Dessornes and D. Scherrer. Tests of the JAPHAR dual mode ramjet engine. *Aerosp. Sci. Tech.*, 9:211–221, 2005.

[26] S. Dhanuka. *An experimental study of the stable and unstable operation of an LPP gas turbine combustor*. PhD thesis, University of Michigan, 2008.

[27] J. Donbar, O. Powell, M. Gruber, and T. Jackson. Post-test analysis of flush-wall fuel injection experiments in a scramjet combustor. *AIAA Joint Propulsion Conference*, AIAA 2001-3197, 2001.

[28] J. M. Donbar, J. F. Driscoll, and C. D. Carter. Reaction zone structure in turbulent nonpremixed jet flames from CH-OH plif images. *Combust. Flame*, 122:1–19, 2000.

[29] J. M. Donbar, M. R. Gruber, T. A. Jackson, C. D. Carter, and T. Mathur. OH planar laser-induced fluorescence imaging in a hydrocarbon-fueled scramjet combustor. *Proc. Comb. Inst.*, 28:679–687, 2000.

[30] J. F. Driscoll. Turbulent premixed combustion: flamelet structure and its effect on turbulent burning velocities. *Progr. Energy Combust. Sci.*, 34:91–134, 2008.

[31] J.F. Driscoll and C. C. Rasmussen. Correlation and analysis of blowout limits of flames in high-speed airflows. *J. Prop. Power*, 21(6):1035–1044, 2005.

[32] J. P. Drummond, R. C. Clayton, and M. Y. Hussani. A numerical model for supersonic reacting mixing layers. *Comput. Method. Appl. M.*, 64:39–60, 1987.

[33] X. Fan, G. Yu, J. Li, X. Zhang, and C.-J. Sung. Investigation of vaporized kerosene injection and combustion in a supersonic model combustor. *J. Prop. Power*, 22(1):103–110, 2006.

[34] R. S. Fry. A century of ramjet propulsion technology evolution. *J. Prop. Power*, 21, 2004.

[35] N. L. Garland and D. R. Crosley. Energy transfer processes in CH a2-delta and b2-sigma in an atmospheric pressure flame. *Appl. Optic.*, 24(23):4229–4237, 1985.

[36] A. Gaydon and H. Wolfhard. *Flames, Their Structure, Radiation, and Temperature.* Chapman and Hall, 1979.

[37] M. Gerstein and P. R. Choudhury. Use of silane-methane mixtures for scramjet ignition. *J. Prop. Power*, 1:399–402, 1985.

[38] R. L. Gordon, A. R. Masri, and E. Mastorakos. Simultaneous rayleigh temperature, OH- and CH2O-LIF imaging of methane jets in a vitiated coflow. *Combust. Flame*, 155:181–195, 2008.

[39] R. L. Gordon, A. R. Masri, S. B. Pope, and G. M. Goldin. A numerical study of auto-ignition in turbulent lifted flames issuing into a vitiated co-flow. *Combust. Theor. Model.*, 11:351–376, 2007.

[40] R. L. Gordon, A. R. Masri, S. B. Pope, and G. M. Goldin. Transport budgets in turbulent lifted flames of methane autoigniting in a vitiated co-flow. *Combust. Flame*, 151:495–511, 2007.

[41] M. R. Gruber, C. D. Carter, D. R. Montes, L. C. Haubelt, P. I. King, and K.-Y. Hsu. Experimental studies of pylon-aided fuel injection into a supersonic crossflow. *J. Prop. Power*, 24:460–470, 2008.

[42] M. R. Gruber, J. M. Donbar, C. D. Carter, and K.-Y. Hsu. Mixing and combustion studies using cavity-based flameholders in a supersonic flow. *J. Prop. Power*, 20(5):769–778, 2004.

[43] W. A. Guttenfelder, G. B. King, J. P. Gore, N. M. Laurendeau, and M. W. Renfro. Hydroxl time series measurements and simulations for turbulent premixed jet flames in the thickened preheat regime. *Combust. Flame*, 135:381–403, 2003.

[44] L. C. Haber and U. Vandsburger. A global reaction model for OH* chemiluminescence applied to a laminar flat-flame burner. *Combust. Sci. Tech.*, 175:1859–1891, 2003.

[45] D. Han and M. G. Mungal. Direct measurement of entrainment in reacting/nonreacting turbulent jets. *Combust. Flame*, 124(3):370–386, 2001.

[46] D. H. Han and M. G. Mungal. Simultaneous measurement of velocity and CH layer distribution in turbulent non-premixed flames. *Proc. Comb. Inst.*, 28:261–267, 2000.

[47] J. M. Hank, J. S. Murphy, and R. C. Mutzman. The X-51A scramjet engine flight demonstration program. *AIAA International Space Planes and Hypersonic Systems and Technologies Conference*, AIAA-2008-2540, 2008.

[48] Y. Hardalupas and M. Orain. Local measurements of the time-dependent heat release rate and equivalence ratio using chemiluminescent emmission from a flame. *Combust. Flame*, 139:188–2007, 2004.

[49] J. E. Harrington and K. C. Smyth. Laser-induced fluorescence measurements of formaldehyde in a methane/air diffusion flame. *Chem. Phys. Lett.*, 202(3,4):196–202, 1993.

[50] E. F. Hasselbrink and M. G. Mungal. Transverse jets and jet flames. Part 1. Scaling laws for strong transverse jets. *J. Fluid Mech.*, 443:1–25, 2001.

[51] E. F. Hasselbrink and M. G. Mungal. Transverse jets and jet flames. Part 2. Velocity and OH field imaging. *J. Fluid Mech.*, 443:27–68, 2001.

[52] W. H. Heiser and D. T. Pratt. *Hypersonic Airbreathing Propulsion.* AIAA Education Series. AIAA, 1994.

[53] W. H. Heiser and D. T. Pratt. Aerothermodynamics of the dual-mode combustion system. In E. T. Curran and S. N. B. Murthy, editors, *Scramjet Propulsion*, pages 569–595. AIAA, 2000.

[54] Y. Huang and V. Yang. Dynamics and stability of lean-premixed swirl-stabilized combustion. *Progr. Energy Combust. Sci.*, 35:293–364, 2009.

[55] H. Huh. *An experimental study of supersonic hydrogen-air flames for scramjet applications.* PhD thesis, University of Michigan, 1996.

[56] C. J. Jachimowski. An analytical study of the hydrogen-air reaction mechanism with application to scramjet combustion. Technical report, NASA Paper 2791, 1998.

[57] L. S. Jacobsen, C. D. Carter, T. A. Jackson, S. Williams, J. B. Barnett, C.-J. Tam, R. A. Baurle, D. B. Bivolaru, and S. Kuo. Plasma-assisted ignition in scramjets:. *J. Prop. Power*, 24:641–654, 2008.

[58] E. Jeong, S. O'Byrne, I.-S. Jeung, and A. F. P. Houwing. Investignation of supersonic combustion with angled injection in a cavity-based combustor. *J. Prop. Power*, 24:1258–1268, 2008.

[59] G. T. Kalghatgi. Blow-out stability of gaseous jet diffusion flames. Part I: In still air. *Combust. Sci. Tech.*, 26:233–239, 1981.

[60] R. J. H. Klein-Douwel, J. Luque, J. B. Jefferies, G. P. Smith, and D. R. Crosley. Laser-induced fluorescence of formaldehyde hot bands in flames. *Appl. Optic.*, 39:3712–3715, 2000.

[61] F. Ladeinde. A critical review of scramjet combustion simulation. *AIAA Aerospace Sciences Meeting*, AIAA-2009-127, 2009.

[62] C. J. Lawn. Lifted flames on fuel jets in co-flowing air. *Progr. Energy Combust. Sci.*, 35:1–30, 2009.

[63] J. Li, F. Ma, V. Yang, K.-C. Lin, and T. Jackson. A comprehensive study of ignition transient in an ethylene-fueled scramjet combustor. *AIAA Joint Propulsion Conference*, AIAA-2007-5025, 2007.

[64] K.-C. Lin, K. Jackson, R. Behdadnia, T. A. Jackson, F. Ma, J. Li, and V. Yang. Acoustic characterization of an ethylene-fueled scramjet combustor with a recessed cavity flameholder. *AIAA Joint Propulsion Conference*, AIAA 2007-5382, 2007.

[65] K.-C. Lin, C.-J. Tam, I. Boxx, C. Carter, K. Jackson, and M. Lindsey. Flame characteristics and fuel entrainment inside a cavity flame holder in a scramjet combustor. *AIAA Joint Propulsion Conference*, AIAA 2007-5381, 2007.

[66] III M. B. Colket and L. J. Spadaccini. Scramjet fuels autoignition study. *J. Prop. Power*, 17:315–323, 2001.

[67] M. S. Mansour, N. Peters, and Y.-C. Chen. Investigation of scalar mixing in the thin reaction zones regime using a simultaneous CH-LIF / rayleigh laser technique. *Proc. Comb. Inst.*, 27:767–773, 1998.

[68] L. A. Marshall, C. Bahm, and G. P. Corpening. Overview with results and lessons learned of the X-43A Mach 10 flight. *AIAA/CIRA International Space Planes and Hypersonics Systems and Technologies Conference*, AIAA-2005-3336, 2005.

[69] T. Mathur, M. Gruber, K. Jackson, J. Donbar, W. Donaldson, T. Jackson, and F. Billig. Supersonic combustion experiments with a cavity based fuel injector. *J. Prop. Power*, 17(6):1305–1312, 2001.

[70] K. R. McManus, T. Poinsot, and S. M. Candel. A review of active control of combustion instabilities. *Progr. Energy Combust. Sci.*, 19:1–29, 1993.

[71] W. Meier, P. Weigand, X. R. Duan, and R. Giezendanner-Thoben. Detailed characterization of the dynamics of thermoacoustic pulsations in a lean premixed swirl flame. *Combust. Flame*, 150:2–26, 2007.

[72] T. Metz, X. Bai, F. Ossler, and M. Alden. Fluorescence lifetimes of formaldehyde (H2CO) in the A1A2-X1A1 band system at elevated temperatures and pressures. *Spectrochimica Acta A*, 60:1043–1053, 2004.

[73] T. Mitani and T. Kouchi. Flame structures and combustion efficiency computed for a Mach 6 scramjet engine. *Combust. Flame*, 142:187–196, 2005.

[74] H. N. Najm, P. H. Paul, C. J. Mueller, and P. S. Wycokoff. On the adequacy of certain experimental observables as measurements of flame burning rate. *Combust. Flame*, 113:312–332, 1998.

[75] M. Nakagawa. *Experimental study of compressibility effects on entrainment and mixing in supersonic planar turbulent bluff-body wakes.* PhD thesis, University of Michigan, 2001.

[76] D. T. Olmstead, M. R. Gruber, M. J. Collatz, R. D. Branam, and K.-C. Lin. Cavity coupled aeroramp injector combustion study. *AIAA Joint Propulsion Conference*, AIAA-2009-5227, 2009.

[77] T. E. Parker, M. G. Allen, R. R. Foutter, W. G. Reinecke, H. H. Legner, S. J. Davis, and W. T. Rawlins. An experimental study of supersonic H2-air combustion in a shock tunnel flow facility. *Proc. Comb. Inst.*, 24:1613–1620, 1992.

[78] P. H. Paul and H. N. Najm. Planar laser-induced fluorescence imaging of flame heat release rate. *Proc. Comb. Inst.*, 27:43–50, 1998.

[79] N. Peters and F. A. Williams. Liftoff characteristics of turbulent jet diffusion flames. *AIAA J.*, 21:423–429, 1983.

[80] R. P. Porter, A. H. Clark, W. E. Kaskan, and W. E. Browne. A study of hydrocarbon flames. *Proc. Comb. Inst.*, 11:907–917, 1967.

[81] R. B. Price, I. R. Hule, and T. M. Sugden. Optical studies of the generation of noise in turbulent flames. *Proc. Comb. Inst.*, 12:1093–1102, 1968.

[82] C. C. Rasmussen. *An experimental study of flame stability in a directly-fueled wall cavity with a a supersonic free stream.* PhD thesis, University of Michigan, 2006.

[83] C. C. Rasmussen, S. K. Dhanuka, and J. F. Driscoll. Visualization of flameholding mechanisms in a supersonic combustor using PLIF. *Proc. Comb. Inst.*, 31:2505–2512, 2007.

[84] A. Ratner, J. F. Driscoll, J. M. Donbar, C. D. Carter, and J. A. Mullin. Reaction zone structure of non-premixed turbulent flames in the intensely wrinkled regime. *Proc. Comb. Inst.*, 28:245–252, 2000.

[85] M. Richter, R. Collin, J. Nygren, M. Alden, and L. Hildingsonn B. Johansson. Studies of the combustion process with simultaneous formaldehyde and OH PLIF. *JSME Int. J.*, 48:701–707, 2005.

[86] M. Ryan, M. Gruber, C. Carter, and T. Mathur. Planar laser-induced fluorescence imaging of OH in a supersonic combustor fueled with ethylene and methane. *Proc. Comb. Inst.*, 32:2429–2436, 2009.

[87] R. W. Schefer, M. Namazian, E. E. J. Filtopoulos, and J. Kelly. Temporal evolution of turbulence/chemistry interaction in lifted, turbulent-jet flames. *Proc. Comb. Inst.*, 25:1223–1231, 2000.

[88] H. Schlichting. *Boundary layer theory.* McGraw-Hill, New York, 1979.

[89] M. D. Slessor, M. Zhuang, and P. E. Dimotakis. Turbulent shear-layer mixing: growth-rate compresibility scaling. *J. Fluid Mech.*, 414:35–45, 2000.

[90] G. P. Smith, D. M. Golden, M. Frenklach, N. W. Moriarty, B. Eiteneer, M. Goldenberg, C. T. Bowman, R. K. Hanson, S. Song, W. C. Gardiner Jr., V. V. Lissianski, and Z. Qin. http://www.me.berkeley.edu/gri_mech. 2009.

[91] M.-B. Sun, Z.-G. Wang, J.-H. Liang, and H. Geng. Flame characteristics in supersonic combustor with hydrogen injection upstream of cavity flameholder. *J. Prop. Power*, 24(4):688–696, 2008.

[92] T. Sunami, P. Magre, A. Bresson, F. Grisch, M. Orain, and M. Kodera. Experimental study of strut injectors in a supersonic combustor using OH-PLIF. *AIAA/CIRA International Space Planes and Hypersonics Systems and Technologies Conference*, AIAA-2005-3304, 2005.

[93] J. A. Sutton and J. F. Driscoll. Optimization of ch fluorescence diagnostics in flames: range of applicability and improvements with hydrogen addition. *Appl. Optic.*, 42(15):2819–2828, 2003.

[94] M. Tamura, P. A. Berg, J. E. Harrington, J. Luque, J. B. Jefferies, G. P. Smith, and D. R. Crosley. Collisional quenching of ch(a), oh(a), and no(a) in low pressure hydrocarbon flames. *Combust. Flame*, 114:502–514, 1998.

[95] J. Tobai and T. Dreier. Effective A-state fluorescence lifetime of formaldehyde in atmospheric pressure CH4-air flames. *Appl. Phys. B*, 74:101–104, 2002.

[96] S. Tomioka, K. Kobayashi, K. Kudo, A. Murakami, and T. Kanda. Performance of supersonic combustors with fuel injection in diverging section. *J. Prop. Power*, 22:111–119, 2006.

[97] S. Tomioka, K. Kobayashi, K. Kudo, A. Murakami, and T. Mitani. Effects of injection configuration on performance of a staged supersonic combustor. *J. Prop. Power*, 19:876–884, 2003.

[98] S. Tomioka, A. Murakami, K. Kudo, and T. Mitani. Combustion tests of a staged supersonic combustor with a strut. *J. Prop. Power*, 17(2):293–300, 2001.

[99] S. M. Torrez, J. F. Driscoll, M. A. Bolender, M. W. Oppenheimer, and D. B. Doman. Effects of improved propulsion modelling on the flight dynamics of hypersonic vehicles. *AIAA Atmospheric Flight Mechanics Conference*, AIAA-2008-6386, 2008.

[100] S. M. Torrez, J. F. Driscoll, D. J. Dalle, and D. J. Micka. Scramjet engine model MASIV: role of mixing chemistry and wave interactions. *AIAA Joint Propulsion Conference*, AIAA-2009-4939, 2009.

[101] Stephen R. Turns. *An Introduction to Combustion.* McGraw-Hill, 2000, Second Edition.

[102] C. M. Vagelopoulos and J. H. Frank. An experimental and numerical study on the adequacy of CH as a flame marker in premixed methane flames. *Proc. Comb. Inst.*, 30:241–249, 2005.

[103] E. R. van Driest. The problem of aerodynamic heating. *Aero. Engrg. Rev.*, 15:26–41, 1956.

[104] J. Vandooren, L. Oldenhove de Guertechin, and P. J. Van Tiggelen. Kinetics in a lean formaldehyde flame. *Combust. Flame*, 64:127–139, 1986.

[105] L. Vanquickenborne and A. Van Tiggelen. The stabilization mechanism of lifted diffusion flames. *Combust. Flame*, 10:59–69, 1966.

[106] H. Wang and A. Laskin. A comprehensive kinetic model of ethylene and acetylene oxidation at high temperatures. Technical report, Internal Report, Department of Mechanical Engineering, University of Deleware, 1998.

[107] K. A. Watson, K. M. Lyons, C. D. Carter, and J. M. Donbar. Simultaneous two-shot CH planar laser-induced fluorescence and particle image velocimetry measurements in lifted CH4/air diffusion flames. *Proc. Comb. Inst.*, 29:1905–1912, 2002.

[108] P. Weigand, W. Meier, X. R. Duan, W. Stricker, and M. Aigner. Investigations of swirl flames in a gas turbine model combustor i. flow field structures, temperature, and species distributions. *Combust. Flame*, 144:205–224, 2006.

[109] C. R. Wilke. A viscosity equation for gas mixtures. *J. Chem. Phys.*, 18:517, 1950.

[110] K. Wohl and F. Welty. Spectrophotometric traverses through flame fronts. *Proc. Comb. Inst.*, 5:746–753, 1954.

[111] Y. Yamasaki and A. Tezaki. Non-linear pressure dependence of A-state fluorescence lifetime of formaldehyde. *Appl. Phys. B*, 80:791–795, 2005.

[112] Y. Yoon. *An experimental study of a generic supersonic combustor.* PhD thesis, University of Michigan, 1994.

[113] G. Yu, J. G. Li, X. Y. Chang, L. H. Chen, and C. J. Sung. Fuel injection and flame stabilization in a liquid-kerosene-fueled supersonic combustor. *J. Prop. Power*, 19:885–893, 2003.

[114] G. Yu, J. G. Li, X. Y. Zhang, L. H. Chen, B. Han, and C. J. Sung. Experimental investigation of flameholding mechanism and combustion performance in hydrogen-fueled supersonic combustors. *Comb. Sci. Tech.*, 174:1–27, 2002.

[115] G. Yu, J. G. Li, J. R. Zhao, L. J. Yue, X. Y. Chang, and C.-J. Sung. An experimental study of kerosene combustion in a supersonic model combustor using effervescent atomization. *Proc. Comb. Inst.*, 30:2859–2866, 2005.

[116] K. H. Yu, A. Trouve', and J. W. Daily. Low-frequency pressure oscillations in a model ramjet combustor. *J. Fluid Mech.*, 232:47–72, 1991.

[117] K. H. Yu, K. J. Wilson, and K. C. Schadow. Effect of flame-holding cavities on supersonic-combustion performance. *J. Prop. Power*, 17(6):1287–1295, 2001.